PhD degree in Systems Medicine (curriculum in Molecular Oncology)

European School of Molecular Medicine (SEMM),

University of Milan and University of Naples “Federico II”

Settore disciplinare: BIO/10

The E3 ubiquitin ligase HECW1 in neuronal homeostasis

Simona Sala

IFOM, Milan

Matricola n. R12077

Tutor: Prof. Simona Polo
IFOM, Milano
University of Milan

PhD Coordinator: Prof. Saverio Minucci

Anno accademico 2020-2021

Alla mia mamma e alla mia famiglia tutta,

"La cosa importante è non smettere mai di domandare. La curiosità ha il suo motivo di esistere. Non si può fare altro che restare stupiti quando si contemplano i misteri dell'eternità, della vita, della struttura meravigliosa della realtà. È sufficiente se si cerca di comprendere soltanto un poco di questo mistero tutti i giorni. Non perdere mai una sacra curiosità."

Albert Einstein

Table of contents

List of abbreviations

AD	Alzheimer's disease
AIP4	Atrophin-1 interacting protein 4
ALFY	Autophagy-linked FYVE protein
ALS	Amyotrophic lateral sclerosis
AMBRA1	BECLIN 1-regulated autophagy protein 1
AMOTL1	Angiomotin like 1
AMPAR	Amino-3-hydroxy-5-methyl-isoxazole-4-propionic acid receptor
AMPK	AMP-activated protein kinase
ANXA11	Annexin A11
ATG	Autophagy-related gene
BafA1	Bafilomycin A1
CAPRIN1	Cell cycle-associated protein 1
CN	Cortical neurons
CNS	Central nervous system
CQ	chloroquine
CRISPR	Clustered Regularly Interspaced Short Palindromic Repeats
DCP1/2	mRNA-decapping enzyme subunit 1/2
DCP1A	mRNA-decapping enzyme 1A
DDX6	DEAD-Box Helicase 6
DFCP1	Double FYVE domain- containing protein 1
DRG	Dorsal root ganglion
DUB	Deubiquitinating enzyme
Dvl-1	Dishevelled-1
E1	Ubiquitin-activating enzyme
E2	Ubiquitin -conjugating enzyme
E3	Ubiquitin-ligase
EDC3/4	Enhancer of mRNA-decapping protein 3 and 4
EEA1	Early Endosome Antigen 1
EGFR	Epidermal growth factor receptor
eIF	Eukaryotic translation initiation factor
ENaC	Epithelial cell sodium channel
EPG5	Ectopic P-Granules Autophagy Protein 5 Homolog
ER	Endoplasmic reticulum

ESCRT	Endosomal sorting complex required for transport
FACS	Fluorescence-activated cell sorting
FGFR	Fibroblast growth factor receptor
FIP200	Focal adhesion kinase family-interacting protein of 200 kDa
FMRP	Fragile X Mental Retardation Protein
FTD	Frontotemporal dementia
G3BP1	Ras GTPase-activating protein-binding protein 1
GABARAP	g-aminobutyric acid receptor-associated protein
GDNF	Glial cell line-derived neurotrophic factor
GFP	Green fluorescence protein
HAP1	Huntingtin-associated protein 1
HECT	Homologous to E6-AP carboxyl terminus
HECW1/2	HECT, C2 and WW domain-containing E3 ubiquitin ligase 1 and 2
HOPS	Homotypic fusion and protein sorting
HSCR	Hirschsprung's disease
Htt	Huntingtin
IF	Immunofluorescence
IGF-1R	Insulin-like growth factor-1 receptor
INPP5E	Phosphoinositide phosphatase inositol polyphosphate-5 phosphatase
IP	Immunoprecipitation
iPSC	Induced pluripotent stem cell
JIP1	JNK-interacting protein 1
KD	Knock down
kDa	Kilodalton
KIF1A	Kinesin Family Member 1A
KO	Knock out
LAMP1/2	Lysosomal associated membrane protein 1/2
LC3	microtubule-associated protein 1 light chain 3
LIR	LC3-interactin region
LLPS	Liquid–liquid phase separation
LC3	Microtubule-associated protein 1 light chain 3
MAP2	microtubule-associated protein 2
MEF	Mouse embryonic fibroblast
mRNP	messenger RNP complex
MS	Mass spectrometry

mTOR	Mammalian target of rapamycin
mTORC1	mTOR complex 1
MVB	Multivesicular body
NaAsO2	Sodium arsenite
NBR1	Neighbor of BRCA1 gene 1
NDP52	Nuclear dot protein of 52 kDa
NEDD4	Neuronal precursor cell-expressed developmentally downregulated gene 4
NPC	Neural precursor cell
OPTN	Optineurin
ORF	Open reading frame
PABP	3’poly-A tail binding protein
PAS	Phagophore assembly site
PAX6	Paired Box 6
PB	P-body
PCR	Polymerase chain reaction
PD	Parkinson's disease
PE	Phosphatidylethanolamine
PI(3,5)P_2	Phosphatidylinositol 3,5-bisphosphate
PI(3)P	Phosphatidylinositol 3-phosphate
PI(4,5)P2	Phosphatidylinositol 4,5-bisphosphate
PI(5)P	Phosphatidylinositol 5-phosphate
PI3K	Phosphoinositide-3-kinase
PI3KC3-C1/2	Class III phosphatidyl-inositol-3-kinase complex 1 and 2
PIC	Pre-initiation complex
PIK-fyve	PI(3)P 5-kinase Fab1
PINK1	PTEN-induced kinase 1
PLEKHM1	Pleckstrin homology domain-containing family M member 1
PTEN	Phosphatase and tensin homolog
PTM	Post-translational modification
Rab	Ras associated binding
Rap2-A	Ras-related protein 2A
Rapa	Rapamycin
RBP	RNA-binding protein
RBR	RING between RING
RING	Really Interesting New Gene

RNF4	Ring finger protein 43
RNP	Ribonucleoprotein
RRMs	RNA recognition motifs
RTA	RNA transport apparatus
RTK	Receptor tyrosine kinases
RTN3	Reticulon 3
SDS-PAGE	Sodium Dodecyl Sulphate – PolyAcrylamide Gel Electrophoresis
SG	Stress granule
sgRNA	Single guide RNA
shRNA	Short hairpin RNA
siRNA	Short interfering RNA
SMURF1/2	SMAD ubiquitination regulatory factor 1and 2
SNAP29	Synaptosomal-associated protein 29
SNARE	Soluble N-ethylmaleimide-sensitive factor-attachment protein receptor
SOD1	Superoxide dismutase-1
SOX2	Sex Determining Region Y-Box 2
STX17	Syntaxin 17
TAX1BP1	Tax1 binding protein 1
TDP-43	TAR-DNA binding protein-43
TEM	Transmission electron microscopy
TFEB	Transcription factor EB
TGF-β	Transforming growth factor-β
TGFBR1	TGF-β type I receptor
TIA1	T cell intracellular antigen 1
TIAR	TIA1-related protein
TOLLIP	Toll-interacting protein
TRAP-∂	Translocon-associated protein-∂
TrkA	Neurotrophic tyrosine kinase receptor type 1
TUJ1	class III beta-tubulin
Ub	Ubiquitin
UBAP2L	Ubiquitin Associated Protein 2 Like
UBD	Ubiquitin-binding domain
ULK1	Unc-51-like kinase-1
UTR	Untranslated region
VAMP8	Vesicle-associated membrane protein 8

VPS	Vacuolar protein sorting
WB	Western blot
WGA	wheat germ agglutinin
WIPI2	WD repeat domain phosphoinositide-interacting protein 2
WT	Wild type
WWP1/2	WW containing protein 1 and 2
XRN1	5'-3' Exoribonuclease 1

Figure index

Table index

Abstract

Ubiquitination is one of the most abundant and versatile post-translation modifications in eukaryotes that affects many biological processes by modifying protein activity, interactions, localization and stability of substrates. E3 ligases have a key function in the process, acting as molecular ubiquitin-substrate matchmakers and providing specificity to the reaction.

In this thesis, we aimed at characterizing the physiological and pathological functions of the human HECW1, a poorly studied E3 ligase which belongs to the NEDD4 family.

HECW1 is preferentially expressed in the central nervous system (CNS) and it has been linked to neurodegeneration, in particular to the familial form of Amyotrophic Lateral Sclerosis (fALS). The Drosophila orthologue Hecw, that we recently identified and functionally characterized, is similarly enriched in the CNS and is involved in the dynamic regulation of RNPs required for neuronal health. The Hecw/HECW1 interactome is enriched in proteins involved in the autophagy/endolysosomal pathway and RNPs dynamics, whose dysfunction promote neurodegenerative diseases. Together these data suggest a protective role of HECW1 in neuronal homeostasis.

To investigate into HECW1 physiological and disease-relevant neuronal function, we optimized a protocol to directly differentiate neurons from human iPSCs and we generated HECW1-KO iPSCs. We found that HECW1 expression in neurons is upregulated during differentiation and downregulated with aging, a typical behavior of components of the ubiquitin proteasome and autophagy pathways. Unbiased proteomic analysis showed deregulation of proteins involved in vesicle traffic and kinase activity in HECW-KO neurons. Targeted immunofluorescence, morphological and EM analysis revealed an accumulation of enlarged organelles positive for the autophagic and endo-lysosomal marker LAMP1 and of endolysosomal/autophagic compartments structures along filaments and in distal axons of HECW1-depleted

neurons. Moreover, distal tips of HECW1-KO neurons showed the accumulation of abnormal, static WGA-aggregates, indicating an impairment in endosomal traffic.

A second category of enriched HECW1 interactors is related to RNA metabolism. Co-immunoprecipitation analysis confirmed HECW1 interaction with the SG protein FMRP and the PB component EDC3. We also measured an increase number of constitutive PBs in HECW1-depleted neurons, suggesting a possible regulatory role of HECW1 in constitutive PB formation or clearance. The two phenotypes observed in HECW1-depleted neurons could be functionally linked, considering the involvement of autophagy in the clearance of persistent RNPs arising from chronic stress or disease mutations.

Taken together, our results have uncovered an involvement of HECW1 in the regulation of the autophagy/endolysosomal pathway in neurons and a possible contribution in controlling the homeostasis of ribonucleoprotein particles. Future studies in motor neurons would help to understand the implications of these results for ASL, a disease where dysregulation of RNA metabolism, cytoplasmic mislocalization of RNA binding proteins and dysfunction in RNP dynamics, along with autophagy impairments appear to be at the basis of the pathogenesis.

1 INTRODUCTION

1.1 Ubiquitination

Ubiquitination is a post-translational modification (PTM) that regulates many biological processes, thus influencing protein stability, localization, activity, interactions and, ultimately, cellular fate (Kerscher et al., 2006). By targeting a large number of cellular proteins, ubiquitination affects virtually all biological pathways including those involved in cell cycle, development, growth, differentiation, cell death, inflammation, autophagy, protein trafficking, and intercellular communication (Dye and Schulman, 2007; Vijay-Kumar et al., 1987).

Ubiquitination, which is a conserved process in all eukaryotic cells, consists in the covalent attachment of a 76 amino acids peptide, ubiquitin (Ub), to target proteins by the sequential action of three classes of enzymes: ubiquitin-activating enzymes (E1s), ubiquitin-conjugating enzymes (E2s) and ubiquitin-ligases (E3s) (Berndsen and Wolberger, 2014) (**Fig. 1**). During this enzymatic cascade, Ub is first activated on its C-terminal glycine (G76) by the E1 enzyme in an ATP-dependent manner, resulting in a high-energy thioester linkage between ubiquitin and the catalytic cysteine of the enzyme. The activated Ub is then transferred to the catalytic cysteine of the E2 enzyme in a trans-thiolation process, and finally covalently attached to a specific substrate by the E3 ligase. Deubiquitinating enzymes (DUBs) ensure the reversibility of this process by removing ubiquitin from the substrates.

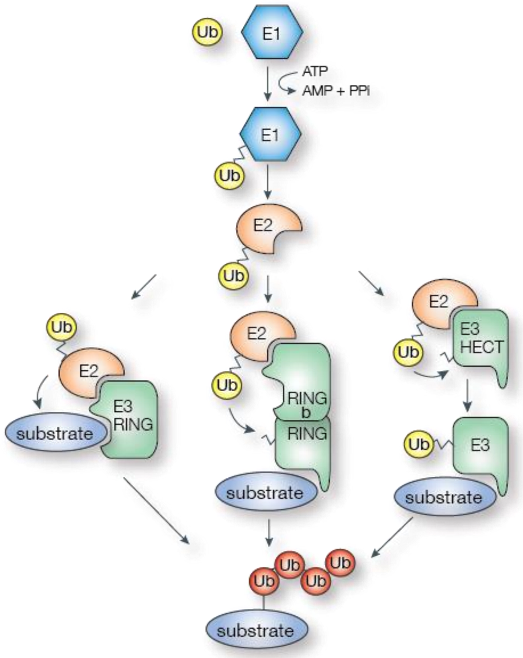

<u>Figure 1 The ubiquitin pathway</u>

Schematic representation of ubiquitination reaction mediated by an E1 ubiquitin-activating enzyme (E1, blue), an E2 ubiquitin-conjugating enzyme (E2, orange) and an E3 ubiquitin ligase (green). Three classes of E3 ubiquitin ligases have been identified: RING ligases (left), RBR (RING-between-RING) ligases (middle), and HECT ligases (right)(adapted from (Woelk et al., 2007).

E3-mediated conjugation to a substrate protein or another Ub moiety is achieved through the formation of an isopeptide bond between the C-terminus of ubiquitin and the ε-amino group of a lysine residue on the substrate protein or Ub itself (Pickart, 2000), or, less commonly, the amino-terminal (N-terminal) methionine of the substrate (Ciechanover and Ben-Saadon, 2004).

Substrates can be mono-, multi- or poly-ubiquitinated where Ub is assembled into polymeric chains through ubiquitination of any of the seven internal lysine residues (Lys6, Lys11, Lys27, Lys29, Lys33, Lys48, and Lys63) or the α-amino group of the N-terminal methionine (Met1) within ubiquitin itself (polyubiquitination) (Swatek and Komander, 2016) (**Fig. 2**). The sequential ubiquitination results in the assembly of different types of homotypic polyubiquitin chains, where Ub is always linked through the same residue, or heterotypic chain, if there are different linkages within the same polymer. Among the heterotypic chains, we can distinguish between mixed chains, with different lysine linkages at successive chain positions, and branched chains, where one ubiquitin moiety is decorated with at least two ubiquitin molecules, forming a fork-shaped polymer (Kulathu and Komander, 2012). Collectively, these multiple types of chains are referred to as the 'ubiquitin code' (Komander and Rape, 2012).

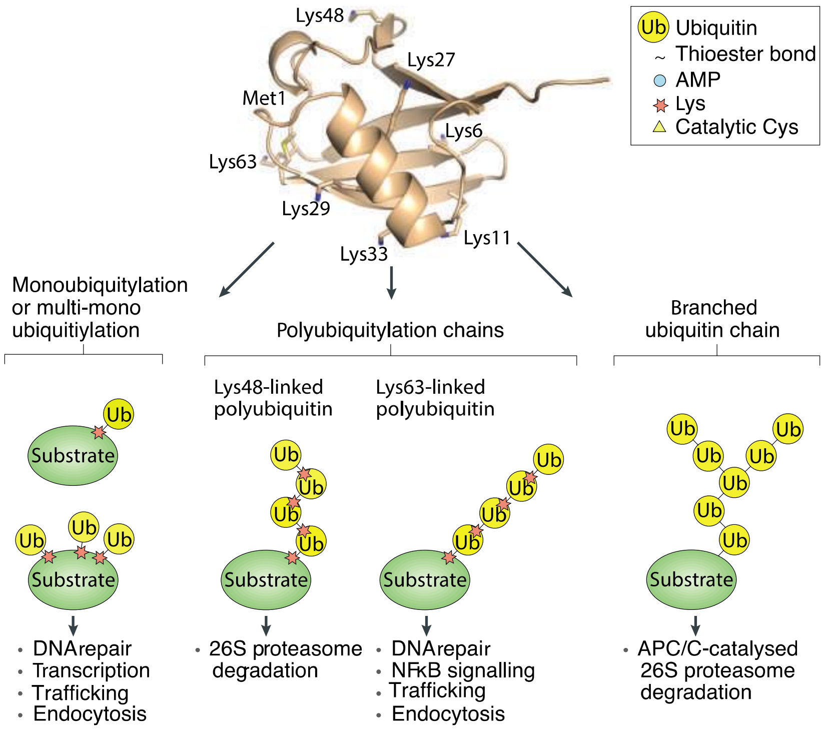

Figure 2 The ubiquitin code

The Ubiquitin molecule. The N-terminus methionine and all the lysine residues involved in chains formation are highlighted. Schematic representation of different types of substrate ubiquitination (Ub in yellow) such as mono, multi-monoubiquitination, polyubiquitin chains and branched ubiquitin chains. Potential outcomes of substrate proteins conjugated with the given ubiquitin linkage are indicated (adapted from (Buetow and Huang, 2016).

As in a code, different Ub modifications are interpreted by the cell as a distinct signal, leading to different outcomes (**Fig. 2**). Mono-ubiquitination influences interaction or localization patterns (Hicke, 2001) and acts preferentially as a non-proteolytic signal to control gene expression, viral budding, DNA repair, and endocytosis (Sigismund et al., 2004). Among the poly-ubiquitin chains, K63- and K48-linked chains are the best characterized. Ubiquitin chains connected through K48 are the most abundant and trigger degradation by the 26S proteasome, a multi-catalytic proteolytic system that degrades polyubiquitinated unfunctional or misfolded proteins into peptides. On the contrary, K63-linked chains are non-proteolytic signals involved in the regulation of many cellular processes, such as DNA repair (Hoege et al., 2002; Stewart et al., 2009), membrane protein trafficking, and endocytosis (Acconcia et al., 2009). This type of chains also regulates the assembly of protein complexes (Spence et al., 2000), such as the mRNA splicing machinery, one of the most dynamic complexes in human cells, in which distinct steps of the splicing reaction are regulated by K63-linked chains (Song et al., 2010). Moreover, K63-linked Ub chains have been linked to the formation of inclusion bodies, aggregates of proteins associated with many neurodegenerative diseases, and the selective degradation of protein aggregates and organelles by autophagy (Tan et al., 2008).

The functional role of the other Ub chains is less characterized (Swatek and Komander, 2016). K6-linked chains have been linked to mitochondria quality control (Akutsu et al., 2016), while K11-linked chains were shown to be involved in proteasomal degradation of cell cycle proteins (Meyer and Rape, 2014). K27 linkages are involved in DNA damage response (Gatti et al., 2015) and innate immunity, while K29-linked chains were suggested to contribute to the negative regulation of Wnt signaling (Akutsu et al., 2016). K33-linked chains have non-degradative functions, working as negative regulators of T-cell antigen receptors and AMPK (AMP-activated protein kinase)-related protein kinase (Akutsu et al., 2016) as well as in post-Golgi protein trafficking (Yuan et al., 2014). Finally, linear M1-linked chains play a key role in inflammatory and immune responses by regulating the activation of the transcription factor NF-κB (Iwai et al., 2014).

Furthermore, Ub molecules themselves can be modified by PTMs, such as acetylation and phosphorylation, thus providing a higher degree of variability in the signal that this modification can generate (Herhaus and Dikic, 2015; Wertz and Dixit, 2008).

1.1.1 E3 ligases: catalysts and matchmakers of the Ubiquitin cascade

While the human genome encodes only for two E1 enzymes and about 40 different E2 enzymes, there are more than 600 different E3 ligases with which E2 enzymes can interact, determining the specificity along the cascade. The recognition of the right target is a key step in the ubiquitination process. Indeed, each singular E3 ligase is able to recognize and ubiquitinate a panel of substrates with high specificity (Buetow and Huang, 2016). Thus, the E3 ligases act both as a catalyst for the reaction, greatly increasing the rate of Ub transfer, and as molecular matchmakers, capable of conferring a high degree of specificity toward substrates and the Ub chain linkage built on them (Berndsen and Wolberger, 2014; Buetow and Huang, 2016).

According to their structure and mechanism of action, E3 ligases are divided into three major classes (**Fig. 1**): the largest class is the RING (Really Interesting New Gene/U-box)-type E3s with about 600 members (Metzger et al., 2014), followed by the HECT (Homologous to E6AP C-Terminus)-type E3s with 28 members (Rotin and Kumar, 2009; Sluimer and Distel, 2018), and the RBR (RING between RING)-type E3s with 14 members (Dove and Klevit, 2017; Reiter and Klevit, 2018; Weber et al., 2019).

RING E3 ligases regulate crucial cellular functions, such as cell cycle, DNA repair, cell signaling, and responses to hypoxia (Deshaies and Joazeiro, 2009). These ligases act as allosteric activators of the E2 enzymes and as a scaffold that simultaneously binds the E2-Ub and the substrate to bring them in close proximity, allowing the direct transfer of the Ub molecules from the E2 enzyme to the target (Dou et al., 2012; Plechanovova et al., 2012). RINGs can act as components of multiprotein complexes, such as in the case of the Cullin-based E3 ligases (Deshaies and Joazeiro, 2009) or as monomeric enzyme. A well-studied example of this latter class is Mdm2, a key degrader of the tumor suppressor p53 (Linke et al., 2008).

The HECT E3 ligases are implicated in protein trafficking, signaling pathways that regulate cell growth, proliferation, and immune response (Rotin and Kumar, 2009).

These enzymes are defined by the presence of the catalytic HECT domain, a 350-residue module first characterized in the human E3 ligase E6-associated protein, E6AP (Huibregtse JM1, 1995) and invariably positioned at the C-terminal of the protein. HECTs catalyze substrate ubiquitination in a two-step reaction: first, they accept and load the activated Ub from the E2 enzyme on their catalytic cysteine via a trans-thiolation reaction; successively, the Ub molecule is transferred to a lysine on the target substrate. According to the domain organization present in the N-terminal part of the proteins, the mammalian HECT E3 ligases can be subdivided into three main sub-families (Scheffner and Kumar, 2014; Weber et al., 2019). The best characterized group is the NEDD4 (Neuronal precursor cell-expressed developmentally downregulated gene 4) family, consisting of nine members in human. This family is characterized by the presence of a C2 domain and two to four WW domains (Fajner et al., 2017) and will be described in detail in the following paragraphs. The second class, the HERC family, is composed of six members and is characterized by one or more regulators of chromatin condensation 1 (RCC)-like domains (RLD) (Sanchez-Tena et al., 2016). The remaining 13 HECTs do not share specific domains at the N-terminus and, for this reason, are classified as “other” HECT ligases (Scheffner and Kumar, 2014; Weber et al., 2019).

The RBR E3 ligases are defined by a RING-HECT-hybrid mechanism that utilizes a E2-binding RING domain, which acts as a scaffold, and a second atypical RING domain (called RING2) that contains a catalytic cysteine that is required for the formation of the E3-Ub intermediate (Metzger et al., 2012; Wenzel and Klevit, 2012). Members of this E3 ligase family mediate various processes, such as regulation of PTMs and protein stability, cellular and stress signaling, cell-cycle control, transcription, RNA metabolism, and translation (Eisenhaber et al., 2007). One of the most studied RBR enzyme is Parkin, whose mutations in the RBR domain are associated with Parkinson's disease (PD) (Shimura et al., 2012).

1.2 NEDD4-family

1.2.1 Domain description

The human NEDD4 family consists of nine members (**Fig. 3**): NEDD4 (also known as NEDD4-1), NEDD4-like (NEDD4-L, also known as NEDD4-2), atrophin-1 interacting protein 4 (AIP4, also known as ITCH), SMAD ubiquitination regulatory factor 1and 2 (SMURF1 and SMURF2), WW containing protein 1 and 2 (WWP1 and WWP2), HECT, C2 and WW domain-containing E3 ubiquitin ligase 1 and 2 (HECW1 and HECW2, also known as NEDL1 and NEDL2); all of which share a common domain architecture with unique functional properties. Starting from the N-terminus, they present a membrane/lipid-binding C2 domain that is responsible for cellular localization, two-to-four WW domains that are involved in substrate interaction, and the catalytic HECT domain at the C-terminus (Fajner et al., 2017; Scheffner and Kumar, 2014).

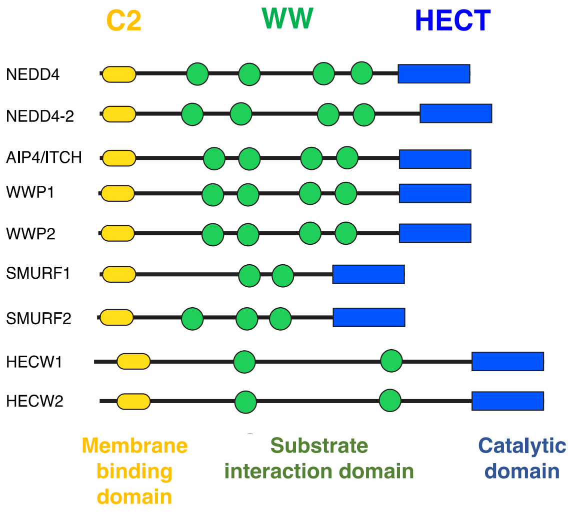

Figure 3 The human NEDD4 family of E3 ligases

Schematic representation of the domain architecture of the nine NEDD4 family members. The C2-WW-HECT E3 modular structure consist of an N-terminal Ca2+/ lipid-binding (C2) domain (yellow oval), a central region containing WW domains (green circles), and a ubiquitin-protein ligase HECT domain (blue rectangles).

The C2 domain is a ~130-residue module, folded in an eight-stranded beta-sandwich structure and was originally described as a calcium-dependent phospholipid binding domain of the protein kinase C (Coussens et al., 1986). Since its discovery, a wide variety of C2-carrying proteins have been identified, pointing to a great functional diversity of this domain. Indeed, the C2 domain can bind calcium, phospholipids, inositol phosphate, as well as proteins (Corbalan-Garcia and Gomez-Fernandez, 2014; Fajner et al., 2017).

The name of the WW domain derives from the presence of two conserved tryptophan residues separated by 20 to 22 amino acids. Structured as a compact module folded in three stranded antiparallel beta-sheets, this domain forms a hydrophobic core where ligand binding occurs (Verdecia et al., 2000). WW domains have a key role in mediating protein–protein interactions via recognition of proline-rich motifs and phosphorylated serine/threonine-proline sites present on the substrate. Found in a variety of unrelated proteins, these domains are further classified into four classes according to the sequence motifs they recognize (Ingham et al., 2005; Sudol and Hunter, 2000). NEDD4 E3 ligases bear the class I type domains, which are able to bind PY motifs (L/PPxY). Notably, WW domains in the same E3 ligase may function independently and can have distinct binding preferences (Persaud et al., 2009). Thus, the WW-rich region in NEDD4 family members serves as a scaffold to recruit proteins and regulators, and provides these enzymes with a versatile platform that still is not fully characterized.

The HECT domain, the defining structural element of this class of ligases, is composed of a bi-lobed structure with a bulkier N-terminal lobe (N-lobe) that contains the E2 binding site and the Ub-binding exosite, a non-covalent Ub-binding site required for enzyme processivity, and a smaller C-terminal lobe (C-lobe) carrying the catalytic cysteine involved in the Ub transfer (Huang L, 1999) (**Fig. 4**). The two lobes are connected by a flexible hinge region that allows the C-lobe to move. This free movement is fundamental for the juxtaposition of the cysteine residues of the E2 enzymes and the E3 ligases during the Ub transfer for the nucleophilic attack of the target lysine to the HECT-ubiquitin (Kamadurai et al., 2013; Kamadurai et al., 2009; Verdecia MA, 2003). In addition to the key catalytic cysteine, some strictly conserved acidic residues present in the C-terminal part of the HECT domain were demonstrated to be fundamental for a proper catalysis (Maspero et al., 2013), potentially contributing to the formation of the active catalytic site, and aiding the positioning of the acceptor Ub.

Importantly, the ability to build linkage-specific Ub-chains via a sequential addition mechanism is an intrinsic feature of the HECT domains, independently from the E2 enzyme that they are coupled with (Sheng et al., 2012). Indeed, the C-terminal part of the C-lobe of the HECT domain possesses all the critical features for chain type specificity, as the substitution of the last three NEDD4 amino acids with the E6AP sequence (not a NEDD4 family member) changes the specificity of the Ub-chain product from pure K63-linked chains, typically created by this family, toward a mixture of K48- and K63-linked chains (Kim and Huibregtse, 2009; Maspero et al., 2013).

Although the NEDD4 family is known to specifically form mono-ubiquitination or K63-linked Ub chains, a few studies reported that NEDD4 substrates are targeted for proteasome-mediated degradation (Fang et al., 2014). A possible explanation is that Ub chain formation can occur in two distinct phases: an initial phase in which chains are synthesized in a unidirectional manner and are linked exclusively through Lys-63 of Ub, followed by a second phase, when chains are elongated in a multidirectional fashion characterized by the formation of mixed Ub linkages and branched structures recognized by the proteasome (French et al., 2017). In addition, NEDD4 can generate K11 linkages, even if at a lower efficiency, and substrates modified in this way are targeted for degradation (Platta et al., 2012). Additional possibilities are represented by specific HECT adaptors that can modify the specificity of chain elongation or by associated DUBs that can further edit the Ub chains generated.

1.2.2 Regulation of HECT activity

In order to prevent excessive ubiquitination of substrates or misdirected auto-ubiquitination that may cause E3 ligase instability, the expression level and the activity of E3 ligases must be finely regulated.

While E3 ligase expression can be controlled by tissue-specific transcription and cellular microenvironment; E3 ligase catalytic activity is regulated in multiple ways, including PTMs, intra- and intermolecular interactions with specific adaptors or DUBs, as well as the strength of E2–E3 interaction (Fajner et al., 2017; Shah and Kumar, 2021) (**Fig. 4**).

One of the commonly employed mechanisms of modulation of the catalytic activity is represented by an intramolecular interaction between the N- and C-terminal regions of the HECT proteins. A pioneering work demonstrated that in the absence of *bona fide* substrates, a subset of NEDD4-family E3 ligases (SMURF2, NEDD4 and NEDD4L) are kept in a catalytically inactive state by intramolecular interaction between the C2 domain and the HECT domain (Wiesner et al., 2007). Subsequent structural studies showed that, in this close conformation, the C2 binds the N-lobe of the HECT and locks the C-lobe in a catalytically incompetent conformation, interfering with Ub thioester formation (Mari et al., 2014; Maspero et al., 2013) (**Fig. 4A**). The intramolecular interaction can also occur via the central region of the enzyme, as is the case of the linker between the WW2 and the WW3 domains of the E3 ligase WWP2, called the 2,3-linker (Chen et al., 2017) (**Fig. 4B**). Different inhibitory conformations may easily coexist and synergize in the same HECT E3 ligase to achieve full enzyme inhibition (Fajner et al., 2017; Wang et al., 2019).

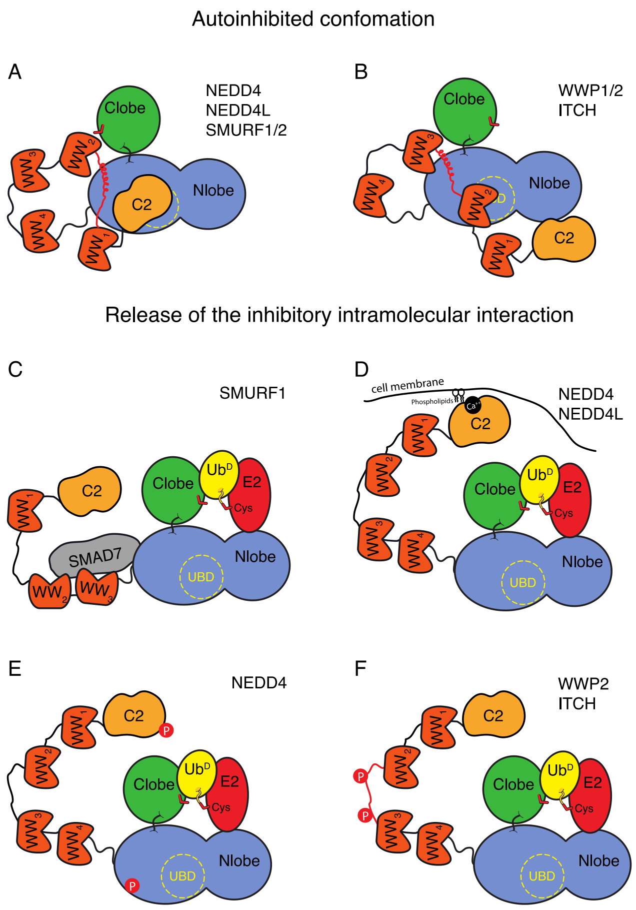

Figure 4 Mechanisms of NEDD4 HECTs regulation

Schematic representation of the intramolecular interactions occurring in NEDD4 family members: N-lobe is in blue, C-lobe is in green, WW domains in orange and C2 in dark yellow.

(A) In NEDD4, NEDD4L and SMURF1-2 the C2 domain mediates the autoinhibited conformation. The C2-binding surface overlaps with the ubiquitin-binding exosite (depicted as yellow dashed circle on the N-lobe) of the N-lobe and locks the C-lobe in a catalytically incompetent conformation.

(B) In WWP1-2 and ITCH, the linker between WW2 and WW3 domain locks the HECT domain in an inactive conformation, blocking the ubiquitin -binding exosite.

Inactive conformations can be released by (C) adaptor binding, (D) Ca2+ flux, (E, F) phosphorylation events (adapted from (Fajner et al., 2017; Wang et al., 2019).

A release of the auto-inhibitory conformation and full ligase activation can occur in various ways (Polo, 2012). In some cases, adaptor proteins may work as activators, like in the case of SMURF2 that is activated by its adaptor protein SMAD7 (**Fig. 4C**). By releasing the C2-mediated auto-inhibition, stimulating the binding of an E2 enzyme, and recruiting SMURF targets, SMAD7 functions at multiple levels to control E3 ligase activity and to ensure specificity in SMURF-catalyzed ubiquitination (Ogunjimi et al., 2005). In other cases, release from inhibition is mediated by signaling as demonstrated by the calcium-mediated membrane translocation of the C2 that re-localizes NEDD4L releasing the HECT activity (Escobedo et al., 2014) (**Fig. 4D**). Another well-characterized example is represented by the receptor tyrosine kinases (RTKs) activation of NEDD4 (Persaud et al., 2009; Persaud et al., 2014): upon epidermal growth factor receptor (EGFR) and fibroblast growth factor receptor (FGFR) activation, a set of tyrosine phosphorylation events in the C2 and HECT domains induced by the downstream tyrosine kinase Src releases the NEDD4 autoinhibitory conformation (Persaud et al., 2009) (**Fig. 4E**). A similar phosphorylation-based mechanism of activation was demonstrated for AIP4 (Gallagher et al., 2006) and, more recently, for WWP2 (Chen et al., 2017) (**Fig. 4F**).

1.2.3 Function in physiology and disease

Each member of the NEDD4 family is involved in various biological mechanisms including protein trafficking, endocytosis, subcellular localization, viral budding, signaling, cellular growth, DNA damage response, and proliferation (Rotin and Kumar, 2009). It is, thus, not surprising that alterations in this family of E3 ligases are implicated in several diseases, spanning from cancer to neurological disorders (Scheffner and Kumar, 2014).

NEDD4 and NEDD4L share ~60% similarity, but present a different expression profile. While NEDD4 is ubiquitously expressed, NEDD4L is selectively expressed in liver, kidney, brain, lung, and heart (Kamynina et al., 2001). Both NEDD4 and NEDD4L play a crucial role in the regulation of electrolyte homeostasis by controlling the surface abundance of the epithelial cell sodium channel (ENaC) subunits (Harvey and Kumar, 1999; Staub et al., 1997). ENaC is expressed in the apical part of epithelial cells, highly expressed in kidney, lung, heart, brain, and colon, where it regulates sodium homeostasis in response to hormones (Rossier et al., 2002). NEDD4 and, especially, NEDD4L are able to bind the PPxY motifs in the C-terminal tail of ENaC and to ubiquitinate the channel (Harvey et al., 2001), causing its internalization and lysosomal degradation (Rotin et al., 2001; Snyder, 2005). Mutations or deletions of the PPxY motif result in the disruption of the interaction between NEDD4/L and ENaC, causing the Liddle's syndrome, a severe disorder that consists in sodium retention and hypertension (Abriel et al., 1999). NEDD4/L activity has been associated with the ubiquitination of other transporters as well, as in the case of the dopamine transporter (DAT) by NEDD4L and the cationic amino acid transporter (CAT-1) by both NEDD4 and NEDD4L (Vina-Vilaseca et al., 2011).

The NEDD4 family has a major role in the regulation of endocytosis and sorting of numerous signaling receptors and transmembrane protein (Polo, 2012) including the epidermal growth factor receptor EGFR (Katz et al., 2002), the insulin-like growth factor-1 receptor (IGF1R) (Cao et al., 2008), the fibroblast growth factor receptor FGFR (Persaud et al., 2011) the hepatocyte growth factor-regulated tyrosine kinase substrate (HGS) (Katz et al., 2002), the guanine nucleotide exchange factor CNrasGEF (Pham and Rotin, 2001), the lysosomal protein LAPTM5 (Pak et al., 2006), and the β2- adrenergic receptor through the adaptor function of β-arrestin proteins (Shenoy et al., 2008). The NEDD4 family members function either as a positive or a negative regulator of transmembrane signaling receptors.

NEDD4 acts as a positive regulator for the IGF-1/Akt kinase signaling in mouse embryonic fibroblasts (MEFs). NEDD4−/− MEFs show a decreased abundance of cell surface IGF1R, reduced mitogenetic activity, and cell growth (Cao et al., 2008). Conversely, NEDD4-dependant ubiquitination of the EGFR results in the down-regulation of the receptor (Katz et al., 2002). EGF stimulation promotes ubiquitination of the EGFR, which recruits the Ub interacting motif (UIM)-containing endocytic adaptors EPS15 and EPSIN-1 to the plasma membrane and, subsequently, HRS to the endosomal membrane. These adaptors are ubiquitinated by NEDD4 through a process known as coupled mono-ubiquitination, which directs the progression of the ubiquitinated receptors toward lysosomal degradation (Polo, 2012; Savio et al., 2016; Woelk et al., 2006). Furthermore, NEDD4 plays a role in viral budding where it ubiquitinates HTLV-1 Gag protein, favoring the release of HTLV-1 viral particles from the cell (Blot et al., 2004).

The transforming growth factor-β (TGF-β) signaling pathway, which regulates cell growth, cell differentiation, apoptosis, and cellular homeostasis, is regulated by several NEDD4-family members. For example, SMURF1 downregulates TGF-β signaling by interacting with the TGF inhibitory Smad7 in the nucleus, causing the translocation of the SMURF1–Smad7 complex to the cytoplasm; SMURF1 then associates with the TGF-β type I receptor (TGFBR1) at the plasma membrane to target it for degradation (Tajima et al., 2003). Previous work indicated that SMURF2 and WWP1 are able to induce the downregulation of TGF-β signaling through the degradation of TGFBR via the Ub-proteasome pathway (Zhang et al., 2001). WWP1 and SMURFs are expressed with distinct patterns in human tissues and carcinoma cell lines, suggesting unique pathophysiological roles for WWP1 and SMURFs. In addition, SMURF2 can ubiquitinate the TGF-signaling activator Smad3, attenuating its activity and, consequently, the TGF-β signaling in the cell (Tang et al., 2011).

From the pathological point of view, NEDD4 family members are frequently overexpressed in different types of cancers, including non-small cell lung cancers (NSCLC), gastric carcinomas, bladder carcinoma, prostate carcinoma, and colorectal carcinomas, and are thought to be a promising anti-cancer drug target (Ye et al., 2014). NEDD4 has been shown to have a role in the development of NSCLCs (Amodio et al., 2010). Knockdown of NEDD4 markedly reduces NSCLC cell proliferation and tumor growth, whereas NEDD4 overexpression facilitates growth of non-transformed lung epithelial cells and the loss of tumor suppressor phosphatase and tensin homolog

(PTEN) (Amodio et al., 2010). However, the role of NEDD4 on PTEN fate has not been validated in further studies performed in NEDD4 knockout mice (Fouladkou et al., 2008).

AIP4 has been involved in the ubiquitination and endocytosis of the Notch receptor and the G-coupled receptor CXCR4 (Chastagner et al., 2008; Marchese et al., 2003). In addition, it plays a role in the immune response and regulates T lymphocyte differentiation by promoting ubiquitination of Jun proteins (Liu, 2007). Furthermore, an emerging number of AIP4 protein targets has been implicated in tumorigenesis and chemosensitivity, such as the p53 family members p63 and p73 (Bernassola et al., 2008).

An oncogenic role has been proposed also for WWP1 based on its gene amplification in 40% of breast and prostate cancers (Chen et al., 2007). The Kruppel-like factors tumor suppressor proteins KLF2 and KLF5 (Chen et al., 2005), and p53 (Laine and Ronai, 2007) are targets of WWP1. WWP1-dependant p53 ubiquitination causes its stabilization and accumulation in the cytoplasm, while inactivating its transcriptional activities (Laine and Ronai, 2007).

SMURF2 overexpression was reported in several types of cancer, in particular in pancreatic and in esophageal squamous cells carcinoma where its aberrant expression was correlated with higher invasiveness (Fukuchi et al., 2002). SMURF1 has been shown to support breast cancer cell growth by facilitating estrogen receptor α signaling, which promotes breast cancer progression (Yang et al., 2018).

NEDD4 and NEDD4L have a significant role in the neuronal context, as they regulate different critical stages of neuronal development and brain function, such as neuronal cell fate determination, neurite outgrowth, axon guidance, and neuronal cell survival.

NEDD4-mediated ubiquitination of the Ras-related protein Rap2A (Rap2A), a negative regulator of neurite outgrowth, inhibits its function, causing a reduction in Rap2A effector kinase activity and enhances neurite development (Kawabe et al., 2010).

NEDD4L mediates multiple mono-ubiquitination of the neurotrophic tyrosine kinase receptor type 1 (TrkA), leading to receptor internalization and sorting toward the late endosome/lysosome pathway (Georgieva et al., 2011).

ENaC is also present in the brain and an increased expression of ENaC has been detected in the brain of NEDD4L null mice, resulting in an increase of sodium levels in the cerebrospinal fluid and highlighting a possible role in salt-induced hypertension (Van Huysse et al., 2012).

In addition, ion channels responsible for excitability and protein involved neurotransmitter signaling have been shown to be targets for NEDD4 and NEDD4L (Donovan and Poronnik, 2013).

NEDD4L regulates the abundance of the glutamate transporters EAAT, EAAT2 and EAAT3/4 (Sopjani et al., 2010), and is therefore a key regulator of an appropriate balance of glutamate at synapses. NEDD4, on its part, regulates glutamate Amino-3-hydroxy-5-methyl-isoxazole-4-propionic acid receptors (AMPARs). In hippocampal neurons, NEDD4-dependat ubiquitination of GluA1-containing AMPARs results in receptor internalization and trafficking to the lysosome (Lin et al., 2011). In the neurodegenerative Alzheimer's disease (AD), the accumulation of the pathogenic peptide amyloid-β (Aβ) decreases surface AMPARs, dendritic spine density and synaptic strength, and alters synaptic plasticity. This reduction in surface AMPARs is mediated by NEDD4-dependant ubiquitination, indicating an important role for NEDD4 and Ub in the synaptic dysfunction associated with the disease (Rodrigues et al., 2016).

In addition, NEDD4 catalyzes the K63-linked polyubiquitination of α-synuclein, a major constituent of Lewy bodies, which are neuropathological markers for PD, and other α-synucleinopathies, which are then targeted to the endosomal-lysosomal pathway (Sugeno et al., 2014; Tofaris et al., 2011).

1.2.3.1 HECW1 and HECW2

HECT, C2 and WW domain-containing E3 ubiquitin ligase 1 (HECW1) and HECW2 represent the largest but less studied members of the NEDD4 family. The genes of HECW1 and HECW2 are located on chromosomes 7 and 2, respectively. These proteins share 69% sequence identity: the amino acid sequences of the catalytic HECTs are 93% identical, and the WW1 and WW2 are 97% and 82% identical, respectively. The major differences lie in the N-terminal unstructured regions of the proteins.

According to the Human Protein Atlas, HECW1 is more selectively expressed, being predominantly present in the central nervous system (CNS) and weakly expressed in the kidney. HECW2 is expressed at the level of the CNS, but also in lung, spleen, testis, and placenta.

1.2.3.2 HECW1

Very little is known about HECW1 in terms of potential functions and substrates. The few reported data suggest its involvement in neurodegenerative diseases. In particular, Nakagawara and co-workers proposed an involvement of HECW1 in the familial form of the ALS (fALS) that arises from germ line mutations in the superoxide dismutase-1 (SOD1) gene (Miyazaki et al., 2004). The authors first identified HECW1 as a component of the Lewy body-like hyaline inclusions in the spinal cord of fALS patients and mutated SOD1 transgenic mice, along with mutant forms of SOD1, the translocon-associated protein-∂ (TRAP-∂) and Dishevelled-1 (Dvl-1). The authors identified Dvl-1 and mutant SOD1 (but not wild type SOD1) as targets for HECW1-dependant ubiquitination and suggested that mutant SOD1, HECW1, Dvl-1, and TRAP-∂ form a complex of ubiquitinated proteins that may lead to motor neuron death in fALS. In addition, transgenic mice overexpressing the human HECW1 developed ALS-like symptoms, such as motor neuron degeneration and muscle atrophy (Zhang et al., 2011). These data, together with the preferential expression of HECW1 in neuronal tissue, suggest the involvement of HECW1 in the pathophysiology of this neurodegenerative disease.

In a cancer context, HECW1 appears to have a positive activity. It was found to be significantly expressed at higher levels in favorable neuroblastomas compared to unfavorable ones (Miyazaki et al., 2004). In neuroblastoma cell lines, HECW1 binds to p53 and enhances its transcriptional activity and pro-apoptotic function, and the expression of both proteins is increased upon cisplatin (CDDP)-mediated apoptosis (Li et al., 2008). A luciferase reporter assay showed that HECW1 enhances the transcriptional pro-apoptotic activity of p53 in a catalytically-independent manner (Li et al., 2008). In addition, the RING ubiquitin ligase Ring finger protein 43 (RNF43) interacts with HECW1 and p53, and suppresses p53-mediated transcriptional activity, suggesting that RNF43 functions as a negative regulator of HECW1 (Shinada et al., 2011). HECW1 was also involved in the regulation of ErbB4, a member of the EGFR family that is important for mammary epithelial cell proliferation and survival (Li et al., 2009). Knockdown of WWP1, AIP4 and HECW1 in T47D breast cancer cell line additively increase the endogenous ErbB4 protein levels in the cells, suggesting a beneficial role of these three E3 ligase in suppressing the ErbB4 expression and function in breast cancer (Li et al., 2009). Finally, HECW1 may have a role in neurofibromatosis type I (NF1); a common autosomal dominant inherited disease characterized by the development of both benign and malignant tumors. Malignant samples revealed a recurrent amplification for a 43 kb region in chromosome band

7p14 (4309182 bp to 43132835 bp), which partially contained the HECW1 gene (Mantripragada et al., 2009).

1.2.3.3 HECW2

Nakagawara and colleagues identified the HECW2 E3 ligase as a p73 interactors, and found that it binds the C-terminal PY motifs of p73 and catalyzes its ubiquitination *in vitro*, leading to its stabilization and enhanced p73-dependent transcriptional activation (Miyazaki et al., 2003). Thus, it seems that both HECW1 and HECW2 are involved in the stabilization and the enhancement of the transcriptional modulatory functions of p53 family members, but with different mechanisms.

HECW2 is regulated during the cell cycle and is ubiquitinated and degraded by the anaphase promoting complex APC/C-Cdh1 during mitotic exit. The function of HECW2 during mitosis is essential, indeed, its depletion causes a marked delay of the metaphase-anaphase transition and its overexpression induces chromosomal mis-segregation, which may induce tumorigenesis (Lu et al., 2013). HECW2 knockout mice show a low body weight, bowel motility defects and die two weeks after birth (Wei et al., 2015). In the same paper, HECW1 KO mice were reported with no phenotype. Further experiment revealed that HECW2 is required for the enteric nervous system (ENS) development, and positively regulates enteric neural precursor proliferation through the glial cell line-derived neurotrophic factor (GDNF)/Akt signaling pathway (Wei et al., 2015). This pathway is essential for proper kidney development and, accordingly, 1/3 of HECW2 knockout mice displayed postnatal unilateral or bilateral kidney hydronephrosis (Qiu et al., 2016).

In another study, O'Donnel and colleagues reported the expression of HECW2 in the human colon and investigated its potential involvement in Hirschsprung's disease (HSCR), a heterogeneous genetic disorder characterized by the absence of ganglion cells in the distal intestine due to a failure of neural crest cells migration (O'Donnell et al., 2016). Compared to normal controls and the ganglionic region of HSCR, HECW2 protein level is markedly decreased in the a-ganglionic region of HSCR, suggesting a critical role for this E3 ligase in the pathophysiology of HSCR (O'Donnell et al., 2016).

HECW2 is also a potential regulator of angiogenesis via its substrate Angiomotin like 1 (AMOTL1), a member of the angiomotin family, fundamental regulators in the control of endothelial cell junction stability and permeability (Choi et al., 2016). HECW2 binds AMOTL1 and enhances its stability via lysine 63-linked ubiquitination. Indeed, HECW2 depletion in human endothelial cells decreases AMOTL1 stability, loosening cell-to-cell junctions and altering subcellular localization of yes-associated protein (YAP) from the cytoplasm into the nucleus (Choi et al., 2016).

1.3 Autophagy

Autophagy is a highly conserved catabolic pathway, which delivers undesirable cytoplasmic materials to the lysosomes for their degradation. Autophagy plays a constitutive role in the quality control of intracellular macromolecules, organelles and protein aggregates that are inefficiently degraded by the proteasome, and is thus required for the maintenance of cellular homeostasis and vital for human health (Wong and Cuervo, 2010). Not surprisingly, autophagic dysfunction or dysregulation has been implicated in several human pathologies, including neurodegeneration.

Studies of mammalian systems have highlighted many other important roles for autophagy in disease. Autophagy is indeed relevant for the degradation of aggregate-prone intracytoplasmic proteins, the cause and hallmark of various neurodegenerative diseases, including AD and other forms of dementia (caused by Tau aggregation), PD (α-synuclein) and Huntington’s disease (mutant Huntingtin) (Bento et al., 2016).

The autophagy pathway can be triggered by various types of stress: a) metabolic stress, such as nutrient deprivation, to provide sources of energy or building blocks for the synthesis of macromolecules; b) damaging stress, to remove injured organelles and macromolecules; c) therapeutic stress (drug treatment); d) morphogenetic changes occurring during development and differentiation, to remove disused cellular structures; e) pathogenic infection, to eliminate invasive microbes and to generate degradation products required for the activation of the innate immune system and antigen presentation; and f) other types of stress such as hypoxia and oxidative stress (Boya et al., 2013; Seranova et al., 2020).

1.3.1 Autophagy pathway

Cargoes are sequestered from the cytosol by formation of double-membrane vesicles called autophagosomes, which delivers the cargoes to the lysosome for degradation and recycling. The process can be divided into several steps: i) autophagy initiation; autophagosome biogenesis divided in ii) development (nucleation) and iii) elongation of the autophagosomal membrane; iv) cargo recognition and engulfment; v) autophagosome maturation; vi) transport, docking and fusion between autophagosome and late endosome/lysosome (fusion); vii) and degradation of the cargos inside the autolysosome (Nakamura and Yoshimori, 2017) (**Fig. 5**).

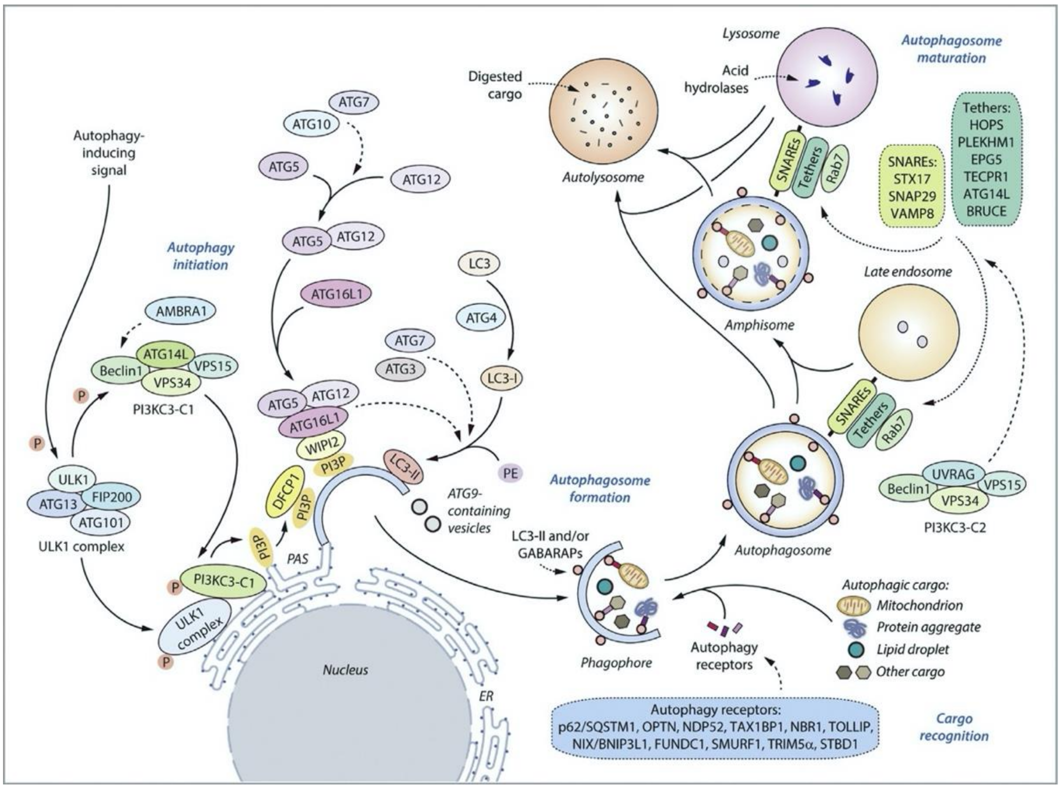

Figure 5 Mechanism of the autophagy process

*Representation of the autophagy pathway from autophagy induction to the digestion of autophagic cargo, showing vesicular compartments, vesicle fusion events and the different protein complexes and factors involved in the pathway (*Seranova et al., 2020*).*

The nucleation step involves the genesis of the phagophore, an isolation membrane structure that derives from the endoplasmic reticulum (ER)-emanating membrane domains, termed “omegasomes”, and/or from other sources like trans-Golgi, recycling endosomes, plasma membrane, and mitochondria (Tooze and Yoshimori, 2010). The phagophore then expands to engulf intracellular autophagic cargo that comprises unwanted macromolecules such as protein aggregates or damaged organelles like mitochondria, thereby sequestering the cargo in a double-membrane structure called the autophagosome. The cargo-loaded autophagosome then matures and traffics toward the microtubule-organizing center via the dynein machinery to come into the proximity of lysosomes. In its way to the lysosome, the autophagosome initially fuses with the late endosome to form a hybrid organelle called amphisome, which then fuses with the lysosome to form the degradative autolysosomes. Alternatively, the autophagosome can directly fuse with the lysosomes (Nakamura and Yoshimori, 2017; Zhao and Zhang, 2019). The final step of the pathway is the degradation of the autophagosome content by the lysosomal digestive enzymes (Bento et al., 2016; Feng et al., 2014; Seranova et al., 2020) (**Fig. 5**).

1.3.1.1 Autophagosome biogenesis

An essential role during autophagosome formation is mediated by the autophagy-related proteins, ATG. These proteins assemble into functional complexes that are activated and recruited to specific membrane structures to initiate the autophagy process (Mizushima et al., 2011; Seranova et al., 2020) (**Fig. 5**). The first one is the ULK1 (unc-51-like kinase-1) complex, which consists of the serine/threonine-protein kinase ULK1 (mammalian orthologue of yeast Atg1) and three scaffold proteins;

FIP200 (focal adhesion kinase family-interacting protein of 200 kDa; also known as RB1CC1), ATG13 and ATG101 (Zachari and Ganley, 2017). Once activated, the ULK1 complex phosphorylates a number of downstream targets, leading to phagosome biogenesis from the phagophore assembly site (PAS) at the ER, which functions as a platform for autophagosome formation (Zhao and Zhang, 2019) (**Fig. 5**). ULK1 complex activity is regulated by different signaling pathways that will be discussed in a following paragraph. Once recruited to the ER, ULK1 phosphorylates the class III phosphatidyl-inositol-3-kinase complex 1 (PI3KC3-C1), which consists of the catalytic subunit VPS34 (vacuolar protein sorting 34), Beclin1, VPS15 (vacuolar protein sorting 15), and ATG14-like (ATG14L). The latter can be substituted by UVRAG (UV Radiation Resistance Associated), generating the PI3KC3-C2 complex, which plays a role in the maturation step of the autophagosome (Bento et al., 2016; Seranova et al., 2020). The activation of the PI3KC3-C1 complex produces phosphatidylinositol 3-phosphate (PI(3)P) at the sites of phagophore initiation (**Fig. 5**). The specialized PI(3)P-enriched subdomains of the ER, the omegasomes, then provide a platform for phagophore nucleation and expansion (Russell et al., 2013; Zhao and Zhang, 2019). PIs favor bending of the membrane into a positive curvature, which may be relevant to phagophore shaping. In addition, PI(3)P recruits the PI(3)P-binding proteins of the WIPI family members, such as WIPI2 (WD repeat domain phosphoinositide-interacting protein 2) and DFCP1 (double FYVE domain- containing protein 1), to support the expansion of the growing membrane (Dooley et al., 2014; Seranova et al., 2020).

Elongation of the autophagosome membrane is regulated by two ubiquitin-like conjugation complexes (**Fig. 5**). The first ubiquitin-like reaction involves the conjugation of the ubiquitin-like protein ATG12 to ATG5 and is catalyzed by the E1-like enzyme ATG7 and the E2-like enzyme ATG10. The ATG5-ATG12 complex then interacts with ATG16L1 to form the ATG5-ATG12-ATG16L1 ternary complex. WIPI2 is required for the recruitment of the ATG16L1-ATG5-ATG12 complex to the forming autophagosome where it acts as an E3-like enzyme, together with ATG7 and the E2-like enzyme ATG3, in the second ubiquitin-like reaction, which is the conjugation of ubiquitin-like molecules of the ATG8 family with the amino group of membrane-resident lipid phosphatidylethanolamine (PE), process also known as ATG8-lipidation (Geng and Klionsky, 2008; Mizushima et al., 2011).

The human genome encodes for six different ATG8 proteins that are divided into two subfamilies: microtubule-associated protein 1 light chain 3 (MAP1LC3 or LC3), which is composed of LC3A, LC3B and LC3C, and the g-aminobutyric acid receptor-associated proteins (GABARAPs) GABARAP, GABARAPL1 and GABARAPL2 (also called GATE-16) (Seranova et al., 2020).

All of these ubiquitin-like proteins are synthesized as precursor proteins that, before lipidation, must be processed at the C-terminal by a family of cysteine proteases, ATG4, that cleaves the C-terminal amino acids to expose a glycine (Fig. 5). Further, ATG7, ATG3 and the ATG12-ATG5-ATG16L1 complex conjugate LC3/GABARAP to PE, resulting in the incorporation of LC3/GABARAP-PE in the growing phagophore where it contributes to phagophore expansion, autophagosome formation and cargo recognition (Geng and Klionsky, 2008; Mizushima et al., 2011). LC3B, for example, is proteolytically cleaved by ATG4 to generate the cytosolic LC3-I, which is then conjugated to PE to generate the membrane-bound form of LC3B-II. The latter is widely used as a marker of autophagosomes since it is the only autophagic protein that stably associates with the mature autophagosomes and remains associated with them until it is trafficked to the lysosome (Green and Levine, 2014).

ULK1 phosphorylates other autophagy pathway components, including the transmembrane protein ATG9 (Fig. 5). ULK1-dependant phosphorylation mediates the translocation of ATG9-positive vesicles to the PAS, where they supply lipid membrane to the expanding phagophore (Karanasios et al., 2016). ATG9 interacts with ATG2, a large protein with regions of homology to VPS13, a lipid transporter between ER and other membranes. Sequence and secondary structure similarities suggest lipid transport roles for ATG2 as well (Kumar et al., 2018), function that was recently confirmed (Chang et al., 2021).

The final closure of the phagophore into autophagosomes is completed by membrane abscission mediated by the endosomal sorting complex required for transport (ESCRT) and accompanied by a change in morphology from elliptical expanding membranes to spherical sealed autophagosomes (Zhao and Zhang, 2019)

Deletion or mutation in gene that act in autophagosome biogenesis, such as FIP200, Beclin1, ATG5, and ATG7, results in failure to form autophagosomes and leads to different defects in the nervous system, such as axonal swelling, accumulation of ubiquitin positive aggregates, neurite atrophy, and finally neuronal loss [reviewed in (Stavoe and Holzbaur, 2019)]. Of note, Beclin1 has been implicated in the resolution of a-synuclein accumulation, characteristic of AD and PD (Pickford et al., 2008; Spencer et al., 2009).

1.3.1.2 Autophagosome maturation into autolysosome

After biogenesis, the maturation of the autophagosome occurs in a stepwise fashion by sequential fusion with different stages of endo-lysosomal compartments, such as multivesicular bodies (MVB) and late endosome, into an amphisome, and subsequently with the lysosome to generate the degradative organelle, namely autolysosome. In this compartment, the inner membrane of the autophagosome and its contents are degraded by lysosomal acid hydrolases, and nutrients are released into the cytosol and recycled for bioenergetics and anabolic pathways (**Fig. 5**). The timing of this fusion is particularly critical and must only happen once the phagophore is sealed (Zhao and Zhang, 2019).

Organelle fusion is primarily coordinated by three sets of proteins: SNARE complexes (soluble N-ethylmaleimide-sensitive factor-attachment protein receptor), Rab GTPases and membrane tethering complexes (Nakamura and Yoshimori, 2017; Zhao and Zhang, 2019). SNAREs are membrane-anchored proteins, localized on opposing membrane compartments that can interact with each other to form a highly energetically favorable complex. Two cognate SNARE complexes act in coordination to mediate fusion of autophagosomes with late endosomes/lysosomes: one complex consists of the autophagosome-localized SNAREs STX17 (Syntaxin 17) and SNAP29 (Synaptosomal-associated protein 29), and the endolysosomal-localized SNARE VAMP8 (Vesicle-associated membrane protein 8); the other complex is composed of the autophagosome SNARE YKT6 and SNAP29 and lysosomal-localized SNARE STX7 (Zhao and Zhang, 2019). Tethering factors capture intracellular trafficking vesicles and bring them closer to targeting membranes, promoting and stabilizing the assembly of SNARE complexes. During autophagosome maturation, different tethering proteins, including EPG5 (Ectopic P-Granules Autophagy Protein 5 Homolog), HOPS (homotypic fusion and protein sorting) and PLEKHM1 (Pleckstrin homology domain-containing family M member 1), simultaneously bind to LC3/GABARAP on autophagosomes and Rab7 on late endosomes/lysosomes to tether the autophagosomes/amphisomes with late endosomes/lysosomes for fusion. Rab2, known to regulate vesicle trafficking at the ER and Golgi, is also involved in autophagosome maturation. It localizes to autophagosomes and recruits the HOPS complex to promote autophagosome maturation (Zhao and Zhang, 2019). Another tethering factor is the Golgi reassembly-stacking protein of 55kDa (GRASP55) which interacts via a LIR (LC3-interactin region) motif with LC3/GABARAP proteins, preferentially with LC3B, and simultaneously binds to the lysosomal associated membrane protein 2 (LAMP2) on late endosomes/lysosomes to promote fusion (Zhang, 2018).

Mutation in tethering would disrupt maturation and fusion of autophagosome with late endosome/lysosome, organelles trafficking and finally degradation of cargo. For example, deficiency in EPG5 causes a severe multisystem disorder known as Vici syndrome characterized by autophagosomes (Nam et al., 2021). Interestingly, epg5−/− knockout mice exhibit damage of cortical and spinal cord neurons and neurodegenerative features resembling human ALS, such as muscle denervation, myofiber atrophy and dramatically reduced survival (Zhao et al., 2013). Epg5 deficiency resulted in accumulation of p62 aggregates and ubiquitin-positive inclusions, impaired endocytic trafficking, and accumulation of TDP-43 cytoplasmic aggregates in cortical and spinal cord neurons (Zhao et al., 2013), one of the major defective aggregation-prone protein implicated in ALS and FTD (Dudman and Qi, 2020; Le Guerroue and Youle, 2021).

Maturation and fusion with lysosomes are also critically regulated by the lipid composition of the lysosomal membrane. Reduction of the lysosomal phosphatidylinositol 3,5-bisphosphate (PI(3,5)P_2) level, synthesized by the PI(3)P 5-kinase Fab1 (PIK-fyve) and degraded by the PI(3,5)P2 5-phosphatase FIG4/VAC14, impairs autophagosome/amphisome–lysosome fusion (Zhao and Zhang, 2019). Indeed, knockdown or chemical inhibition of PIK-fyve decreases the levels of PI(3,5)P2 on lysosomes, leading to increase in lysosome size and reduction in lysosome number and accumulation of the lipidated form of LC3, characteristic of autophagosomes. As a consequence, cells experience severe autophagy defects due to the loss of lysosomal function (de Lartigue et al., 2009). These effects could be explained by two mechanisms: lack of PI(3,5)P2 on lysosomes can either render an acceptor late endosome/lysosome compartment refractory to fusion or lead to a defect in the acidification that is necessary for lysosomal degradation. Interestingly, mice with mutations in PIK-fyve or VAC14 accumulate LC3-II and the late-endosome/lysosome protein LAMP2 in in regions of the brains that undergo degeneration and are enriched in cytoplasmic inclusion bodies positive for the autophagy-receptor p62 and ubiquitin (Ferguson et al., 2009).

Lipid composition of autophagic organelles must be tightly regulated during the whole process. In neurons, the phosphoinositide phosphatase inositol polyphosphate-5 phosphatase E (INPP5E) has been identified as a regulator of the lysosome-autophagosome fusion step (Hasegawa et al., 2016; Nakamura and Yoshimori, 2017). INPP5E downregulates lysosomal PI(3,5)P_2 and this causes a stabilization of the actin filaments on the lysosome surface, an essential step for fusion. Inhibition of INPP5E causes the accumulation of autophagosomes that cannot proceed further.

In addition to lipids and proteins directly implicated in membrane fusion, the cytoskeleton is essential for the fusion step as well (Nakamura and Yoshimori, 2017). Autophagosomes form randomly throughout the cytoplasm, whereas late endosomes and lysosomes are predominantly found in the perinuclear region. Therefore, once complete and closed, autophagosomes are delivered to the perinuclear region taking advantage of the microtubule network and the kinesin/dynein–dynactin motor complexes (Nakamura and Yoshimori, 2017). The issue of organelle trafficking is even more relevant in neurons, in which autophagosomes are predominantly generated in the axon and must reach the lysosomes that are primarily concentrated in the soma.

1.3.1.3 Autophagy receptors for mediating selective autophagy

Autophagy can be divided into bulk autophagy and selective autophagy. Bulk autophagy, the main autophagic response to starvation, degrades cytosolic components in a non-selective manner. On the other hand, selective degradation of specific cargoes, such as damaged organelles, aggregated proteins or pathogens requires, in addition to the canonical autophagy machinery, specific signals on the substrate/s and a specific class of proteins referred to as autophagy receptors (Johansen and Lamark, 2020; Khaminets et al., 2016) (**Fig. 5**).

While certain types of selective autophagy employ Ub-independent signals for cargo recognition, ubiquitination has been linked to the majority of the selective autophagy pathways (Khaminets et al., 2016).

Cargo receptors involved in Ub-dependent selective autophagy are responsible for selectivity in autophagy. They all share two common domains: a ubiquitin-binding domain (UBD) through which they bind the specific cargo, and an LC3-interaction region (LIR) motif which allows interaction with the expanding phagophore to occurs (Johansen and Lamark, 2020). The LIR motif was first identified in the C-terminus of p62 (also known as SQSTM1), the major and most characterized selective autophagy-receptor, whose UBD predominantly binds linear and K63-linked Ub chains over K48-linked Ub (Pankiv et al., 2007). Supporting the importance of p62 in autophagy, mutations in p62 are implicated in amyotrophic lateral sclerosis (ALS) and frontotemporal dementia (FTD), neurodegenerative diseases characterized by accumulation or toxic protein aggregates (Fecto et al., 2011; Menzies et al., 2017; Rubino et al., 2012)

Other examples of autophagy receptors are OPTN (optineurin) (Korac et al., 2013), NDP52 (nuclear dot protein of 52 kDa) (Thurston et al., 2009), TAX1BP1 (Tax1 binding protein 1) (Lazarou et al., 2015; Tumbarello et al., 2015), NBR1 (neighbor of BRCA1 gene 1) (Kirkin et al., 2009; Lazarou et al., 2015), TOLLIP (Toll-interacting protein) (Lu et al., 2014), and AMBRA1 (BECLIN 1-regulated autophagy protein 1) (Di Rita et al., 2018).

The best characterized pathway of selective autophagy is the ubiquitin-dependent clearance of damaged mitochondria that is regulated by the serine/threonine kinase PINK1 and the E3 ubiquitin ligase Parkin (Schmidt et al., 2021). PINK1 acts as a sensor of mitochondrial damage. In healthy mitochondria, PINK1 is rapidly imported into the mitochondria and degraded. However, upon mitochondrial damage, it is stabilized on the outer mitochondrial membrane where it homo-dimerizes and autoactivates. PINK1 then phosphorylates Ub conjugated to mitochondrial outer membrane proteins, which recruits cytosolic Parkin. Bound to phospho-Ub, Parkin is itself phosphorylated by PINK1, turning on its E3 ubiquitin ligase activity to ubiquitinate numerous mitochondrial proteins with mono- and short-chain K6 or K11 Ub signals, thus providing more ubiquitin substrates for PINK1 to establish a positive feedback loop. The ubiquitination of the mitochondrial membrane recruits the autophagy receptor proteins OPTN, NBR1, NDP52, and TAX1BP1, which facilitate encapsulation of the mitochondria within the growing autophagosome (Moore and Holzbaur, 2016; Schmidt et al., 2021). This pathway is implicated in neurodegeneration since multiple loss-of-function mutations in either PINK1 or Parkin are known to cause autosomal recessive juvenile onset PD, while mutations in OPTN are associated with ALS.

The specific quality control regulation of the ER is mediated by another selective form of autophagy, referred to as ER-phagy. Multiple ER-associated proteins possess a LIR motif that mediates binding to LC3-family proteins, including FAM134B (also known as RETREG1, reticulophagy regulator 1), reticulon 3L (RTN3) and CCPG1 (cell cycle progression 1) (Grumati et al., 2018). FAM134B and RTN3 have been proposed to function in the basal remodeling of ER membranes by autophagy, while CCPG1 expression is induced by ER stress (Grumati et al., 2018).

Beside cargo receptors, selective autophagy machinery requires other accessory factors, designed as autophagic adaptor. An example is ALFY (autophagy-linked FYVE protein, also known as WDFY3), a PI3P-binding protein that does not harbor the UBD domain but, by binding to p62, LC3/GABARAP proteins and ATG5, acts as a scaffold linking the ubiquitinated protein aggregates with the autophagosome markers, thus facilitating the removal of protein aggregates (Filimonenko et al., 2010; Simonsen et al., 2004). *In vivo* studies support a role for ALFY in aggrephagy, as the *Drosophila* mutant blue cheese demonstrates accumulation of ubiquitin-positive inclusions, neurodegeneration and shortened lifespan (Finley et al., 2003).

1.3.2 Signaling pathways regulating autophagy

Different signaling pathways activate autophagy. The most characterized one is represented by nutrient signaling where the major signaling node is the mammalian target of rapamycin (mTOR), a serine-threonine kinase that senses and integrates, among other signals, cellular nutrients. mTOR is found in two distinct protein complexes, mTOR complex 1 (mTORC1) and mTOR complex 2 (mTORC2), but only mTORC1 directly regulates autophagy (Saxton and Sabatini, 2017). Under nutrient-sufficient conditions, mTORC1 directly shut-down autophagy by phosphorylating the ULK1 complex, suppressing ULK1 activity (Zachari and Ganley, 2017). Besides ULK1 phosphorylation, mTORC1 also indirectly inhibits autophagy by phosphorylating AMBRA1, which, in turn, can reduce ULK1 stability and its kinase activity (Nazio et al., 2013). Nutrient deprivation activates the AMP-activated protein kinase (AMPK), which phosphorylates and deactivates of mTORC1 provoking the activation of the ULK1 complex. In addition, AMPK induces autophagy independently of mTORC1 via binding to and phosphorylation of ULK1 and Beclin1 (Seranova et al., 2020).

Finally, mTORC1 prevents autophagy by phosphorylating the transcription factor EB (TFEB) and sequestrating it in the cytoplasm. TFEB is a master transcriptional regulator of genes involved in several steps of the autophagic pathway, such as genes required for autophagy initiation (BECN1, ATG9B and WIPI1), phagophore elongation (GABARAP, MAP1LC3B and ATG5), autophagosome maturation (UVRAG and RAB7), and cargo recognition (p62) (Di Malta et al., 2019; Settembre et al., 2011). A similar TFEB phosphorylation and inactivation is also promoted by the serine/threonine-protein kinase Akt. Akt inhibition promotes autophagy via nuclear localization of TFEB that enable the transcription of target genes (Palmieri et al., 2017).

A number of mTORC1-independent autophagy pathways have been described. Most of these pathways involve second messenger molecules such as IP3 (inositol 1,4,5-trisphosphate), Ca2+ (calcium), cAMP (30,50- cyclic adenosine monophosphate), and NO (nitric oxide) that negatively influence autophagy when their intracellular levels rise (Seranova et al., 2020).

Autophagy can also be regulated by Phosphatidylinositol 5-phosphate (PI(5)P), which is synthesized by PIK-fyve and required for autophagosome formation. Increased cellular levels of PI(5)P, by the addition of exogenous PI(5)P or silencing of the PI(5)P4-kinases type II that transforms PI(5)P into Phosphatidylinositol 4,5-bisphosphate (PI(4,5)P2), boost autophagosome formation, and autophagosome and autolysosome numbers, whereas depletion of PI(5)P, by the PIK-fyve inhibitor YM-201636 or PIK-fyve silencing, results in decreased numbers of autophagosome precursors and mature autophagosomes (Vicinanza et al., 2015).

Chemical modulation of autophagy can be achieved via direct inhibition of mTORC1 or by targeting the mTORC1-independent pathways by small molecules (Rubinsztein et al., 2012). Examples of mTOR inhibitors are rapamycin and Torin1. mTOR-independent autophagy inducers, instead, include the AMPK activator metformin and trehalose (Rubinsztein et al., 2012). Natural compounds such as resveratrol, which inhibits mTOR, and spermidine and vitamin D3, which lead to increased Beclin1 and ATG gene expression may also induce autophagy (Seranova et al., 2020).

Conversely, lysosomotropic agents, such as chloroquine (CQ) and Bafilomycin A1 (BafA1), impair autophagosome maturation and degradation, inhibiting autophagosome–lysosome fusion. Being a specific inhibitor of the vacuolar type H-

ATPase (V-ATPase) present on lysosomes, BafA1 also inhibits lysosome acidification (Rubinsztein et al., 2012).

1.3.3 Neuronal autophagy

Autophagy is particularly important in neurons. The long-lived nature of neuronal cells and their inability to undergo division predisposes them to the toxic effects of accumulated misfolded proteins or damaged organelles that cannot be diluted by cell division, a strategy commonly employed by mitotic cells. Neurons must therefore highly rely on quality control mechanisms, such as autophagy, for maintaining neuronal homeostasis and preventing axon degeneration. While starvation robustly decreased mTORC1 signaling also in neurons, it does not induce autophagy as it does in other cell types. Furthermore, pharmacological inhibition of mammalian target of rapamycin with Torin1 is not sufficient to markedly upregulate neuronal autophagy (Maday and Holzbaur, 2016). These observations suggest that the primary physiological function of autophagy in neurons may not be to mobilize amino acids and other biosynthetic building blocks in response to starvation, in contrast to findings in other cell types (Kochl et al., 2006; Mejlvang et al., 2018). Rather, high basal constitutive autophagy in neurons may function to regulate neuronal development and homeostasis by balancing synthesis and degradation, especially within distal axonal processes distant from the soma (Maday and Holzbaur, 2016). The breakdown of these mechanisms is a hallmark of aging and negatively impacts neuronal health in neurodegenerative disease (Menzies et al., 2017).

Compared to non-neuronal cells, neurons present particular dynamics and compartmentalization of autophagy (**Fig. 6**). Autophagosome biogenesis takes place mainly in the distal axon while proteolytically active lysosomes are enriched in the soma. Thus, robust retrograde transport of autophagosomes along the axons delivers them to the soma to facilitate degradation of organelles and protein aggregates formed far from where the degradation steps of autophagy occur (Stavoe and Holzbaur, 2019).

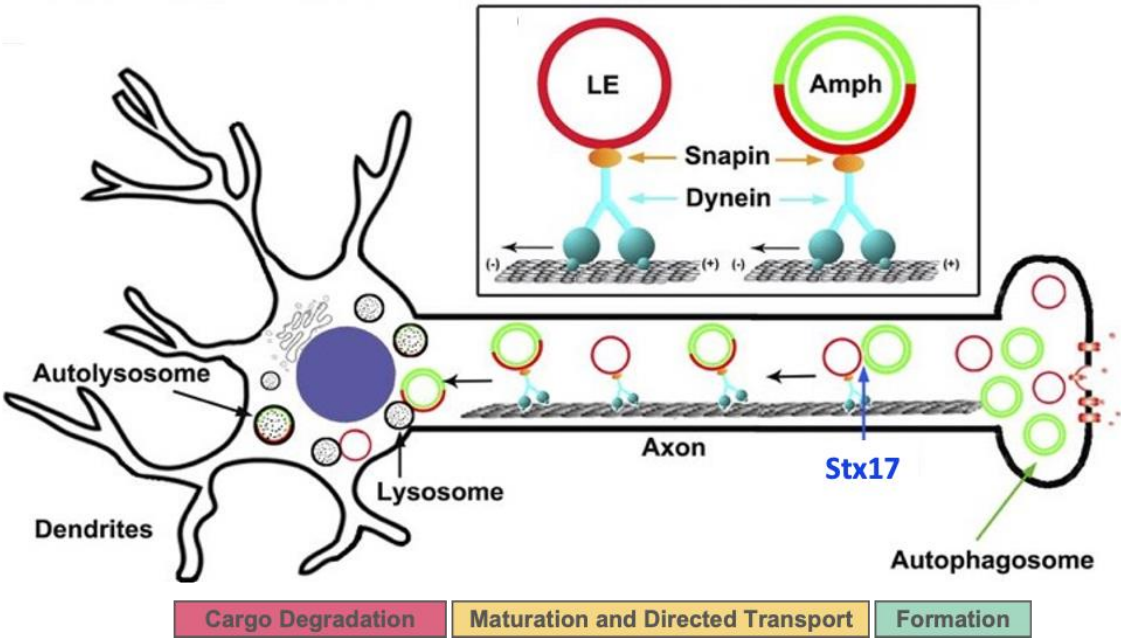

<u>Figure 6 Autophagy in neurons</u>

Model of compartmentalized autophagy in neurons. LE-loaded dynein–snapin complex driving AV for retrograde trafficking along axons. Autophagosomes (green) form at distal axons and fuse with late endosome (LE, red) to form amphisome (Amph). Fusion is mediated by SNAREs proteins, such as syntaxin 17 (Stx17) and dynein– snapin complexes mediate amphisomes retrograde trafficking to the soma, where mature acidic lysosomes are mainly located (adapted from (Cheng et al., 2015).

1.3.4 Spatial organization of autophagy in neurons

The structure of highly polarized neuronal cells is generally divided into three compartments: the soma, or cell body, and two different types of neuronal processes, or “neurites”, that arise from the soma, which are the axon that can grow from a few micrometers to meters and the dendrites, which are shorter but form elaborate and highly branched networks (**Fig. 6**). The soma is the primary site of both biosynthetic and degradative pathways, and thus ribosome-bound rough-ER and Golgi are enriched in this compartment, as are degradative organelles such as lysosomes. The axon is an elongated process that extends from the soma to synaptic sites - up to 1 meter away in humans - which are the primary sites for signal transmission to other cells. Mature axons are enriched in some organelles, including the ER and endosomes, but there is a lack of other organelles such as Golgi. Axonal late endosomes/lysosomes are present in the axon but appear to be less acidified and have a lower complement of degradative enzymes than those found in the soma (Stavoe and Holzbaur, 2019).

The morphology of neuronal cell and the differences in organelles composition between different regions of the cell result in a striking feature of the autophagy pathway in neurons, the spatial specificity, with the majority of autophagosome biogenesis events occurring in the distal axon. Dual-label live cell imaging of primary dorsal root ganglion (DRG) neurons expressing GFP-LC3B in conjunction with other fluorescently-labeled autophagy components has revealed the spatiotemporal kinetics of the axonal autophagosomes assembly under constitutive conditions. *De novo* biogenesis events are consistently observed at the axon terminal, using upstream markers such as ATG13 and ATG5. Overall, the well-organized and ordered recruitment pathway for autophagosome assembly observed in neurons resembles the dynamics observed in non-neuronal cells (Maday and Holzbaur, 2014) (**Fig. 5**). In contrast to the induction of autophagy in nutrient-limiting conditions observed in non-neuronal cells, axonal autophagosomes form constitutively in growth-promoting conditions with a specific temporal and spatial process (Maday and Holzbaur, 2014). Kinetic analysis of the dynamics of autophagosome formation demonstrates a stepwise assembly process that follows a stereotypical time course, with each biogenesis event occurring within minutes and components recruited with definite kinetics (Maday and Holzbaur, 2014). Gradually, over the course of several minutes, ATG13 puncta become GFP-LC3B-positive. As the intensity of the GFP-LC3B fluorescence increases, the ATG13 signal declines, indicating dissociation of the kinase complex from the elongating phagophore. In contrast, GFP-LC3B fluorescence stably persists, indicating the continued stable association of lipidated LC3B with the mature autophagosome (Maday and Holzbaur, 2014). While autophagosome are constitutively generated at the axon terminals, their formation is only rarely observed in dendrites or soma under resting conditions (Maday and Holzbaur, 2014). Most strikingly, *de novo* formation of new autophagosomes along the length of the axon is also very rare under baseline, constitutive conditions, emphasizing the high degree of compartmentalization and spatial regulation controlling autophagosome biogenesis in primary neurons. In mouse primary hippocampal neurons, basal autophagosome biogenesis was observed in the cell body, but autophagosomes generated in the soma were characteristically distinct, less dynamic and mature compared to axonally-generated autophagosomes (Maday and Holzbaur, 2016).

In the distal axon, the majority of the ATG13 puncta form on or near the ER, and newly formed autophagosomes include ER markers, two indications that axonal omegasome form on and from ER membrane (Maday and Holzbaur, 2014). Indeed, the ER is extensively present and the main available membrane source in the axon. During autophagosome assembly, the membrane is also trafficked to the elongating phagophore in ATG9-positive carrier vesicles and the kinesin motor KIF1A (Kinesin Family Member 1A) is required to supply the axon with newly synthesized ATG9 (Stavoe et al., 2016).

Once formed, autophagosomes bind to microtubules within the axon terminal thanks to the interaction with microtubule motor proteins (Maday et al., 2012). After an initial phase of bidirectional movement, autophagosomes undergo a switch to highly processive unidirectional retrograde transport toward the cell body driven by dynein and regulated by scaffolding proteins, such as JIP1 (JNK-interacting protein 1), Htt (huntingtin) and HAP1 (huntingtin-associated protein 1) (Wong and Holzbaur, 2014). During their transit toward the soma, autophagosomes encounter and fuse with late endosomes and lysosomes, leading to increasingly acidic and degradation-competent autolysosomes (Maday et al., 2012).

A useful tool to examine autophagosome maturation is the pH sensitive fluorescent probe mCherry-EGFP-LC3 (Pankiv et al., 2007). Before acidification, this protein appears yellow in merged images because of the fluorescence of both mCherry and GFP. Once the lumen of the organelle is acidified, the GFP is preferentially quenched, and only the red fluorescence remains (Pankiv et al., 2007). While this probe was observed to mark newly formed autophagosomes at the axon tip with both red and green fluorescence, as autophagosomes reached the soma, the GFP signal became preferentially quenched, consistent with the increasing acidification of the lumen. The pH-sensitive dye LysoTracker Red, that specifically marks acid organelles, confirmed this model, as most distal autophagosomes were not labelled while autolysosomes in the proximal axon and the soma were strongly positive for LysoTracker signal (Maday et al., 2012).

Autophagosome maturation is induced by the fusion of a nascent autophagosome with a late-endosome that happens at the exit of a newly formed autophagosome from the axon tip (Maday et al., 2012). Maday and colleagues showed that, upon initial formation, distal autophagosomes are negative for the late endosome/lysosome marker LAMP1. In contrast, axonal autophagosomes are LAMP1-positive. This initial fusion event with a distal late endosome may be required to recruit dynein motors to the autophagosome (Maday et al., 2012).

In primary DRG neurons, STX17, forming a SNARE fusion complex with SNAP29 and VAMP8, mediates the fusion of autophagosomes with late endosome/lysosomal organelles already loaded onto microtubules through interaction with the adaptor protein Snapin that binds to the motor protein dynein (Cheng et al., 2015) (**Fig. 6**). Blocking the fusion with late endosome/lysosome by knockdown of STX17 inhibits autophagosome transport along the axons while inhibition of retrograde motility blocks maturation of autophagosomes (Cheng et al., 2015). Indeed, impairing late endosome loading onto microtubules with Snapin or Htt depletion, results in autophagosome accumulation at the axon tips, inhibition of autophagosome acidification, and lack of degradation of the engulfed cargoes (Cheng et al., 2015; Wong and Holzbaur, 2014).

Although lysosomes have been found also in axons, axonal-lysosomes lack the full complement of degradative enzyme characteristic of the somal-lysosomes (Cheng et al., 2018). Thus, the active retrograde transport required for autophagosome maturation may function to drive autophagosomes toward more proteolysis-competent lysosomes enriched in the soma.

Suprisingly, the constitutive autophagy that constantly takes place in neuronal axons seems to be nonselective in regard to cargo capture and degradation. Live cell studies suggest a ‘big gulp’ approach, in which the developing phagophore engulfs the local cytosol, which may include mitochondrial fragments or aggregated proteins, to facilitate protein turnover and to maintain homeostasis (Maday et al., 2012). In addition to this nonselective pathway, however, there is a growing list of cargoes in the neuron that are turned over by selective autophagy. Mitophagy is the best understood example of selective autophagy within this context. Other selective pathways that have a fundamental role in maintaining neuronal health are ER-phagy, aggrephagy and granulophagy, the removal of RNA granules (Stavoe and Holzbaur, 2019).

1.3.5 Autophagy in neuronal homeostasis and aging

The autophagy pathway plays a critical role in maintaining neuronal homeostasis, as loss or mutation in a variety of proteins involved in different steps of the pathway results in the accumulation of protein aggregates, damaged organelles or RNA granules aggregated proteins, neurite degeneration, and neuron loss, all common hallmarks of neurodegenerative diseases.

In addition to neurodegenerative related gene deletion/mutation, numerous studies have demonstrated links between autophagy dysfunction and aging, itself one of the major risk factors for many neurodegenerative diseases such as HD, AD and PD, ALS and FTLD, and tauopathies (Niccoli and Partridge, 2012). Many organisms show decreased autophagy-related gene expression or lower protein levels and/or signs of autophagic function deterioration with age (Hansen et al., 2018). For example, autophagy gene transcripts decrease with age in the brain of fruit fly *Drosophila melanogaster*, including Atg2, Atg8a (LC3/GABARAP in mammals), Atg18 (WIPI1 and WIPI2 in mammals) and bchs (ALFY in mammals) (Simonsen et al., 2008) while protein levels of LC3 and ATG7 decline with age in mouse and human muscle (Carnio et al., 2014).

Independently of expression levels, PTMs, such as phosphorylation, and subcellular localization of autophagic proteins could alter autophagic function with age in neurons (Stavoe and Holzbaur, 2019). Recently, Stavoe and colleagues found that aging could affect the rate of constitutive autophagosome biogenesis and induce morphological changes of autophagic structures in neurons through regulation of the dynamics and phosphorylation state of WIPI2 (Stavoe et al., 2019; Stavoe and Holzbaur, 2020). They identified frequent production of stalled multilamellar autophagic vesicles in neurons from aged mice that remained ATG13-positive and failed to recruit lapidated LC3 and to develop into LC3B-positive autophagosomes. Importantly, depletion of WIPI2 in neurons from young adult mice was sufficient to decrease the rate of autophagosome biogenesis to that of aged mice, while ectopically expressing WIPI2 effectively restored autophagosome biogenesis in aged neurons (Stavoe and Holzbaur, 2019).

Finally, in addition to initial autophagosome biogenesis, lysosomal integrity has been shown to decrease with age in neurons (Nixon, 2017).

1.4 Interplay between ubiquitination and autophagy

As in the case of the ubiquitin proteasome system (UPS), ubiquitination directly regulates multiple steps of the autophagy pathway: Ub selectively labels autophagy targets that are then bound by autophagy receptors; the upstream autophagy regulators ULK1 and Beclin1 are labelled with non-degradative Ub-chains that favor protein complex assembly and activation upon nutrient starvation or mTOR inactivation; the stability of pro-autophagy factors, such as AMBRA1 and PINK1 is negatively regulated by Ub and proteasomal degradation (Khaminets et al., 2016; Melino et al., 2019). Importantly, the autophagic pathway is often activated to compensate for reduced UPS activity, allowing cells to reduce the load of accumulated proteasome-specific substrates.

Many ubiquitin E3 ligases have been shown to be clearly involved in autophagy (Grumati and Dikic, 2018; Melino et al., 2019). The best-studied example is Parkin, which coordinates a cycle of ubiquitination events occurring at the membrane of the damaged mitochondria that ultimately results in the degradation of the organelles (Yamano et al., 2016).

A huge number of RING-finger E3 ligases have been primarily implicated in the regulation of upstream components of the autophagic machinery, such as mTORC1, the ULK1 complex and the PI3KC3-C1 complex (Grumati et al., 2018). For example, TRAF6 (TNF receptor-associated factor 6)-mediated K63-polyubiquitination promotes stabilization, self-association and activation of ULK1. Similarly, TRIM16 (Tripartite motif-containing protein 16) associates with and catalyzes K63-linked polyubiquitination of ULK1 and BECLIN1, leading to their stabilization (Grumati et al., 2018). K48-polyubiquitination-mediated degradation of autophagy proteins, instead, is needed to terminate the autophagy response. The CDL (Cullin-dependent E3 ubiquitin ligases) complexes are the main E3 ligases involved in this step. CDL4, for example, catalyzes the K48-linked ubiquitination of ULK1, BECLIN1 and VPS34, leading to their degradation (Grumati et al., 2018).

Different evidences suggest that also a few HECT E3 ligases, among which members of the NEDD4 family, are involved in the early steps of the autophagy response. Their activities influence the regulation of autophagy initiation, nucleation of the phagophore and autophagosome formation (Melino et al., 2019) (**Fig. 7**).

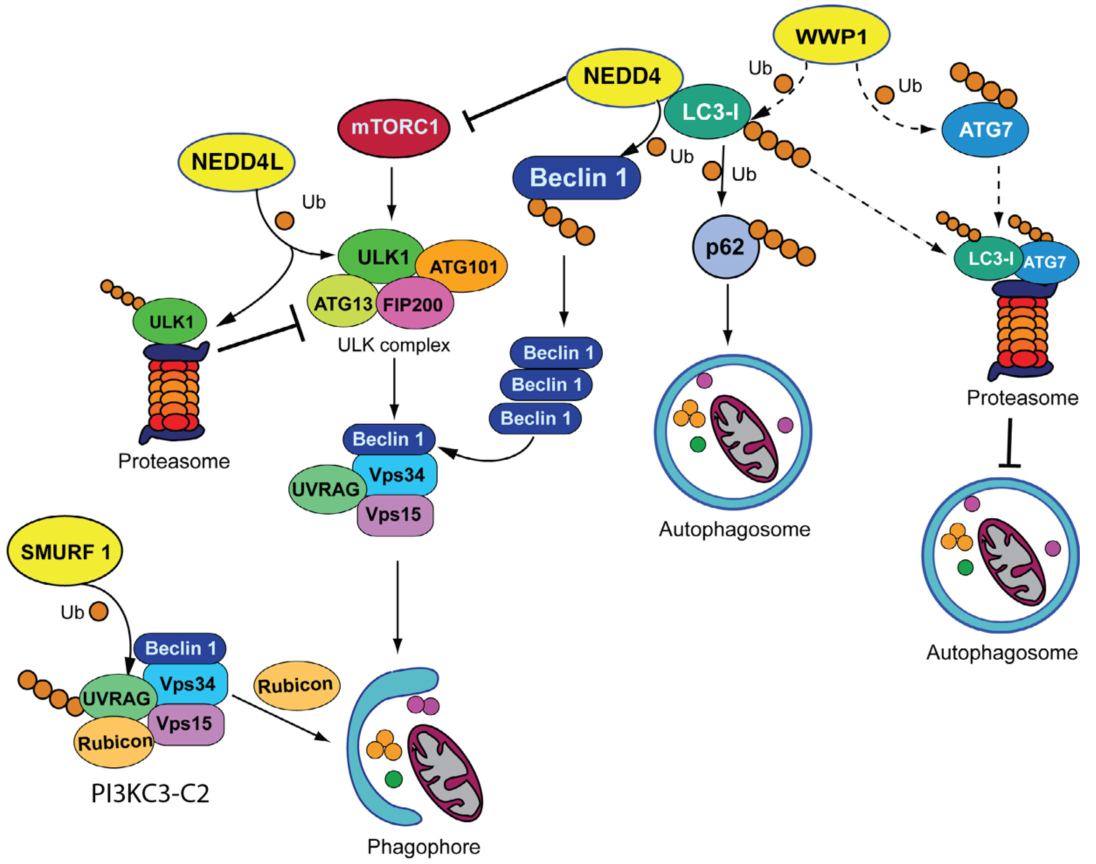

<u>Figure 7 Regulation of the main phases of the autophagic pathway by members of NEDD4 family of E3 ligases</u>

NEDD4 promotes autophagy by negatively modulation of the phosphorylation levels of mTOR; K6- and K27-mediated stabilization of BECLIN 1; and interaction with LC3 and K63-ubiquitination of p62. NEDD4L acts as an E3 for ULK1 and targets ULK1 for proteasomal degradation as an early response to nutrient deprivation. WWP1 negatively regulates autophagy possibly through the disposal of both LC3 and ATG7. SMURF1 promotes phagophore nucleation by catalyzing K29- and K33-linked UVRAG polyubiquitylation, and subsequent displacement of the inhibitory component Rubicon from the PI3KC3-C2 complex (adapted from (Melino et al., 2019).

NEDD4 knockdown impairs starvation and rapamycin-induced activation of autophagy and increases the phosphorylation levels of mTOR, suggesting a role for NEDD4 in promoting autophagy activation through the down-regulation of mTORC1 signaling (Sun et al., 2017) (**Fig. 7**). In addition, NEDD4 controls autophagosome biogenesis by interacting with LC3 through a LIR motif located between the C2 and the WW domains (Sun et al., 2017). The proposed model is that the LC3-NEDD4 interaction is important to recruit NEDD4 to the phagophore and to activate its ligase activity, which ultimately is required for p62 ubiquitination (Sun et al., 2017) (**Fig. 7**). The NEDD4-dependant K63 ubiquitination of p62 has been found important for its function in inclusion body autophagy (Lin et al., 2017). In addition, NEDD4-mediates K6- and K27-linked polyubiquitination of BECLIN 1, which results in protein stabilization, and thus potentiates autophagy (Pei et al., 2017) (**Fig. 7**).

NEDD4L is involved in a negative control mechanism that limits autophagy overactivation and allows cells to survive prolonged starvation conditions (Nazio et al., 2013). In response to nutrient deprivation, ULK1 protein levels are destabilized through the activity of NEDD4L, which ubiquitinates ULK1 for degradation by the proteasome (**Fig. 7**) (Nazio et al., 2013). Other evidences suggest that NEDD4L can also induce autophagy in particular stress conditions. In response to ER stress inducers, NEDD4L is upregulated through sXBP1, a transcription factor that regulates the expression of genes that are necessary for ER recovery. Once induced, NEDD4L enhances ER stress-induced autophagy (Wang et al., 2016).

The NEDD4 family member WWP1 functions as a negative regulator of the autophagic pathway. WWP1 knockdown in acute myeloid leukemia (AML) cells leads to autophagy induction, which is accompanied by increased total levels of LC3 and ATG7 and accumulation of the LC3-lipidated form (Melino et al., 2019) (**Fig. 7**). Although the mechanism remains to be clarified, this result suggests that WWP1 could favor degradation of proteins that are involved in the elongation and closure of the autophagosome membrane to prevent the formation of the organelle (Melino et al., 2019).

Another HECT E3 ligase, HUWE1 (HECT, UBA And WWE Domain Containing E3 Ubiquitin Protein Ligase 1), is relevant to restrain basal autophagy. Under basal condition, this enzyme is involved in the degradation of the mTOR effector protein WIPI2 (Wan et al., 2018). Following autophagy induction, mTORC1 is inactivated and, hence, WIPI2 remains in a dephosphorylated form, which is not able to interact with and be degraded by HUWE1 (Wan et al., 2018).

By contrast, phagophore formation is enhanced by SMURF1-mediated ubiquitination of UVRAG, a component of the PI3KC3-C2 complex, which impairs its interaction with Rubicon, a negative regulator of autophagosome maturation, ultimately enhancing PI3KC3-C2 activity (Feng et al., 2019).

The breakdown of both the UPS and the autophagy–lysosomal pathway is a hallmark of aging, the primary risk factor for most neurodegenerative diseases. As both autophagy defects and the deregulation of HECT E3 ligases play a relevant role in neurodegeneration, an interesting possibility is that HECT E3 ligases might contribute to pathological conditions, at least in part, through autophagy regulation (Melino et al., 2019). Certainly, a general reduction in proteasomal- and autophagosomal-mediated degradation occurs during aging, increasing the amount of potentially neurotoxic proteins and RNA-protein aggregates in neurons.

1.5 Spatio-temporal control of mRNA translation in neurons

Many neurodegenerative diseases are linked to autophagy defects and protein aggregation. Another hallmark of neuronal pathologies is the presence of RNA-protein aggregates and deficit in the RNA metabolism in general.

Importantly, not all mRNAs are programmed for immediate translation right after transcription. Delayed translation of selected mRNAs allows transcripts to be transported or stored until developmental or environmental cues request the expression of their coded proteins. This process is fundamental, particularly in polarized cells, such as germ cells and neurons, to establish functionally distinct compartments and structures, both during development and in mature neurons. To meet the rapidly changing metabolic needs of axons and dendrites, neurons indeed rely on specialized mechanisms to synthesize proteins locally and on demand. This process is achieved by translational control of localized mRNAs that allows protein expression to happen in specific subdomains and confers the ability to rapidly trigger protein synthesis at distant synaptic surfaces. In addition to gather them where they are needed the most, local mRNA and protein concentration help to prevent proteins from being expressed and localized in areas where their function could be deleterious (Glock et al., 2017).

In neurons, the translational spatiotemporal control is regulated by the RNA transport apparatus (RTA), that constantly shuttles transcripts from the cell body to remote areas of the neurons (Fernandopulle et al., 2021) (**Fig. 8**). The RTA consists of cis-acting elements within RNA molecules, proteins that bind them to generate RNA-protein granules, and adaptor complexes that link the granules to motor proteins. A defect in this apparatus have devastating consequences for neuronal homeostasis and functionality; impairs the functions promoted by proteins distally synthesized and leads to toxic aggregates. Indeed, molecular defects in each component of this apparatus are linked to a huge spectrum of neurodegenerative diseases (Fernandopulle et al., 2021; Nagano and Araki, 2021; Nussbacher et al., 2019).

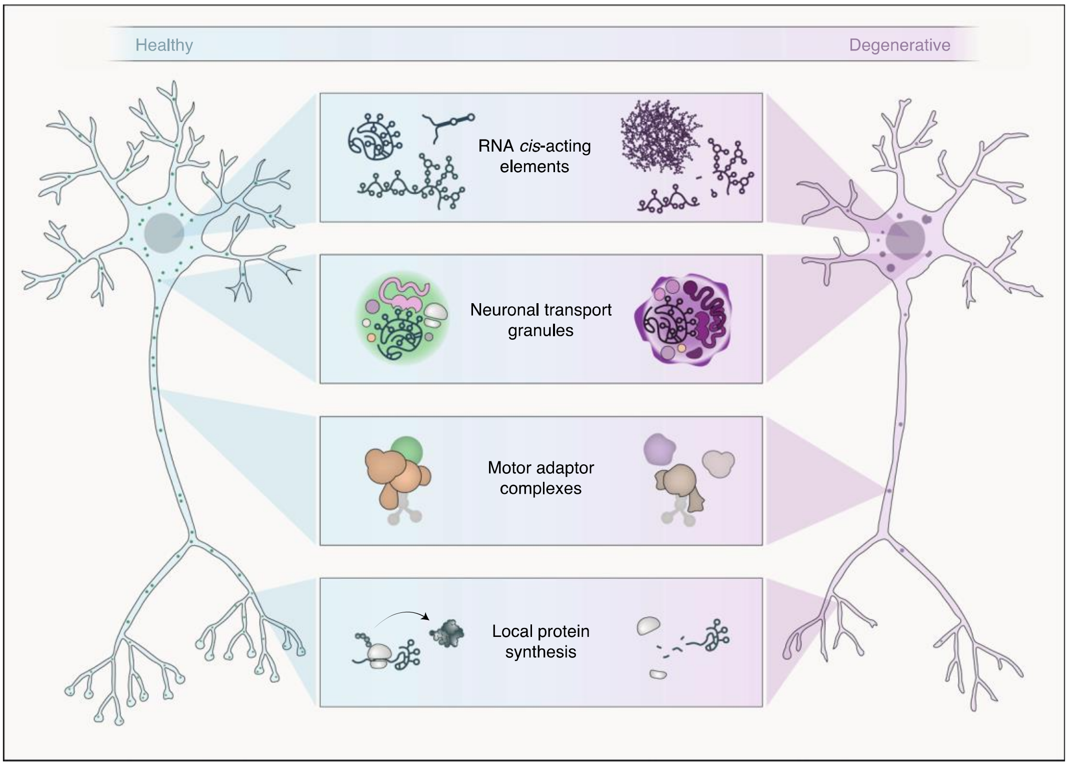

Figure 8 The RNA transport apparatus in healthy and degenerated neurons

*Acting together, Cis-acting elements within RNA molecules, proteins involved in the generation of RNA-protein neuronal transport granules, and motor adaptor complexes that link the granules to motor proteins, enable proper mRNA localization and translation in axons and dendrites. Genetic and age-related dysfunction of RNA regulatory elements, transport granule proteins, or motor adaptor complexes often leads to degenerative disease by impairing local protein synthesis (*Fernandopulle et al., 2021*).*

1.5.1 mRNA regulation in ribonucleoparticles

To achieve a temporal and spatial control of mRNA translation, the messenger RNA must be sequestered from the translational machinery and packed into ribonucleoprotein (RNP) complexes that regulate their stability, trafficking and translational repression. RNA transport and packaging into RNP complexes is a process that begins co-transcriptionally in the nucleus, and persist by remodeling in the cytoplasm. As RNAs are transcribed, several RNA-binding proteins (RBPs) bind individually or in complex to particular sequences and secondary structure on the nascent transcript, from the spliceosome to the capping enzyme complex and polyadenylation machinery. Key features for the proper RNP assembly, mRNA targeting, translational efficiency, and stability are cis-regulatory elements generally localized in the 3’ untranslated region (UTR) of the transcript, where secondary structures like loops and hairpins are generally formed (Tushev et al., 2018). Repeated secondary structures, sequence motifs and nucleobase modifications in neuronal transcripts coordinately bind trans-acting protein complexes that control mRNA stabilization, localization to the destination sites and translational state.

In order to prevent messenger RNA translation, different repressors can act at different levels of the multistep process of protein synthesis, including initiation, elongation and termination.

Most of the repressors inhibit the initiation phase (Besse and Ephrussi, 2008). During initiation, the eukaryotic translation initiation factor complex eIF4F (composed of the cap-binding factor eIF4E, the RNA helicase eIF4A and the scaffold protein eIF4G) binds the methylated guanosine cap at the mRNA 5’ end. Thereafter, the messenger RNA is circularized through the interaction between eIF4G and the 3’poly-A tail binding protein (PAPB), facilitating the recruitment of the 40S ribosomal subunit and the pre-initiation complex. Translation repressors, called eIF4E-BP (eIF4E-binding protein), commonly bind the cap-binding protein eIF4E, inhibiting the interaction between eIF4E and eIF4G, thus the formation of the initiation complex (Besse and Ephrussi, 2008). An example of eIF4E-BP is the protein CYFIP1/Sra1, which contributes to the translational repressor activity of the RBP Fragile X Mental Retardation Protein (FMRP) in neurons (Napoli et al., 2008). The other initiation factors can be target of translation repressors as well. The helicase eIF4A, for example, is targeted by the mammalian non-coding RNA BC1 in dendrites (Lin et al., 2008).

Inhibition of translation initiation can also be achieved by blocking 60S ribosome subunit recruitment, as is the case of the repressor ZBP1 (Z-DNA Binding Protein 1), which prevents assembly of a competent ribosome on beta-actin mRNAs in mouse hippocampal neurons (Huttelmaier et al., 2005). A second, efficient mechanism relies on the modulation of the mRNA poly-A tail. Long poly-A tails promote recruitment of PABP and initiation of translation. RNPs take advantage of this mechanism and act as repressors by recruiting the deadenylation complex that reduces poly-A length, inhibiting the recruitment on the mRNA of translation activators (Kim and Richter, 2006; Zaessinger et al., 2006). mRNA can be silenced also by oligomerization into dense particles, which reduce ribosome accessibility (Chekulaeva et al., 2006). These mechanisms are not mutually exclusive. In fact, to ensure a precise control of translation, localization of mRNA is controlled by several repressors that act redundantly at multiple levels of translation.

Once the mRNA reaches the final destination, mRNA must be released from transitional repression at the right time. Translational de-repression in response to spatial cues is mainly caused by changes in repressor or activator affinity for target mRNAs, which can be induced by competitive binding with locally expressed proteins, or by post-translational modification of RBPs. Some examples that are relevant for neuronal cells will be discussed in the next paragraphs.

1.5.2 RNA granules

As mentioned above, locally transcribed mRNAs are assembled and transported in large RNPs, which are referred to as RNA granules. RNPs generally contain several ribosomal subunits, translation factors, decay enzymes, helicases, scaffolds, and RNA binding proteins.

RNPs do not exist as conventional soluble complexes like many other protein assemblies in the cell that are usually surrounded by membranes. Instead, owing to multivalent and dynamic interactions between RNA and protein components, RNA granules form distinct liquid bodies that de-mix from the rest of the liquid cytosol. This process of liquid–liquid phase separation (LLPS), or biomolecular condensation, generates ‘membrane-less organelles’ (Boeynaems et al., 2018; Fan and Leung, 2016; Fernandopulle et al., 2021).

The liquid properties of RNPs enable different RNA and protein components to dynamically associate with each other while excluding unrelated components present in the cytoplasm, thus facilitating translational control (for example, miRNA binding and ribosome accessibility). Membrane-less organelles can also dynamically exchange components with the cytosol or other organelles, enabling regulated RNA flux and RNA metabolism. In addition, thanks to this dynamic nature, RNPs can quickly assemble and disassemble in response to stress or stimuli.

Phase transition from solute to liquid-like, gel-like and solid states is influenced by various factors including temperature, local protein and RNA concentrations, or the amino acid composition and post-translational modifications of the RBPs (Boeynaems et al., 2018; Chong and Forman-Kay, 2016). These proteins typically contain prion-like or low complexity domains that are important for RNP liquid–liquid phase separation (Fan and Leung, 2016). The RNA recognition motifs (RRMs) inherent to RBPs also regulate LLPS, in part by binding RNA in order to increase the local RNA concentration, in part by binding other proteins, such as chaperones and nucleocytoplasmic transporters, which directly control the propensity of RBPs to self-associate (Wolozin and Ivanov, 2019).

In addition to multi-domain proteins, phase transitions can be triggered by other macromolecules capable of multivalent interactions, including the RNA itself, which can self-assemble and serve as a scaffold for the binding of multiple RNA-binding proteins (Fan and Leung, 2016). Finally, post-translational modifications, such as ubiquitination and phosphorylation have also been observed to enhance or inhibit assembly of RNPs (Chong and Forman-Kay, 2016; Fan and Leung, 2016; Tsang et al., 2019).

There are many different types of RNA granules that vary in terms of localization, composition and function (**Fig. 9**). In the cytoplasm, RNA granules include stress granules (SGs), P-bodies (PBs), transport granules, storage granules, activity-dependent granules, and myo-granules (Buchan and Parker, 2009; Fernandopulle et al., 2021; Parker and Sheth, 2007) (**Fig. 9**).

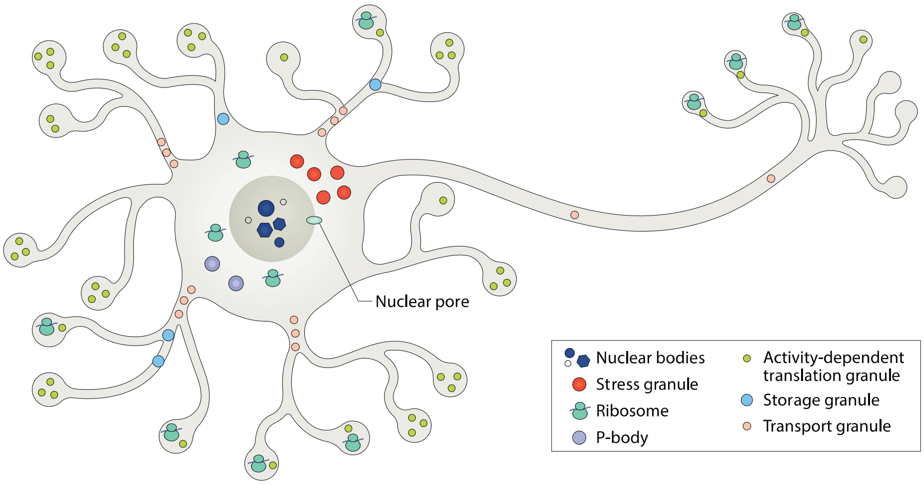

Figure 9 Types of membraneless organelles present in neurons

Overview of the different types and localization of RNA granules present in neurons, with nuclear bodies in the nucleus, stress granules and P-bodies in the neuronal soma, transport granules and storage granules in the axon and dendrites, and activity-dependent granules in the synapses (adapted from(Wolozin and Ivanov, 2019).

PBs, main sites of irreversible mRNA silencing, contain components of both non-sense mediated decay pathway and RNA-induced silencing complex, and do not contain ribosomal components (Parker and Sheth, 2007). SGs, instead, contain temporally stalled mRNA, whose translation is stopped in response to environmental stress, such as heat, oxidative stress, UV irradiation, and hypoxia (Buchan and Parker, 2009). Being the consequence of abortive translation, SGs contain specifically stalled 48S pre-initiation complex and translation initiation factors, together with several other mRNA binding and scaffold proteins. Despite the differences, SGs and PBs are spatially, compositionally and functionally linked (Kedersha et al., 2005): they share several protein components, they can harbor the same species of mRNA and they can physically associate with one another. This evidence suggests that SGs act as sites of mRNA triage in which individual transcripts are sorted for storage, re-initiation, or delivered to mRNA-decay-competent-PB for degradation (Kedersha et al., 2005).

Other specialized RNPs are Transport granules that are responsible for delivering packaged mRNAs from the cell body to a distant site in the neurites, where local protein synthesis can take place (Fernandopulle et al., 2021). These RNPs display constitutive bidirectional movement along axons and dendrites, and are composed of a heterogenous complex of RBPs, ribosomal components and RNA (Fernandopulle et al., 2021) (**Fig. 8**).

1.5.2.1 Stress Granules

SGs controls mRNA metabolism promoting mRNA translational repression upon stresses and have been implicated in the pathogenesis of many diseases, including cancer, neurodegeneration, inflammatory disorders, and viral infections (Wolozin and Ivanov, 2019).

Historically, the term “stress granule” was used to describe phase-dense cytosolic particles that contain polyadenylated mRNAs, PABP and T cell intracellular antigen 1 (TIA1) (Kedersha et al., 1999). These proteins coalesced with mRNAs to form SGs upon heat shock stress or oxidative stress induced by NaAsO2 treatment. Stress-induced formation of SGs in mammalian cells was strictly dependent on phosphorylation of the α-subunit of eIF2α, providing the first indication that SGs are connected to mRNA translation (Kedersha et al., 1999). Since these granules quickly dissolved upon stress removal, SGs were also postulated to be sites of temporary mRNA storage and triage (Anderson and Kedersha, 2008).

The core components of SGs are the messenger RNP (mRNP) complexes, including translationally arrested pre-initiation complexes (PICs) consisting of the small 40S (but not the large 60S) ribosomal subunits, mRNAs and associated translation initiation factors (Hofmann et al., 2021; Markmiller et al., 2018). Many RBPs contribute to SG assembly and disassembly. The so-called SG-nucleators, are required for the condensation of PICs into SGs and act by directly binding to mRNAs and interacting with the translational machinery. SG-nucleating RBPs include, among others, Ras GTPase-activating protein-binding protein 1 (G3BP1), TIA1 and TIA1-related protein (TIAR), FMRP, cell cycle-associated protein 1 (CAPRIN1) and Ubiquitin Associated Protein 2 Like (UBAP2L) (Cirillo et al., 2020; Hofmann et al., 2021; Markmiller et al., 2018; Riggs et al., 2020). Other RBPs play auxiliary roles by bringing specific mRNAs into SGs via sequence-specific interactions with their mRNA targets. Gene expression or deletion experiments suggest that only PICs and a limited number of specific RBPs are essential for the formation of a stable SG 'core' (Wheeler et al., 2017; Wolozin and Ivanov, 2019). Once assembled, the core recruits more SG nucleators and serves as a platform for the formation of more dynamic peripheral 'shell'-like structure around them, consisting of other proteins and mRNPs (Wheeler et al., 2017; Wheeler et al., 2016). The exact composition of SGs is variable and depends on the triggering stressor and the cell type (Fan and Leung, 2016; Markmiller et al., 2018).

SGs are in dynamic equilibrium with polysomes, the actively translating fraction of cytoplasmic ribosomes (Kedersha et al., 2000). When polysomes are disassembled in response to stress or pharmacological interventions (for example, following treatment with the antibiotic puromycin, which causes premature protein synthesis termination), there is an increase in the pool of untranslated mRNPs in PICs, which favors SG assembly. By contrast, an increase in mRNPs in the polysome-associated fraction, or inhibition of translation elongation (for example, by treatment with cycloheximide, blocking translation elongation and freezes ribosomes on mRNAs), disfavors SG assembly (Kedersha et al., 2000). Thus, the formation of SGs is tightly connected to the translational status in the cell, and the dynamic link between SG and translational control distinguishes SGs from many other RNA granules.

1.5.2.2 P-Bodies

Different from SGs that are induced by stress, PBs are constitutively present in mammalian cell lines and appear as droplets averaging 0.5 um in diameter (Standart and Weil, 2018), generally smaller than the SGs whose diameter can range from 0.4 to 5 µm (Fan and Leung, 2016). PBs are involved in RNA decay and in the coordinated storage of mRNAs encoding regulatory functions.

PBs contain various proteins related to RNA metabolism that belong to the categories of mRNA decay, translational control and RNA interference: 5’–3’ decay [mRNA-decapping enzyme subunit 1/2 (DCP1/2), 5'-3' Exoribonuclease 1 (XRN1)], de-capping activators [Enhancer of mRNA-decapping protein 3 and 4 (EDC3 and EDC4), Protein PAT1 homolog 1, (PAT1B) and Sm-like proteins 1-7 (LSM1-7)], deadenylating [CCR4 and Poly(A)-Nuclease Deadenylation Complex Subunit 3 (PAN3)] or adenylating factors [Cytoplasmic Polyadenylation Element Binding Protein 1 (CPEB1)], miRNA-mediated silencing factors [Argonaute RISC Component 1-4 (AGO1-4), GW182], nonsense-mediated decay factors [Regulator of nonsense transcripts 1 (UPF1), SMG5, SMG7], and the translational repression pathway factors [DEAD-Box Helicase 6 (DDX6), the eIF4E-binding protein Eukaryotic translation initiation factor 4E transporter (4E-T), as well as eIF4E, Pumilio RNA Binding Family Member 2 (PUM2), FMRP, Embryonic Lethal, Abnormal Vision, Drosophila, Homolog-Like 1 (ELAV1)] (Standart and Weil, 2018).

PBs contain only untranslated mRNAs and no ribosomal RNAs. They can also recruit small noncoding RNAs (ncRNAs), including transfected siRNAs and endogenous miRNAs (Standart and Weil, 2018). The presence of many translation repressors is an indicator of the storage function of these RNPs.

Several PB proteins are important for assembly, a few of them limit PB size or number, whereas others, including both translation repression and decay factors, are required for PB maintenance. However, only three proteins have been found to be essential for mammalian PB formation: DDX6, 4E-T and, to a lesser extent, LSM14A (Ayache et al., 2015).

1.5.2.3 Neuronal transport granules and mRNA transport in neurons

Compared to non-neuronal cells, the 3′ UTR regions of neuronal mRNAs are substantially longer and contain more secondary structures critical for RNPs assembly. Within neurons themselves, mRNAs that localize to neurites are longer, enriched in secondary structures, and have a longer half-life than the transcript localized in the soma (Fernandopulle et al., 2021; Tushev et al., 2018). High stability is required to distally localize transcripts that are subjected to long trafficking times and temporally specific protein synthesis and neuronal transcript UTRs contain specific sequence motifs to antagonize de-adenylation and miRNA binding and promote stabilizing RBP interactions.

But regulatory signals are not restricted to the 3’UTR. The 5’UTR as well includes specific sequence motifs and secondary structures. A single transcript might use the 3′ UTR for localization in one neuronal subtype and the 5′ UTR in another cellular subtype. Alternatively, one UTR might be used to direct transport to a general region, while the other for subregional specification, for example axon and synapsis, respectively, rendering their regulation extremely complex and controlled (Meer et al., 2012). Sequences and secondary structures within the coding region have also been proposed to act as cis-regulating sequences (Rotem et al., 2017). Presumably, the combinatorial use of multiple regulatory motifs within a transcript attracts a collection of RBPs, which unambiguously act to specify its destination and temporal translation.

Intrinsic qualities of neuronal mRNAs might also be a risk factor. Repeated sequences within the long 3′ UTRs of neurite-localized transcripts might predispose these mRNAs to self-scaffold, aggregate and disrupt cellular function in the disease setting (Tushev et al., 2018). Recent work suggests that repeat-rich RNA molecules can spontaneously aggregate to form solid aggregates; an example is the hexanucleotide repeat expansion in the C9ORF72 transcript, linked to both ALS and FTD (Jain and Vale, 2017). In addition, being enriched in secondary structures that confer scaffolding function to the transcript, these RNAs could bring together a group of RBPs, facilitating toxic protein aggregation or depleting a functional pool of proteins that remain enclosed in the RNPs. There are over 2,000 known RBPs in the human genome, with a few that are expressed solely or predominantly in neurons [for example, ELAVL and Rna-binding fox (RBFOX) proteins] and many that are expressed broadly but with neuron-specific roles (for example, FUS and FMRP) (Fernandopulle et al., 2021).

Other important components of neuronal granules are microtubule motor proteins kinesin and dynein that drive their movement along the axon. These motor proteins link their cargoes (mainly organelles) to microtubules and drive them in an anterograde transport outward from the soma to the distal axon (kinesin), or in a retrograde transport back from the axon to soma (dynein) (Maday et al., 2014) (**Fig. 10A**). Frequently, cargoes have both motor types bound simultaneously, to avoid either distal accumulation or distal depletion of cellular components.

As membrane-free phase-separated droplets, RNA granules are unique cargoes that require particular scaffolds and adaptors equipped to interface between a liquid body and a traditional protein complex (Fernandopulle et al., 2021). Multiple evidence suggest that conventional protein adaptors are also implicated in the motility of these membrane-less organelles (**Fig. 10A**). RBPs present in transport granule, such as FMRP, SFPQ (Splicing Factor Proline and Glutamine Rich), and ZBP1, form conventional soluble complexes with kinesin light chain (KLC), a protein adaptor for kinesin (Davidovic et al., 2007; Fukuda et al., 2021; Wu et al., 2020). Point mutations in either the RBP or the KLC disrupt this binding and impair localization of specific mRNAs bound by those RBPs (Fukuda et al., 2021; Wu et al., 2020). Direct binding of FMRP to the dynein binding protein bicaudal D (BIDC2) is instead required for dynein-dependent transport of FMRP granules in *Drosophila* neurons (Bianco et al., 2010).

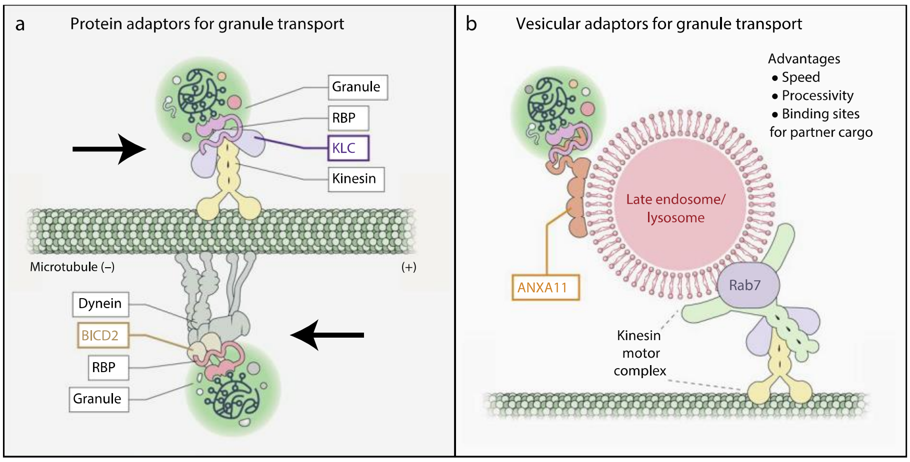

Figure 10 Motor adaptors for RNA transport

A) KLC and BICD2 each bind RBPs and molecular motors (kinesin or dynein, respectively) simultaneously, enabling transport granule trafficking.

B) The LE/Lys is a recently characterized vesicular adaptor between transport granules and microtubule-based motors. This system requires the secondary adaptors Rab7 (between the motor complex and the LE/Lys) and ANXA11 (between the LE/Lys and transport granule) (adapted from (Fernandopulle et al., 2021).

In addition to conventional protein complexes, different types of RNA granules can use membrane-bound organelles coupled to motor proteins as vehicles to promote microtubule-dependent transport (**Fig. 10B**). The process of docking onto other membrane-bound organelles is known as "hitchhiking". This concept of RNA hitchhiking was first identified in non-mammalian system, such as filamentous fungi, in which RNA granules hitchhike on moving endosomes during long-distance trafficking (Baumann et al., 2012; Pohlmann et al., 2015).

A recent study revealed a role for this mechanism of transport also in higher-order organisms, and more precisely in neurons. Works performed in the model system

Xenopus laevis found that mRNAs, ribosomes and transport granules all co-traffic with late endosomes along the axons of retinal ganglion cells, and that these complexes serve as translation platforms to supply axonal mitochondria with new protein synthesis (Cioni et al., 2019). RNA-bearing late endosomes often pause on mitochondria, and mRNAs encoding proteins for mitochondrial function, present in these granules, are translated on Rab7a endosomes. Disruption of Rab7a function with Rab7a mutants, including those associated with Charcot-Marie-Tooth type 2B neuropathy, markedly decreases axonal protein synthesis, impairs mitochondrial function and compromises axonal viability (Cioni et al., 2019). In addition, Rab7 scaffolds both kinesin and dynein effector assemblies on late endosome/lysosome, indirectly facilitating RNA hitchhiking, axonal RNA transport and local translation (Fernandopulle et al., 2021).

A separate study demonstrated, in human iPSC (induced pluripotent stem cell)-derived neurons, the dependence of axonal RNA granule motility on lysosomal trafficking (Liao et al., 2019). Using a combination of live-cell imaging, *in vitro* assays, and proximity-labelling proteomics, this study revealed that RNA granules hitchhike on LAMP1-positive vesicles during microtubule-dependent transport, which enables their long-distance trafficking in mammalian cells (Liao et al., 2019). Liao and colleagues identified the RNA granule-associated phosphoinositide-binding protein Annexin A11 (ANXA11) as the 'secondary adaptor' that acts as a bridge between the lysosome and the transport granule (**Fig. 10B**). ANXA11 possesses a C-terminal domain that binds endo-lysosomal lipids and an N-terminal prion-like low complexity domain that enables the protein to undergo biomolecular condensation. As a result, ANXA11 binds the lysosomal surface through a folded polypeptide–lipid interaction and integrates into the transport granule through phase separation (Liao et al., 2019). Importantly, known ALS-associated mutations of ANXA11 disrupt docking between RNA granules and lysosomes, consequently impeding RNA granule transport and localized translation in neurons (Liao et al., 2019).

1.5.3 Local translation

After a long travel that can last from hours to days, the RNPs arrive at the final destination, where protein synthesis initiates upon stimulus-dependent changes to both protein and RNA (Fernandopulle et al., 2021)(**Fig. 8**). Examples of spatial cues are synaptic signaling in dendrites and guidance signals in developing axonal growth cone. RNA release is modulated by granule rearrangements that results from post-translational modifications and chaperone interactions. Src kinase phosphorylation of ZBP1, RNA binding protein that promotes translocation of the beta-actin transcript in a translationally silent state, releases bound mRNA and is necessary for β-actin translation in dendrites (Huttelmaier et al., 2005). Given that Src activity is restricted to the cell periphery, local activation of β-actin translation can be modulated through the spatially restricted activity of this kinase (Huttelmaier et al., 2005).

Another RNP component that is regulated by phosphorylation is the repressor FMRP: in its phosphorylated state, FMRP is found associated with stalled ribosomes, causing repression of mRNA translation. In contrast, upon neuronal stimulation by mGluR, FMRP is dephosphorylated by the protein phosphatase 2A (PP2A), ultimately leading to de-repression of translation (Narayanan et al., 2007).

A protein that is positively regulated by phosphorylation is the cytoplasmic polyadenylation element binding protein CPEB, that upon phosphorylation by Aurora-kinase family promotes poly-A tail elongation of specific transcripts (Mendez and Richter, 2001). In neurons, this CPEB phosphorylation can be induced, for example, by *N*-methyl-D-aspartate (NMDA) receptor stimulation (Huang et al., 2002).

PTM of different RNP components can be expected to have distinct effects on the translational status of different granule types (Fernandopulle et al., 2021). For example, phosphorylation of FUS and hnRNPA2 (Heterogeneous Nuclear Ribonucleoprotein A2) reduces their phase separation while phosphorylation of FMRP and TDP-43 (TAR-DNA binding protein-43) promotes phase separation (Monahan et al., 2017; Tsang et al., 2019).

Modifications of RNAs themselves also modulate translation. RNA nucleases, such as dicer and argonaute proteins, are known components of neuronal PBs and might effect changes in RNA through regulated docking and co-condensation events with transport granules as well (Zeitelhofer et al., 2008).

Other travelling components essential for translation are ribosomes that can reach distal sites of neurites from multiple possible sources and through different mechanisms. Some RNA-binding proteins, such as FMRP, bind ribosomes and, therefore, incorporate them into transport granules (Blackwell et al., 2010). The coupling of ribosomes to plasma membrane receptors also exists and has been proposed as a mechanism linking signals to local translation (Fernandopulle et al., 2021). Cue stimulation of growing *Xenopus laevis* retinal ganglion cell axons induces rapid dissociation of ribosomes from receptors and the selective translation of receptor-specific mRNAs (Koppers et al., 2019). Finally, ribosomes might reach neurites in association with late-endosomes by a hitchhiking process, possibly in coordination with transport granules (Cioni et al., 2019).

1.6 RNA-autophagy interplay

Disrupted RNA metabolism, aberrant formation and enhanced aggregation of RNP granules, along with their impaired clearance are crucial pathological events that contribute to neuronal toxicity and consequently to the development of a range of neurological and muscular disorders including Multi-System Proteinopathy (MSP), Pagets disease, Amyotropic Lateral Sclerosis (ALS), and Frontotemporal Lobar Degeneration (FTLD) (Mandrioli et al., 2020). The clearest examples are TDP-43 and

FUS that are SG markers commonly found in the cytoplasmic inclusions in ALS patient samples. Many of the ALS mutations contribute to disrupt TDP-43 and FUS shuttling between the nucleus and cytoplasm, increase their aggregation ability and lead to the formation of less dynamic, non-fluid gels granules (Dudman and Qi, 2020; Wolozin and Ivanov, 2019). Protein quality control mechanism plays a vital role in removing toxic protein/RNA aggregates, and several RNAs and associated ribonucleoprotein complexes are specifically recruited to autophagosome and subsequently degraded in the lysosome (Abildgaard et al., 2020).

Emerging evidence has revealed intricate connections between RNA/RNPs and autophagy that goes beyond RNPs clearance (Abildgaard et al., 2020). As discussed earlier, RNA granules can use membrane-bound organelles, such as lysosomes and late endosomes, as vehicles to promote long-range transport to distal sites via microtubule-dependent transport (Cioni et al., 2019; Liao et al., 2019), indicating a role for autophagy and the endosomal-lysosomal pathway not only in the clearance but also in the transport of RNA (**Fig. 10B**).

Moreover, recent studies have revealed a significant number of novel autophagy regulators with RNA-related functions, indicating roles for RNA and associated proteins not only as cargoes, but also as autophagy pathway regulator (Abildgaard et al., 2020).

1.6.1 Granulophagy, the autophagic clearance of RNPs

Dysfunctional RNPs can be cleared by a specific type of selective autophagy called ‘granulophagy’ (Buchan et al., 2013; Frankel et al., 2017). Mutations inhibiting autophagy upstream of autophagosome formation cause SG and P-body accumulation both in yeast and mammalian cells. Indeed, MEFs bearing homozygous deletion of ATG7 showed a basal level of constitutive SGs, and an evident defect in SG resolution after heat stress (Buchan et al., 2013). In addition, chemical activation of autophagy increased the rate at which SGs were cleared following the relief of stress, that was instead slowed down by autophagy inhibition. A role for the tyrosine kinase Syk in autophagy-dependent SG clearance has been revealed (Krisenko et al., 2015). Treatment of cells with inducers of SGs, such as sodium arsenite (NaAsO2) or a proteasome inhibitor leads to the recruitment of Syk to SGs. This recruitment requires the phosphorylation of Syk on tyrosine 342 and 346 that enables Syk to interact with the SG component Grb7. This recruitment promotes the formation of autophagosomes around SGs, their clearance from cells through autophagy and enhances the survival of cells in which SGs are induced (Krisenko et al., 2015).

Another excellent example of proteins involved in the autophagy-mediated clearance of RNPs is represented by Cdc48/VCP (Buchan et al., 2013) whose mutations predispose humans to AMLS, FTLD, inclusion body myopathy, and multisystem proteinopathy. With a screen performed in yeast, Parker and colleagues identified over 100 genes that are involved in the modulation of SGs and/or PBs trough autophagy, including the vacuolar ATPase VCP. VCP depletion with either siRNAs or inhibitors leads to a defect in the clearance of SGs both in human and in yeast cells., similar to the VCP pathological mutations that lead to constitutive accumulation of stress granules which contain TDP-43 (Buchan et al., 2013). Thus aging-related autophagy decline affects SGs and PBs dynamics and aberrant SGs and PBs might in turn promote the pathology of aging and aging-associated diseases.

Whether this mechanism of RNA granule clearance is utilized to remove other types of RNPs still needs to be defined, however, these and other studies suggest that, in line with its traditional degradative role, autophagy can selectively degrade RNA, RBP and RNP complexes, with important consequences for RNA homeostasis, global gene expression programs and finally neuronal homeostasis.

1.7 HECW1 role in the autophagy pathway, RNP dynamics and neuronal homeostasis

1.7.1 HECW1 interaction with proteins implicated in mRNA processing, vesicle trafficking and autophagy

Identification of proteins that could be either interactors or substrates is a required starting point for the identification of a protein cellular function; and for HECW1, few substrates (mutant SOD1G93A and Dishevelled-1) (Miyazaki et al., 2004; Zhang et al., 2011) and few interactors (TRAP-delta, p53 and RNF43) are known (Li et al., 2008; Li et al., 2009; Shinada et al., 2011).

With the aim to characterize the full interactome of HECW1, our lab performed a co-immunoprecipitation (CO-IP) coupled with Mass Spectrometry (MS) analysis, an approach based on the identification of interacting proteins upon selective enrichment by immunoprecipitation. To obtain a comprehensive view of the HECW1 interactome, the endogenous HECW1 was immunoprecipitated, using a home-made monoclonal anti-HECW1 antibody, from lysates of different cell lines: HeLa (cervical cancer), A172 and T98G (glioblastoma) cells. In parallel, an anti-GFP antibody was used to immunoprecipitate a GFP-fused-HECW1 transfected into 293T cells.

Gene Ontology analysis performed to examine the main function of the identified proteins revealed an enrichment in mRNA binding proteins implicated at various steps of mRNA processing, and in proteins involved in vesicle trafficking and autophagy (candidate interactors are listed in **Table 1**).

Among them, there are mRNA translational repressors like FMRP, and known components and assembling factors of different RNPs, such as DCP1A, EDC3 and ILF3 for the PBs (Parker and Sheth, 2007; Standart and Weil, 2018), G3BP1 and UBAP2L for SGs (Buchan and Parker, 2009; Cirillo et al., 2020; Wolozin and Ivanov, 2019), and DDX6, a protein shared by SGs and PBs (Riggs et al., 2020). Of note, FMRP is a component of SGs and of the neuronal transport granules, required to transport mRNA from the neuronal soma to distant site of axon and dendrites (Fernandopulle et al., 2021). Proteins involved in mRNA processing are the top hit category also in the Drosophila Hecw interactome, characterized in a parallel study performed in the laboratory (Fajner et al., 2021) with few candidates identified in both the human and the Drosophila datasets, such as DDX6/Me31B, UBAP2L/lingerer and FMRP/Fmr1. Of particular interest is the P-body component Lingerer, known to associate with Fmrp and other RNA-binding proteins to modulate their repressive functions and endowed with a ubiquitin associated (UBA) domain (Baumgartner et al., 2013; Thapa et al., 2020).

The analysis also identified several proteins involved in vesicle trafficking and membrane fusion, such as SNX2 and SNX29, members of the sorting nexins (SNXs) family of proteins involved in protein trafficking regulation (Vieira et al., 2021; Worby and Dixon, 2002), and CTTN (cortactin) required for autophagosome–lysosome fusion (Nakamura and Yoshimori, 2017); together with components of the autophagic pathway, such as ATG2A, that transfers phospholipids from the endoplasmic reticulum to the growing phagophore (Chang et al., 2021), and the chaperon BAG3, involved in autophagy-dependent degradation of polyubiquitinated proteins (Gamerdinger et al., 2009). Other class of interactors were members of cell-junctions and components of the spliceosome.

These data suggest the involvement of HECW1 in the regulation of mRNA processing, vesicular trafficking and the autophagy pathway.

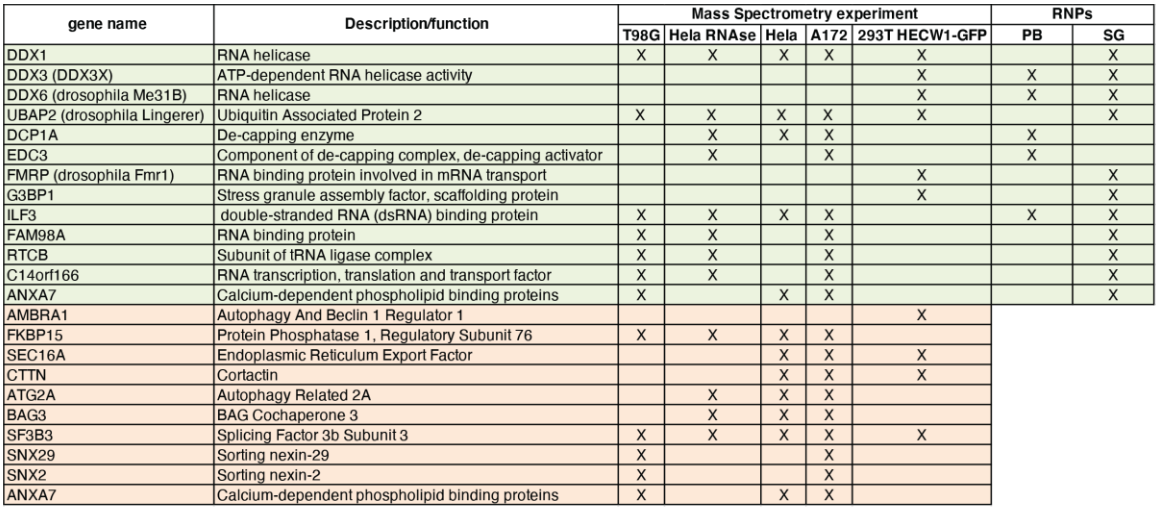

gene name	Description/function	Mass Spectrometry experiment					RNPs	
		T98G	Hela RNAse	Hela	A172	293T HECW1-GFP	PB	SG
DDX1	RNA helicase	X	X	X	X	X		X
DDX3 (DDX3X)	ATP-dependent RNA helicase activity					X	X	X
DDX6 (drosophila Me31B)	RNA helicase					X	X	X
UBAP2 (drosophila Lingerer)	Ubiquitin Associated Protein 2	X	X	X	X	X		X
DCP1A	De-capping enzyme		X	X	X		X	
EDC3	Component of de-capping complex, de-capping activator		X		X		X	
FMRP (drosophila Fmr1)	RNA binding protein involved in mRNA transport					X		X
G3BP1	Stress granule assembly factor, scaffolding protein					X		X
ILF3	double-stranded RNA (dsRNA) binding protein	X	X	X	X		X	X
FAM98A	RNA binding protein	X	X		X			X
RTCB	Subunit of tRNA ligase complex	X	X		X			X
C14orf166	RNA transcription, translation and transport factor	X	X		X			X
ANXA7	Calcium-dependent phospholipid binding proteins	X		X	X			X
AMBRA1	Autophagy And Beclin 1 Regulator 1					X		
FKBP15	Protein Phosphatase 1, Regulatory Subunit 76	X	X	X	X			
SEC16A	Endoplasmic Reticulum Export Factor			X	X	X		
CTTN	Cortactin			X	X	X		
ATG2A	Autophagy Related 2A		X	X	X			
BAG3	BAG Cochaperone 3		X	X	X			
SF3B3	Splicing Factor 3b Subunit 3	X	X	X	X	X		
SNX29	Sorting nexin-29	X			X			
SNX2	Sorting nexin-2	X			X			
ANXA7	Calcium-dependent phospholipid binding proteins	X		X	X			

Table 1 Partial list of proteins identified as HECW1 interactors in IP-MS experiments

The tables list examples of proteins that were identified as HECW1 interactors in the CO-IP-MS experiments described in the text. Green, proteins involved in mRNA binding and processing; red, proteins involved in vesicle trafficking and autophagy. The presence of the proteins in the interactome of a particular experiment is indicated with an 'x'. For mRNA-related proteins, an 'x' also indicates in which RNPs these proteins are mainly found. PB, p-bodies; SG, stress granules.

1.7.2 The HECW1 Drosophila orthologue Hecw and its role in neuronal homeostasis and RNPs dynamic regulation

Our lab recently identified and molecular characterized Hecw, the fourth member of the Drosophila melanogaster Nedd4 family, the single ortholog of the human HECW1 and HECW2 (Fajner et al., 2021). This gene encodes for a K63-specific E3-ligase and is preferentially expressed in the fly gonads and, as for the human HECW1, in the central nervous system.

We demonstrated that Hecw is required for maintaining neuronal health. Hecw mutant or KO flies, indeed, show premature aging, neuromotor defects and brain tissue vacuolization, which resulted from neuronal death in the CNS, as measured by TUNEL assay (Fajner et al., 2021), phenotypes all reminiscent of neurodegenerative processes in humans. Overexpression of Hecw causes reduction in longevity, similarly to that observed in Hecw mutants (Fajner et al., 2021). These observations indicate that the activity of this E3 ligase needs to be tightly regulated to protect neurons from premature neurodegeneration. Our results are reminiscent of the ones obtained with transgenic mice overexpressing the human HECW1 that display neuronal loss in the spinal cord and develop ALS-like symptoms, such as motor neuron degeneration and muscle atrophy (Zhang et al., 2011).

Correlative observations indicate a role of Hecw in the autophagy pathway. Hecw-mutant neurodegenerative phenotype, indeed, closely resembles the ones caused by the lack of the positive autophagy regulator Atg7 (Juhasz et al., 2007). In addition, Hecw expression decline with aging (Fajner et al., 2021), a pattern characteristic of components of the autophagy pathway and, more in general, proteins responsible for protein homeostasis and quality control (Vilchez et al., 2014). In support of this hypothesis, Hecw overexpression led to re-localizing of Ref(2)p (fly orthologue of the human autophagy receptor p62) in cytoplasmic puncta, and preliminary experiments of starvation-induced autophagy in the flies' ovaries suggest a possible autophagic impairment in the absence of Hecw (unpublished data). Taken together, these observations suggest that this E3 ligase has a role in neuronal homeostasis and protect neurons from premature neurodegeneration, at least in part working at the level of the autophagy pathway.

We also demonstrated a pivotal role of Hecw and ubiquitin in regulating the activity of RNA binding proteins and in maintaining the liquid-like nature of RNPs in oogenesis and neurons (Fajner et al., 2021). Neurons of young adult Hecw mutant flies' brains, indeed, present enlarged RNPs which were not dissolved upon treatment with hexanediol, an aliphatic alcohol that disrupts weak hydrophobic bonds typical promoters of liquid droplets. We also provided compelling evidence that Hecw-mediated ubiquitination of the substrate Fmrp is needed for the diffusive exchange in and out of RNP compartments (Fajner et al., 2021). Reduced ubiquitination of Fmrp in Hecw-mutant flies impairs its translational repressor activity, resulting in altered expression of Fmrp targets, such as Orb in nurse cells and Profilin in neurons (Fajner et al., 2021), a known ALS causative gene (Wu et al., 2012). Interesting, Profilin mutant mouse model replicates the key features of ALS including adult-onset, progressive motor neuron loss accompanied with progressive motor weakness ending in paralysis and death (Yang et al., 2016). We hypothesized that Hecw have a positive role in maintaining neuronal homeostasis and its absence could have an impact on neurodegenerative disorders like ALS.

Based on this mechanistical evidence, we propose a linear cascade of events (**Fig. 11**) in which Hecw-dependent ubiquitination, by adding an additional surface of interaction to Fmrp, could enable precise spatiotemporal recruitment of repressive components and ribosomes, thereby "turning off" protein synthesis locally.

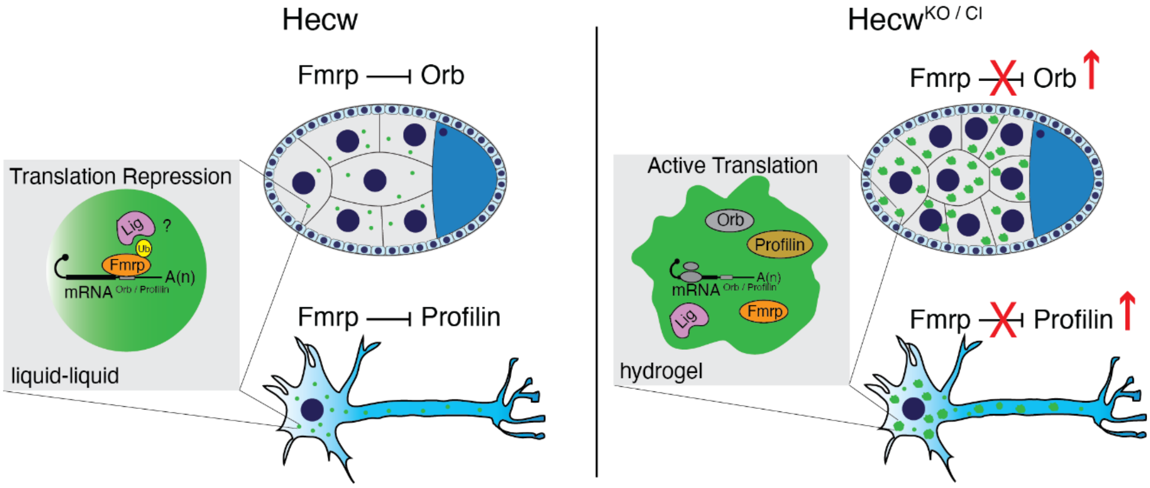

Figure 11 Ubiquitin increases Fmrp phase-separation propensity and translational repression

Proposed model of RNP regulation by Hecw. In normal conditions, both in ovary and in neurons, Hecw ubiquitinates Fmrp and contributes to the maintenance of its translational repression activity, possibly through the interaction with the ubiquitin receptor Lingerer (indicated with a question mark in the figure). In the absence of Hecw, RNPs transition to a less dynamic gel-like state, Fmrp translational repression is lost and Orb mRNA and Profilin mRNA are actively translated

2 AIM OF THE THESIS

Previous results obtained in the lab demonstrated a protective role for the *Drosophila melanogaster* Hecw in neuronal homeostasis and showed an involvement of HECW1/Hecw in autophagy and RNPs dynamics. The aim of this study was to characterize the physiological and pathological functions of the human NEDD4-E3 ligases HECW1 in neurons, where this enzyme is specifically expressed.

To this aim, we optimize protocol for the differentiation of neurons from human iPSCs and we generated HECW1-KO iPSCs. In parallel we also tested HECW1 depletion in A549 cells.

With these tools, we investigated into HECW1 function following on the one hand an unbiased approach, using proteomics and transcriptomics methods to identify cellular pathways perturbed by HECW1-depletion in iPSC-derived neurons, and on the other hand a data-driven analysis, investigating the effect caused by the lack of HECW1 on the autophagy pathway and RNPs dynamics.

3 MATERIALS AND METHODS

3.1 Buffers

3.1.1 Phosphate-buffered saline (PBS)

NaCl	137 mM
KCl	2.7 mM
Na_2HPO_4	10 mM
KH_2PO_4	2 mM

3.1.2 Tris-buffered saline - Tween (TBS-T)

NaCl	137 mM
KCl	2.7 mM
Tris-HCl pH 7.4	25 mM
Tween-20	0.1%

3.1.3 10X Sodium Dodecyl Sulphate – PolyAcrylamide Gel Electrophoresis (SDS-PAGE) running buffer

Glycine	192 mM
Tris-HCl pH 8.3	250 mM
SDS	1%

3.1.4 50X Tris-Acetate-EDTA (TAE)

Tris base	2 M
Acetic acid	1 M
EDTA pH 8	10 mM

3.1.5 1X JS buffer

Hepes pH 7.4	50 mM
NaCl	150 mM
Glycerol	10%
Triton X-100	1%
$MgCl_2$	1.5 mM
EGTA	5 mM

500X protease inhibitor cocktail from Calbiochem, sodium pyrophosphate pH 7.5 20 mM, sodium fluoride 250 mM, PMSF 2 mM and sodium orthovanadate 10 mM were added to the buffer immediately before usage.

3.1.6 1X Radioimmunoprecipitation assay (RIPA) buffer

Tris-HCl pH 8	50 mM
NaCl	150 mM
NP-40	1%
SDS	0.1%
Deoxycholic acid	1%

500X protease inhibitor cocktail (Calbiochem), 20 mM sodium pyrophosphate pH 7.5,50 mM sodium fluoride, 2 mM PMSF 10 mM sodium orthovanadate in HEPES pH 7.5, 25 μM PR619 (non-selective, reversible inhibitor of deubiquitinases DUBs) and 2 mM PMSF were added to the buffer immediately before usage.

3.1.7 SDS buffer

Tris-HCl pH 7.4	0,1 M
SDS	4,8%
Glycerol	10%

500X protease inhibitor cocktail from Calbiochem and DTT 1mM were added to the buffer immediately before usage.

3.1.8 Laemmli buffer

SDS	8%
Tris-HCl pH 6.5	200 mM
Glycerol	40%
DTT	400 mM
Bromophenol blue	0.4%

The Laemmli buffer was prepared as a 4X or 2X stock solution and stored at -20°C.

3.1.9 1,25x A69 nucleofection buffer

Na phosphate	37.5 mM
HCl	6.25 mM
MgCl2	12.5 mM
HEPES	25 mM
Glucose	13.75 mM
NaCl	125 mM
Ca(NO3)2	0.525 mM

The A69 buffer was prepared as 1,25X stock solution and diluted at 1X working solution in water.

3.2 Reagents

3.2.1 siRNAs

Protein (siRNA ID)	siRNA sequence 5’-3’	Source
HECW1 (s22968)	GGACAGCUGCAAUUCCGAUTT	Life Technologies

3.2.2 Primary antibodies

Protein	Species	Use	Identifier	Source
HECW1	mouse	WB 1:2000	IA8	Generated in house
HECW1	mouse	IF 1:1000	HN13	Generated in house
HECW1	rabbit	IF 1:500	SI1052	Generated in house
HECW1	rabbit	WB 1:500	HPA007593	Sigma
GAPDH	mouse	WB 1:5000	sc-32233	Santa-Cruz Biotechnology
NESTIN	mouse	WB 1:500	10C2_sc-23927	Santa-Cruz Biotechnology
		IF 1:500		
PAX6	rabbit	WB	sc-81649	Santa-Cruz Biotechnology
		IF 1:200		
SOX2	rabbit	WB	D6D9_3579	Cell Signaling
		IF 1:100		
TUJ1	rabbit	WB 1:5000	802001	BioLegend
		IF 1:1000		
TUJ1	mouse	WB 1:1000	801201	BioLegend
		IF 1:1000		
HECW2	rabbit	WB 1:1000	SI1055	Generated in house
AIP4	mouse	WB 1:1000	611199	BD Biosciences
NEDD4	rabbit	WB 1:5000	809	Generated in house
GFP	rabbit	WB 1:5000	G1544	Sigma
		IF 1:1000		
OCT4	rabbit	IF 1:300	C30A3_2840	Cell Signaling
MAP2	rabbit	WB 1:2000	AB5622	Merck-Millipore
LAMP1	mouse	IF 1:1000	H4A3_CD107a	BD Pharmingen
LC3	rabbit	IF 1:200	PM036	MBL International Corporation
P62	rabbit	IF 1:500	BML_PW9860	Enzo Life Science
FK2	mouse	IF 1:250	BML_PW8810-0100	Enzo Life Science
FLAG	mouse	WB 1:2000	M2	Sigma
EDC3	rabbit	WB 1:3000	16486-1-AP	Proteintech
		IF 1:100		
DCP1A	rabbit	WB 1:1000	ab47811	Abcam
		IF 1:800		

FMRP	rabbit	WB 1:1000	4317	Cell Signaling
		IF 1:100		
G3BP1	mouse	WB 1:1000	611126	BD Biosciences
		IF 1:1000		
TIAR1	mouse	WB	610352	BD Biosciences
		IF 1:100		
UBAP2L	rabbit	WB 1:2000	A300-534A	Bethyl
		IF 1:200		
DDX6	rabbit	WB 1:2000	A300-461A	Bethyl
		IF 1:500		
ILF3	rabbit	WB 1:2000	A303-651A	Bethyl

3.2.3 Secondary antibodies

Antibody	Use	Identifier	Source
Donkey anti-Mouse Alexa 488	IF (1:400)	A-21202	Thermo Fischer Scientific
Donkey anti-Mouse Cy3	IF (1:400)	715-165-150	Jackson lab
Donkey anti-Mouse Alexa 647	IF (1:400)	A-31571	Thermo Fischer Scientific
Donkey anti-Rabbit Alexa 488	IF (1:400)	A-21206	Thermo Fischer Scientific
Donkey anti-Rabbit Cy3	IF (1:400)	711-165-152	Jackson lab
Donkey anti-Rabbit Alexa 647	IF (1:400)	A-31573	Thermo Fischer Scientific
Donkey anti-Goat Cy3	IF (1:400)	705-605-003	Jackson lab
Donkey anti-Goat Alexa 647	IF (1:400)	A-21447	Thermo Fischer Scientific
Anti-Mouse HRP	WB (1:5000)	GENA931	GE Healthcare
Anti-Rabbit HRP	WB (1:5000)	GENA934	GE Healthcare

3.3 Molecular biology techniques

3.3.1 Agarose gel electrophoresis

DNA samples were loaded on 0.8%-2% agarose gels along with DNA markers (1kb or 100bp DNA Ladder, NEB). The gels were made in TAE buffer containing GelRed (Biotium, 41003), according to the manufacturer’s instructions, and run at 80 V until desired separation was achieved. The DNA bands were visualized under a UV lamp.

3.3.2 Transformation of competent cells

Competent TOP10 or StBl3 (Invitrogen) cells were incubated with DNA on ice for 30 minutes and then subjected to a heat shock for 30 seconds at 42°C. The cells were reincubated on ice for additional 5 minutes and, then, 300 µl of SOC medium were added and the cells were incubated at 37°C for 1 hour before plating them onto agar plates with appropriate antibiotics. The plates were incubated overnight at 37°C.

3.3.3 Minipreps

Individual colonies were used to inoculate 10 ml LB (containing the appropriate antibiotics) and grown overnight at 37°C. The suspensions were centrifuged for 10 minutes at 4000 rpm at 4°C. Minipreps were performed with the Wizard Plus SV Minipreps Kit (Promega) following the manufacturer's instructions. The plasmids were eluted in 50 µl nuclease-free water.

3.3.4 Large scale plasmid preparation

Cells containing transfected DNA were expanded into 200 ml cultures overnight. Plasmid DNA was isolated from these cells using the Macherey-Nagel Maxi-prep kit according to the manufacturer's instructions.

3.3.5 Constructs and plasmids

The following constructs were purchased from addgene

pT7-EGFP-C1-HsDCP1a (#25030);

pT7-EGFP-C1-HsRCK (#25033);

pT7-EGFP-C1-HsEDC3 (#25032);

pFRT-TODestFLAGHA-hFMRP-iso1 (#48690).

Phage-UbiC-G3BP1-GFP-GFP (Addgene #119950) was kindly provided by Tiziana Bonaldi.

The pEGFP-HECW1 and pCDNA3.1-FLAG-HECW1 were previously generated in our laboratory.

The pEGFP-C2-ILF3 vector was generated starting from the p34-pTO-Nter-STREP-HA-NF90 vector (kindly provided by Tiziana Bonaldi). The ILF3 DNA sequence was PCR amplified using the following oligos to insert EcoRI and SmaI restriction site at the ends of the product:

Forward with EcoRI site at 5’: 5-CGGAATTCATGCGTCCAATGCG-3

Reverse with SmaI site at 5’: 5-TCCCCCGGGCTAGGAAGACCCAAAATC-3

digested with EcoRI and SmaI and then cloned into the EcoRI-SmaI-linearized pEGFP-C2 vector using the Quick Ligation system (NEB, #M2200S).

The pEGFP-C2-UBAP2L vector was generated starting from the pLIX403-UBAP2L-mCherry vector (purchased from Addgene, #105286). The UBAP2L DNA sequence was PCR amplified using the following oligos to insert XhoI and EcoRI restriction site at the ends of the product:

Forward with XhoI site at 5’: 5-CCGCTCGAGCATGATGACATCGGTGGG-3

Reverse with EcoRI site at 5’: 5-CGAATTCTTAGTTGGCCCCCCAGC-3

digested with XhoI and EcoRI and then cloned into the XhoI-EcoRI-linearized pEGFP-C2 vector using the Quick Ligation system (NEB, #M2200S).

The pEGFP-C2-FMRP vector was generated starting from the pFRT-TODestFLAGHAhFMRPiso1 vector (purchased from Addgene, #48690). The FMRP DNA sequence was PCR amplified using the following oligos to insert EcoRI and SmaI restriction site at the ends of the product:

Forward with EcoRI site at 5’: 5-CGGAATTCATGGAGGAGCTGGTGG-3

Reverse with SmaI site at 5’: 5-TCCCCCGGGTTAGGGTACTCCATTCACGAG-3

Digested with EcoRI and SmaI and then cloned into the EcoRI-SmaI-linearized pEGFP-C2 vector using the Quick Ligation system (NEB, #M2200S).

pSLIK-NEO-GFP-HECW1-WT was previously generated in our laboratory. GFP-HECW1 were cloned into pENT and recombination into pSLIK_Neo was performed according to the standard protocol.

pSLIK-NEO-GFP-HECW1-CS was generated by recombination of pENT-GFP-HECW1-CS into pSLIK-NEO performed according to the standard protocol.

For the generation of catalytic inactive HECW1 (C1574S) site directed mutagenesis was performed using the Quick-Change Mutagenesis Kit (StrataGene), following the manufacturer's instructions with the following oligos:

Forward 5'- CCCAGGGCACACACAAGCTTCAACCGACTGGATC-3'

Reverse 5'- GATCCAGTCGGTTGAAGCTTGTGTGTGCCCTGGG-3' .

pLKO-PURO-TetOn-shRNA-HECW1 plasmids were generated by cloning shRNA oligos against HECW1 into the "all-in-one" pLKO-Tet-On according to the standard protocol (Wiederschain et al., 2009). Briefly, the stuffer DNA was removed from pLKO-Tet-On by AgeI/EcoRI digestion and replaced with annealed overlapping oligos encoding the desired shRNA and containing overhangs compatible with AgeI/ EcoRI sites.

The selected oligo sequences are:

#968 FOR:

5'-CCGGGCTCCGCAATTTCTACAGATTCTCGAGAATCTGTAGAAATTGCGGAGCTTTTTG-3'

#968 REV:

5'-AATTCAAAAAGCTCCGCAATTTCTACAGATTCTCGAGAATCTGTAGAAATTGCGGAGC-3'

3'UTR FOR:

5'-CCGGGCCTAGACATACGGTGCAAATCTCGAGATTTGCACCGTATGTCTAGGCTTTTTG-3'

3'UTR REV:

5'-AATTCAAAAAGCCTAGACATACGGTGCAAATCTCGAGATTTGCACCGTATGTCTAGGC-3'

CDS FOR:

5'-CCGGTCATTGCCACTGGCATATAATCTCGAGATTATATGCCAGTGGCAATGATTTTTG-3'

CDS REV:

5'-AATTCAAAAATCATTGCCACTGGCATATAATCTCGAGATTATATGCCAGTGGCAATGA-3'

3.4 Cell culture

3.4.1 Coating

3.4.1.1 Matrigel/Geltrex coating

Matrigel or Geltrex coating solution was prepared diluting 250ul of the stock solution (Matrigel, Corning, 354277; Geltrex, ThermoFisher A1413202) in 25ml of DMEM/F12 medium. Coating solution was added to well/plates and incubated at 37°C for at least 1 hours or overnight. Coated plated were then stored at 4°C or immediately used. At the time of plating, coating solution was removed and replaced with culture and cells.

3.4.1.2 Poly-D-Lysine/laminin coating

Poly-D-lysine (PDL, 50μg/ml, diluted in DPBS from a 1mg/ml stock solution) was added to each well/plates and incubated overnight at 37°C. PDL was removed and plates were washed three times with sterile water. Laminin (10μg/ml, diluted in Milli-Q water from a 1mg/ml stock solution, SIGMA L2020) was added to the well/plates and incubated at 37°C for at least 2 hours or overnight. Coated plated were then stored at 4°C or immediately used. At the time of plating, coating solution was removed and replaced with culture and cells.

3.4.1.3 Poly-L-ornithine coating

Poly-L-ornithine (PLO, Sigma, P3655) was resuspended in Milli-Q water to the final working concentration of 0,1mg/ml, added to each well/plates and incubated overnight at 37°C. After PLO removal, plates were washed three times with sterile water and let dry. Coated plates were used immediately or stored at 4°C for up to 1 week.

3.4.2 Cell lines

3.4.2.1 Commercial cell lines

A549 cells were cultured in Dulbecco's Modified Eagle Medium (DMEM) containing 10% FBS and 2 mM L-Glutamine.

HeLa cells were grown in GlutaMAX™-Minimum Essential Medium, MEM (Gibco Invitrogen), supplemented with 10% Fetal Bovine Serum South American (Invitrogen), sodium pyruvate 1 mM (Euroclone), non-essential amino acids (Euroclone), and 2 mM glutamine.

HEK-293T cells (ICLC) were maintained in DMEM, supplemented with 10% FBS and 2 mM L-glutamine.

HPSI0613-iPSCs were obtained from HipSci (ECACC).

iPSC-NGN2 were kindly provided by Michael Ward, NINDS (Fernandopulle et al., 2018; Wang et al., 2017). Briefly, these cells are generated by the established WTC-11 human iPSC line and are engineered to harbor expression cassette for both the doxycycline-inducible reverse transcriptional activator (rtTA3G) and NGN2 driven by the tet response element (TRE3G) inserted into the AAVS1 "safe harbor" locus in order to support an efficient protocol for their differentiation into neurons (referred to as i3Neurons) (Fernandopulle et al., 2018; Wang et al., 2017). All cell lines were tested for mycoplasma at each batch freezing with both PCR and a biochemical test (MycoAlert, Lonza). All iPSC lines were maintained as feeder-free cells in mTeSR1 medium (Stem Cell Technologies) on Matrigel (Corning)-coated dishes.

3.4.2.2 Induced pluripotent stem cell (iPSC) culture conditions

Each vial of iPSCs was thawed at room temperature, diluted 1:10 in DPBS, centrifuged at 1200 rpm for 5 min at room temperature, and resuspended in 2 mL mTesR1 medium (Stem Cell Technologies) with 10μm ROCK inhibitor (Y-27632 dihydrochloride, HY-10583, MedChemtronica AB). Cells were then plated into one well of a Matrigel-coated 6-well plate, and cultured in a cell culture incubator at 37°C and 5% CO2. 24h later medium was replaced with fresh mTeSR1 without Rock inhibitor, cells were maintained in culture as colonies at maximum confluency of 70% by substituting the medium every day. For subculturing procedure cells were washed once with DPBS, then incubated in 500 μM EDTA in DPBS for 3 min at room temperature. EDTA was removed from the well, 1ml of mTesR1 was added, colonies were dissociated gently scraping the bottom of the well with the end of the pipet, resuspended in a total 2 mL mTesR1 medium supplemented with 10um ROCK inhibitor and transferred to fresh Matrigel-coated wells. The medium was changed M-TeSR1 media without ROCK inhibitor 24 hours after plating.

For iPSCs cryopreservation, 70% confluent iPSCs were dissociated with EDTA and collected in cryopreservation medium composed by a mixture of 20% dimethyl sulfoxide (DMSO) (Sigma-Aldrich) and 80% Knock-out serum replacement (KSR) medium (Gibco, 10828010).

3.4.2.3 Generated cell lines

HECW1-KO A549-clone 14S6 was previously generated in our laboratory by CRISPR/Cas9 approach.

HECW1-KO-A549 cells stably expressing a dox-inducible WT or catalytic inactive (CS) GFP-fused HECW1 were generated through lentiviral infections with the corresponding pSLIK-GFP vectors. HECW1-KO A549-14S6 cells were transduced with lentiviral particles containing pSLIK-NEO-GFP-HECW1-WT; pSLIK-NEO-GFP-HECW1-CS or pSLIK-NEO empty vector (EV) as control. After selection with 400 ug/ml neomycin, to obtain homogeneous cell populations, cells were treated with 0.5um/ml doxycycline to induce GFP-HECW1 expression and GFP-positive cells were sorted by Fluorescence-activated cell sorting (FACS) in 96-well plates for the generation of single cell clones. A bulk population was used for EV cells. Clones were tested to assess GFP-HECW1 expression after induction with 0.5um/ml doxycycline. For all experiments shown, clone Cl2_WT and Cl1_CW were used.

A549 and HECW1-KO-A549-14S6 cells stably expressing the tandem probe mRFP-GFP-LC3 was previously generated in our laboratory.

To generate the stable doxycycline-inducible iPSC-GFP-HECW1 cell line, HPSI0613-iPSCs were transduced with lentiviral particles containing pSLIK-NEO-GFP-HECW1-WT and selected in mTeSR1 medium supplemented with neomycin for ten days. For GFP-HECW1 expression, doxycycline was added to the medium at a concentration of 0.5um/ml for 24h and GFP-positive cells were sorted by FACS and pooled. iPSC-GFP-HECW1 sorted cell population was assessed for homogeneous GFP-HECW1 expression after doxycycline induction.

For the generation of stable Hela-shRNA-HECW1 cell lines, Hela were transduced with lentiviral particles containing pLKO-PURO-TetOn-shRNA-HECW1-968; pLKO-PURO-TetOn-shRNA-HECW1-3’UTR or pLKO-PURO-TetOn-shRNA-HECW1-CDS. After the infection, cells were selected with puromycin and the resulting bulk population was to test shRNA efficiency in depleting HECW1 after doxycycline induction.

For the generation of stable iPSC-shRNA-HECW1 cell lines, HPSI0613-iPSCs were transduced with lentiviral particles containing pLKO-PURO-TetOn-shRNA-HECW1-968; pLKO-PURO-TetOn-shRNA-HECW1-3’UTR or pLKO-PURO-TetOn-shRNA-HECW1-CDS. After the infection, cells were selected with puromycin. iPSC-shRNA-HECW1-968 were chosen as the knockdown cell line (referred to as iPSC-shRNA-HECW1).

3.4.2.3.1 Crispr/Cas9-gRNA ribonucleoprotein (RNP) mediated generation of iPSC-NGN2-HECW1-KO clones

To generate iPSC-NGN2-HECW1-KO clones we used Crispr/Cas9-gRNA ribonucleoprotein (RNP) complex system composed of two non-coding in vitro transcribed RNAs, the CRISPR RNA (crRNA) and the trans-activating crRNA (tracrRNA) in addition to the Cas9 protein (in collaboration with the Genome Editing facility in IFOM). The crRNAs recognize target sequences while the tracrRNA is made up of a longer stretch of constant bases that provide the “stem loop” structure bound by the

Cas9. Different crRNAs were designed targeting different region of HECW1 gene (target transcript NM_015052.5), using the MIT CRISPR design tool (http://crispr.mit.edu/, Zhang Lab, MIT). Target sequences are of 20 nt length and require a NGG Protospacer Adjacent Motif (PAM), that serves as a binding signal for Cas9. We selected those crRNA sequences that had fewer predicted off-targets, and three were used for electroporation. The gRNA previously used to generate A549-KO cells was utilized as well (Guide 3).

The crRNA sequences are:

Guide 3 (exon 4): 5'- GCGGCTCCTTGCACCGGCGT -3'

Guide 4 (exon 11): 5'- CTTCTCCTCGCAAGACGACG -3'

Guide 5 (exon 13): 5'- CCACATAAAAGACCCGCCCG -3'

Guide 6 (exon 16): 5'- CAAAATTGCGAGCATCCCGT -3'

Briefly, 1x10^6 iPSC-NGN2 were electroporated with precomplexed RNPs consisting of a crRNA and the tracrRNA (2500 nmol of RNAs in total) and 1250 nmol of Cas9 protein (produced by the Cell Culture Facility in IFOM) via Nucleofection (Lonza, 2B-Nucleofector X-unit) using nucleofection buffer A69 and program A-013 in a large (100 μl) cuvette according to the manufacturer’s recommended protocol. Cells were then plated onto Matrigel-coated plates into mTeSR1 medium. The four different electroporated populations were screened by PCR followed by TIDE (Tracking of Indels by Decomposition) analysis (Brinkman et al., 2014) and guide 5 and guide 6 were selected based on gRNA activity and target cut efficiency. Cells were then serially diluted to yield clonal populations and single colony were isolated and that showing correct iPSC morphology, viability and growth were further expanded. Clones were then screened by PCR-TIDE analysis for the presence at the target region of frameshift mutation and the absence of in-frame mutation and WT allele. Two clones per guide were selected: clone 5.5 and 5.15 for Guide 5, and clone 6.7 and 6.17 for Guide 6.

3.4.3 Differentiation protocols

3.4.3.1 Generation of Neuronal Precursor Cells (NPCs)

NPC-GFP-HECW1 and NPC-shHECW1 cells were generated from iPSC-GFP-HECW1 or iPSC-shRNA-HECW1, respectively, according to the protocol published by Yan and colleagues (Yan et al., 2013). Briefly, iPSCs were split as cell clumps into Matrigel-coated six-well plates at low density to reach a 20% of confluency in one day. Approximately 24 hours after splitting (day 0), culture medium was switched from mTeSR1 to Gibco PSC Neural Induction Medium (Life Technologies) containing Neurobasal medium and Gibco PSC neural induction supplement. Neural induction medium was changed every other day from day 0 to day 4 of neural induction. After day 4, neural induction medium was changed every day as cells reached confluence. At day 7, NPCs were washed once with DPBS, then incubated in Accutase (Life Technologies) for 5 min at 37°C. Cellular clumps were dissociated into single cells by pipetting the accutase solution, diluted 1:10 in DPBS, centrifuged at 1200 rpm for 5 min at room temperature. Cells were resuspended in Neural Expansion Medium containing 50% Neurobasal medium, 50% DMEM/F12, neural induction supplement and 2mM L-Glutamine, and counted. Cells were then plated on Geltrex-coated six-well plates at a density of 0.5–1 × 106 cells per well and medium was supplemented with 10μm ROCK inhibitor. NPC expansion medium (without ROCK inhibitor) was changed every and NPCs were spitted when they reached confluence.

For NPCs cryopreservation, confluent NPCs were Accutase-dissociated and collected in NPC expansion medium with 10% dimethyl sulfoxide (DMSO) (Sigma-Aldrich).

3.4.3.2 Differentiation of NPCs into Cortical Neurons

Differentiation of NPC into cortical neurons was carried out as previously described by Yan and collogues (Yan et al., 2013) with minor changes to the protocol. Briefly, for neuron differentiation, accutase-dissociated NPCs were plated onto PDL-laminin -

coated plates at a density of 0,75-1 × 10^6 cells/well of a six-well plates in NPC expansion medium supplemented with ROCK inhibitor. 24 hours after plating, culture medium was switched to a neuronal differentiation medium consisting of neurobasal medium, 2% B-27 (Gibco, 17504044), 10 ng/ml brain-derived neurotrophic factor (BDNF, PeproTech, 450-02), 10 ng/ml glial cell-derived neurotrophic factor (GDNF, PeproTech, 450-10), 200 μM l-ascorbic acid (Sigma-Aldrich) and CultureOne supplement (Gibco). For imaging analysis, NPCs were plated on glass-coverslip in 24 well plate at a density of 2x10^5 cells/well. Neurons were maintained in culture for at least 14 days and medium was changed every 3.

3.4.3.3 Differentiation of iPSC-NGN2 into i3Neurons

i3Neurons were differentiated with a simplified two-step protocol (pre-differentiation and maturation) (Fernandopulle et al., 2018). For pre-differentiation, at day 0 iPSC-NGN2 cells were dissociated with accutase and plated as single cells on Matrigel-coated six-well plates at a density of 1-1,5 × 10^6 cells/well or on 10cm-matrigel coated dishes at a density of 8-10x10^6 cells/dish in Induction Medium containing Advanced DMEM/F12, N2 supplement (Gibco, 17502048), Non-essential amino acids (NEAA) and L-glutamine supplemented with 2mg/ml of doxycycline (2 mg/mL) and ROCK inhibitor. 24 h later, ROCK inhibitor was removed and medium was daily changed for three days. At day 3, pre-neurons were accutase-dissociated, counted, and plated on poly-L-ornithine (Sigma, P3655) coated plates (7,5 × 10^5 cells in 6-well plate or 8-10x10^6 cells in 10cm plate) in Cortical Neuron Culture Medium containing Neurobasal medium, B-27 supplement (Gibco, 17504044), 10 ng/mL of BDNF (PeproTech, 450-02), 10 ng/mL of NT3 (PeproTech, 450-03) and 1 mg/ml of laminin (Sigma, L2020), supplemented with 2mg/ml of doxycycline and ROCK inhibitor. At day 4, ROCK inhibitor was removed and half-medium change was performed twice a week until the desired time point of differentiation was reached. Doxycycline was maintained in the medium for all the duration of the differentiation.

3.4.3.4 I3Neurons differentiation on the compartmentalized microfluidic devices

In order to physically separate the neuronal axons from the soma and the dendrites, i3Neurons differentiation was performed on a 2-compartment PDMS microfluidic device (XC450, XONA Microfluidics), according to the manufacturer's instructions. Briefly, the device was first treated with XC Pre-coat solution and then coated with 0,1mg/ml PLO, as described in the protocol. At day 3 of iPSC-NGN2 differentiation, pre-neurons were accutase-dissociated, counted and resuspended into Cortical Neuron Culture Medium. 1x10^5 cells were loaded into each of the two left wells of the device. After 5 minutes, that allow the cells to attach to the surface of the device, 150ul of culture medium, supplemented with 2mg/ml of doxycycline and ROCK inhibitor, were added to each of the 2 left and 2 right wells of the device. 24 h later, medium was changed to remove ROCK inhibitor and half-medium changes were then performed twice a week.

3.4.4 Transfection and transduction

3.4.4.1 siRNA transfection

For transient HECW1-KD in iPSC-NGN2 derived i3Neurons neurons, cells were transfected with LipofectAMINE RNAi MAX reagent from Invitrogen, according to the manufacturer's instructions, using Neurobasal Medium instead of OptiMEM Reduced Serum Media to prepare the transfection mixture. Pre-neurons were subjected to a single transfection in suspension at day 3 of differentiation, using 20 nM final concentration of the desired siRNA. Transfection mixture and cell suspension were then combined together and directly plated on PLO-coated plates. The day after, cells medium was replaced with fresh Cortical Neuron Culture Medium and kept in culture until the desired time point of differentiation was reached. .

3.4.4.2 DNA transfection

DNA transfections were performed using the calcium phosphate transfection method. HEK-293T cells were plated on 10 cm cell culture dishes in order to achieve a 50% confluency on the day of transfection. The DNA/CaPO4 complex was formed by mixing 10 µg of DNA and 240 mM CaCl2 with the HBS solution. The solution containing the DNA/CaPO4 complex was added to the cell culture medium. Cells were incubated overnight at 37°C with the transfection mixture and the culture medium was changed one day after the transfection. For immunoprecipitation assays, cells were lysed 48 hours after the transfection.

3.4.4.3 DNA transduction and virus concentration

For the generation of cell lines that stably incorporate exogenous DNA, DNA transduction through lentiviruses or retroviruses was performed.

For DNA transduction through lentiviruses, HEK-293T cells were transfected with 10 µg of the transfer DNA together with plasmids encoding for GAG, POL, ENV (VSVG) and REV retroviral proteins, through the calcium phosphate transfection method. The DNA plasmids and 240 mM CaCl2 were mixed with HBS solution in order to generate DNA/CaPO4 complexes. The day after transfection, the medium was replaced with half volume of fresh medium in order to concentrate the virus. 24 h later, the viral supernatant was collected and supernatant was passed through PVDF 0.45 µm Millipore filters and directly used to infect target cells after addition of 8 µg/ml polybrene. For preparation of large amount of concentrated virus, filtered supernatant was supplemented with PEG-it Virus Precipitation Solution in a 4:1 ratio and then moved at 4°C for 3 days. The supernatant-PEG solution was centrifuged at 2800 rpm for 30min at 4°C. Sedimented viral particles were resuspended in 1/20 of original volume using PBS and dispensed in 100ul aliquots. Concentrated virus can be stored at -80°C.

Fresh collected supernatant was used to infect plated A549-14S6 while concentrated virus was used to infect plated HPSI0613-iPSC cells after adding 8 μg/ml polybrene. 24 hours after the infection, selection of infected cells was performed by adding 400 μg/ml neomycin or 0,2μg/ml puromycin.

3.5 Real Time PCR

RNA from the desired cell lines was extracted using Maxwell® RSC simplyRNA tissue kit (Promega) according to manufacturer's instructions. Concentration and purity were determined by measuring optical density at 260 and 280 nm using a Nanodrop spectrophotometer. cDNA was generated from 1μg of RNA using the Applied Biosystems™ High-Capacity cDNA Reverse Transcription Kit (Thermo Fisher Scientific). Samples were analyzed by the Real Time PCR facility through the TaqMan method with the following probes (Applied Bioscience):

HECW1	Hs00389648_m1
HECW2	Hs01372347_m1
NEDD4	Hs00406454_m1

The amplicon expression in each sample was normalized to GAPDH mRNA content.

3.6 Protein procedures

3.6.1 Cell lysis

After washing with 1X PBS, cells were pelleted and the dry pellet was either frozen at -80°C or directly processed. Cell pellets were lysed in RIPA buffer and incubated for 20 minutes on ice. Lysates were cleared by centrifugation at 13200 rpm for 30 minutes at 4°C. Pellet from iPSC and neurons were sonicated with Bioruptor Plus (high intensity, 60s ON, 20s OFF, 5 cycles) before centrifugation. Protein concentration was measured by the Bradford assay (Biorad) following the manufacturer's instructions.

3.6.2 SDS-Polyacrylamide gel electrophoresis (SDS-PAGE) and Western blot (WB)

Proteins were denatured by adding 4X Laemmli Buffer and by boiling at 95°C for 5 minutes. Proteins were then separated on precast gradient gels (4–20% TGX precast gel, Bio-Rad) by SDS-PAGE and transferred to nitrocellulose membranes by Transblot Turbo (BIO-RAD). Ponceau staining was used to determine the efficiency of the protein transfer onto the membrane. Membranes were blocked for 1 hour in 5% milk in TBS supplemented with 0.1% Tween (TBS-T). After blocking, the filters were incubated with the primary antibody, diluted in TBS-T 5% milk, for 1 hour at room temperature (RT), or overnight at 4°C . After washes, the membranes were incubated with the appropriate horseradish peroxidase (HRP)-conjugated anti-mouse or anti-rabbit secondary antibodies (GE Healthcare) diluted in TBS-T for 30 minutes at room temperature. After washes, the bound secondary antibody was detected with ECL (GE Healthcare). Western blots were visualized using films (GE Healthcare) or Chemidoc (Bio-Rad).

3.6.3 Immunoprecipitation (IP)

HEK-293T cells were transfected with the indicated constructs. After 48 hours, the cells were lysed in JS buffer and incubated for 20 minutes on ice. Lysates were cleared by centrifugation at 13200 rpm for 20 minutes at 4°C. Anti-GFP IP was performed by incubating 1 mg lysate with anti-GFP lama conjugated beads (home-made) for 2 hours at 4°C. Precipitated immunocomplexes were washed, loaded on a precast gradient gel (4–20% TGX precast gel, Bio-Rad) and analyzed by WB.

For immunoprecipitation of the endogenous HECW1, iPSC-derived neurons and A549 cells were lysed in RIPA buffer and incubated for 20 minutes on ice. Lysates were cleared by centrifugation at 13200 rpm for 30 minutes at 4°C. Anti-HECW1 IP was performed by incubating 400ug of lysate with 1ug of HECW1 antibody (home-made, SI1052) for 2 hours at 4°C. Protein G agarose beads (Zymed) were then added and incubated for an additional 2 hours at 4°C. Precipitated immunocomplexes were washed, loaded on a precast gradient gel (4–20% TGX precast gel, Bio-Rad) and analyzed by WB.

3.7 Cell assays

3.7.1 Growth curve

For the growth assays, Cell Titer-Glo Luminescent Cell Viability Assay was used. This assay determines the number of viable cells by measuring ATP, which indicates the presence of metabolically active cells. 14S6-ev, 14S6-Cl2_WT and 14S6-Cl1-CS were seeded in 96-well plates at a concentration of 3500 cells/well. At plating and every 24 hours for 3 days, cells from three different wells per lines were lysed with Cell Titer-Glo Luminescent Cell Viability Assay reagent (Promega, G9242) and luminescence (RLU) was read using the Envision plate reader.

3.7.2 Immunofluorescence (IF)

For immunostaining of fixed cells, cells were plated on uncoated coverslips for A549 cells or coated with Matrigel for iPSCs, Geltrex for NPCs, PDL/laminin for NPC-derived neurons or PLO for i3Neurons. In case of drugs treatments, cells were incubated with 100uM of chloroquine (CQ), or with 5uM Rapamycin (Rapa, Medchem, HY-10219) in combination with 100 nM Bafilomycin A1 (BafA1, Selleck, B1793), in culture medium at 37°C for 2h before fixation. Cells were rinsed twice with 1X PBS and fixed with 4% paraformaldehyde (PFA) for 10 minutes at room temperature. After fixation, the cells were rinsed three times in 1X PBS and permeabilized with 1X PBS 0,2% bovine serum albumin (BSA) – 0.1% Triton for 10 minutes. In order to minimize aspecific antibodies interactions, the coverslips were incubated with 1X PBS-T 2% BSA (Blocking solution) for 45 minutes. Primary antibodies were diluted in 1X PBS 1% BSA and the incubation was performed for 1 hour and 30min at RT. After three washes in 1X PBS, the cells were incubated with secondary antibodies conjugated with fluorophores diluted in 1X PBS

1% BSA for 30 minutes at RT. The cells were then washed three times in 1X PBS. To label the nuclei, DAPI (Sigma-Aldrich, cat. D9542), diluted 1:5000 in 1X PBS, was added to the cells for 10 minutes at RT. The coverslips were mounted on glass slides using Mowiol Mounting Medium (Calbiochem).

For LAMP1 and EEA1 staining, cells fixed with PFA were incubated with Saponin blocking buffer (2% BSA, 0.1% saponin, in PBS) for 45 minutes. Primary antibodies were diluted in 1X PBS 1% BSA 0.1% saponin and the incubation was performed for 1 hour and 30min at RT. After three washes in 1X PBS, the cells secondary antibodies conjugated with fluorophores diluted in 1X PBS 1% BSA 0.1% saponin was added, followed by incubation for 45 minutes at RT. The cells were then washed three times in 1X PBS and DAPI staining was performed to label the nuclei.

The coverslips were mounted on glass slides using Mowiol Mounting Medium (Calbiochem).

Widefield images were acquired with an Olympus BX61 upright microscope coupled to a Photometrics Coolsnap EZ black and white camera using U PLAN APO 40X/0.85NA dry objective. The software used for image acquisition was Metamorph (Molecular Devices). For LAMP1-compartments and P-bodies quantification, images were acquired with a DeltaVision Elite system (GE Healthcare) based on an Olympus IX71 inverted microscope coupled to a sCMOS camera using a PLAN APO 60x/1.42NA oil immersion objective. The software used for image acquisition was softWoRx version 7.0.0.

Confocal microscopy was performed with a Leica TCS SP5 or SP8 confocal laser scanning system based on a Leica DMI 6000B inverted microscope. The images were acquired with HCX PL APO 63X/1.4NA oil immersion objective or HC PL APO 40X/0.95NA dry objective. The software used for acquisitions were Leica LAS AF for SP5 and Leica LAS X for SP8.

3.7.2.1 IF on the XC450 microfluidic devices

Immunofluorescence staining of the neurons culture on the microfluidic device was performed according to the manufacturer's instructions. Briefly, at the final time point of differentiation, the medium was removed and the cells were immediately fixed with 4% PFA for 30 minutes at room temperature. After fixation, the cells were washed twice in 1X PBS for 5 minutes and permeabilized with 1X PBS 0,2% BSA – 0.1% Triton for 30 minutes. The device was then incubated with 1X PBS-T 2% BSA (Blocking solution) for 30 minutes. Primary antibodies were diluted in 1X PBS 1% BSA and the incubation was performed overnight at 4°C. After three 10 minutes-washes in 1X PBS, the cells were incubated with secondary antibodies conjugated with fluorophores diluted in 1X PBS 1% BSA for 30 minutes at RT. The cells were then washed three times in 1X PBS for 5 minutes. To label the nuclei, DAPI (Sigma-Aldrich, cat. D9542), diluted 1:5000 in 1X PBS, was added to the left wells for 10 minutes at RT. The coverslips were mounted on glass slides using Mowiol Mounting Medium (Calbiochem).

Confocal microscopy was performed on a Leica TCS SP5 laser confocal scanner mounted on a Leica DMI 6000B inverted microscope equipped with a HC PL APO 40X/0.95NA dry objective and tiling was applied to obtain a high-resolution image of an entire neurons. The software used for image acquisitions was Leica LAS AF.

3.7.3 Quantification of HECW1 depletion effect on LAMP1-enlargment

To quantify the effect of HECW1 depletion on the LAMP1-positive compartments, two different analyses were performed: measurement of the cellular area covered by LAMP1 signal or of its intensity.

3.7.3.1 Quantification of LAMP1 area

Ctrl and HECW1-KD i3Neurons were differentiated for 10 days. To inhibit autophagy, cells were treated with 100uM of Chloroquine (CQ) for 2 hours before fixation. Fixed cells were stained for LAMP1, EEA1 (used as an approximation of the cell's area) and

DAPI, and Z-stack images (0.2 μm intervals) were acquired using confocal microscopy (Leica TCS SP5). In order to evaluate the Lamp1 signal, a custom Fiji plugin was developed (Schindelin et al., 2012). The plugin extracts the cells' area from the Maximum Z-Projection of the EEA1 staining channel. Then a median filter (radius 4 pixels) and a gaussian filter (radius 2 pixels) are applied to reduce the noise and smooth the image, and the cells' area is recognized using the ImageJ MinError thresholding schema (https://imagej.net/plugins/auto-threshold#minerrori). Similarly, the late-endosomes/lysosomes' region is recognized from the Maximum Z-Projection of the LAMP1 staining channel, using the ImageJ Huang thresholding schema (https://imagej.net/plugins/auto-threshold#huang). Then a median filter (radius 2 pixels) and a background removal estimated as the mean intensity of a region drawn by hand are applied to reduce the noise. The area of LAMP1 signal was then normalized on the cell's area.

3.7.3.2 Quantification of LAMP1-intensity

Ctrl, HECW1-KD and HECW1-KO i3Neurons were differentiated for 10 days. To inhibit autophagy, the cells were treated with 100uM of Chloroquine (CQ) for 2 hours before fixation. Fixed cells were stained for LAMP1, TUJ1 and DAPI and images were acquired every 0.2 μm of the focal plane using z-stack function with a DeltaVision Elite system (GE Healthcare). Fiji software was used to measure the intensity of the LAMP1 signal for each cell from the Maximum Z-Projection. Then, areas of interest were manually selected in order to isolate single or few somas, and mean and integrated fluorescence intensity of LAMP1 were extracted. Integrated density was corrected for background intensity signal with the following formula: corrected total fluorescence = integrated density – (area of selected region*mean intensity of background). The mean intensity of LAMP1 per cells was calculated measuring the ratio between the background corrected intensity and the number of cells present in the area of interest. Statistical analysis on the obtained data were performed on Prism (version 9.0) using ANOVA test.

3.7.4 LysoTracker Vesicles Analysis

To label and track lysosomes and acidic vacuoles in living cells, the fluorescent dye nM LysoTracker Red DND-99 (Thermo scientific, L7528) was used. i3Neurons were differentiated on MatTek dishes (P35G-1.5-14-C-GRID MatTek Corporation) for 30 days and then incubated with 75 nM LysoTracker in culture medium for 30 minutes at 37°C. After dye removal, time-lapse experiments ware performed using a Thunder Imaging System (Leica) based on a Leica DMi8 microscope equipped with a Leica DFC9000 GT sCMOS camera and with heating and CO2 perfusion devices from Okolab. The images were acquired every 2 minutes and 30 seconds with a HC PL APO 63X 1.4NA oil immersion objective using Leica LAS X software. The images were then processed to measure the fraction of motile and static particles and the average speed. In order to extract these parameters, lysotracker-particle tracking analysis was performed using Fiji Trackmate plugin (Schindelin et al., 2012; Tinevez et al., 2017). Particles were considered stationary if they moved less then 2 μm. As a control, to inhibit autophagy, cells were treated with 10nM of Bafilomycin A1 for a total of 4h and Lysotracker was added for the last 30 minutes of treatment.

3.7.5 Wheat germ agglutinin live staining

To label endocytic-originated vesicles in living cells, Wheat Germ Agglutinin (WGA) fluorescent Conjugate was used in combination with lysotracker that labels acidic organelles. i3Neurons were differentiated on MatTek dishes (P35G-1.5-14-C-GRID MatTek Corporation) and, at day 30, cells were incubated with 10 ug/ml WGA-Alexa Fluor-488 Conjugate (Thermo scientific, W11261) and 75 nM LysoTracker Red DND-99 (Thermo scientific, L7528) in culture medium for 30 minutes at 37°C. After dye removal, live-cell imaging was performed with a Spinning Disk UltraVIEW VoX

(PerkinElmer) based on a Nikon Ellipse Ti inverted microscope equipped with a Hamamatsu EM-CCD C9100-50 camera. The images were acquired every 2 minutes and 30 seconds with a PLAN APO VC 60X/1.4NA oil immersion objective using the Volocity software (PerkinElmer). During the imaging, the cells were maintained at 37°C in humified atmosphere and 5% CO2 using Okolab incubator system.

3.7.5.1 Wheat germ agglutinin live staining on XONA-chip device

To observe WGA-positive structures in specific neuronal regions and track their transport along the axons, i3Neurons were differentiated on XONA-chip microfluidic devices and double WGA staining was performed at day 24. First, WGA-Alexa Fluor-488 Conjugate (Thermo scientific, W11261) was added in the somatic compartment at a concentration of 10ug/ml and incubated for 30 minutes at 37°C. To avoid WGA diffusion into the axonal side, fluidic isolation was achieved by creating a volume difference between the two compartments with the lesser volume in the somatic compartment. WGA was then removed from the somatic region and replaced with fresh dye free-medium, while a smaller volume of medium supplemented with 10ug/ml of WGA-Tetramethylrhodamine Conjugate (orange, Thermo scientific, W849) was added to the axonal compartment and incubated for 30 minutes at 37°C. WGA-orange was then removed and replaced with fresh dye-free medium. Live-cell imaging was performed using an Olympus Spinning Disk CSU based on an Olympus IX83 inverted microscope equipped with an Andor iXon Ultra camera. The images were acquired with a U PLAN S APO 100x/1.35NA silicone immersion objective using CellSens software (Olympus). During the imaging, the cells were maintained at 37°C in humified atmosphere and 5% CO2 using Okolab incubator system. Live-cell imaging on the somatic side was performed during washout incubation of the axonal side.

3.7.6 P-bodies quantification

Ctrl and HECW1-KO i3Neurons were differentiated on PLO-coated coverslip for 24 days. To dissolve P-Bodies, prior to fixation cells were incubated with 4% 1,6 hexanediol at room temperature for 5 minutes, or with 7.5 ug/ml of cycloheximide (CHX, SIGMA 239763) for 2 hours and 30 minutes at 37°C. Fixed cells were stained for DCP1A, TUJ1 and DAPI. Images were acquired every 0.2 μm of the focal plane using z-stack function with a DeltaVision Elite system (GE Healthcare). To quantify the number of P-bodies per cells, the images were processed using ImageJ software with the Analyze particle tool. First, Z-stacks from all the channels were combined to produce maximum projection, then background signal was subtracted and a manually-set threshold mask was applied. Particle size was limited to those smaller than 1 μm^2 and circularity range set to 0-1. The number of P-bodies was assessed in a selected area containing a single or few cells. When analyzed more than one cell per area, the mean number of P-bodies per cells was calculated measuring the ratio between the total number of P-bodies and the number of cells present in the area of interest. Statistical analysis on the obtained data were performed on Prism (version 9.0) using ANOVA test.

3.7.7 Transmitted electron microscopy (TEM)

Ctrl, HECW1-KD and HECW1-KO i3Neurons were differentiated on MatTek dishes (P35G-1.5-14-C-GRID MatTek Corporation) at a concentration of 7,5x10^5 cells/dish. The cells were then processed for electron microscopy as previously described (Cutrona et al., 2013; Fusella et al., 2013; Kumar et al., 2014; Mironov et al., 2004). A brief description of each process is presented below. Cells were fixed with 4% paraformaldehyde and 2,5% glutaraldehyde (EMS, USA) mixture in 0.2 M sodium cacodylate pH 7.2 for 2h at RT, followed by 6 washes in 0.2 sodium cacodylate pH 7.2 at RT. Then cells were incubated in 1:1 mixture of 2% osmium tetra oxide and 3%

potassium ferrocyanide for 1h at RT followed by 6 times rinsing in cacodylate buffer. Then the samples were sequentially treated with 0.3% Thiocarbohydrazide in 0.2 M cacodylate buffer for 10 min and 1% OsO4 in 0.2 M cacodylate buffer (pH 6,9) for 30 min. Then, samples were rinsed with 0.1 M sodium cacodylate (pH 6.9) buffer until all traces of the yellow osmium fixative have been removed (Beznoussenko and Mironov, 2015; Beznoussenko et al., 2014). The samples were subsequently subjected to dehydratation in ethanol, and embedded in Epoxy resin at RT and polymerized for at least 72 h in at 60 °C in the oven. Embedded samples were then sectioned with diamond knife (Diatome, Switzerland) using Leica EM UC7 ultramicrotome. Sections were analyzed with a Tecnai 20 High Voltage EM (FEI, Thermo Fisher Scientific; The Netherlands) operating at 200 kV.

From the images acquired at day 10 of differentiation, we quantified endocytic and autophagic vacuoles assessing, for each sample, the percentage of fields positive for these structures on the total number of field analyses, considering as positive each image presenting at least an endocytic and autophagic vacuole.

3.7.8 Correlative light-electron microscopy (CLEM)

A549 and HECW1-KO-A549-14S6 cells stably expressing mRPF-GFP-LC3 were plated on MatTek dishes (P35G-1.5-14-C-GRID MatTek Corporation) at a concentration of 1,5x10^5 cells/dish. 24 hours later, cells were treated with 100uM of Chloroquine (CQ) for 2 hours before fixation and then fixed for Correlative light-electron microscopy (CLEM) analysis as described by Mironov and Besnoussenko (Mironov and Beznoussenko, 2013). In brief, cells were fixed with Fixative 1 (0.05% glutaraldehyde, 4% PFA in 0.15 M Hepes pH 7.2) for 5 minutes, and then with Fixative 2 (4% PFA in 0.15 M Hepes pH 7.2) three times for 10 minutes. Immediately before acquisition, the cells were then washed three times in 0.2 M Hepes pH 7.2. Images were acquired with a Leica inverted SP5 microscope equipped with HCX PL APO CS2 20x/0.75 dry objective. GFP signal was used to identify and select cells positive for LC3-puncta. These cells were subjected to the optical sectioning and the Z-stacking was performed. Immediately after confocal acquisition, Hepes was replaced with Fixative 2 and the samples were subjected to the procedure of immune EM labelling with an antibody against GFP using the Nanogold enhancement procedure as it was described (Beznoussenko and Mironov, 2015; Beznoussenko et al., 2014). Briefly, the cells were washed 3 times in PBS and incubated with blocking solution for 30 min at RT. Then cells were incubated with primary anti GFP antibody (Abcam ab6556) a diluted 1:100 in blocking solution overnight at 4°C. On the following day, the cells were washed 3 times with PBS and incubated with goat anti-rabbit Fab fragments coupled to 1.4 nm gold particles (diluted in blocking solution 1:100) for 2h and washed 6 times with PBS. Meanwhile, the activated Gold Enhance TM-EM was prepared according to the manufacturer's instructions and 200 µl were added into each sample well.

The reaction was monitored by a conventional light microscope and was stopped after 5-10 min when the cells had turned "dark enough" by washing several times with PBS. Then cells were fixed with of 2,5 % paraformaldehyde and 2,5% glutaraldehyde (EMS, USA) mixture in 0.1 M sodium cacodylate pH 7.4 for 2h at RT, followed by 6 washes in 0.1 sodium cacodylate pH 7.4 at RT. Then cells were incubated in 1:1 mixture of 2% osmium tetraoxide and 3% potassium ferrocyanide for 1h at RT followed by 6 times rinsing in cacodylate buffer. Then the samples were sequentially treated with 0.3% Thiocarbohydrazide in 0.2 M cacodylate buffer for 10 min and 1% OsO_4 in 0.2 M cacodylate buffer (pH 6,9) for 30 min. The samples were subsequently subjected to dehydratation in ethanol, and embedded in Epoxy resin at RT and polymerized for at least 72 h in a 60 °C oven (Beznoussenko et al., 2016).

Z-stack images were printed and during trimming of the pyramid and its sharpening these images were constantly used for orientation. Embedded samples were then sectioned with diamond knife (Diatome, Switzerland) using Leica EM UC7 ultra microtome. Sections were analyzed with a Tecnai 20 High Voltage EM (FEI, Thermo Fisher Scientific; The Netherlands) operating at 200 kV.

3.8 Transcriptomic Analysis

3.8.1 RNA-seq methodology for transcriptomics analysis

At the third day of differentiation pre-neurons generated from iPSC-NGN2 were transfected with siRNA for HECW1 and plated on PLO-coated plates at a density of 10x10^6 cells/plate (as described in section 3.4.4.1). At day 10 RNA was extracted from ctrl and HECW1-KD neurons as previously described (section 3.5). Samples were collected from four different biological replicates. RNA was quantified using a Nanodrop spectrophotometer, and its integrity assessed using Agilent Bioanalyzer 2100 with Nano Rna kit(RIN > 8). mRNA-seq indexed library preparation was performed starting from 500 ng of total RNA with the TruSeq stranded mRNA (Illumina) according to the manufacturer's instructions. Indexed libraries were quality controlled on Agilent Bioanalyzer 2100 with High Sensitivity DNA kit, quantified with Qubit HS DNA, normalized and pooled to perform a multiplexed sequencing run. 1% PhiX control was added to the sequencing pool, to serve as a positive run control. Sequencing was performed in PE mode (2x75nt) on an Illumina NextSeq550Dx platform, generating on average 60 million PE reads per sample.

3.8.2 Bioinformatics analysis of transcriptomics data

Raw data were aligned to the human hg38 reference genome with STAR v2.7 (PMID:23104886) with the parameter --quantMode GeneCounts in order to obtain gene counts.

To explore the similarity of the samples, we performed a Principal Component Analysis considering the 500 genes with the highest variance in their expression among samples.

Differential expression analysis between each HECW1-kd and its control was performed in R with the DESeq2 (v1.26.0, (Love et al., 2014)) package after gene counts normalization. Genes with an absolute log2 fold change > 0.5 were considered deregulated between KD and control samples.

Gene Set Enrichment Analysis for gene sets of the GO Biological Process, Reactome and KEGG, was performed with the enrichR R package (Chen et al., 2013) on the list of the deregulated genes shared among four or three replicates, considering up and downregulated genes either separately or together.

The Heatmap showing the expression levels of neuronal genes was generated in R with the ComplexHeatmap Bioconductor package ((Gu et al., 2016), DOI: 10.18129/B9.bioc.ComplexHeatmap) on the genes counts normalized by the sample average expression.

3.9 Proteomics Analysis

3.9.1 Cell lysis and samples preparation for MS analysis

At the third day of differentiation pre-neurons generated from iPSC-NGN2 were transfected with siRNA for HECW1 and plated on PLO-coated plates at a density of 10x10^6 cells/plate (as described in section 3.4.4.1). At day 10 cells were washed with 1X PBS, pelleted and the dry pellet was frozen at -80°C. Pellet were collected from three different biological replicates.

In-solution digestion of proteins was performed using the iST Sample Preparation Kit (P.O.00001, from PreOmics) following the manufacturer protocols, which consists in a first phase of lysis, reduction and alkylation of the sample, followed by overnight digestion. Briefly, cell pellets were resuspended in 100ul of LYSE solution, which denatures, reduces and alkylates proteins at the same time, sonicated with Diagenode Bioruptor (high intensity, 30s ON, 30s OFF, 10 cycles) and boiled at 95°C for 10 minutes. Protein concentration was measured by the BiCinchonic acid Assay (BCA

Assay, Thermoscientific) according to the manufacturer procedure. 150 µg of proteins were then digested adding an equal volume of DIGEST solution (a LysC-trypsin mix) and incubated overnight at 37 °C on a thermomixer at 500 rpm. The following day peptides were cleaned-up and concentrated (Kulak et al., 2017; Kulak et al., 2014; Sielaff et al., 2017). 100µl of STOP solution were added to each sample and mixed over 1 minute at room temperature at 500 rpm. Each sample was then transferred in an individual cartridge (supplied by the kit) placed in a waste-tube, and centrifuged for 2 minutes at 4000 rpm. 100ul of WASH-1 solution were added to the cartridge, followed by centrifugation for 2 min at 4500 rpm. A second wash was similarly performed with WASH-2 solution. To elute the peptides, the cartridge was then placed into fresh collection tubes and peptides were recovered by centrifugation at 4000 rpm for 2 min using 60ul/sample of elute solution. The elution step was repeated twice. Eluted peptides were vacuum-dried in SpeedVac and reconstituted in 300ul of 0,1% TFA. Peptides were then fractionated in 8 fractions with the Pierce™ High pH Reversed-Phase Peptide Fractionation Kit (ThermoFisher, 84868) following the manufacturer protocols (Pirmoradian et al., 2013; Yang et al., 2012). To allow deep proteome sequencing, it is often necessary to reduce the complexity of the sample by fractionating it orthogonally before LC/MS analysis. The Hph kit uses high pH reverse phase chromatography to separate peptides for hydrophobia and provides excellent orthogonality to the gradients used in LC-MS. In fact, for the Hph fractionation we used a high pH buffer, the Triethylamine at decreasing concentration, while for the LC chromatography we used a mixture of phases with acidic pH consisting of acetonitrile and formic acid. Briefly, reconstituted samples were loaded onto a high-pH spin column (after column pre-conditioning as described in the manufacturer protocol) placed into a 1,5ml tube, and centrifuged at 5500 rpm for 2 minutes. Following addition of 300ul of milliQ and a second centrifugation, columns were moved into a new tube.

300 µL of elution solution composed by TA 0,1% and ACN 5% were loaded onto the column and centrifuge at 5500 rpm for 2 min, and flow-through was collected and labelled as fraction 1. Elution step was repeated for the remaining gradient fractions using the appropriate elution solutions (TA 0,1% and ACN, 7,5%, 10%, 12,5%, 15%, 17,5%, 20%, 50, corresponding to the fraction 2 to 8) and collected in new fresh tubes. Each of the fractions was then vacuum-dried in SpeedVac, resuspended in 10 µL of buffer A (0,1% FA), vortex for 30 second and finally sonicated for 10 minutes before LC-MS/MS analysis.

3.9.2 Nanoflow liquid chromatography and tandem-mass spectrometry (nLC-MS/MS)

3 µL peptide mixtures were analyzed by online nanoflow liquid chromatography tandem-mass spectrometry (LC–MS/MS) using an EASY-nLC™ 1000 (Thermo Fisher Scientific, Odense, Denmark) connected to a Q-Exactive instrument (Thermo Fisher Scientific) through a nanoelectrospray ion source. The nano LC system was operated in one column set-up with a 25-cm analytical column (75 µm inner diameter, 350 µm outer diameter) packed with C18 resin (ReproSil, Pur C18AQ 1.9 µm, Dr Maisch, Germany) configuration. Solvent A was 0.1% FA in ddH2O, and solvent B was 80% ACN with 0.1% FA. Samples were injected in an aqueous 1% TFA solution at a flow rate of 500 nl/min. Peptides were separated with a gradient of 0–40% solvent B over 100 min followed by a gradient of 40–60% in 5 min and 60–95% over 5 min at a flow rate of 250 nl/min in the EASY-nLC 1000 system. The mass spectrometer was controlled by Xcalibur software (Thermo Scientific) and operated in data-dependent acquisition (DDA) mode so as to automatically switch between full-scan MS and MS/MS acquisition. Survey full scan MS spectra (from *m/z* 300–1350) were analyzed in the Orbitrap detector with resolution *R* = 60 000 at *m/z* 200. The ten most intense peptide ions with charge states ≥2 were sequentially isolated to a target value of 3e6 and

fragmented by higher energy collision dissociation (HCD) with a normalized collision energy setting of 28%. The maximum allowed ion accumulation times were 20 ms for full scans and 100 ms for MS/MS, and the target value for MS/MS was set to 1e5 (R = 15 000 at m/z 200). The dynamic exclusion time was set to 20 s for Q-Exactive instrument. Standard mass spectrometric conditions for all experiments were: spray voltage, 2.4 kV; no sheath and auxiliary gas flow.

3.9.3 Protein identification

Acquired spectra were matched in the human database, version 3.68, by MaxQuant, version 1.2.0.18, which performed peak list generation, protein identification via the Andromeda search engine, and protein quantitation based on SILAC. The selected protease was trypsin (cleaving at the C terminus of Lys and Arg, unless followed by Pro), with a maximum of two missed cleavages allowed. Cysteine carbamidomethylation and methionine oxidation were set as fixed and variable modifications, respectively. The mass tolerance was set at 10 ppm for MS spectra (Fourier transform MS) and 0.5 Da for MS/MS spectra (ion trap MS).

After MaxQuant analysis, proteins identified by at least two peptides, of which at least one was unique, were considered as high-quality identifications and were further analyzed. For the iBAQ calculation and the saturation assay, proteins identified based on at least two unique peptides were considered. In the case of redundancy in protein identification (peptides matching multiple protein groups), we reported the leading protein in the "protein groups" output table from MaxQuant. Normalized ratios were used for all assays.

Perseus package version 1.2.0.16 was used for the annotation of Gene Ontology terms for the identified proteins.

Protein identifications were accepted if they could be established from at least 2 out of 3 experiments at a probability greater than 95.0% and contained at least 2 identified peptides.

To highlight regulated differentiation proteins, we have imposed in the volcano plot only the raw p-value using as cutoff or p-value 0.01 or 0.05. With these parameters, differentially regulated proteins emerge.

4 RESULTS

4.1 Human neuronal model

4.1.1 HECW1 expression in neurons

According to the Human Protein Atlas, HECW1 is selectively expressed in specific human tissues, and it is predominantly expressed in the central nervous system (**Fig. 12A**). From Western blot (WB) analysis of neuronal precursor cells (NPCs) and cortical neurons (CN) kindly provided by colleagues in our Institute, we observed that HECW1 was not detectable in NPCs, while it was expressed after 20 and 40 days of differentiation into CN (**Fig. 12B**). In addition, the HECW1 neuronal protein level was higher than that of the A549 lung cancer cell line where we initially studied HECW1 (see Appendix).

These observations confirm that HECW1 is specifically expressed in human neurons, and together with HECW1 reported implication in ALS (Miyazaki et al., 2004; Zhang et al., 2011), and the protective role in neuronal homeostasis of the *Drosophila* Hecw ortholog (Fajner et al., 2021), prompted us to investigate its physiological and pathological role in neurons.

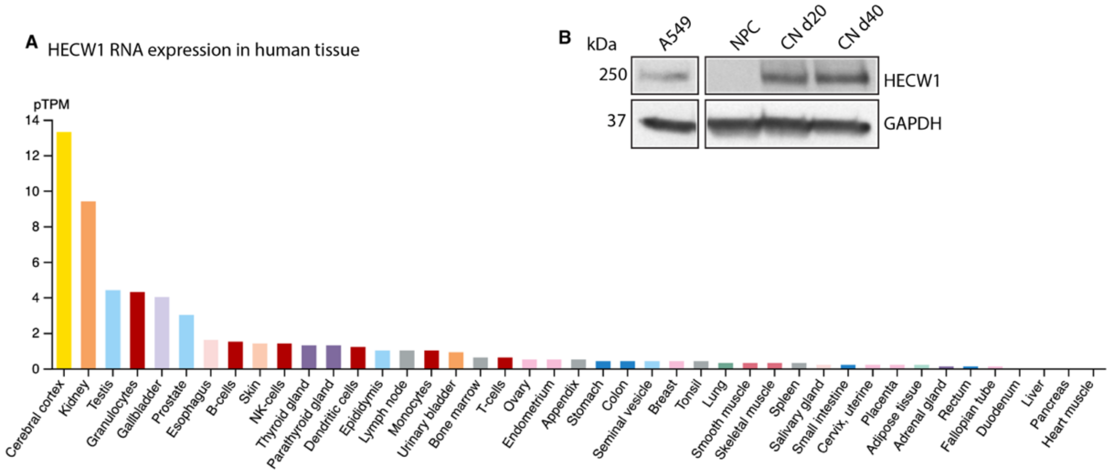

Figure 12 HECW1 is specifically expressed in human neurons

A) RNA expression profile of HECW1 in normal human tissues as for Human Protein Atlas. Color coding is based on tissue group.

B) HECW1 expression in A549 cells, NPCs and the derived CN determined by WB after 20 and 40 days of differentiation. NPC: neuronal precursor cell; CN: cortical neurons.

4.1.2 Small molecule-based neuronal differentiation protocol

4.1.2.1 Generation of iPSC-derived neurons

To obtain an *in vitro* cellular model to study HECW1 function in human neurons, we set out to establish a protocol for *in vitro* differentiation of iPSCs into neurons and to produce HECW1-modified iPSC lines to study the effect of HECW1-overexpresison or deletion in neurons. As this approach was not set up in our laboratory, we first implemented and optimized few protocols to generate cultures of neuronal cells from iPSCs.

The first approach used relies on the combination of small molecules and pathway inhibitors to drive iPSCs toward neuronal development, passing through the intermediate step of NPCs (**Fig. 13A**) (Yan et al., 2013). In this method, iPSC-derived NPCs are plated on PDL-laminin coated plates in neuronal differentiation medium for two weeks or later experimental endpoints for more mature neurons, and half of the medium is changed twice every week (**Fig. 13A**; see also Materials & Methods).

To assess the differentiation efficiency of the protocol, we collected samples for WB, RT-qPCR and immunofluorescence (IF) analyses after 15 and 36 days of differentiation, and assessed expression of NPCs and neuronal markers.

As expected, we observed downregulation of the SOX2 protein, a key transcriptional factor for maintaining stemness, as well as the intermediate filament NESTIN and the transcriptional factor PAX6 (NPC markers), indicating a loss of pluripotency already after 15 days of differentiation, which was more pronounced on day 36 (**Fig. 13B**). IF analysis performed in parallel, confirmed the expression of the specific neuronal tubulin Tuj1 in the neuronal populations already at day15 of differentiation (**Fig. 13C**).

We then analyzed HECW1 expression by WB, RT-qPCR and IF. As previously observed, HECW1, not expressed in NPCs, was highly induced along the differentiation, both at the protein and mRNA levels (**Fig. 13B-C-D**). Importantly, we were able to detect the endogenous protein HECW1 also by IF (**Fig. 13D**): while NPCs were almost negative for HECW1-staining, its expression was evident in CN, where it was localized mainly in the cytoplasm but also along filaments. This result confirmed the validity of our antibody that was not able to detect HECW1 in A549 cells due to its low level of expression (see Appendix).

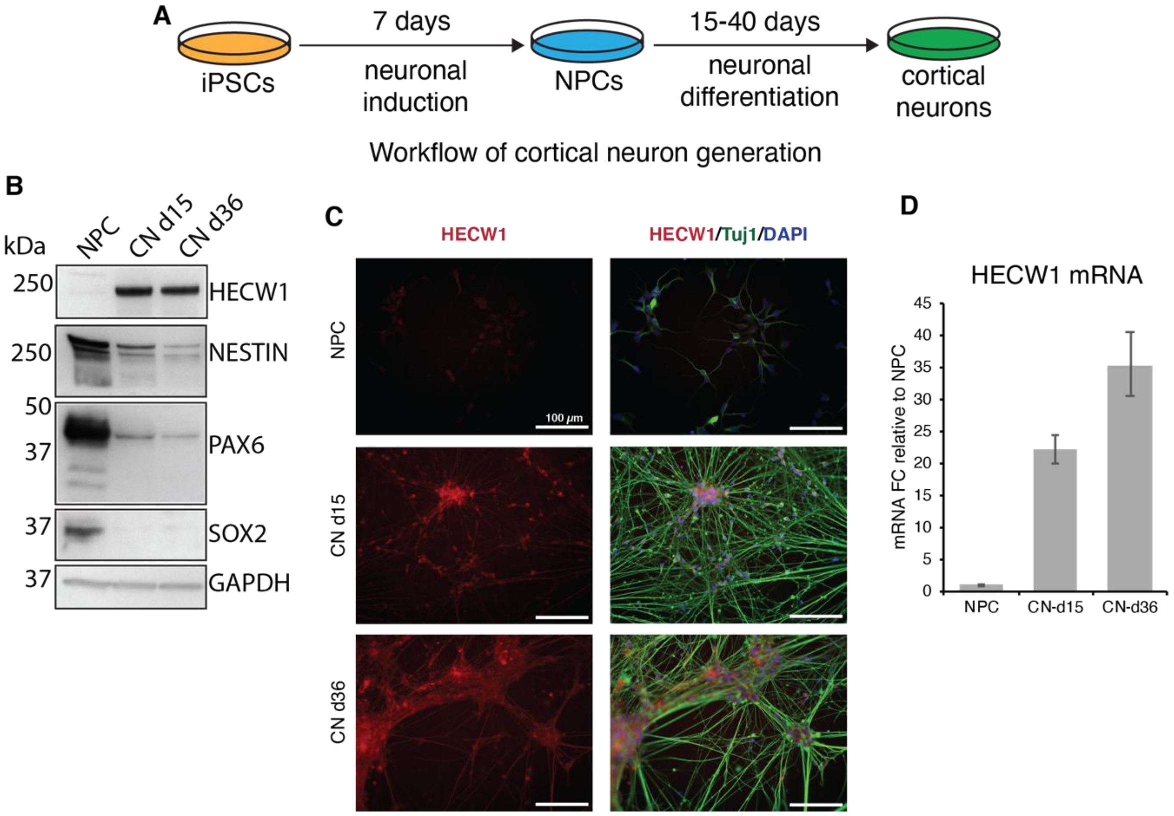

Figure 13 HECW1 expression is induced during differentiation of NPCs into cortical neurons

A) Workflow of differentiation of human iPSCs into cortical neurons passing through the intermediate step of neuronal precursor cells. iPSCs are plated and maintained in culture in iPSC medium. On day 0 of differentiation, the medium is switched to neural induction medium, which is changed on day 2, 4 and 6. On day 7 after neural induction, NPCs are collected and plated in neuronal differentiation medium. Half of the medium is changed every 3 days until neurons are collected at the indicated time points.

B) WB analysis of NPCs and cortical neurons collected at the indicated time points of differentiation, as indicated, showing downregulation of the NPCs markers NESTIN, PAX6 and SOX2 in parallel with HECW1 induction.

C) IF analysis of NPCs and cortical neurons, showing expression of the neuronal marker Tuj1 (green) and HECW1 (red) after 15 and 36 days of differentiation. The nuclei are shown in blue (DAPI). Scale bar: 100 µm.

D) RT-qPCR analysis of HECW1 mRNA as in A. The reported expression levels are relative to NPCs. iPSC: induced pluripotent stem cells; NPC: neuronal precursor cell; CN: cortical neurons.

We then analyzed the expression of other ubiquitin ligase members of the NEDD4 family, namely HECW2, NEDD4 and AIP4 (**Fig. 14**). Differently from HECW1, these E3 ligases were already present in NPCs, and they did not show a further increase during differentiation. In the case of NEDD4 a slight decrease in the protein level was measured on day 36. These results suggest a selective regulation, and possibly a specific role, of HECW1 in cortical neurons.

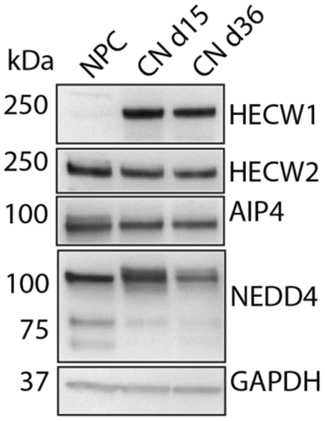

Figure 14 NEDD4 family member expression in NPCs and derived cortical neurons

WB analysis of NPCs and cortical neurons collected at the indicated time points of differentiation, as indicated (same samples used in the WB analysis reported in Figure 13). CN: cortical neurons.

4.1.2.2 Generation and characterization of iPSC-overexpressing or depleted for HECW1

To investigate the physiological and pathological role of HECW1 in human neurons, we decided to generate iPSCs that stably express GFP-HECW1 or a shRNA for HECW1, from which we could obtain neurons overexpressing or depleted for HECW1.

For HECW1-overexpression, we infected iPSCs with a virus carrying the lentiviral vector pSLIK-NEO-TetOn-GFP-HECW1-WT, harboring neomycin resistance and a doxycycline-inducible version of GFP-HECW1 (**Fig. 15A**). We selected cells using neomycin and finally sorted the population expressing GFP-HECW1 upon doxycycline-induction. WB analysis confirmed the enrichment upon sorting (**Fig. 15B**) and IF analysis showed the expected cytoplasmic HECW1-localization (**Fig. 15C**).

To generate the HECW1-knockdown (KD) cell line, we took advantage of a lentiviral vector pLKO-PURO-TetOn-shRNA-HECW1, bearing a doxycycline inducible shRNA targeting HECW1 and puromycin resistance for selection (**Fig. 15D**). We designed and tested three different shRNAs: shRNA-968, targeting the same sequence of previously validated siRNA oligo; shRNA-CDS, targeting another region in the coding sequence; and shRNA-3'UTR, targeting the untranslated region at the 3' of HECW1 mRNA.

Since HECW1 is not expressed in undifferentiated iPSCs, we tested the shRNAs efficiency by depleting the protein in HeLa cells which express a decent amount of HECW1. After infection and selection, using puromycin, we induced the shRNA expression by addition of doxycycline and verified HECW1-depletion by WB analysis (**Fig. 15E**). Based on the depletion efficiency, we selected the shRNA-968 for iPSCs infection.

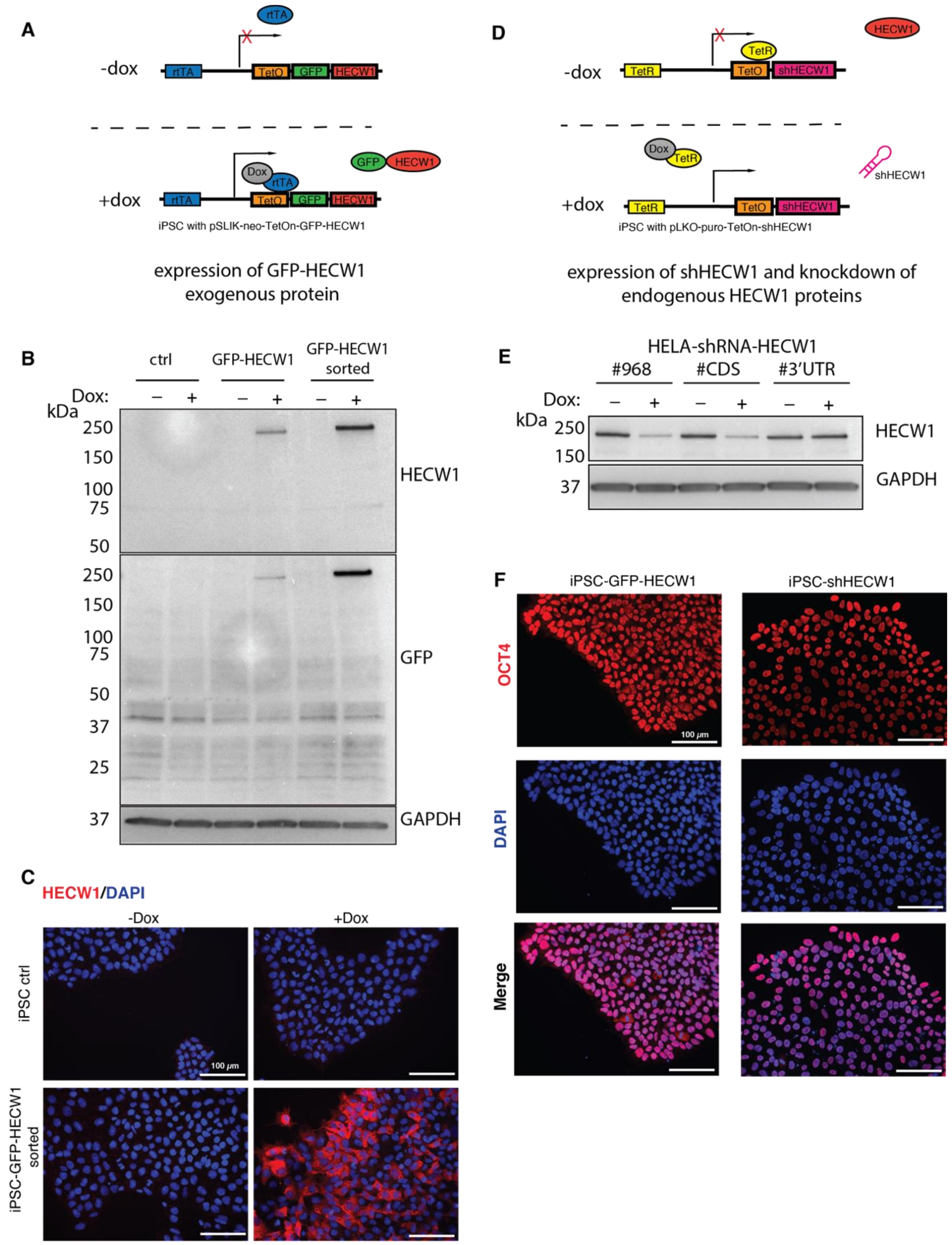

__Figure 15 Generation and characterization of iPSC-GFP-HECW1 and iPSC-shRNA-HECW1 lines__

A) A schematic representation of the TetOn GFP-HECW1-expressions system. Cells were infected with a single lentiviral virus expressing the doxycycline-inducible reverse transcriptional activator rtTA, neomycin resistance gene and GFP-HECW1. Upon Doxycycline addition to the medium, rtTA binds to the tetracycline operator TetO sequence upstream of the promoter and GFP-HECW1 expression is induced. CMV: cytomegalovirus.

B) iPSCs were infected with virus carrying the pSLIK-NEO-TetOn-GFP-HECW1-WT lentiviral vector, selected for neomycin resistance and sorted for GFP-HECW1 expression upon treatment with doxycycline (Dox, *0,5ug/ml for 48 hours). WB with the indicated antibody was performed to assess expression of the full-lent GFP-HECW1 fusion protein. Dox: doxycycline.*

C) IF analysis of the same cells as in B, showing expression of HECW1 in the cytoplasm of GFP-sorted cells upon treatment with doxycycline. HECW1 is stained in red and the nuclei in blue (DAPI). Scale bar: 100 μm.

D) A schematic representation of the TetOn shRNA-mediated HECW1-depletion system. Cells were infected with a single lentiviral virus expressing the tetracycline repressor TetR, puromycin resistance gene and shRNA-HECW1. In the absence of doxycycline, expression of the shRNA is repressed by TetR bound to the upstream tetracycline operator TetO sequence. Upon doxycycline addition to the medium, TetR is displaced from the TetO sequence and shHECW1 expression is induced.

E) HeLa cells were infected with virus carrying the pLKO-puro-TetOn-shHECW1 containing shRNA targeting HECW1 mRNA in the coding sequence (#968 and #CDS) or in the 3'UTR (#3'UTR), selected for puromycin resistance and treated with doxycycline (Dox, 0,5ug/ml for 48 hours) to induce shRNA expression and HECW1 depletion. WB was performed to assess HECW1 depletion. CDS: Coding Sequence; UTR: Untranslated Region.

F) IF analysis showing homogeneous expression of the pluripotency cellular marker OCT4 in the nuclear cellular compartments of iPSC-GPF-HECW1 and iPSC-shHECW1 lines. OCT4 is stained in red and the nuclei in blue (DAPI). Scale bar: 100 μm.

Infected cells were selected with puromycin and evaluated for the expression of the nuclear pluripotent marker octamer-binding protein 4 (OCT4) by IF analysis. Both the iPSC-GFP-HECW1 and the iPSC-shHECW1 lines were positive for OCT4, which is correctly expressed in the nucleus (**Fig. 15F**). Both lines exhibited iPSC-like morphology; uniform colonies with clean edges, which lacked spontaneously-differentiating cells.

4.1.2.3 Generation and characterization of NPC-overexpressing or depleted for HECW1

As iPSCs appear pluripotent and suitable for neuronal generation, they were differentiated into NPCs, the intermediate step between pluripotent stem cells and neurons (**Fig. 13A**) using a protocol that allows the generation of expansible and cry-preservable NPCs in seven days, without the need of rosette formation and isolation (Yan et al., 2013). To this aim, we plated iPSC-GFP-HECW1 and iPSC-shHECW1 in iPSC medium, which was then switched to neural stem cell induction medium 24 hours later (day 0 of induction) (**Fig. 13A**). At day 7 after induction, we dissociated the cells and plated them in NPC maintaining medium for their characterization performed by measuring induction of the NPC markers PAX6 and NESTIN and loss of the iPSC marker OCT4. As shown by the IF analysis, the majority of NPC-GFP-HECW1 and NPC-shHECW1 cells were positive for the three tested NPC markers (**Fig. 16A-B**). PAX6 and SOX2 staining overlapped with DAPI, indicating their nuclear expression, while NESTIN was present only in the cytoplasm. No OCT4-positive cells were observed (**Fig. 16A-B**).

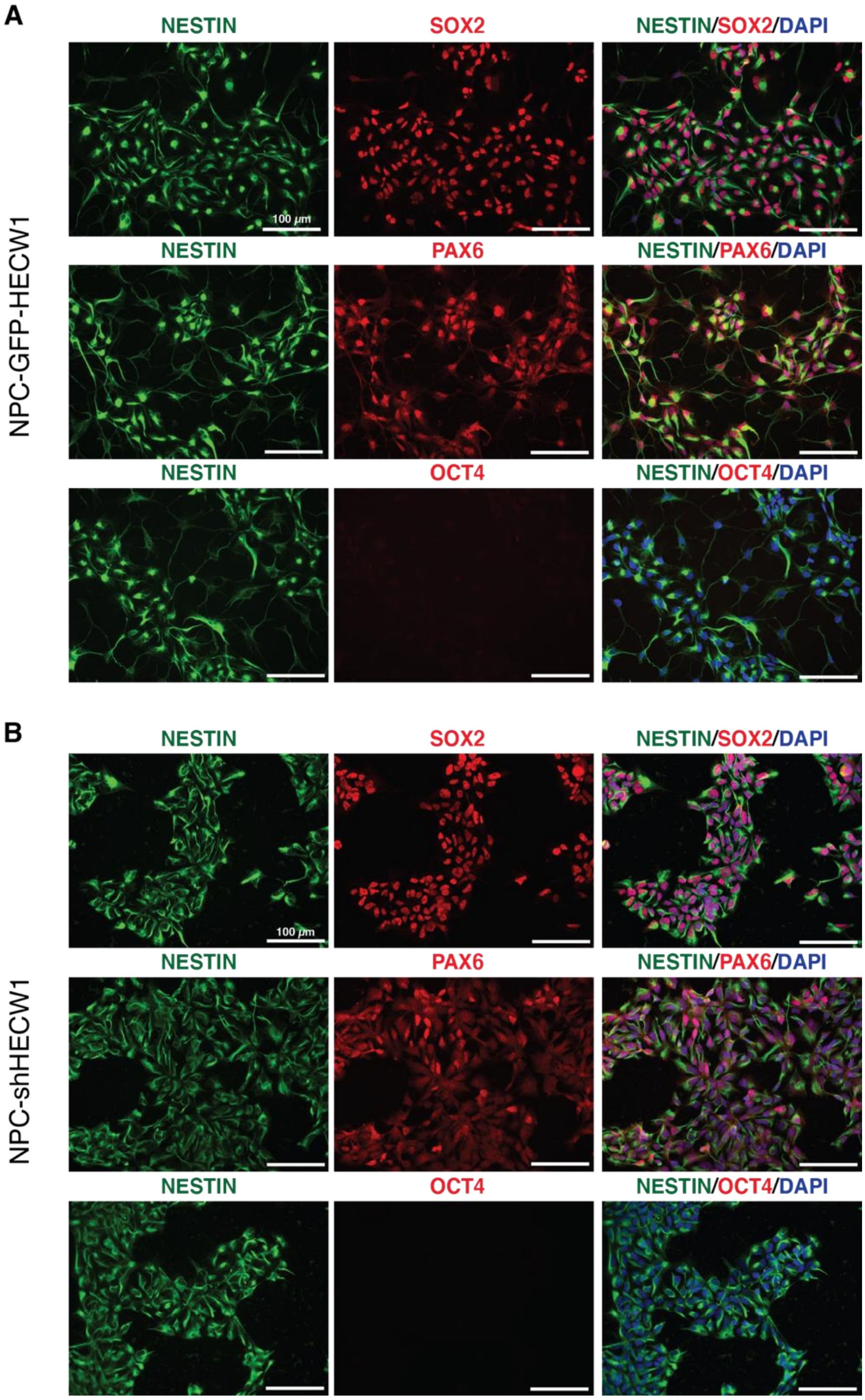

Figure 16 Characterization of NPC-GFP-HECW1 and NPC-shRNA-HECW1 lines

IF analysis of A) NPC-GFP-HECW1 and B) NPC-shHECW1 showing homogeneous expression of the NPC markers SOX2 (top), PAX2 (middle) and NESTIN, and the absence of the pluripotency cellular marker OCT4 (bottom panels). SOX2, PAX6 and OCT4 are stained in red, NESTIN in green and the nuclei in blue (DAPI). Scale bar: 100 µm.

Having confirmed their neuronal precursor phenotype, NPCs were then differentiated into cortical neurons, according to a previously described protocol (Yan et al, 2013), in the presence or absence of doxycycline, to evaluate both NPCs differentiation potential and HECW1 overexpression or deletion in the derived neurons.

4.1.2.4 Differentiation of HECW1-overexpressing neurons

We first validated the overexpression model. To this aim, we differentiated NPC-GFP-HECW1 cells into cortical neurons in the presence or absence of doxycycline to induce GFP-HECW1 expression (**Fig. 15A**). We collected neurons at day 15 and day 33 of the differentiation and performed WB, RT-qPCR and IF analyses.

As shown by phase contrast images, a neuronal network was observed at day 33 independently of the doxycycline-treatment (**Fig. 17A**). WB analysis confirmed the downregulation of the NPC markers NESTIN and SOX2, which decreased during differentiation, both in untreated and doxycycline-treated cells (**Fig. 17B**).

As expected, the endogenous HECW1 expression was induced during differentiation, in the untreated sample, both at the protein (**Fig. 17B**) and mRNA levels (**Fig. 17C**, grey bars). Doxycycline treatment strongly induced the expression of the GFP-HECW1 fused protein already in NPCs (**Fig. 17B**), and led to a more than 20-fold increase in HECW1 mRNA expression compared to untreated cells (**Fig. 17C**). IF analysis in NPC-GFP-HECW1 cells showed, upon treatment with doxycycline, cytoplasmic localization of HECW1 and a complete colocalization between GFP and HECW1 (**Fig. 17D**).

Nevertheless, despite the continuous presence of doxycycline in the medium, GFP-HECW1 expression was not maintained during the differentiation. As shown by WB analysis, a decrease in the GFP-HECW1 protein levels is evident already on day 15 compared to NPC, and a further loss is observed on day 33 (**Fig. 17B**). Similarly, even if higher than that of untreated NPC, HECW1-mRNA levels dropped. Neurons treated or not with doxycycline showed similar HECW1-mRNA levels, suggesting the loss of expression of the GFP-HECW1 exogenous version (**Fig. 17C**). Accordingly, IF analysis showed a very low frequency of GFP-positive neurons at day 15, which were almost absent at day 33, where the signal from HECW1 was comparable in treated and untreated cells, reflecting the level of endogenous protein (**Fig. 17E**).

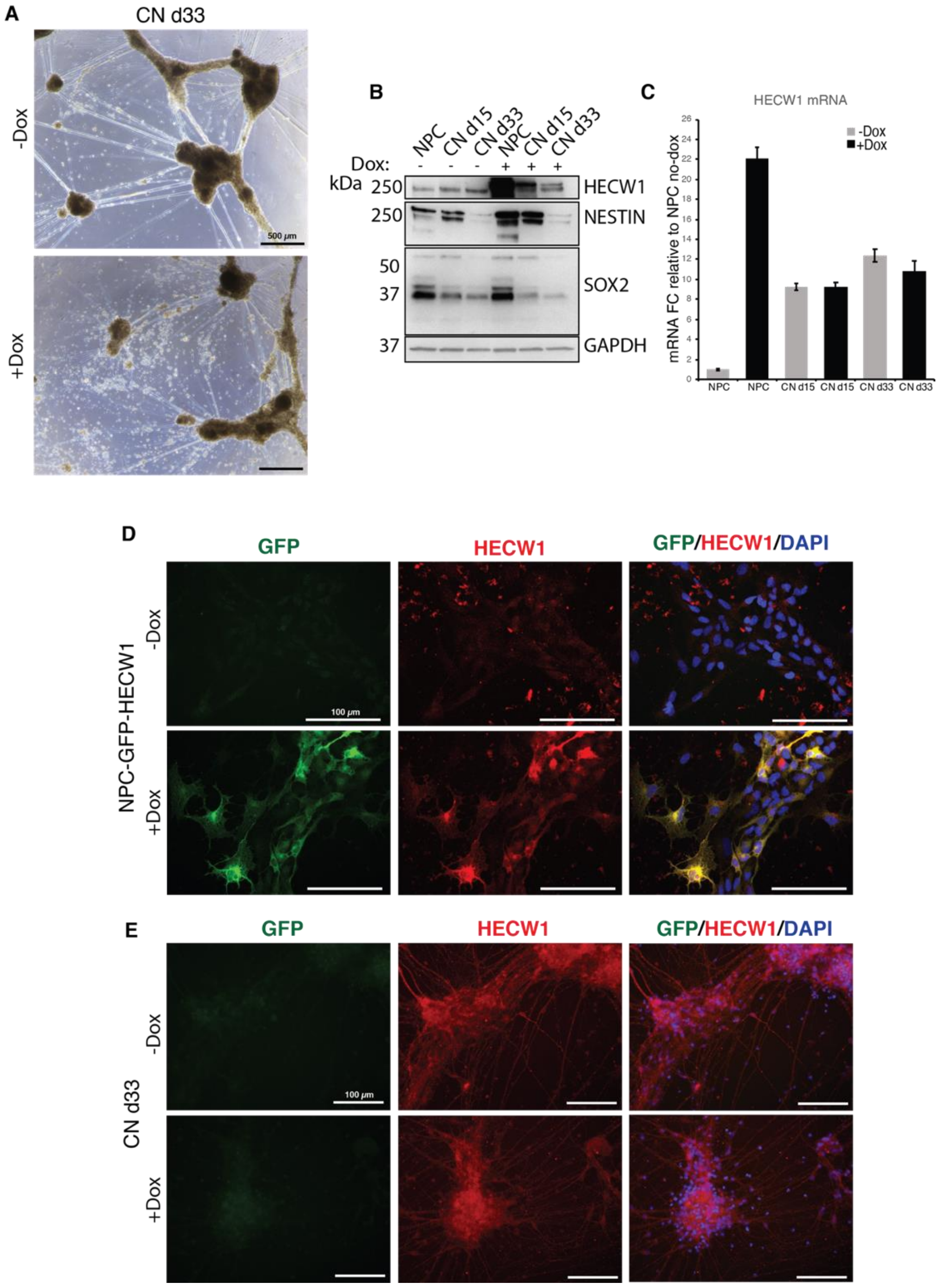

__Figure 17 Generation of cortical neurons from NPC-GFP-HECW1__

A) Phase-contrast images of untreated and doxycycline-treated NPC-GFP-HECW1-derived cortical neurons on day33 of differentiation. For treated cells, 0,5 ug/ml of doxycycline was added in the culture medium for the entire duration of differentiation. Scale bar: 500 µm.

B) WB analysis, as indicated, of NPCs and cortical neurons collected at the indicated time points of differentiation, with or without doxycycline treatment to induced HECW1 expression, to asses downregulation of NPC markers and expression of HECW1.

C) RT-qPCR analysis of HECW1 expression in cells treated and collected at the same time points as in A. The reported expression levels are relative to untreated-NPCs.

D) IF analysis of NPC-GFP-HECW1 untreated or treated with 0,5 ug/ml of doxycycline for 48 hours. HECW1 is stained in red, GFP in green and the nuclei in blue (DAPI). Scale bar: 100 µm.

E) IF analysis of untreated and doxycycline-treated NPC-GFP-HECW1-derived cortical neurons on day33 of differentiation. HECW1 is stained in red, GFP in green and the nuclei in blue (DAPI). Scale bar: 100 µm. CN: cortical neurons; NPC: neuronal precursor cell; dox: doxycycline.

Unfortunately, we realized that heterologous expression driven by the cytomegalovirus promoter (CMV) is limited in differentiated neurons (Fernandopulle et al., 2018) and this could be the cause of GFP-HECW1 expression failure.

4.1.2.5 Differentiation of HECW1-depleted neurons

The Tet-responsive element that drives the expression of the shRNA-HECW1 in the pLKO-PURO-TetOn-shRNA-HECW1 lentiviral vector lies within the H1 promoter that is not silenced in neurons (Wiederschain et al., 2009). Therefore, we proceeded with the generation of neurons from NPC-shHECW1 for the evaluation of the HECW1 depletion. We differentiated the NPC population containing the pLKO-PURO-TetOn-shRNA-HECW1 twice but in both cases we experienced high mortality in both untreated and doxycycline-treated populations and we had to interrupt the differentiation and collect cells at day 12. WB analysis showed that at this time point the NPC marker NESTIN was still expressed (**Fig. 18A**). Nonetheless, WB and RT-qPCR analyses confirmed the induction of HECW1 both at the protein and mRNA levels in untreated neurons compared to NPC (**Fig. 18A-B**). However, similar HECW1 expression and induction was measured in doxycycline-treated neurons in which the shRNA should be expressed (**Fig. 18A-B**). This negative result is possibly due to inefficient shRNA expression, but also to low efficiency of iPSCs infection. Indeed, since NPCs lack endogenous HECW1, we could not monitor the percentage of shRNA-harboring cells (i.e., the percentage of neurons in which the construct is present) at the beginning of differentiation.

Another general problem we faced while working with this small molecule-based differentiation protocol was the poor efficiency and reproducibility, that often lead to a mixed population of neural progenitors and various neural and glial cell types. Samples we collected at day 12 were indeed enriched in still-undifferentiated NPCs and this complicated the analysis even further.

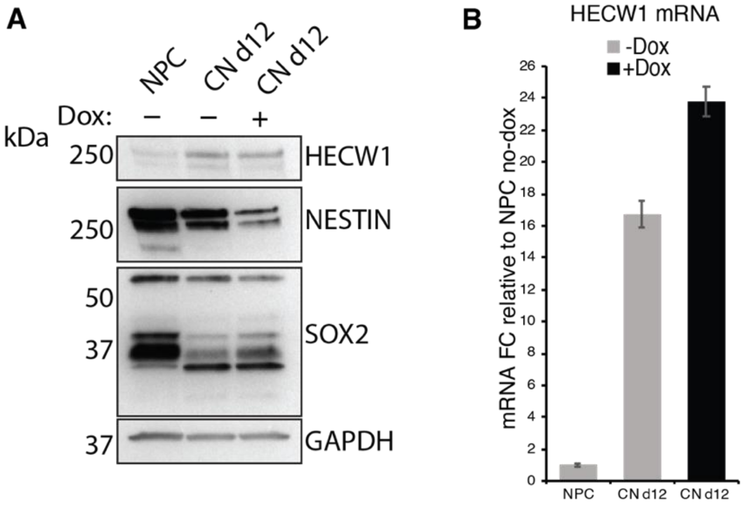

__Figure 18 Generation of cortical neurons from NPC-shHECW1__

A) WB analysis, as indicated, of NPCs and cortical neurons collected on day 12 of differentiation, with or without doxycycline treatment to induced HECW1 depletion, to asses downregulation of NPC markers and expression of HECW1. For treated cells, 0,5 ug/ml of doxycycline was added to the culture medium.

B) RT-qPCR analysis for HECW1 expression in cells treated and collected at the same time points as in A. The reported expression levels are relative to untreated-NPCs. CN: cortical neurons; NPC: neuronal precursor cell; dox: doxycycline.

4.1.3 NGN2 transcription factor-mediated differentiation protocol

4.1.3.1 Generation of iPSC-derived neurons

The various problems we faced, such as complex media formulations, lengthy protocols, poor efficiency and reproducibility, and consequently difficulties in scale up and omics analyses, prompted us to search for a different protocol.

We thus moved to a different approach that directly generates neurons from an iPSC line in which the expression of an integrated neurogenin 2, NGN2, can be induced by doxycycline. NGN2 is the master neuronal transcriptional factor and its expression directly converts iPSCs into a pure population of neurons, termed i3Neurons (integrated, inducible, and isogenic), in less than two weeks, without the need to pass through the intermediate step of NPCs (**Fig. 19A**) (Fernandopulle et al., 2018). In this protocol, iPSC-NGN2 cells are first plated on Matrigel-coated plates in induction medium supplemented with doxycycline for three days to induce NGN2 expression and neuronal differentiation. At day 3, pre-neurons are re-plated on PLO-coated plates in cortical neuron culture medium and maintained in culture, changing half of the medium twice every week (**Fig. 19A**; for details see Materials & Methods).

Following this protocol, we obtained a pure population of neurons that exhibited a neuron-like morphology, with distinct soma and neuritic elongations in 10 days from the iPSC plating, and mature neuronal morphology within three weeks of differentiation (**Fig. 19B**).

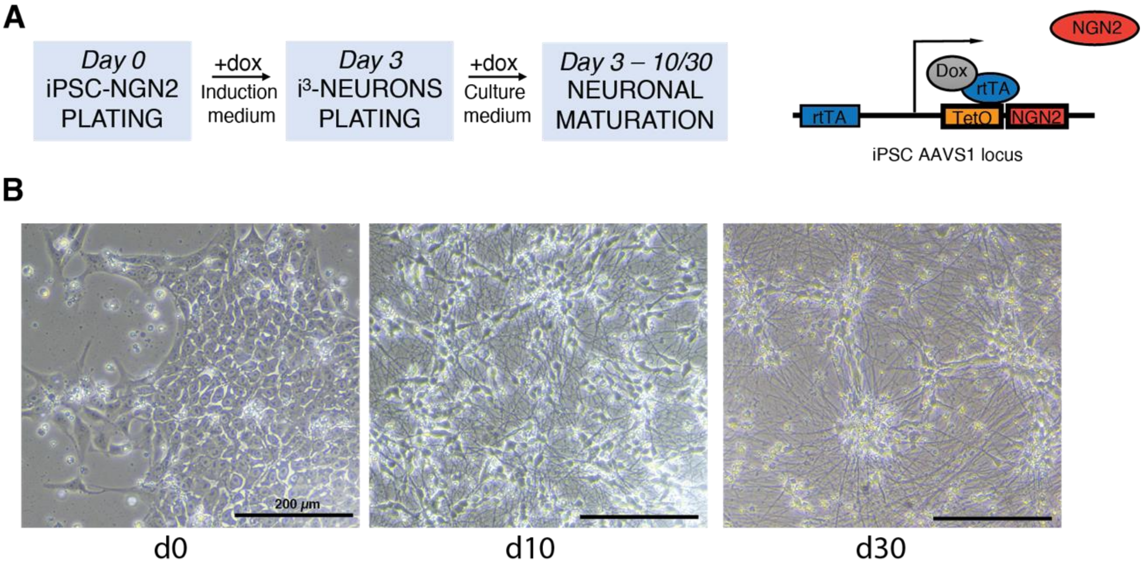

<u>Figure 19 Transcription factor-mediated differentiation of iPSC-NGN2 into a pure and homogeneous population of neurons</u>

A) Flow diagram of the two-step procedure for generating i3-Neurons from an iPSC line in which the expression of an integrated neurogenin 2, NGN2, into the AAVS1 locus can be forced with doxycycline induction. iPSCs are plated on day 0 and kept in induction medium complemented with 2ug/ml of *doxycycline (dox) until day 3, when the early neurons are collected and plated in cortical neuron culture medium supplemented with 2ug/ml of doxycycline. rtTA: doxycycline-inducible reverse transcriptional activator; TetO: tetracycline operator. Scale bar: 200 µm.*

B) Representative phase-contrast images throughout the differentiation of i3Neurons (d: day), showing a drastic change in cell-morphology from iPSC-colony to neuronal network.

We collected neurons at different time points of differentiations to measure the expression of iPSC and neuronal markers and the induction of HECW1. By WB analysis we confirmed the downregulation of the iPSC marker SOX2 and the induction of the neuronal marker Tuj1, already after 10 days and throughout the time course of differentiation (**Fig. 20A**). IF analysis confirmed the expression of Tuj1 in nearly the whole population of neurons at day 10 (**Fig. 20B**). Confirming previous observation, HECW1 was not expressed in iPSCs, but it was highly induced during the differentiation procedure, both at the protein and mRNA levels (**Fig. 20A-C**). IF staining, as well, showed the presence of HECW1 after 10 days of differentiation, compared to the negative HECW1-staining of iPSCs (**Fig. 20B**). Interestingly, HECW1 protein levels, which continued to increase until day 25 of differentiation, decreased at later time points of differentiation (day 28), in parallel with the behavior of its mRNA, as measured by RT-qPCR (**Fig. 20A-C**).

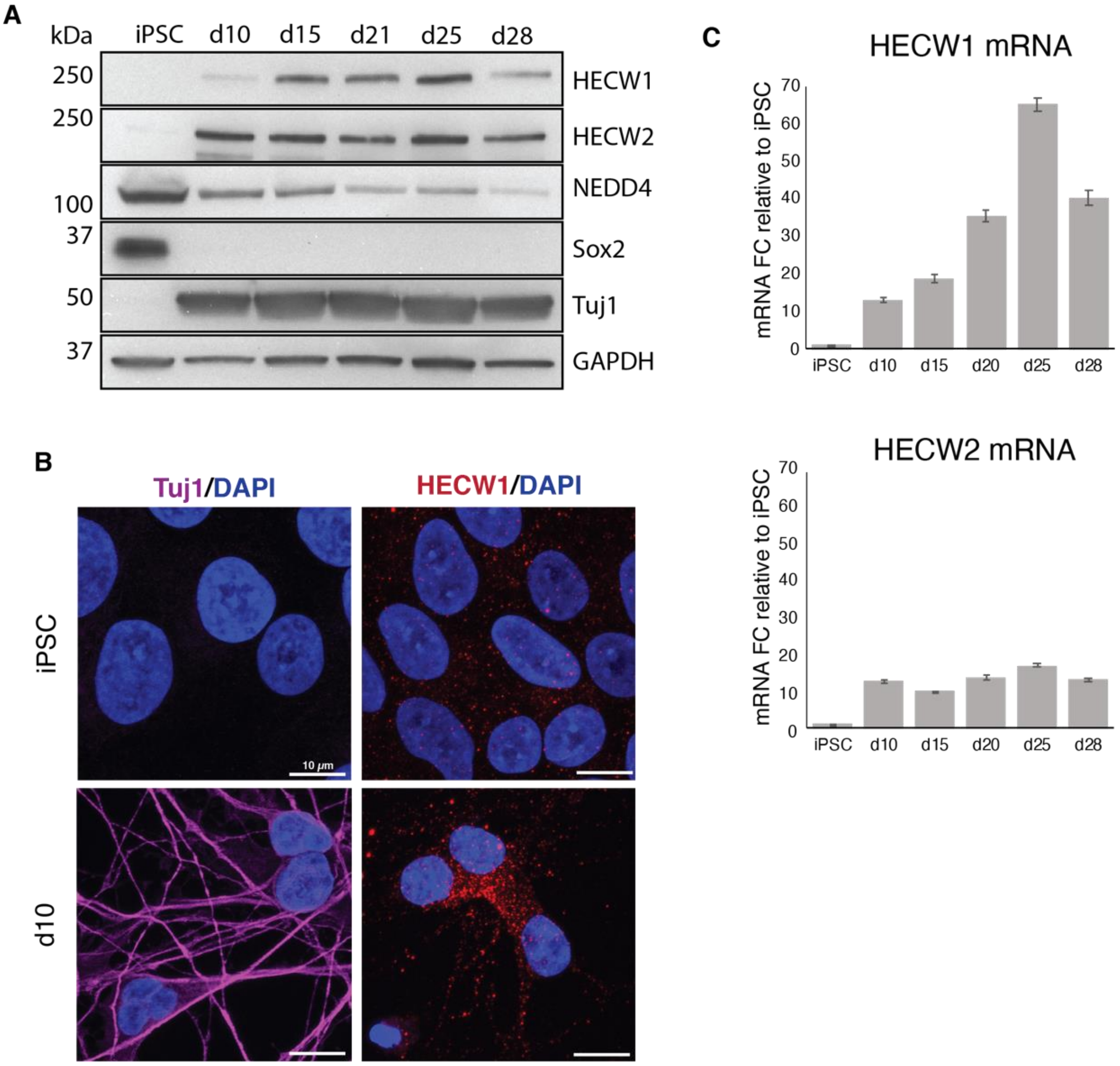

Figure 20 HECW1 is specifically induced during differentiation of iPSC-NGN2 into neurons

A) WB analysis, as indicated, of iPSCs and neurons collected at the indicated time points of differentiation, showing downregulation and upregulation of iPSC and neuronal markers, respectively, and specific modulation of HECW1.

B) IF analysis of iPSCs and neurons showing the expression of the neuronal marker Tuj1 and HECW1 after 10 days of differentiation. HECW1 is stained in red, Tuj1 in magenta and the nuclei in blue (DAPI). Scale bar: 10 μm.

C) RT-qPCR analysis of HECW1 and HECW2 mRNA at the same time points as in A. The reported expression levels are relative to iPSC.

We then examined the expression of other NEDD4 family members, and found that NEDD4 was downregulated during differentiation (**Fig. 20A**), while HECW2 showed an increase in its expression at day 10 compared to iPSCs, and then remained stable until the endpoint of the experiment (**Fig. 20A-C**). These results confirmed findings obtained with previous protocol.

4.1.3.2 siRNA-mediated HECW1 depletion in neurons

Having established the feasibility of the NGN2 system and the high induction of HECW1 in neurons, we set up to investigate the effects of HECW1 depletion during differentiation in mature neurons.

As a first approach, we knocked down HECW1 expression during the differentiation of iPSC into neurons through siRNA-mediated gene silencing. To this aim, we transfected pre-neurons on the third day of differentiation (day of replating, **Fig. 19A**) with siRNA for HECW1 and cultured them for 10 days before collection. The siRNA transfection resulted non-toxic, reproducible and highly efficient in depleting HECW1 (**Fig. 21A**).

Control and HECW1-KD neurons presented similar neuronal morphology and differentiation efficiency (**Fig. 21B**). In addition, as shown by the IF staining, Tuj1 and the microtubule-associated protein 2, MAP2, another neuronal specific protein, were detected in nearly all the cells in both cell populations, indicating an efficient conversion of iPSCs into neurons also in the absence of HECW1 (**Fig. 21C**).

The absence of a major defects indicates that HECW1 is not an essential gene for neuronal differentiation, as we also observed for Hecw in the *Drosophila* model (Fajner et al., 2021).

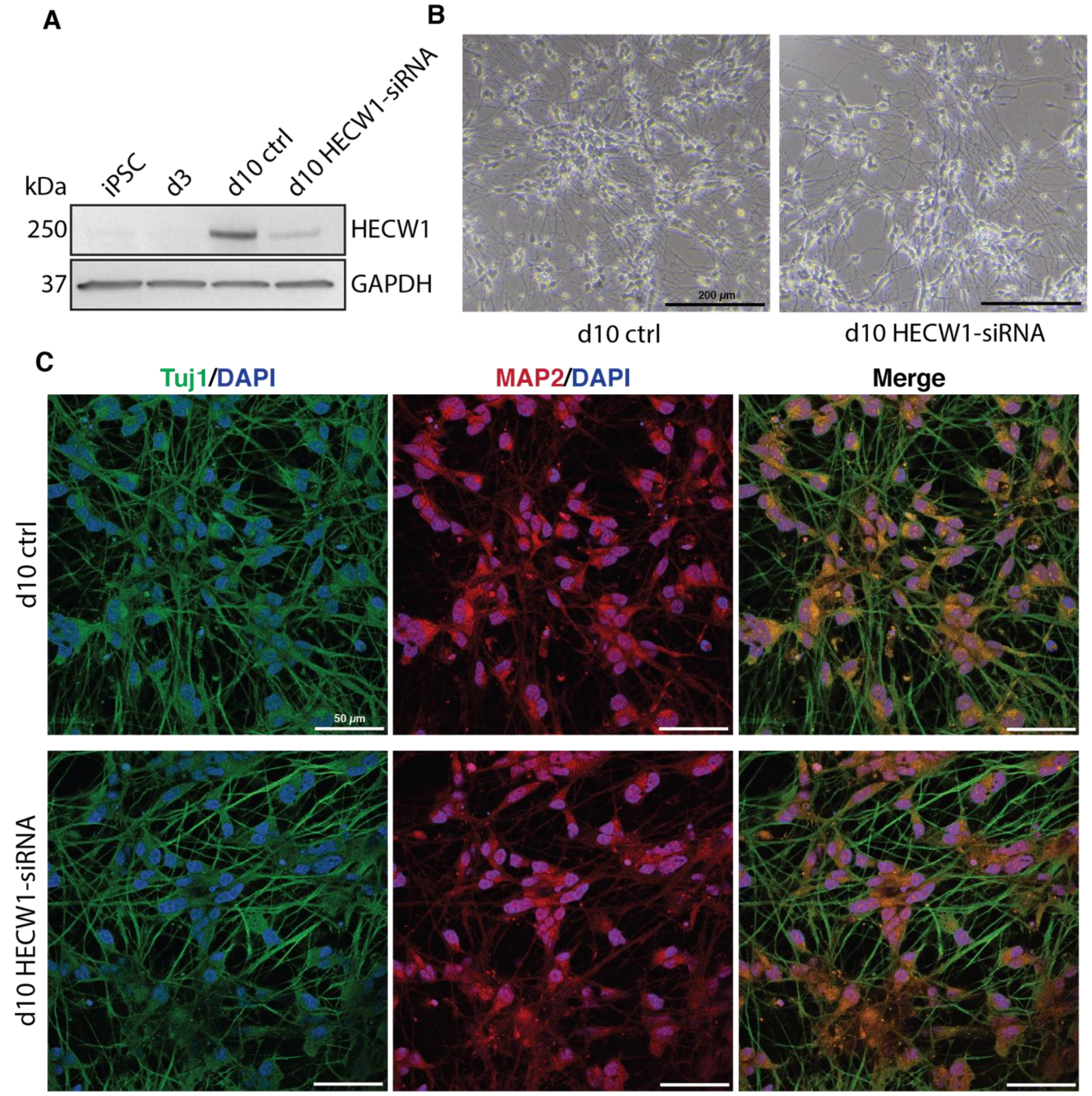

Figure 21 HECW1-siRNA-mediated depletion is efficient and non-toxic in neurons

A) Cells were transfected with HECW1-siRNA on the third day of differentiation (d3) and WB analysis was performed after 10 days of differentiation to assess HECW1 depletion.

B) Phase-contrast images demonstrating neuronal morphology. Scale bar: 200 µm.

C) IF analysis showing expression of the neuronal markers Tuj1 and MAP2. Tuj1 is stained in green, MAP2 in red and the nuclei in blue (DAPI). Scale bar: 50 µm.

4.1.3.3 Generation and characterization of iPSC-HECW1-KO clones

To avoid the need for siRNA transfection and to obtain a stable depletion of HECW1, we decided to generate iPSC-HECW1-KO clones via CRISPR-cas9 ribonucleoprotein-mediated genome editing. We electroporated NGN2-iPSCs with the Cas9 protein and four different gRNAs designed to target HECW1 (see Materials & Methods). Based on activity and target cut efficiency, we selected two guides, called guide 5 and guide 6, which are positioned on exon 13 and exon 16, respectively, of HECW1 (**Fig. 22A-B**). From each gRNA, we selected single clones based on iPSC morphology, viability and growth, and screened them by PCR for HECW1-editing as the HECW1 protein is not expressed in iPSCs.

We identified two clones per guide with a deletion that caused coding alteration. All clones are full KO clones. Clones 5.5 and 5.15 (guide 5) are homozygous for a 5-bp deletion that generates a premature stop codon in exon 15. Clone 6.7 has a homozygous 1-bp deletion that, similarly, generates a premature stop codon in exon 16. Clone 6.17 has a compound heterozygosity of deletions, with 1-bp deletion in one allele and 5-bp on the other allele (**Fig. 22C-D**).

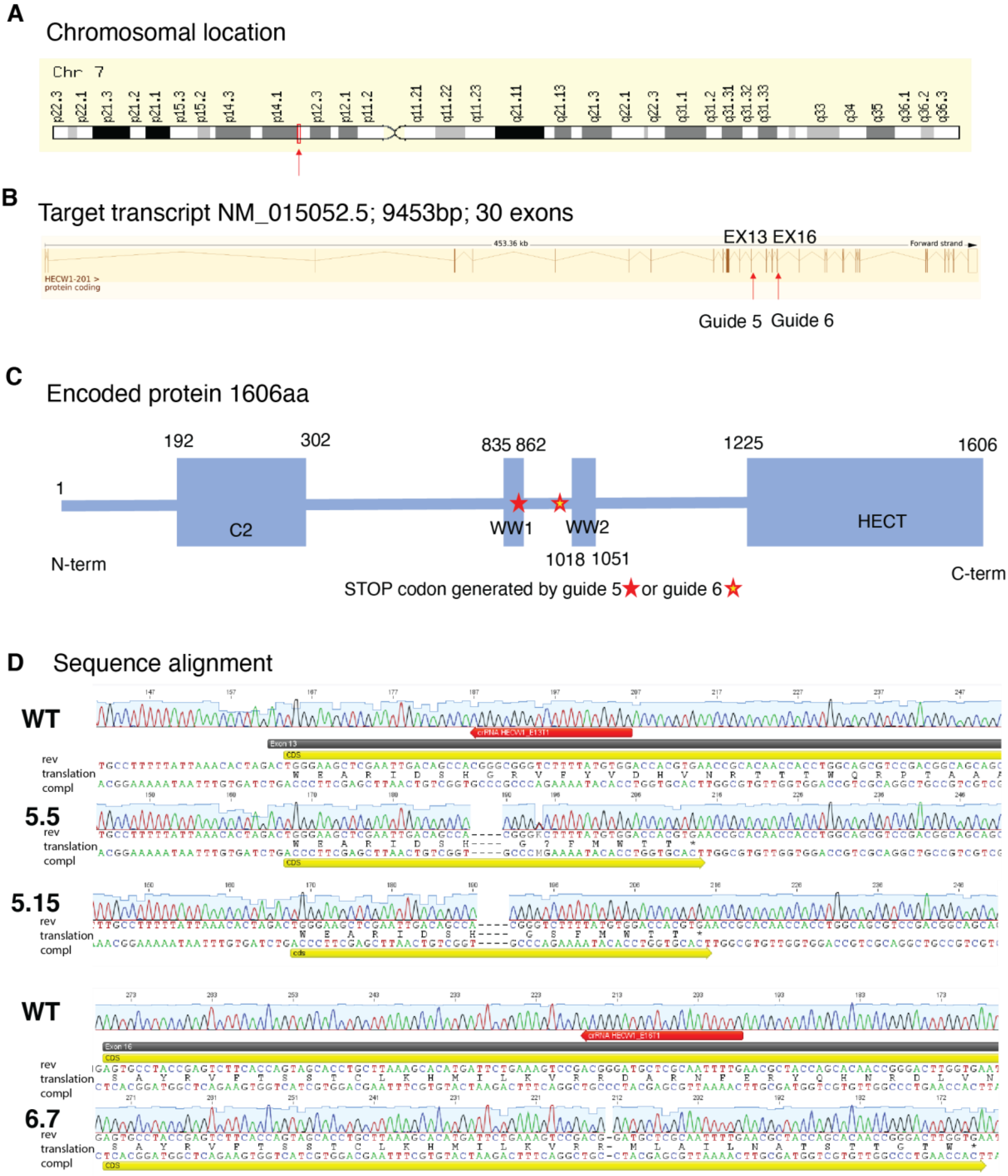

Figure 22 HECW1-KO induced by CRISPR-cas9 system in iPSCs

A) Position of HECW1 on chromosome 7 is shown in red.

B) HECW1 transcript showing exons and target sites for the two selected gRNAs, guide 5 and guide 6. EX: exon.

C) A schematic representation of the HECW1 protein, with the premature stop codons generated by the gRNAs indicated by stars. C2: C2 domain ($Ca2^+$-binding domain); WW: WW domain (substrate interaction); HECT: homologous to E6AP C-terminus (catalytic domain).

D) Sequence alignment between WT and HECW1-KO clones, showing DNA and predicted aa-sequences. In mutant sequences, deletions are indicated with dashes and the premature stop codon is indicated with an asterisk.

4.1.3.4 Generation and characterization of HECW1-KO neurons

We then tested the generated clones for differentiation into neurons and HECW1 depletion. To this aim, we differentiated control and iPSC-HECW1-KO clones for 10 days and collected sample for WB and RT-qPCR analyses. All the four tested clones exhibited similar neuronal morphology and differentiation efficiency as the control, with no sign of major defects in viability, as expected (**Fig. 23A**).

While induced in control neurons, HECW1 protein was not detectable in neurons generated from the four iPSC-KO clones (**Fig. 23B**). This result was also confirmed by immunoprecipitation (IP) analysis (**Fig. 23C**). In contrast to the total absence of the protein, HECW1 mRNA was present and induced during differentiation both in control and HECW1-KO clones (**Fig. 23D**). Thus, we concluded that, in spite of the presence of premature stop codons, the transcripts were not subjected to nonsense-mediated decay (NMD). Notably, the same results were obtained in the *Drosophila* KO lines (Fajner et al., 2021).

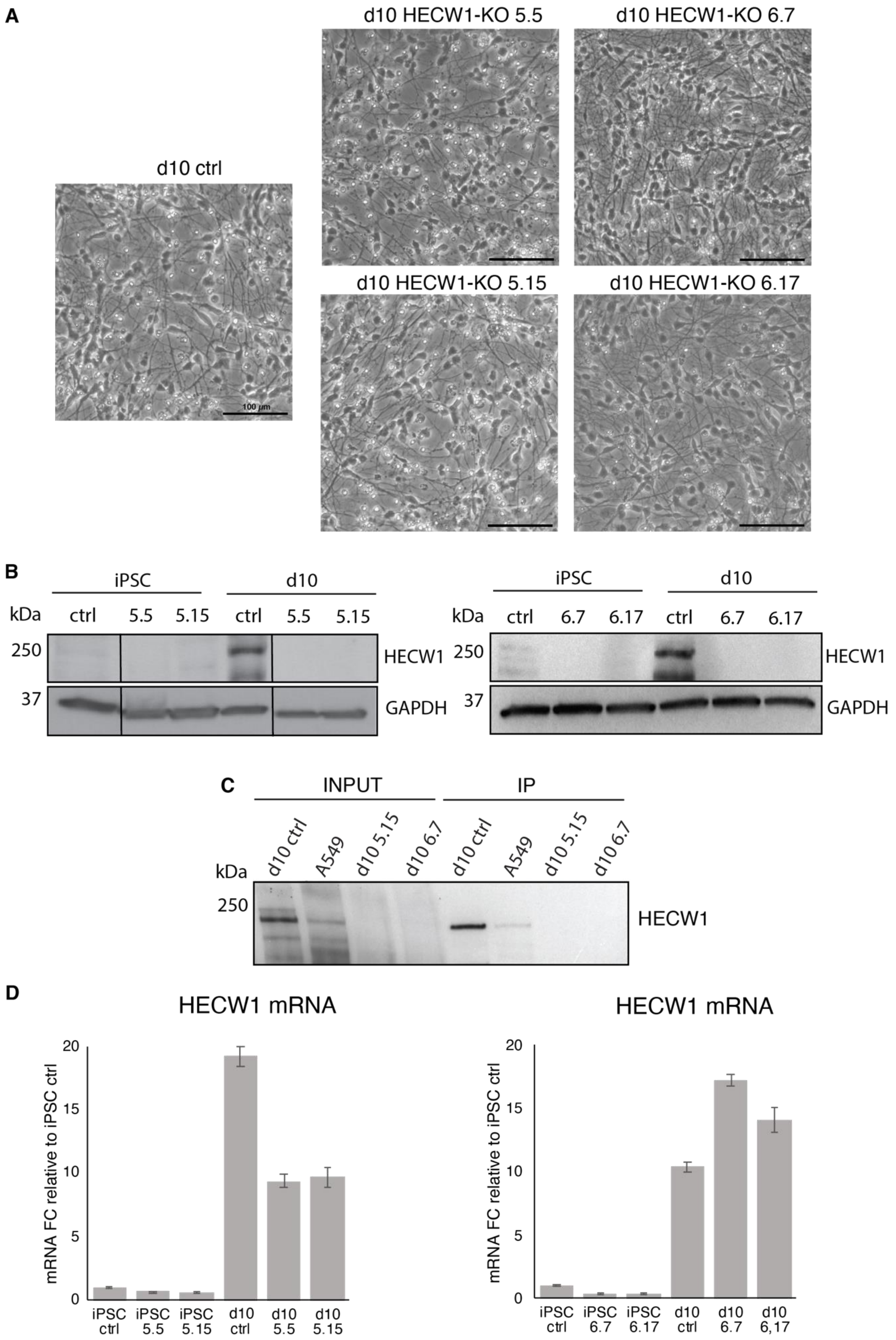

Figure 23 iPSC-HECW1-KO clones efficiently generate viable neurons depleted for HECW1 protein

A) Phase-contrast images demonstrate neuronal morphology for both control (ctrl) and HECW1-KO neurons on day 10n. Scale bar: 100 µm.

B) WB analysis of samples as in A to asses HECW1 depletion.

C) HECW1 antibody was used for IP and WB of A549 cells, or ctrl and HECW1-KO neurons on day 10 of differentiation.

D) RT-qPCR analysis of samples as in A/B, showing induction of HECW1 mRNA during. The reported expression levels are relative to iPSC-ctrl.

Based on neuronal morphology and health, the clone 5.15 was selected for further characterization.

WT control and 5.15 clones were differentiated for 10 and 30 days and samples collected for WB and RT-qPCR analyses. HECW1-KO did not lead to major defects in the viability at day 30 where mature neurons presented a neuronal network similar to that of the control (**Fig. 24A**). WB analysis showed induction of the neuronal tubulin Tuj1 and downregulation of the pluripotent marker SOX2 in both control and HECW1-KO neurons, both at early time point of differentiations and in more mature neurons (**Fig. 24B**). The analysis also confirmed the complete absence of HECW1 protein in HECW1-KO neurons on day 10 and day 30 of differentiation, in contrast to the differentiation-dependent HECW1-induction in control neurons (**Fig. 24B**). HECW1-depletion was also confirmed by IF analysis (**Fig. 24C**), where only control neurons, indeed, showed a clear HECW1 dotted staining in the soma and neurites.

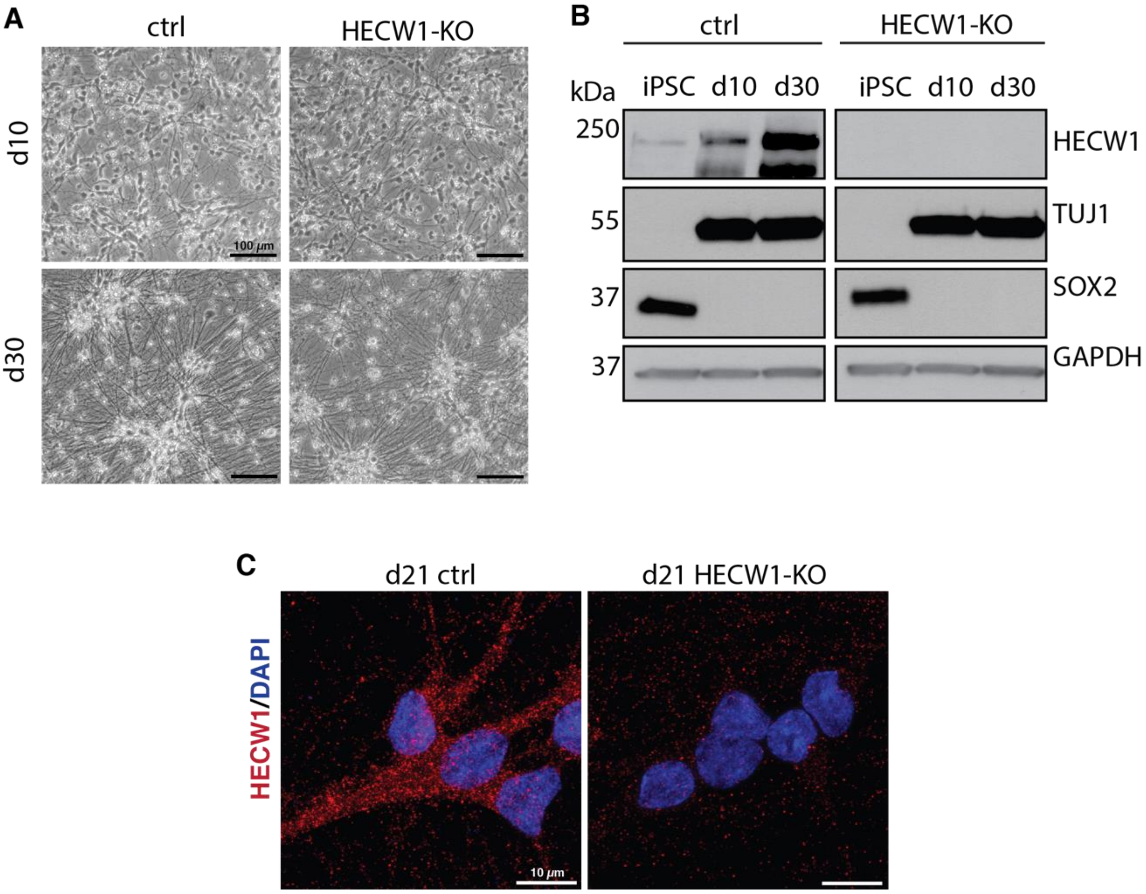

<u>Figure 24 iPSC-HECW1-KO clone efficiently generates viable mature neurons depleted for HECW1 protein</u>

A) Phase-contrast images demonstrate neuronal morphology of control (ctrl) and HECW1-KO neurons after 10 and 30 days of differentiation. Scale bar: 100 µm.

B) WB analysis, as indicated, of control (ctrl) and HECW1-KO iPSCs and neurons collected at the indicated time points of differentiation, showing downregulation and upregulation of iPSC and neuronal markers, respectively, and complete loss of HECW1 in HECW1-KO neurons.

C) IF analysis of ctrl and HECW1-KO neurons after 21 days of differentiation, showing HECW1 expression and absence, respectively. HECW1 is stained in red and the nuclei in blue (DAPI). Scale bar: 10 µm.

4.2 Transcriptomics and proteomics analyses of HECW1-depleted neurons

To identify the cellular processes influenced by HECW1-depletion in neurons in an unbiased way, we subjected control and HECW1-KD neurons to transcriptome and proteome analyses and investigated differences in their global expression pattern.

4.2.1 Transcriptomic analysis of HECW1-KD neurons

By taking advantage of the RNA-Sequencing-based transcriptome technology, we first performed a gene expression analysis of RNA extracted from control and HECW1-KD neurons after 10 days of differentiation. To improve the robustness of our analysis we collected four biological replicates from each line.

Confirming that both the control and HECW1-KD iPSCs correctly differentiated into neurons, high levels of pan-neuronal genes, such as specific neuronal cytoskeleton TUBB3 (Tuj1), MAP2 and NEFM, and synaptic genes SYP and DLG4, were measured in all of the samples (**Fig. 25**). In addition, all of the samples showed a low expression of markers for progenitor cells, such as the pluripotent gene NANOG and the neuronal progenitor marker CDH1, and markers for non-neuronal cells, namely glial and astrocytes, such as GFAP and S100B. This gene expression profile indicated that all the iPSC lines were well-differentiated into cortical neurons with preferential expression of markers for dopaminergic (e.g., LMX1B), cholinergic (e.g., ACHE) and glutamatergic (e.g., GLS) neurons, versus genes of serotoninergic (e.g., TPH1) and GABAergic (e.g., GABRA1) neurons, which were expressed at low levels, suggesting a uniform neuronal differentiation. Thus, this analysis confirmed the potentiality and efficiency of the NGN2-differentiation protocol, which generates *bona fide* neurons already after 10 days of differentiation.

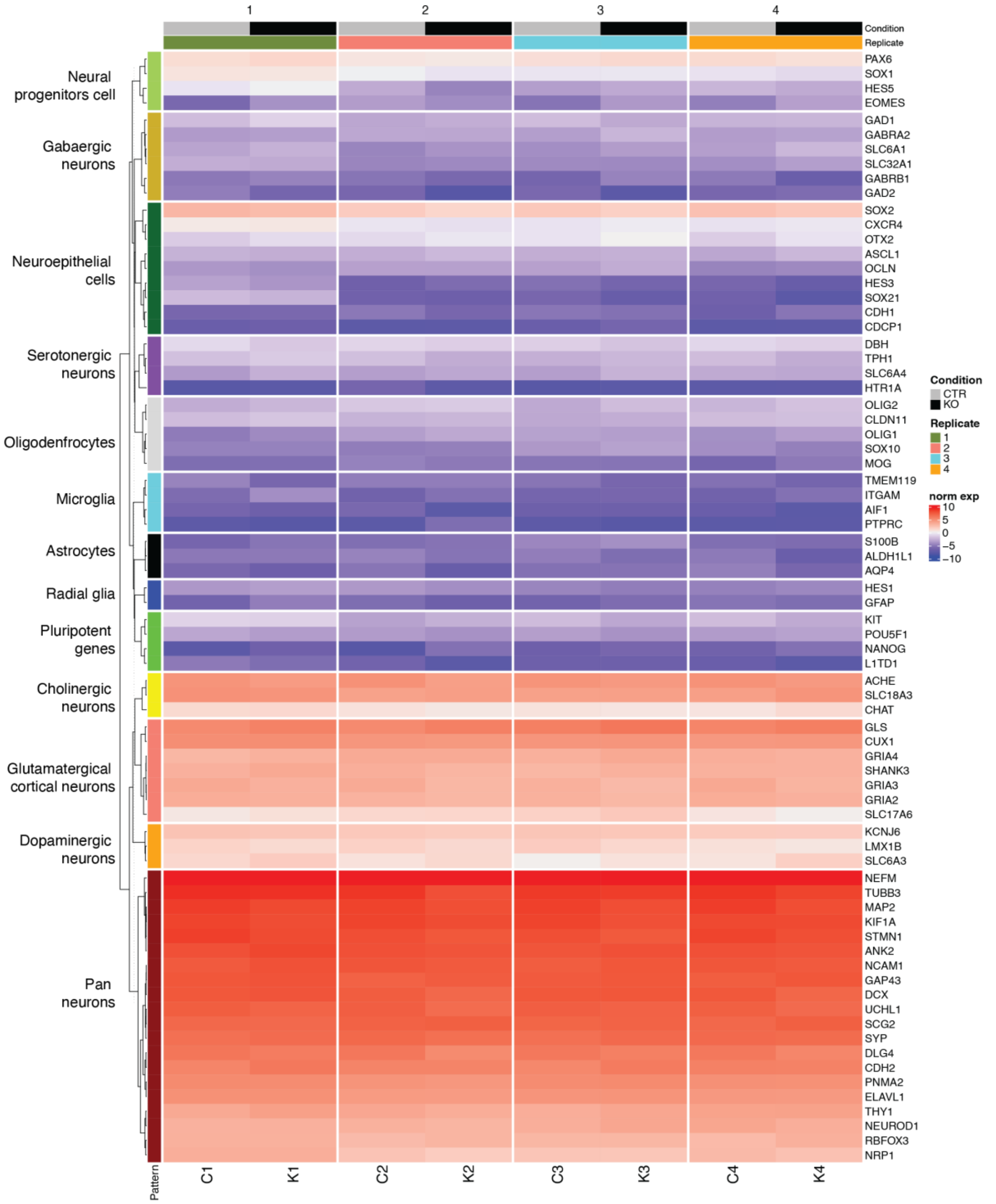

<u>Figure 25 NGN2-neurons show homogeneous expression of neuronal genes</u>

Gene expression was assayed by RNA-Seq-based transcriptomic analysis in control (ctrl) and HECW1-KD neurons on day 10 of differentiation, using four separate biological replicates.

Heatmap with the expression levels of genes listed on the right and showing high expression of neuronal genes in all samples. Genes are grouped based on cell-type expression; legend for grouped color is indicated on the left. Log2 signal intensity values for any single gene in a sample were normalized against the average expression level of all the genes in that particular sample and colors range from −10.0 blue to +10.0 red (expressed lower and higher than the average gene expression, respectively).

In order to assess sample similarity, we also performed a Principal Component Analysis (PCA), which revealed that the RNA expression profile of each HECW1-KD sample was more closely related to that of the control sample from the same replicate than the profiles of other HECW1-KD samples (**Fig. 26A**). The observation that iPSC-derived neurons clustered accordingly to the experimental replicate and not to the HECW1 expression indicated that one of the biggest sources of variability among the samples was the replicate of origin and not HECW1-status.

Next, in order to identify significantly deregulated genes, we compared the RNA expression profiles of control and HECW1-KD neurons. Given the great variability among replicates, we identified the deregulated genes (log2FC > 0.5) of each HECW1-KD sample compared to its control and overlapped the lists of deregulated genes from the four biological replicates, thus obtaining a list of 321 common genes, among which only 53 were deregulated in the same direction in all replicates (35 and 18 genes were upregulated or downregulate) with a limited fold change (**Fig. 26B**). A considerable portion of non-coding genes was also present (27 and 11 protein-coding genes, and 8 and 7 ncRNA/pseudogenes, among the upregulated and the downregulated genes, respectively).

Since PCA showed that replica number 1 clustered separately from the other three replicas (**Fig. 26A**), we decided to repeat the analysis, this time taking into consideration only the three replicas with the closest transcriptome profiles. We obtained a list of 602 common genes, of which 189 were deregulated in the same direction in all three replicas, with 85 and 104 genes, respectively, upregulated or downregulated in HECW1-KD versus control neurons (**Fig. 26C**). Again, a considerable portion of non-coding genes was identified (57 and 67 protein-coding genes, and 28 and 37 ncRNA/pseudogenes among the upregulated the downregulated genes, respectively).

A Gene Set Enrichment Analysis was run on the common up- or downregulated genes identified in both analyses in order to identify pathways and biological processes affected by HECW1 KD. Statistical overrepresentation test showed no significant result (p<0,05). These data, altogether, indicate that HECW1 KD did not have a major impact on neuronal transcriptional profile at early time points of differentiation (10 days).

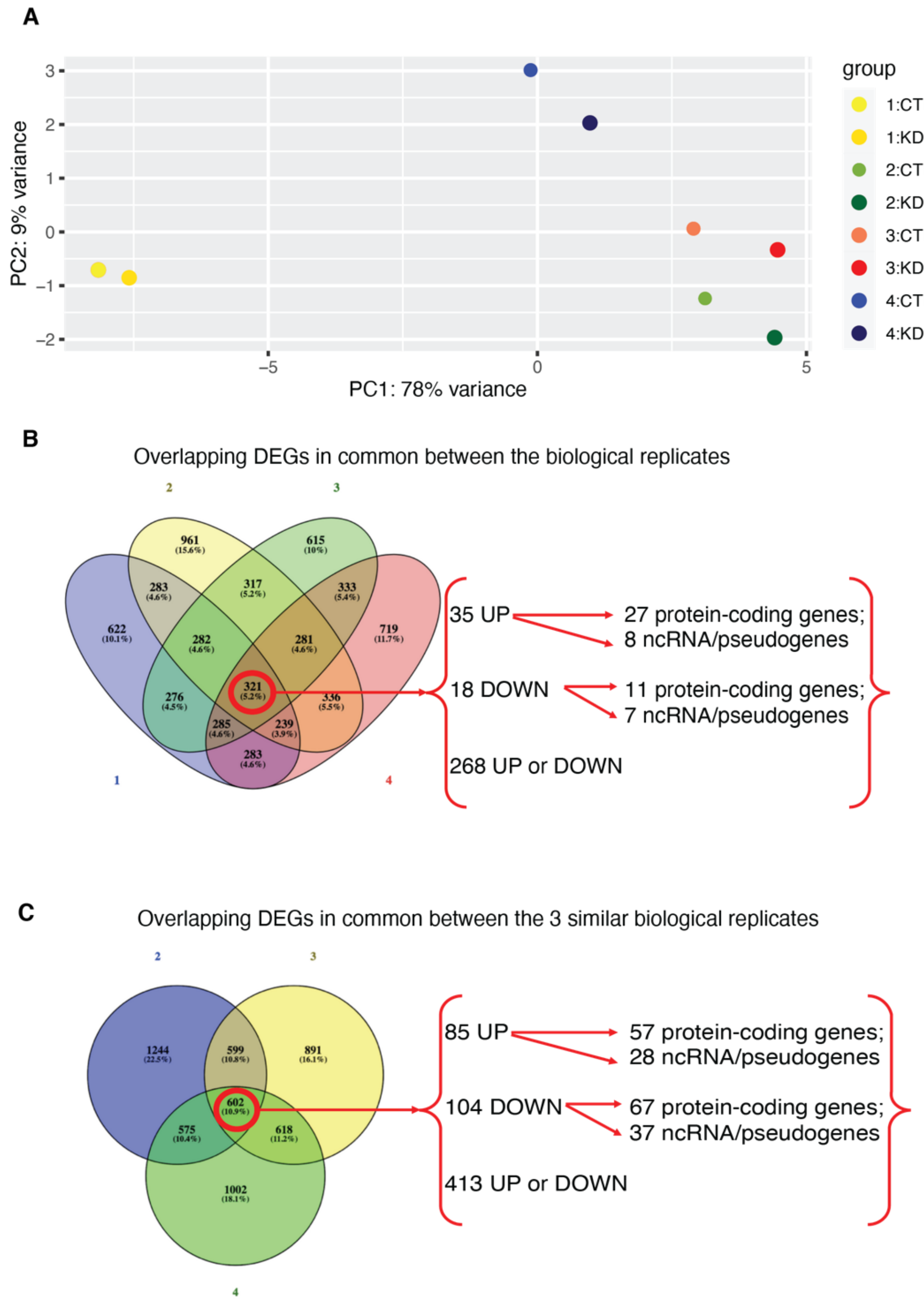

Figure 26 Transcriptional profiling of HECW1-KD neurons

Gene expression was assayed by RNA-Seq-based transcriptomic analysis in ctrl and HECW1-KD neurons at 10 days of differentiation from four separate biological replicates.

A) Principal component analysis (PCA) of control (ctrl) and HECW1-KD neurons showing clusterization according to the experimental replicate.

B) Venn diagrams of differentially expressed genes in control (ctrl) and HECW1-KD neurons from 4 different replicates.

C) Venn diagrams of differentially expressed genes between control (ctrl) and HECW1-KDneurons from the three more similar replicates (as seen in A).

4.2.2 Proteomics analysis of HECW1-KD neurons

To identify specific proteins that may by regulated by HECW1 in neurons, we evaluated the impact of HECW1-depletion on the neuronal proteome. We collected lysates from control and HECW1-KD neurons (three biological replicates from each line) at day 10 of differentiation and, through Mass Spectrometry (MS), we performed a label-free quantitative proteomics analysis (**Fig. 27A**). We extracted and identified around 7000 proteins from each sample (**Fig. 27B**). More than 95% of the identified proteins were present in all samples, indicating high reproducibility (**Fig. 27B**).

We then generated a Volcano plot comparing control and HECW1-KD neurons to graphically reveal alterations in proteome abundance (**Fig. 27C**). We observed an overall limited change between control and HECW1-KD neurons, with 202 differentially expressed proteins (p-value <0,05), the majority of which were characterized by a small range of differences (180/202 -0,7<log2FC>0,7).

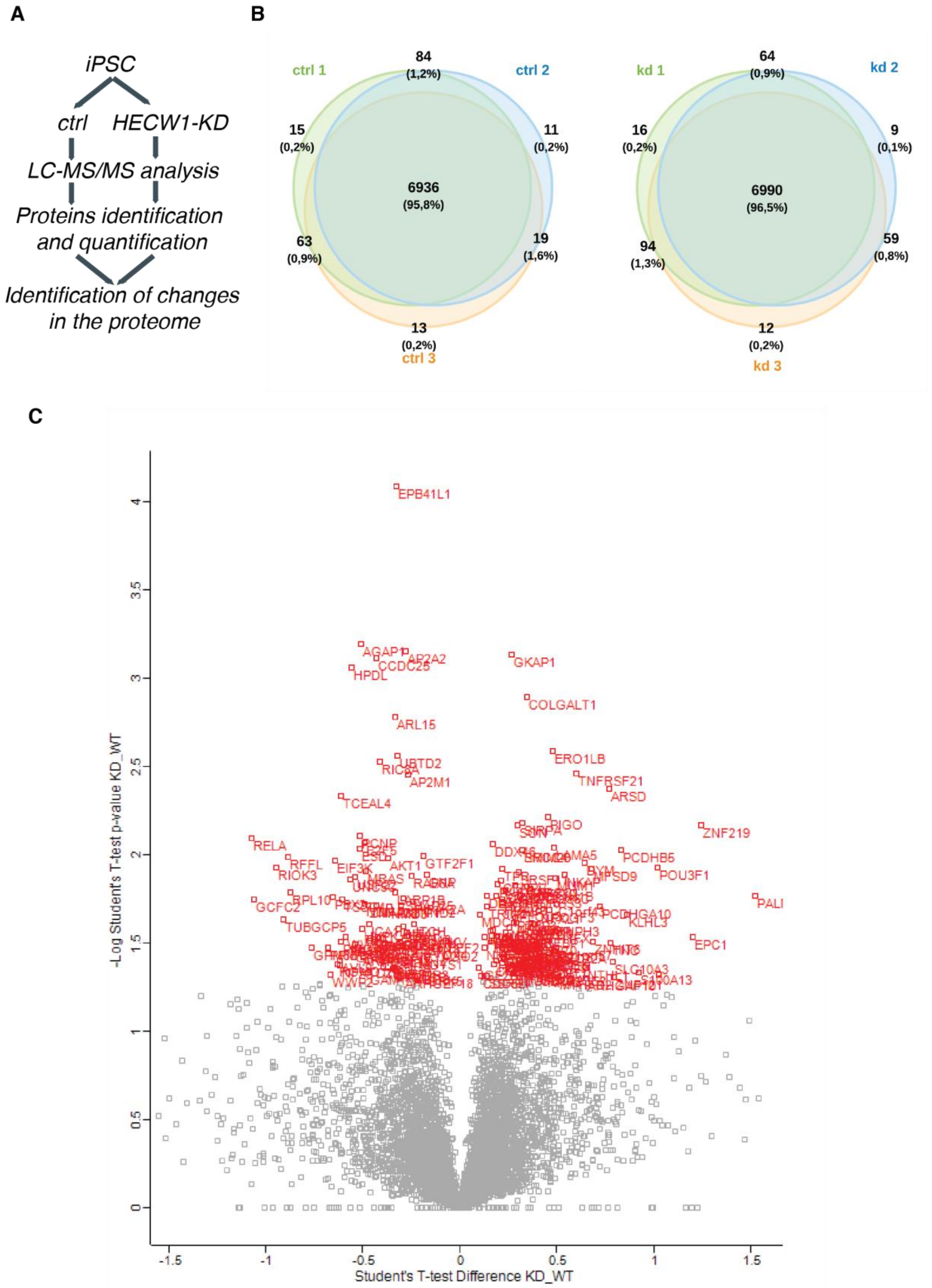

Figure 27 Total proteomic analysis in HECW1-KD neurons

A) A scheme of the proteomic analysis.

B) Venn diagrams of the identified proteins in the three biological replicates of control (ctrl) and HECW1-KD samples.

C) Representative Volcano plot analysis comparing control (ctrl) and HECW1-KD neurons on day 10 of differentiation. The negative logarithmic p-values derived from the statistical test are plotted (y-axis) *against the differences between the protein quantification in HECW1-KD versus control (ctrl) (x-axis). Red points show significantly differentially abundant proteins (p-value <0.05). 86 and 166 proteins were found to be significantly less abundant (left) or more abundant (right), respectively, in the HECW1-KD-neurons compared to control neurons.*

Nevertheless, by GO analysis for molecular function, we observed an evident enrichment in specific protein categories, the most prominent related to vesicle trafficking and kinase activity, mainly for downregulated proteins, and to RNA metabolism, mainly for upregulated proteins. **Table 2** lists the top 10 GO molecular functions enriched in the downregulated- and the upregulated protein lists.

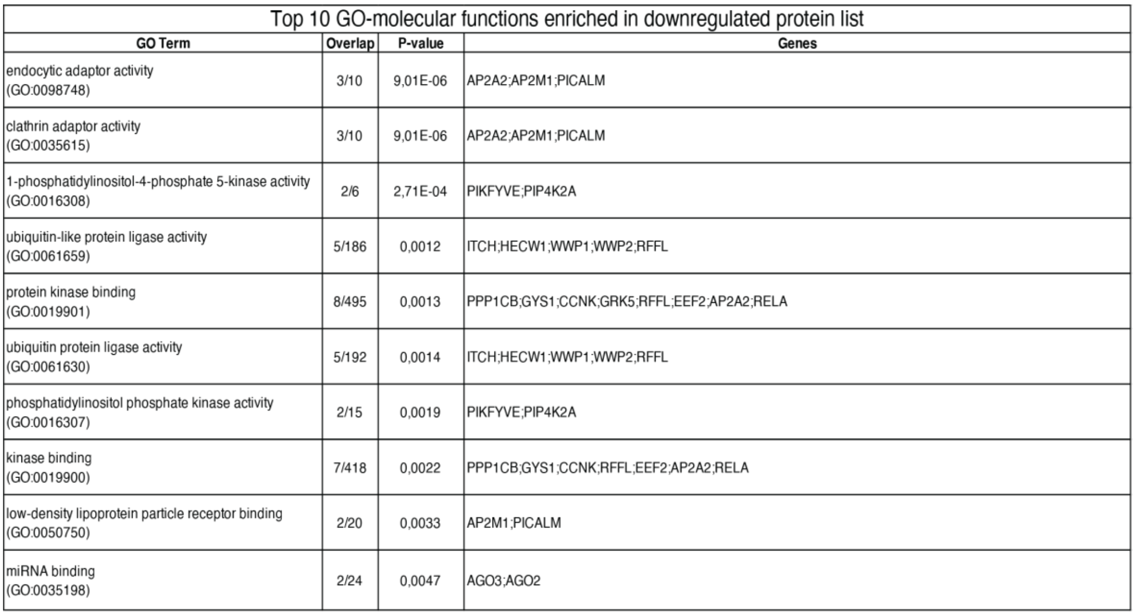

Top 10 GO-molecular functions enriched in downregulated protein list

GO Term	Overlap	P-value	Genes
endocytic adaptor activity (GO:0098748)	3/10	9,01E-06	AP2A2;AP2M1;PICALM
clathrin adaptor activity (GO:0035615)	3/10	9,01E-06	AP2A2;AP2M1;PICALM
1-phosphatidylinositol-4-phosphate 5-kinase activity (GO:0016308)	2/6	2,71E-04	PIKFYVE;PIP4K2A
ubiquitin-like protein ligase activity (GO:0061659)	5/186	0,0012	ITCH;HECW1;WWP1;WWP2;RFFL
protein kinase binding (GO:0019901)	8/495	0,0013	PPP1CB;GYS1;CCNK;GRK5;RFFL;EEF2;AP2A2;RELA
ubiquitin protein ligase activity (GO:0061630)	5/192	0,0014	ITCH;HECW1;WWP1;WWP2;RFFL
phosphatidylinositol phosphate kinase activity (GO:0016307)	2/15	0,0019	PIKFYVE;PIP4K2A
kinase binding (GO:0019900)	7/418	0,0022	PPP1CB;GYS1;CCNK;RFFL;EEF2;AP2A2;RELA
low-density lipoprotein particle receptor binding (GO:0050750)	2/20	0,0033	AP2M1;PICALM
miRNA binding (GO:0035198)	2/24	0,0047	AGO3;AGO2

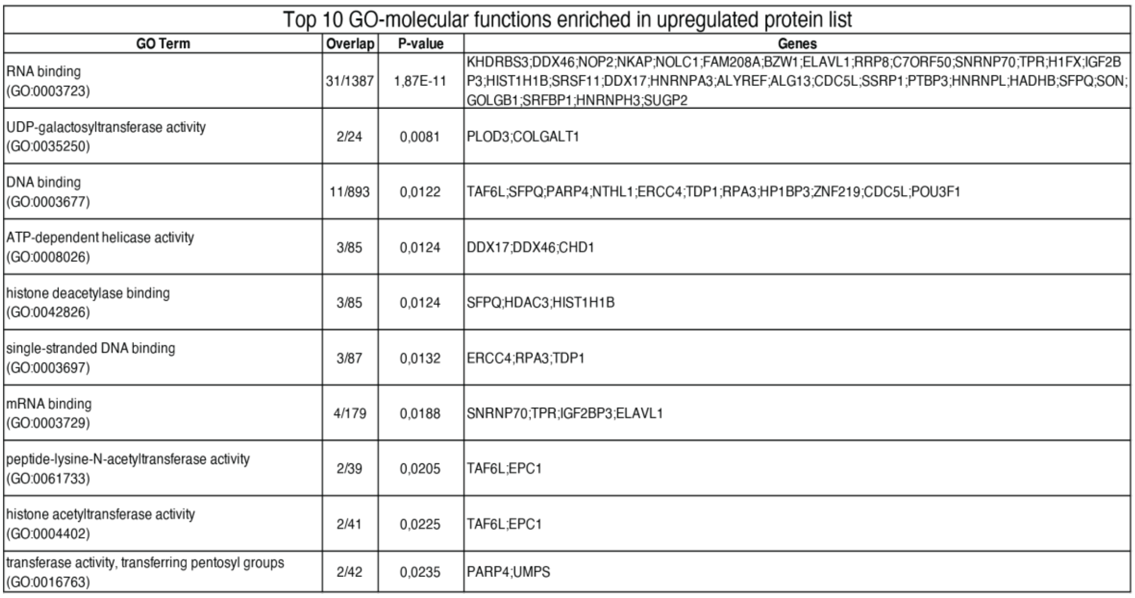

Top 10 GO-molecular functions enriched in upregulated protein list

GO Term	Overlap	P-value	Genes
RNA binding (GO:0003723)	31/1387	1,87E-11	KHDRBS3;DDX46;NOP2;NKAP;NOLC1;FAM208A;BZW1;ELAVL1;RRP8;C7ORF50;SNRNP70;TPR;H1FX;IGF2BP3;HIST1H1B;SRSF11;DDX17;HNRNPA3;ALYREF;ALG13;CDC5L;SSRP1;PTBP3;HNRNPL;HADHB;SFPQ;SON;GOLGB1;SRFBP1;HNRNPH3;SUGP2
UDP-galactosyltransferase activity (GO:0035250)	2/24	0,0081	PLOD3;COLGALT1
DNA binding (GO:0003677)	11/893	0,0122	TAF6L;SFPQ;PARP4;NTHL1;ERCC4;TDP1;RPA3;HP1BP3;ZNF219;CDC5L;POU3F1
ATP-dependent helicase activity (GO:0008026)	3/85	0,0124	DDX17;DDX46;CHD1
histone deacetylase binding (GO:0042826)	3/85	0,0124	SFPQ;HDAC3;HIST1H1B
single-stranded DNA binding (GO:0003697)	3/87	0,0132	ERCC4;RPA3;TDP1
mRNA binding (GO:0003729)	4/179	0,0188	SNRNP70;TPR;IGF2BP3;ELAVL1
peptide-lysine-N-acetyltransferase activity (GO:0061733)	2/39	0,0205	TAF6L;EPC1
histone acetyltransferase activity (GO:0004402)	2/41	0,0225	TAF6L;EPC1
transferase activity, transferring pentosyl groups (GO:0016763)	2/42	0,0235	PARP4;UMPS

Table 2 TOP 10 Gene Ontology-molecular function categories enriched in downregulated and upregulated proteins in HECW1-KD neurons

This result points again to a possible role of HECW1 in regulating RNA metabolism, vesicle trafficking and autophagy.

4.3 The role of HECW1 in neuronal autophagy and the endo-lysosomal pathway

Prompted by the proteomics data and the phenotype observed upon HECW1-depletion in the A549 cells (Appendix 1) and in the *Drosophila* model (see Introduction), we decided to study the effects of HECW1-depletion on autophagy and the endo-lysosomal system in the iPSC-derived neuronal model.

4.3.1 HECW1-depletion impacts on the LAMP1-compartment

By image analysis, we monitored the accumulation of autophagic structures using specific markers, such as LAMP1 for autophagic and endo-lysosomal organelles, and LC3 for autophagosomes and amphisomes, in basal condition or upon treatments to induce or block the autophagic flux.

First, we generated control and HECW1-KD neurons, and analyzed them after 10 days of differentiation. We examined the abundance and size of lysosomes immunostaining the neurons with the lysosomal marker LAMP1. As a positive control for LAMP1-vesicle enlargement, neurons were treated with chloroquine (CQ), a chemical compound that mainly inhibits autophagy by impairing autophagosome fusion with lysosomes (Mauthe et al., 2018).

As expected, CQ treatment in control neurons resulted in an increase in the size of LAMP1 structures compared to untreated cells, which were characterized by smaller structures (**Fig. 28A**). Interestingly, HECW1-depletion resulted in a similar LAMP1 enlargement. HECW1-KD neurons, indeed, presented large round LAMP1-compartements already in basal condition, resembling the ones observed in control neurons treated with CQ (**Fig. 28A**).

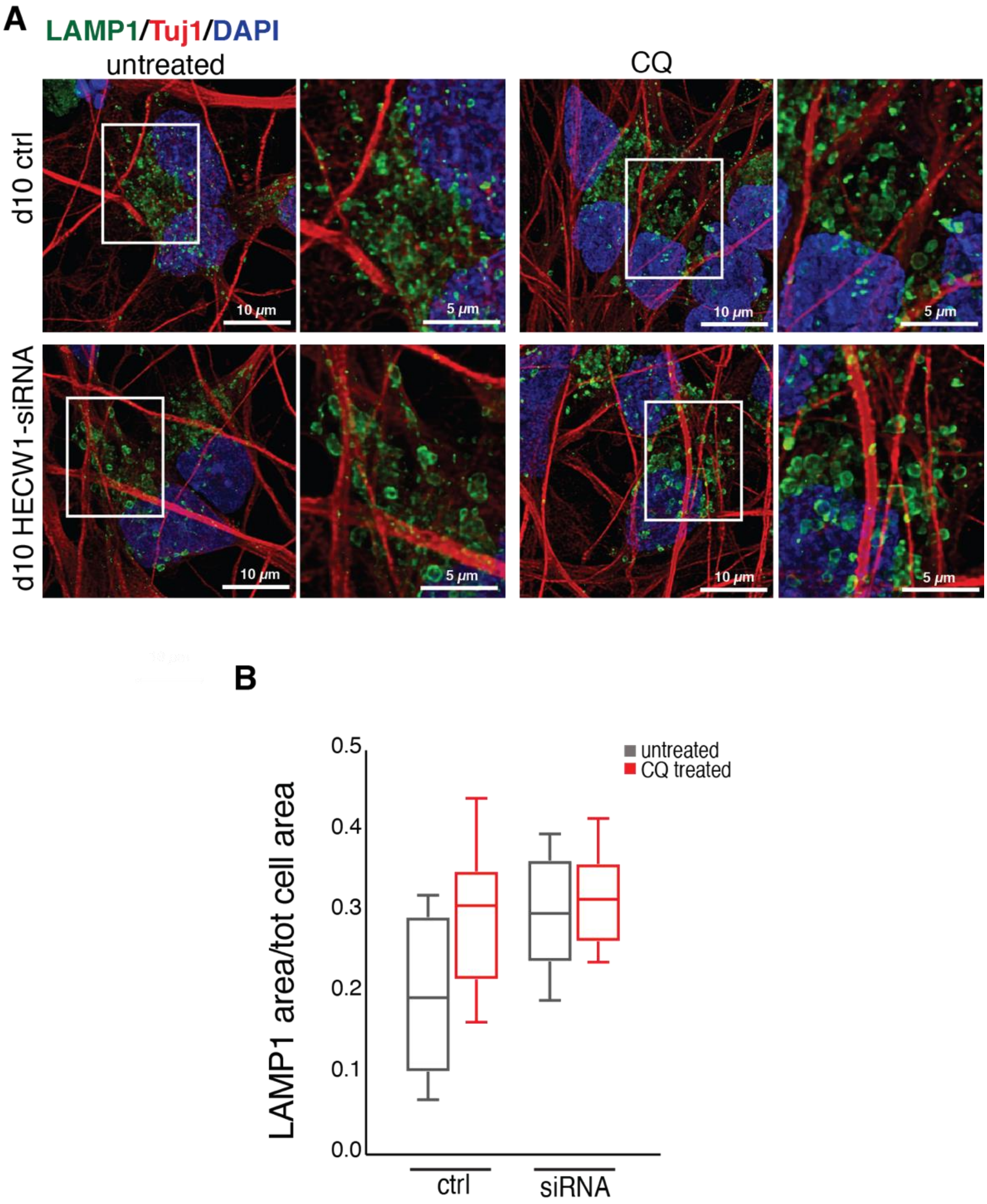

Figure 28 HECW1-KD neurons exhibit enlarged LAMP1-compartments

A) IF analysis of control (ctrl) and HECW1-KD neurons after 10 days of differentiation, untreated or treated with 100uM of chloroquine (CQ) for 2 hours, showing large LAMP1-positive accumulations in treated control, untreated HECW1-KD and treated HECW1-KD-treated neurons, compared to untreated control neurons. Tuj1 is stained in red, LAMP1 in green and the nuclei in blue (DAPI). Scale bar: 10 µm. Zoomed images of the insets (white box) are shown on the right side of each image.

B) Quantification of LAMP1 area normalized to the total area of the cells in control (ctrl) and HECW1-KD neurons on day 10 of differentiation, untreated or treated with 100uM of chloroquine for 2 hours.

The enlarged LAMP1-compartments we observed in HECW1-KD neurons were negative for the early endosome antigen 1, EEA1, and no accumulation of EEA1-positive/LAMP1-negative structures were observed (**Fig. 29**). These observations suggest that HECW1-KD impacts on the late endosome/lysosome without disturbing the early endosome.

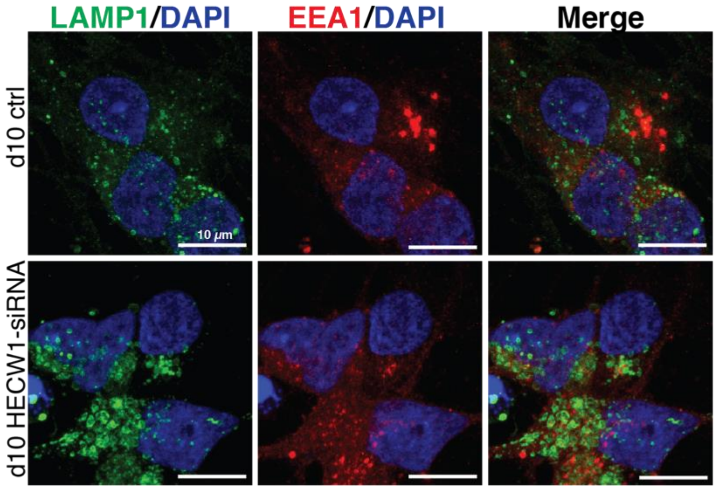

Figure 29 HECW1-KD neurons do not present EEA1 aggregates

IF analysis of control (ctrl) and HECW1-KD neurons after 10 days of differentiation, for LAMP1 and the early endosome marker EEA1. LAMP1 is stained in green, EEA1 in green and the nuclei in blue (DAPI). Scale bar: 10 µm.

To quantify the observed LAMP1-enlargment, we measured the ratio between the area of the cell covered by LAMP1 and the total area, in both untreated and CQ treated neurons. In the untreated condition (**Fig. 28B**, grey bars), we measured an increase upon HECW1-KD, which notably corresponds with the one observed upon CQ treatment in control neurons (**Fig. 28B**). The limited number of images acquired for this particular experiment did not allow statistical testing of the phenotype.

To better confirm the effect of HECW1-depletion on LAMP1-compartments, we repeated the staining and quantification, working with a larger sample size and comparing control neurons with both HECW1-KD and KO neurons. To this aim, control and HECW1-KO-iPSCs were differentiated into neurons, in parallel with control cells transfected with HECW1-siRNA. After 10 days of differentiation, untreated and CQ treated neurons were processed for LAMP1 and Tuj1 staining.

In line with what we observed in the previous experiment, IF images showed an increased LAMP1-intensity in both HECW1-KD and KO neurons compared to control neurons (**Fig. 30A**). We quantified the phenotype by measuring the mean intensity of LAMP1 signal per cell. In the absence of CQ (**Fig. 30B**, grey bar), HECW1-depletion (both KD and KO) led to a statistically significant increase in LAMP1 measurement compared to control (p-value <0,0001), similar to that of CQ-treated control neurons (**Fig. 30B**). This quantitative analysis strongly indicates that HECW1-depletion alone leads to LAMP1-vesicle enlargement/accumulation in iPSC-derived neurons.

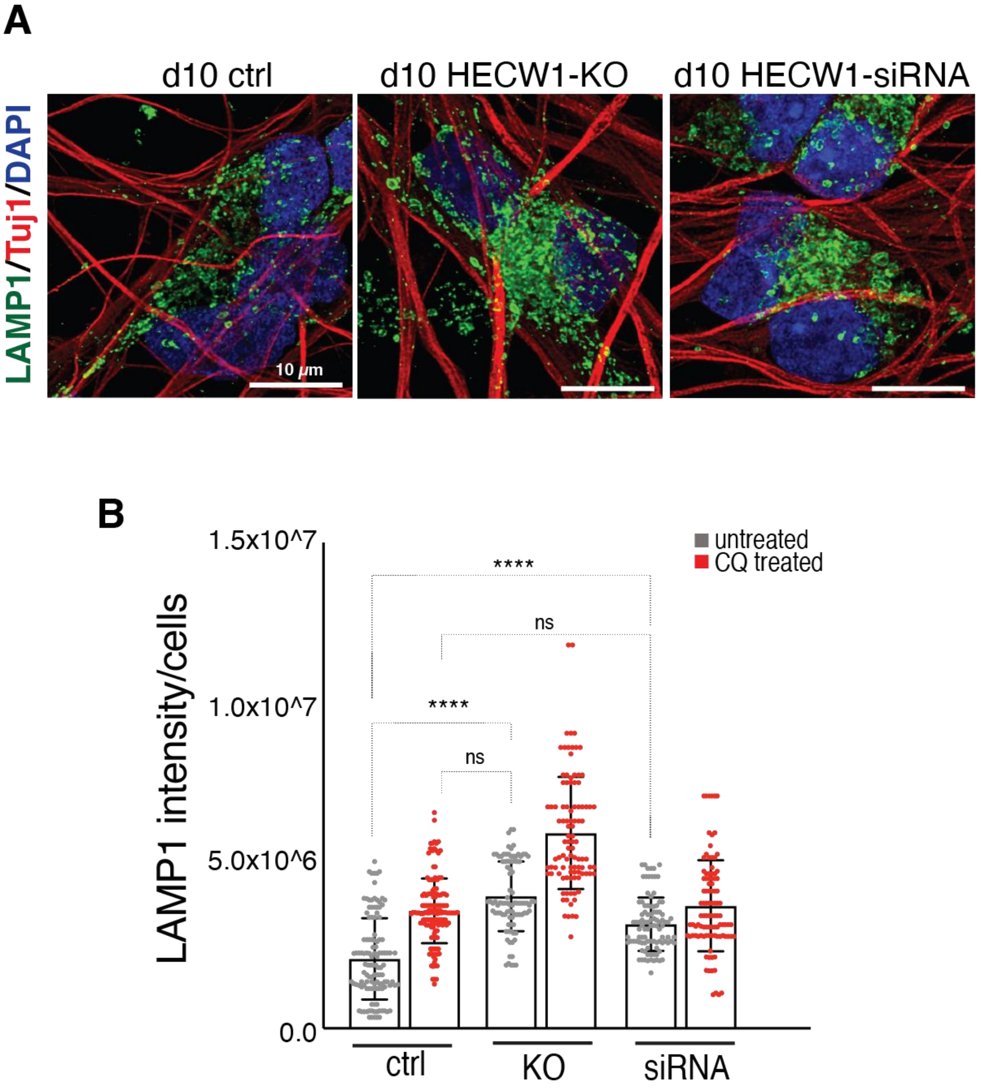

<u>Figure 30 HECW1-depletion leads to LAMP1-enralgerment in neurons</u>

A) IF analysis of control (ctrl), HECW1-KO and HEWC1-KD neurons after 10 days of differentiation, showing large LAMP1-positive accumulations in KO and KD neurons compared to control neurons. Tuj1 is stained in red, LAMP1 in green and the nuclei in blue (DAPI). Scale bar: 10 μm.

*B) Quantification of LAMP1 intensity per cells in control (ctrl), HECW1-KO and HECW1-KD neurons on day 10 of differentiation, untreated or treated with 100uM of chloroquine for 2 hours. CQ: chloroquine; ns: not statistically significant; ****: p-value <0,0001 (counted >100 cells per sample)*

Next, we investigated LAMP1-enlargment in more mature neurons. To this end, we differentiated control and HECW1-KO iPSCs for 30 days and treated them with a combination of the autophagy modulators rapamycin and bafilomycin A1. Rapamycin stimulates autophagy by inducing autophagosomes formation; bafilomycin A1, on the contrary, acts as an autophagy inhibitor by impairing lysosome acidification and fusion with autophagosome. As expected, induction and concomitant inhibition of autophagy in control neurons resulted in a striking increase in the number and size of LAMP1 structures compared to untreated control cells, which were characterized by smaller structures (**Fig. 31**, left panels), similar to early control neurons (**Fig. 28A**). In sheer contrast, untreated HECW1-KO neurons presented accumulation of enlarged LAMP1 structures already in basal conditions (**Fig. 31**, top right panel), bigger than the LAMP1 structures observed in untreated control neurons, however, comparable with treated-neurons.

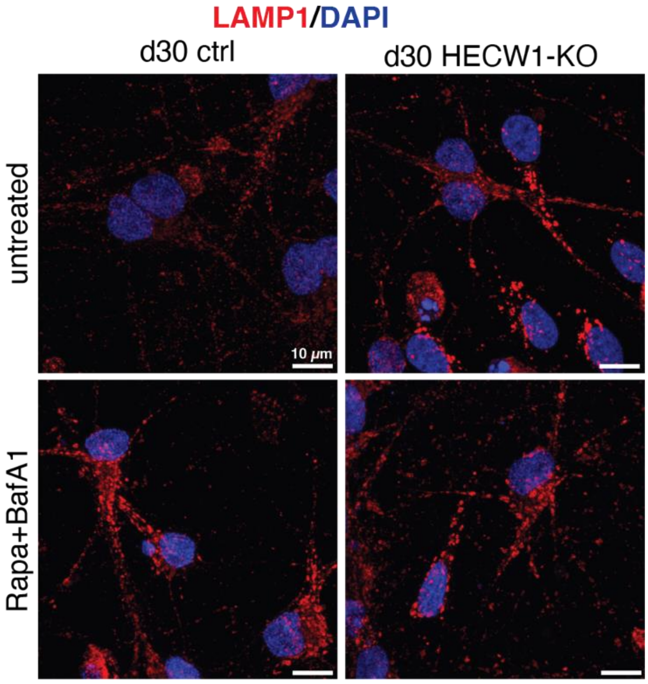

Figure 31 HECW1-KO mature neurons exhibit LAMP1 enlargements

IF analysis of control (ctrl) and HECW1-KO after 30 days of differentiation, untreated or treated with 5 uM rapamycin (Rapa) and 100 nM bafilomycin A1 (BafA1) for 2 hours, showing large LAMP1-positive accumulations in treated control (ctrl), untreated and treated KO neurons, compared to untreated control (ctrl). LAMP1 is stained in red and the nuclei in blue (DAPI). Scale bar: 10 µm.

To gain additional insight into the impact of HECW1-depletion on autophagy and the endo-lysosomal system, to characterize the nature of the accumulated vesicles and to identify eventual accumulation of ubiquitinated-autophagic cargo, we performed immunostaining analysis with the autophagosome/amphisome marker LC3. LC3 is the selective autophagy receptor for recruitment of ubiquitinated proteins into autophagosome P62, and ubiquitin. From LAMP1-LC3 co-immunostaining, we found that the enlarged LAMP1-compartments observed in HECW1-KO neurons on day 30 of differentiation were negative for LC3 and LC3-positive/LAMP1-negative structures were absent (**Fig. 32A**). Similar results were observed in HECW1-KD neurons on day 10 of differentiation (data not shown).

Next, we performed co-immunostaining of control and HECW1-KO neurons on day 30 of differentiation for P62 and ubiquitin. HECW1-depletion did not lead to accumulation of P62 and we did not observe any re-localization of ubiquitin from a diffuse cytoplasmic staining to puncta (**Fig. 32B**).

These observations indicate that the structures accumulated in HECW1-depleted neurons are more likely late endosomes or lysosomes, rather than amphisomes or autolysosomes formed by the fusion of autophagosomes with late endosomes or lysosomes, respectively, and that HECW1-depletion does not have a major impact on P62-ubiquitin-dependent autophagy.

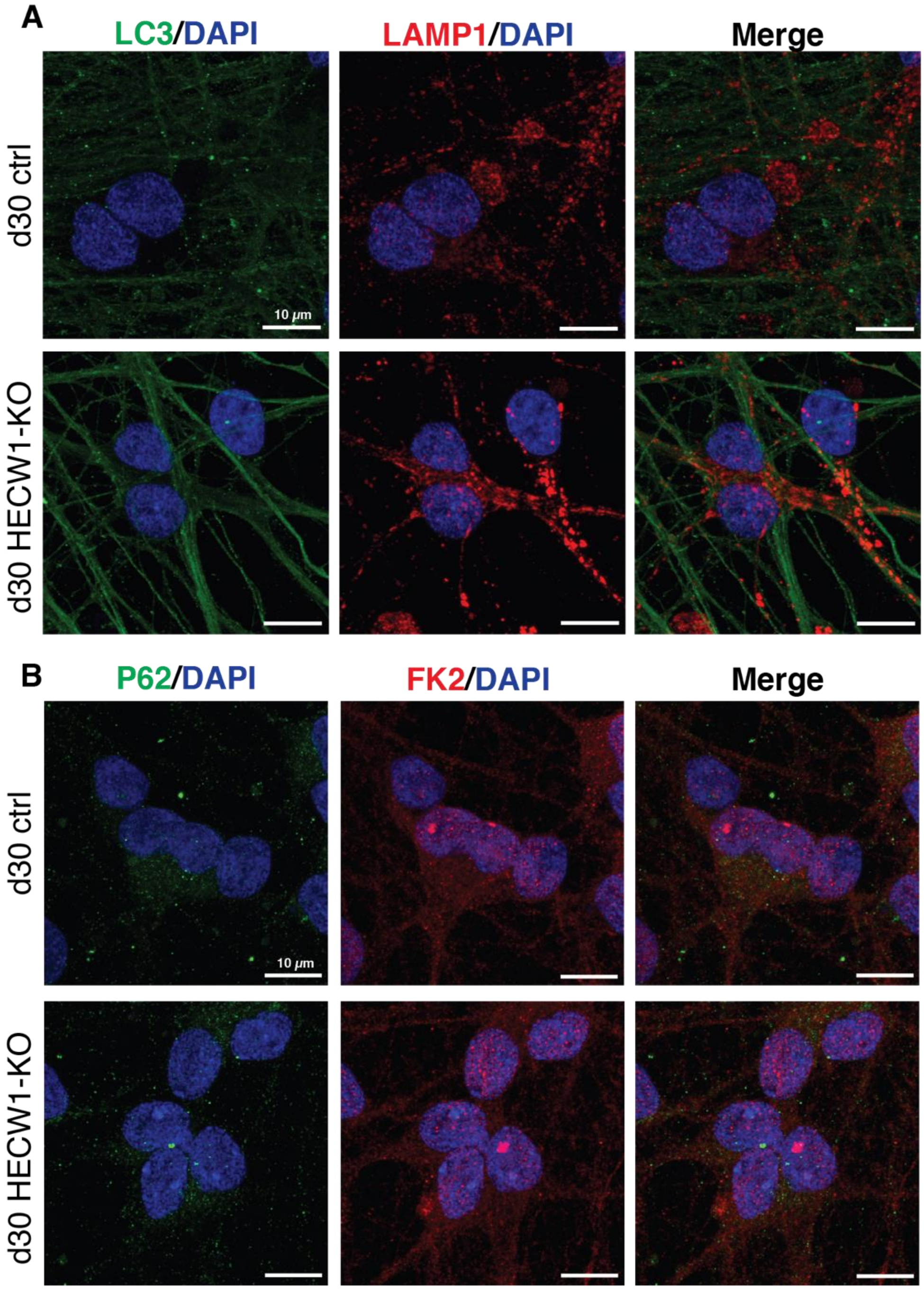

Figure 32 HECW1-KO neurons do not present LC3, P62 or ubiquitin aggregates

A) IF analysis of control (ctrl) and HECW1-KO neurons, after 30 days of differentiation, for LAMP1 and the autophagosome marker LC3. LAMP1 is stained in red, LC3 in green and the nuclei in blue (DAPI). Scale bar: 10 µm.

B) IF analysis of control (ctrl) and HECW1-KO neurons, after 30 days of differentiation, for the autophagy receptor P62 and the ubiquitin-antibody FK2. P62 is stained in green, FK2 (Ubiquitin) in red and the nuclei in blue (DAPI). Scale bar: 10 µm.

4.3.2 Late endosome/lysosome trafficking in neurons is not altered in the absence of HECW1

Since we observed an accumulation of late endosomes/lysosomes in the neuronal soma, we wondered whether late endosome/lysosome dynamics and trafficking of these organelles along neurites was affected in HECW1-deplated neurons. We, therefore, took advantage of the fluorescent probe LysoTracker Red. Due to its fluorophore conjugation to a weak base, LysoTracker specifically accumulates into spheric low PH organelles, and is thus a selective marker for late endosomes and lysosomes.

We differentiated control and HECW1-KO neurons for 30 days, incubated them with LysoTracker and performed live cell imaging and tracing of LysoTracker-labeled vesicles. In both control and HECW1-KO neurons, LysoTracker-positive puncta were highly concentrated in the soma and distributed in single distinct particles along filaments. No major differences in Lysotracker-puncta density were present between control and HECW1-KO neurons, and vesicle accumulation was not observed (**Fig. 33A**).

While somatic puncta were mainly static, LysoTracker particles were highly motile along filaments and we, therefore, measured their motility by assessing the fraction of motile/static particles and their average speed in control and HECW1-KO neurons. The fraction of motile/static particles remained about the same upon HECW1-depletion, with around 70% and 65% of static particles and 30% and 35% of motile particles in control and HECW1-KO neurons, respectively (**Fig. 33B**). Also, average particle speed was comparable between the two samples (**Fig. 33C**). As a control for LysoTracker specific staining of acidic organelles, we treated neurons with the lysosomal acidification inhibitor bafilomycin A1. As expected, LysoTracker staining was almost completely abolished in both control and HECW1-KO neurons, in which only a few static puncta were detected (data not shown). This analysis suggests that HECW1-depletion does not have an impact on lysosome/late endosome trafficking and does not have a major effect on the acidity of the lysosomes.

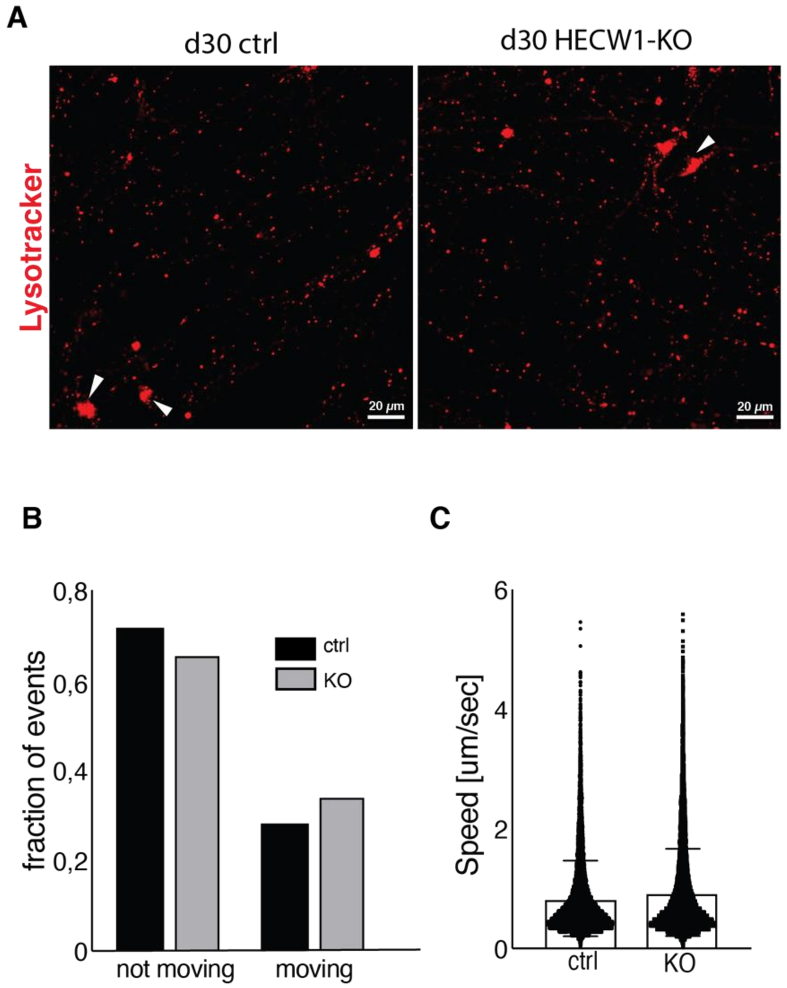

Figure 33 LysoTracker staining and quantification in HECW1-KO neurons

A) Live IF images of control (ctrl) and HECW1-KO neurons on day 30 of differentiation, stained with 75nM of LysoTracker Red DND-99 for 30 minutes before acquisition. White arrowheads indicate neuronal soma. B-C) Measurement of LysoTracker-particle dynamics in control (ctrl) and HECW1-KD neurons: percentage of moving particles (B); average speed (C).

4.3.3 HECW1-depletion leads to neuritic accumulation of aberrant endocytic and autophagic vacuoles

To further characterize the impact of HECW1-deplation on the autophagy/endo-lysosome pathway, we decided to extend our analysis using electron microscopy (EM) to better observe the structure of endocytic and autophagic vacuoles. This technique, indeed, preserves the native membrane ultrastructure and allows the identification of different organelles according to their morphology.

In collaboration with the electron microscopy facility at IFOM, we first analyzed control and HECW1-KD neurons, differentiated for 10 days and then processed for EM analysis. We found that, in the region of the soma, control neurons showed the recurrent presence of small electron-dense spherical organelles, enclosed by a single membrane and with a diameter of about 0.5μm (**Fig. 34A**, top panels). This morphology is typical of endo-lysosome/lysosome structures that in neurons are mainly localized in the somatic compartment.

Interestingly, these structures were less detectable in HECW1-KD neurons, which, instead, were enriched in larger electron-lucent vacuoles (about 1.0 μm in diameter) containing intralumenal membranes and other amorphous material, consistent with an autophagic component (**Fig. 34A**, bottom middle and right panels). We also detected mainly empty vacuoles with only one or a few small vesicles inside, resembling multivesicular bodies (MVB), endosomes containing intraluminal small vesicles that increase in number with gradual maturation of early into late endosome (**Fig. 34A**, bottom left panel). These electron-lucent organelles were reminiscent of the ones observed in A549-HECW1-KO cells (**Fig. 47B**, Appendix).

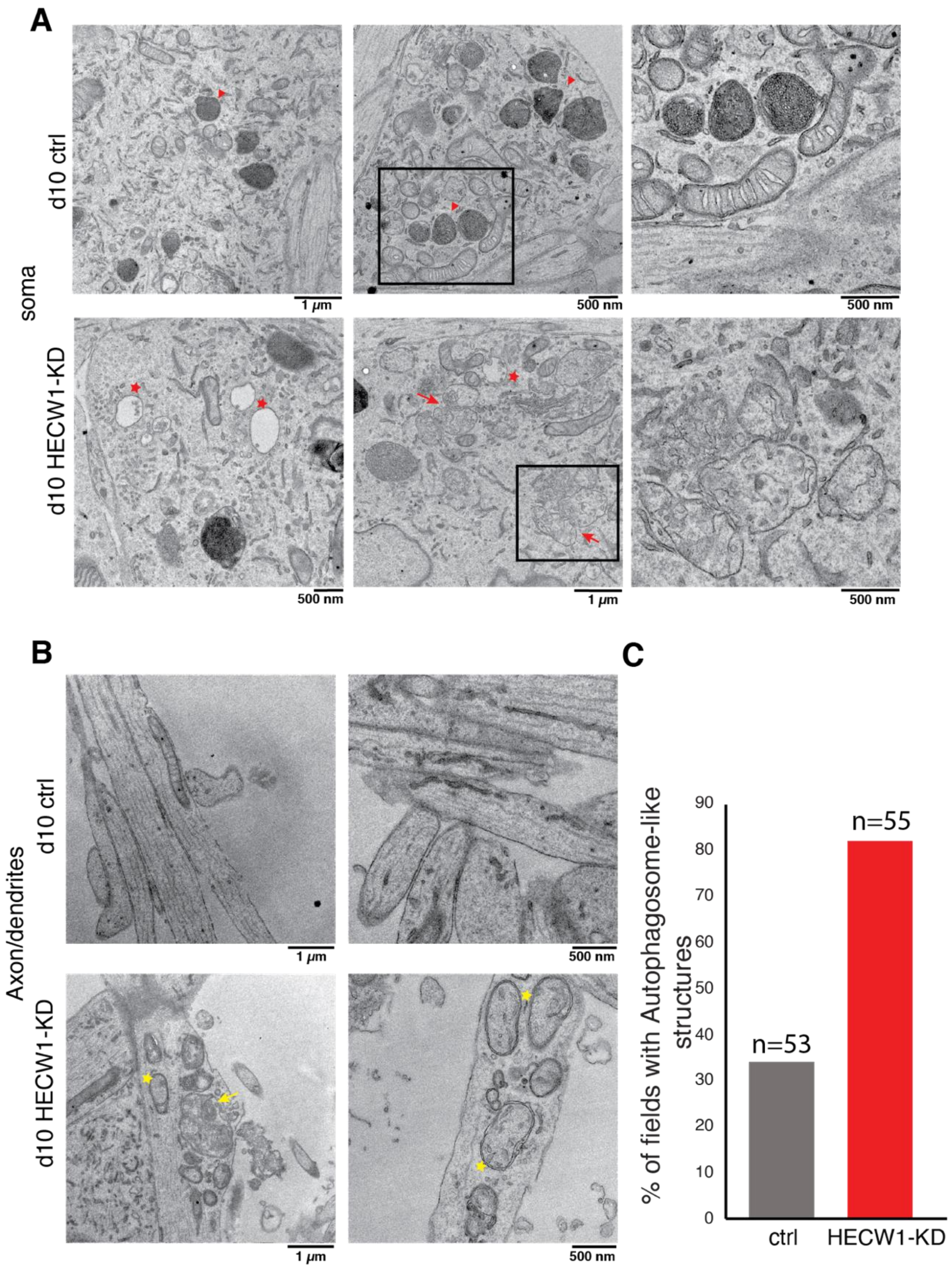

Figure 34 HECW1-KD leads to an aberrant accumulation of autophagosome-like structures in neuronal processes

Control and HECW1-KD neurons after 10 days of differentiation were fixed with 4% PFA/Glutaraldehyde buffer and processed for EM acquisition.

A) EM showing, in the soma of HECW1-KD neurons, loss of electrodense organelle, endo-lysosome/lysosome (red arrowhead), and enrichment in electron-lucent compartments with amorphous and membranous inclusions (red arrows) or MVB-like (red stars) structures. Zoomed images of the insets (black box) are shown on the right side of each image. Representative images of 35–40 electron micrographs are shown. Scale bar as indicated.

B) EM showing aberrant accumulation of double-membrane autophagosome-like structures along neurites of HECW1-KD neurons. Yellow arrows indicate multilamellar membranes; yellow stars indicate vacuoles containing heterogeneous contents. Representative images of 50–55 electron micrographs are shown. Scale bar as indicated.

C) Percentage of fields positive for autophagosome-like structures in control (ctrl) and HECW1-KD neurons. n: number of fields counted.

Disturbances within endocytic and autophagic vacuoles were even more evident along axons and dendrites (collectively called neurites). Accumulation of double-membrane autophagosome-like structures were frequently detected in HECW1-KD neuronal neurites, while barely detectable in control neurons (**Fig. 34B**). Many of these vacuoles contained heterogeneous content (**Fig. 34B**, bottom right panel), while other contained multiple, ruffled double membranes, thus presenting a multilamellar (onion skin-like) structure (**Fig. 34B**, bottom left panel). Quantitative analysis, assessing the percentage of positive fields for these structures, showed a clear higher frequency of autophagosome-like structures accumulation in the filaments of HECW1-KD neurons compared to control neurons (**Fig. 34C**).

To investigate this phenotype in more mature neurons, we generated neurons from control and HECW1-KO iPSC lines and performed EM analysis after 30 days of differentiation. The three representative images reported in **Fig. 35A** show a clear accumulation of aberrant structures in the neurites and distal tips of HECW1-KO neurons, barely detectable in control neurons (**Fig. 35A**). This phenotype was even stronger than the one observed in HECW1-KD early neurons (10 days of differentiation).

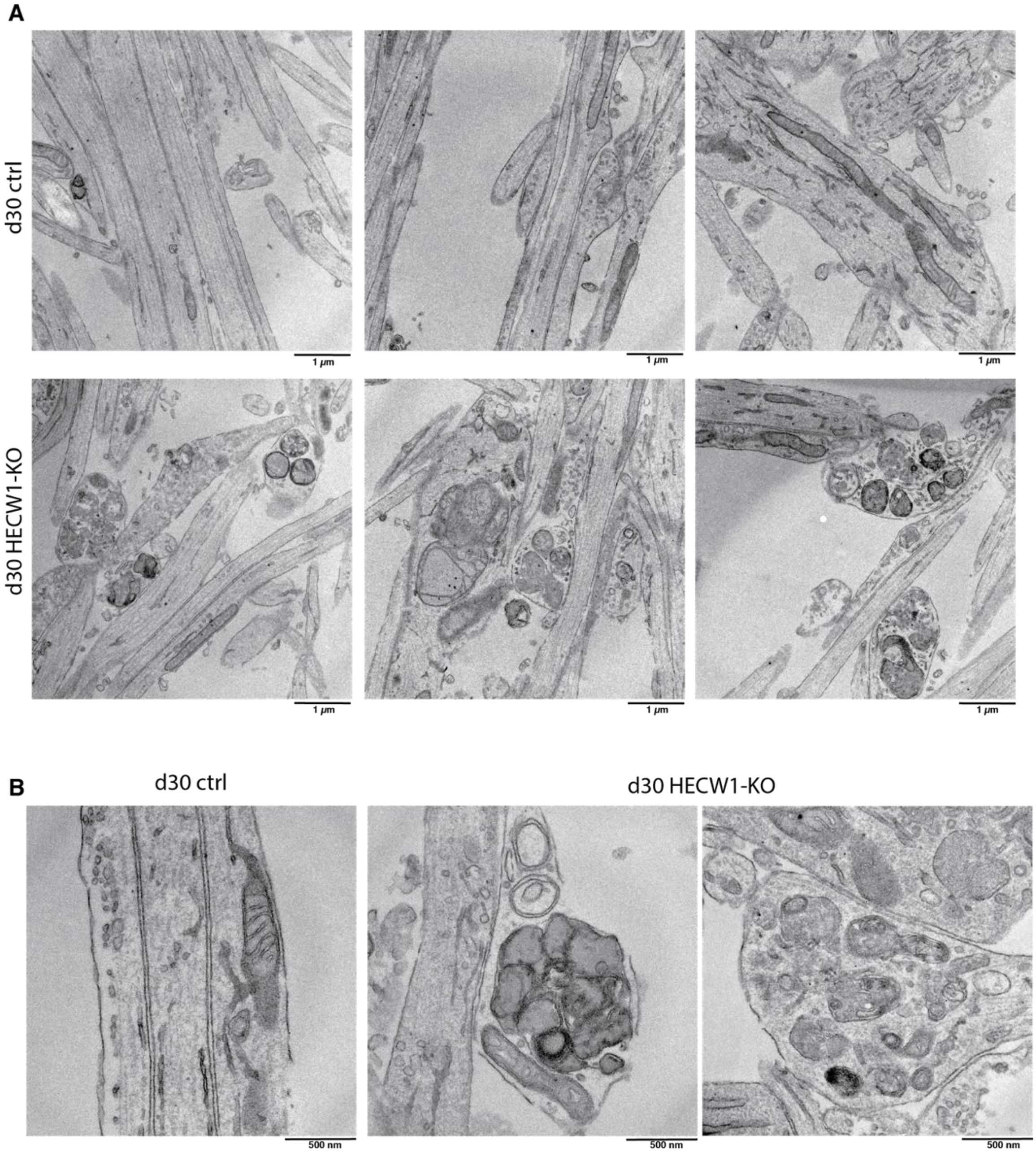

Figure 35 HECW1-KO leads to an aberrant accumulation of autophagosome-like structures in neuronal processes

A) Control (Ctrl) and HECW1-KO neurons after 30 days of differentiation were fixed with 4% PFA/Glutaraldehyde buffer and processed for EM acquisition. EM showing aberrant accumulation of double-membrane autophagic vacuoles along neurites of HECW1-KO neurons.

B) Higher magnification of images as in A.

Representative images of 35–50 electron micrographs are shown. Scale bar as indicated.

As observed in HECW1-KD neurons (**Fig. 34B**), a closer examination of the accumulated vacuoles revealed different morphological features (**Fig. 35A-B**): some vacuoles appeared largely devoid of internal structures with only few small internal vesicles, while others contained intralumenal membranes and electron-dense material and presented a multilamellar structure, consistent with aberrant autophagy/endo-lysosome pathway-related components.

Taken together, these data strongly indicate that the absence of HECW1 leads to an accumulation of autophagic/endolysosomal-related structures along neuronal filaments, maybe affecting vacuole formation/maturation. Interestingly, the defect becomes more evident with the age of the neurons.

4.3.4 HECW1-depletion leads to wheat germ agglutinin aggregate formation in neurons

To better characterize the nature of the accumulated structures detected in HECW1-depleted neurons and test whether they derive from the endosomal system, we decided to perform a wheat germ agglutinin (WGA)-immunostaining. WGA is a lectin that specifically binds cell surface glycoproteins and enters cells by adsorptive endocytosis. These properties have made the WGA an established marker for the endocytic trafficking pathway and for vesicles with endocytic origins, such as late endosomes.

To detect and follow WGA-positive structures in the soma and along filaments, we differentiated control and HECW1-KO iPSCs for 30 days and added WGA in the medium for 30 minutes before live IF analysis.

Endocytosis of WGA occurred without evident defects or obvious changes in the intensity or number/size of WGA puncta in the cell body of HECW1-KO neurons compared to control neurons. Both control and HECW1-KO soma presented mainly static small WGA dots (**Fig. 36A**). Even if less frequent, similar dots were also distinctively detectable along filaments of both lines (**Fig. 36B**). Interestingly, we observed an accumulation of large WGA aggregates in HECW1-KO filaments, indicating an increase in the size of endosomal compartments in neuronal protrusions (**Fig. 36B**), consistent with the accumulation of endo-lysosome pathway-related structures detected upon HECW1-depletion (**Fig. 34-35**).

The WGA staining was performed in combination with the fluorescent probe LysoTracker red to mark acidic organelles. Both the small WGA puncta and the large WGA aggregates were LysoTracker-negative, indicating a low acidic property of these structures (**Fig. 36B**).

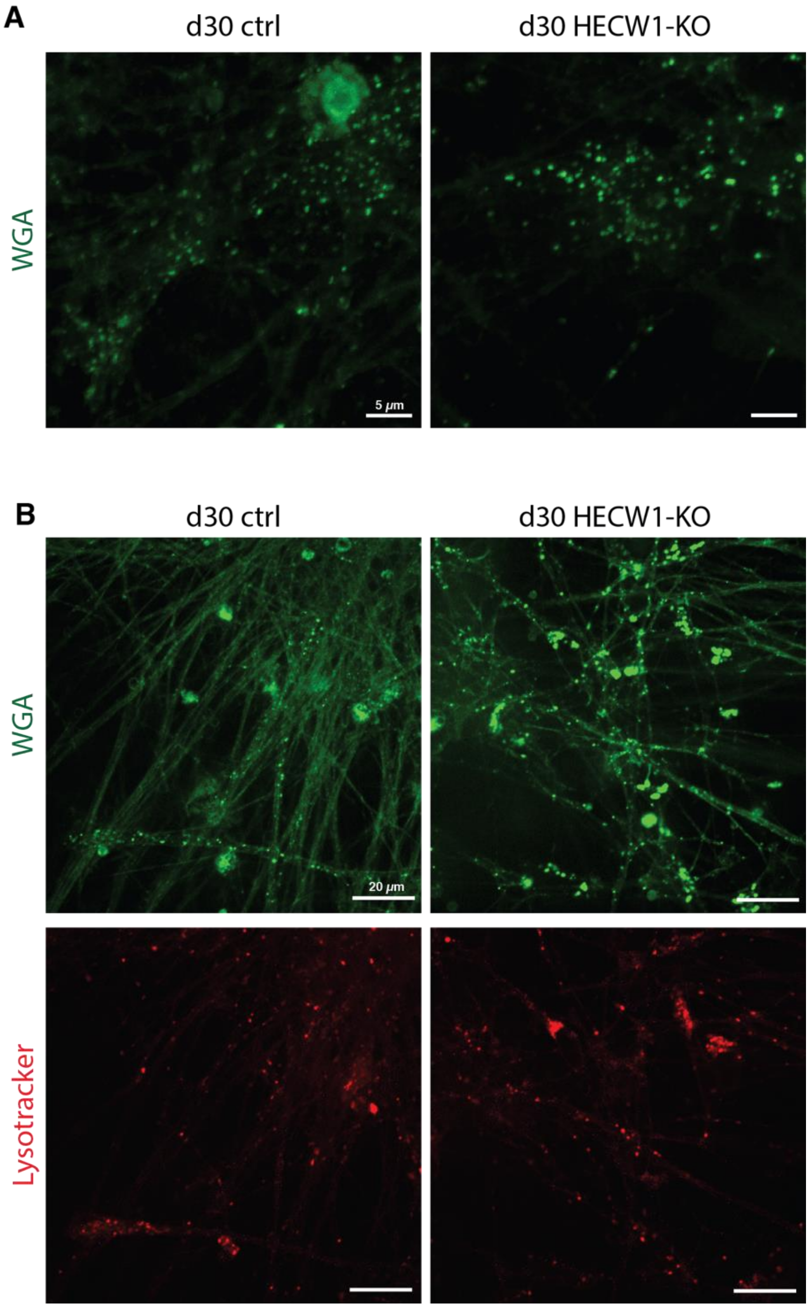

<u>Figure 36 HECW1-depletion leads to an aberrant accumulation of WGA-positive large structures in neuronal processes</u>

Control and HECW1-KO neurons on day 30 of differentiation were supplemented with a combination of 10 mg/ml WGA-green and 75nM of LysoTracker Red DND-99 for 30 minutes before live cell images.

A) Representative images showing WGA dots in the soma of control (ctrl) and HECW1-KO neurons. WGA is stained in green. Scale bar: 5 µm.

B) Representative images showing accumulation of WGA-positive (top right panel) Lysotracker-negative (bottom right panel) aggregates in HECW1-KO neurons. WGA is stained in green, Lysotracker in red. Scale bar: 20 µm.

4.3.5 Neuronal compartmentalized culturing system

The traditional neuronal culture approaches that we used resulted in random outgrowth of axons and dendrites. With the aim to characterize organelle-trafficking and organelles in specific regions of neurons, we implemented a compartmentalized culturing system that physically separates axons from soma and dendrites (**Fig. 37**). This basic 2-compartment configuration consists of two parallel microfluidic channels separated by a series of smaller perpendicular microgrooves (**Fig. 37A**). Primary or stem cell-derived neurons are plated in one of the microfluidic channels, and are allowed to settle and attach to the bottom surface of the device, then, neurites are extended over the course of differentiation. Many protrusions find their way into the microgrooves, which are small enough to prevent soma from entering. Physically restricted and unable to turn around, neuronal protrusions grow straight into the adjacent compartment (axonal compartment) where they are isolated (**Fig. 37A**).

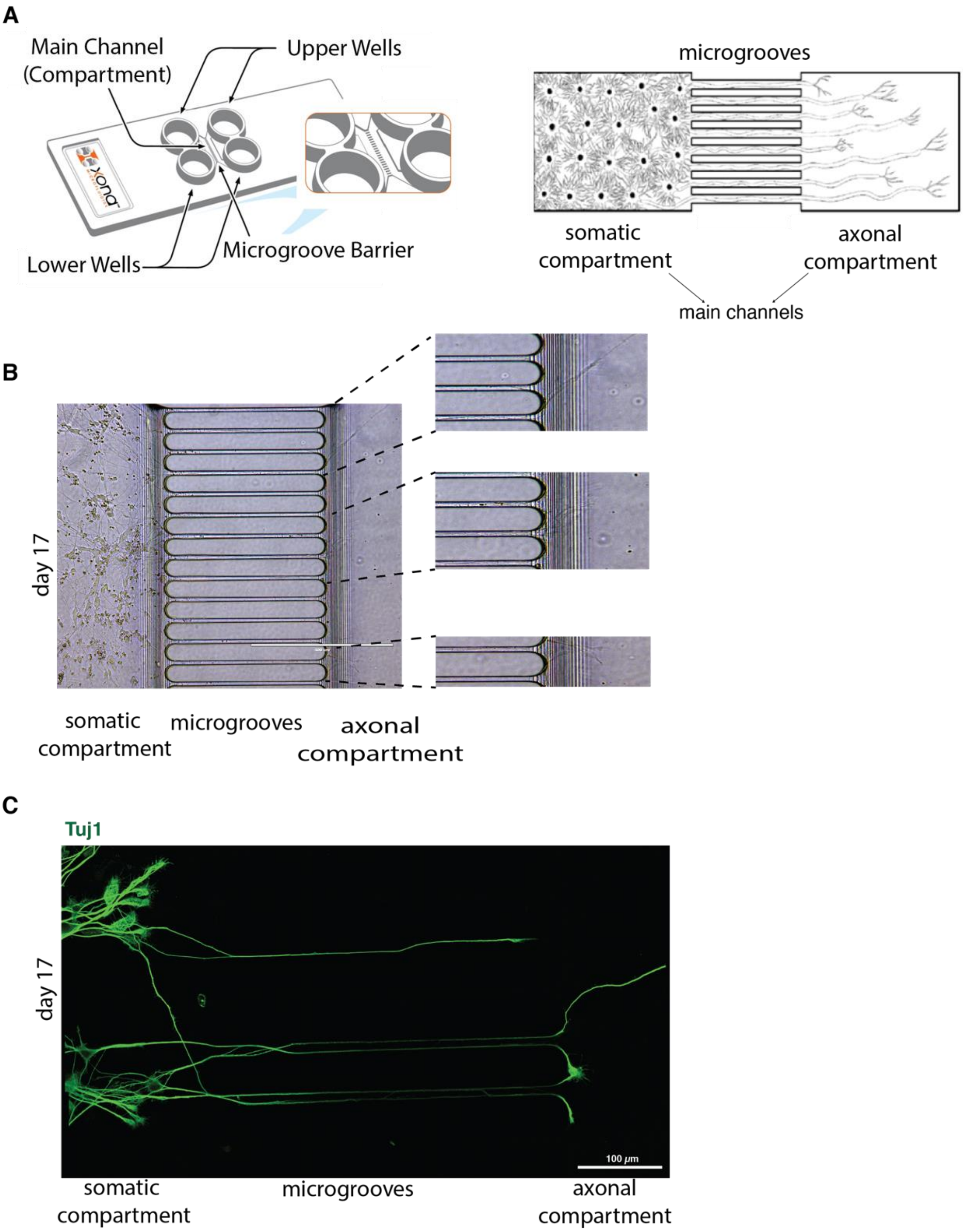

Figure 37 Neuronal compartmentalized culturing system

A) A schematic representation of the XONACHIP microfluidic device for compartmentalized neuronal culture.

B) Phase-contrast images of control (ctrl) neurons differentiated for 17 days in the microfluidic devise, showing neuronal soma and protrusion in the somatic region and axonal growth throughout the microgrooves and in the axonal compartment. Scale bar: 400 μm. Zoomed images are shown on the right side.

C) IF analysis of control (ctrl) neurons after 17 days of differentiation in the microfluidic device with the neuronal marker Tuj1, stained in green. Scale bar: 100 μm.

To assess the feasibility of this device with the NGN2-protocol, on day 3 of differentiation (the day of replating, **Fig. 19A**) we seeded pre-neurons on the two left-wells to allow them to differentiate and mature in the main channel, extending their axons along the microgrooves and reaching the other side of the device. As with the traditional approach, the cells changed to an elongated morphology within 24 hours and neurites could be identified in the somatic compartments already 1-2 days after plating. Over the course of 5 days of maturation, axonal growth was detectable in the microgrooves. On day 17 of differentiation, we clearly observed protrusions in the axonal side of the device (**Fig. 37B**). We then fixed and immunostained the cells in the device for Tuj1 to mark entire neurons from the somatic to the axonal compartments (**Fig. 37C**).

4.3.6 HECW1-depletion leads to wheat germ agglutinin aggregates formation in axonal tips

To observe WGA-structures in specific neurons and track their transport along axons, we repeated the WGA live image analysis in neurons differentiated in the compartmentalized culturing device (**Fig. 38A**). To this aim, we plated control or HECW1-KO pre-neurons (day 3 of differentiation) in the two left wells of the microfluidic device and allowed the neurons to differentiate and extend their protrusions throughout the grooves. After three weeks of differentiation, a similar amount of axonal protrusion was detectable in the right compartment of both control and HECW1-KO neurons (**Fig. 38B**).

On day 24 of differentiation, we performed live cell staining with a combination of WGA-green, added in the somatic compartment, and WGA-orange, added in the axonal compartment, thus providing a means to distinguish between endocytic vesicles originated in different neuronal regions (**Fig. 38A**).

To follow the fate of endocytosed vesicles and synchronize internalization, WGA was removed from the medium after 30 minutes of incubation, and neurons were maintained in dye-free medium for additional 30 minutes before live acquisition. WGA-green staining showed a strong background and diffuse signal; nevertheless, a few distinct dots were observed. These WGA-green vesicles were mainly stationary and almost exclusively present in the soma from where they originated (**Fig. 38C**, top left). Only after 1 hour of acquisition, we started to observe minor anterograde movements of WGA-green dots along microgrooves toward the axonal side. An even smaller number of the WGA-green dots reached the axonal compartments (data not shown). Similar behavior was observed in HECW1-KO neurons. As for control neurons, we only detected small static WGA-green puncta in the somatic compartment (**Fig. 38C**, left). WGA-orange staining was brighter with red dots easily distinguishable (**Fig. 38C**, right). For the first 30 minutes of acquisition, WGA-orange axonal vesicles were mainly static, or characterized by a bidirectional oscillatory movement near the microgrooves. No WGA-dots were present in the somatic compartment. However, once inside the microgrooves, WGA-orange dots acquired a clear retrograde movement and reached somatic compartments, where they were still highly motile. **Fig. 38D** reports a static image of WGA-orange dots in the soma (left) and along grooves (right). Again, we did not observe major differences in the frequency or dynamics of small WGA-green and WGA-orange vesicles between control and HECW1-KO neurons. On the contrary, in HECW1-KO axonal-tips, we observed an accumulation of large static WGA-orange aggregates, which were not detectable in control neurons (**Fig. 38C**, right). These aggregates were reminiscent of the WGA-green aggregates observed in HECW1-KO neurons plated and differentiated with the traditional neuronal culture approach (**Fig. 36**).

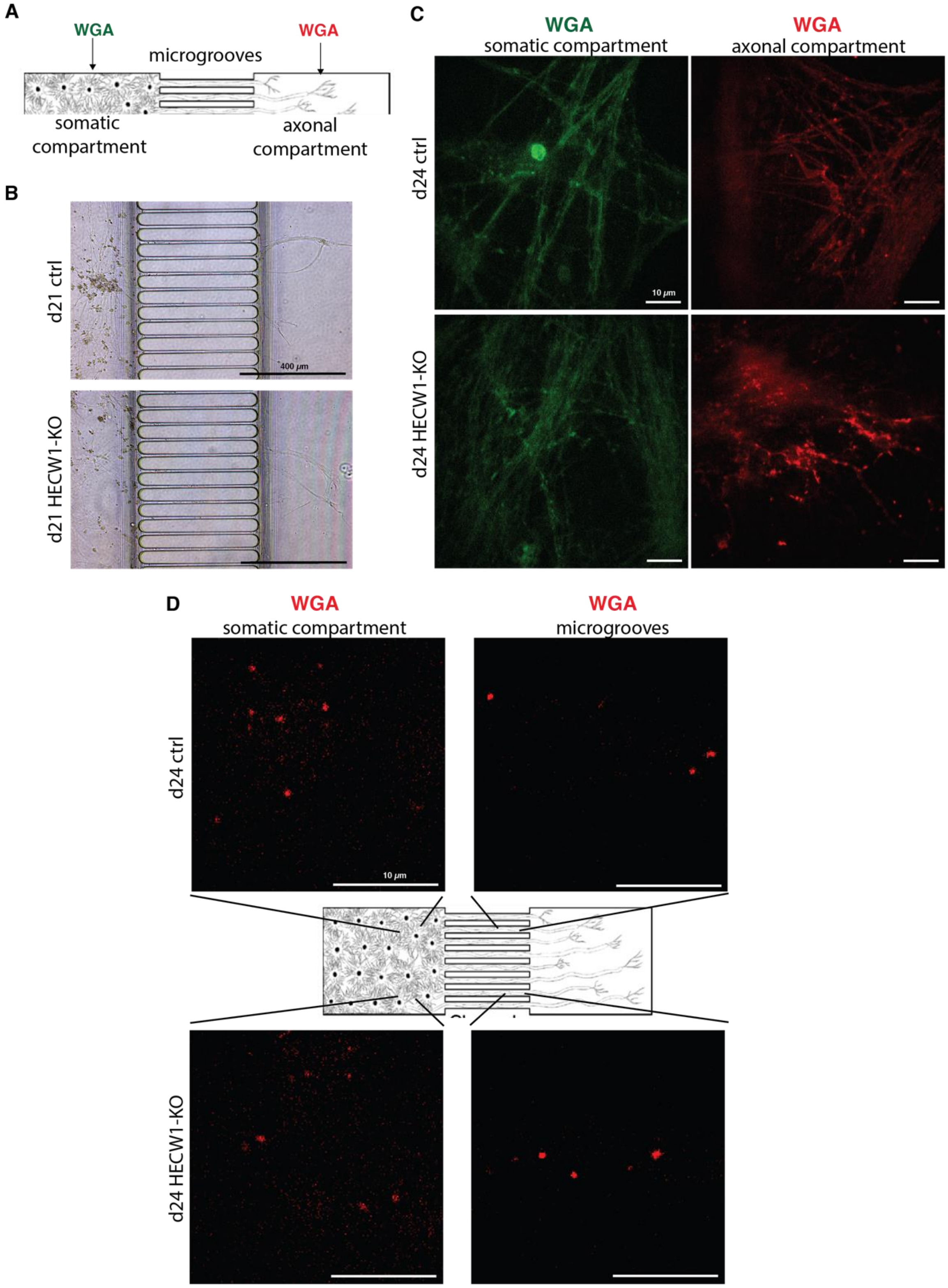

Figure 38 HECW1-depletion leads to an apparent aberrant accumulation of WGA-positive structures in axons

A) A schematic representation of differentiation and live WGA-staining of neurons cultured in the microfluidic device. Day 3 control (ctrl) or HECW1-KO pre-neurons were plated in the left somatic compartments and protrusions reached into the axonal compartments during a differentiation period of 24 days. WGA-green was added in the somatic compartment at a concentration of 10 mg/ml for 30 minutes and was then removed for a wash of 30 min. Subsequently, WGA-orange was added in the axonal *compartment at a concentration of 10 mg/ml for 30 minutes and then removed. Live cell imaging was performed with a spinning disk microscope.*

B) Phase-contrast images of control (ctrl) and HECW1-KO neurons differentiated in the microfluidic devise taken for 21 days. Axonal growth is visible in the axonal compartment for both control (ctrl) and HECW1-KO neurons. Scale bar: 400 µm.

C) Representative images of WGA-green staining in the somatic compartments (left) and WGA-orange staining in the axonal compartments (right) of control (ctrl) and HECW1-KO neurons. A single frame of time lapse video is shown. Scale bar: 10µm.

D) Representative images of WGA-orange staining in microgrooves and axonal compartments of control (ctrl) and HECW1-KO neurons. A single frame of time lapse video is shown. Scale bar: 10µm.

Taken together, these data revealed that HECW1-depletion leads to the accumulation of autophagic/endolysosomal-related structures along neuronal filaments, and WGA-live staining indicates, for at least some structures, an endocytic origin.

4.4 HECW1 role in RNPs dynamics

We recently provided compelling evidence for a critical role of *Hecw* in the regulation of the activity of RNA binding proteins and the dynamics of RNP granules (Fajner et al., 2021) in *Drosophila melanogaster*. Interestingly, most of the significant proteins identified in both the human HECW1 (Table 1) and the *Drosophila* Hecw interactome are related to mRNA metabolism, among which different RNP components are listed. In addition, proteomics analysis performed in iPSC-derived neurons suggests that HECW1 depletion influences the level of proteins involved in RNA metabolism (paragraph 4.2.2).

Prompted by these data and the clear link between impaired RNP assembly, disassembly and trafficking, and the generation of protein aggregates that are toxic for neurons (Mandrioli et al., 2020), we decided to investigate the potential role of HECW1 in the regulation of RNP dynamics in human neurons.

4.4.1 HECW1 interaction with RNPs components

We focused our attention on few candidate interactors, specifically the PB components DCP1A, EDC3 and ILF3, the SG proteins UBAP2L, G3BP1 and FRMP, and the promiscuous DDX6, the human orthologue of the *Drosophila* ME31B whose granules are affected by the lack of Hecw activity (Fajner et al., 2021). These candidates were selected based on their fundamental role in RNP dynamics and the reported implications in neurodegenerative diseases (Standart and Weil, 2018; Wolozin and Ivanov, 2019).

To validate the interaction between HECW1 and FMRP, we overexpressed FMRP-FLAG in HEK293T cells together with GFP-HECW1 or GFP alone (as a negative control) and performed a co-IP with anti-GFP antibody conjugated beads. As visible in **Fig. 39**, the anti-GFP beads were able to co-immunoprecipitated FMRP-FLAG only in the presence of GFP-HECW1, thus validating the interaction between these two proteins.

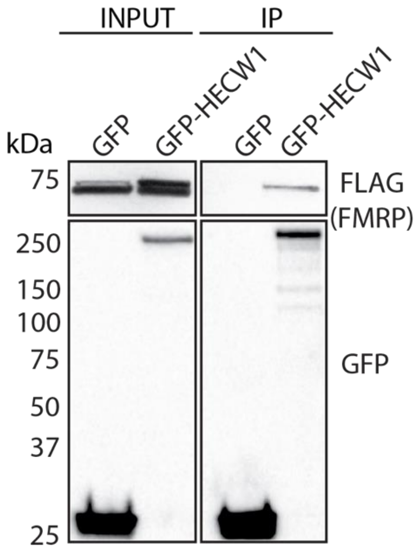

Figure 39 HECW1 interaction with FMPR

GFP antibodies were used for IP of HEK-293T cells co-transfected with a Flag-FMRP construct and GFP-HECW1 or GFP alone. The co-IP of FMRP was assessed by WB using an anti-Flag antibody.

To evaluate the localization of the candidate HECW1 interactors as well as their dynamics of the RNPs to which they belong, we opted for a fluorescent tag. We generated constructs carrying the GFP-tagged version of all the seven selected candidates and performed co-IP experiments expressing them together with FLAG-HECW1 in HEK293T cells. Anti-GFP beads appears to co-immunoprecipitate FLAG-HECW1 in all the cases, suggesting that all of them are “bona fide” HECW1 interactors, with EDC3 showing the strongest interaction (**Fig. 40**). The experiment was repeated several times with similar results and we now intend to stably express GFP-EDC3 and other candidates in a HeLa-shRNA-HECW1 cell line, in which HECW1 depletion can be induced by doxycycline. This will allow us to follow the interaction between RNPs and HECW1 at the endogenous level, in normal conditions or under particular stress conditions in order to see if modulation of RNP dynamics may change the level of interaction.

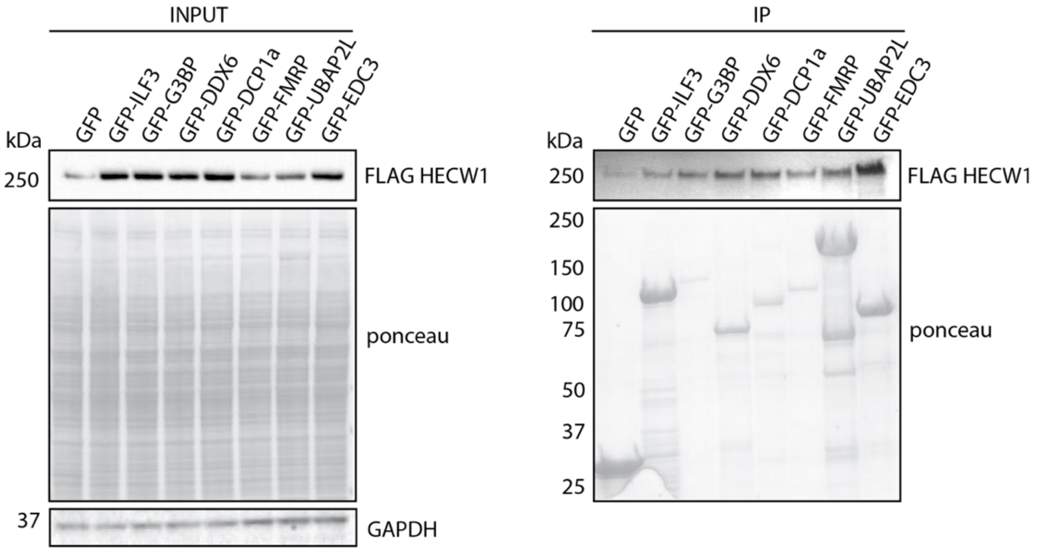

Figure 40 The interaction of HECW1 with RNP components

GFP antibodies were used for IP of HEK-293T cells co-transfected with a HECW1-FLAG construct and GFP-ILF3, GFP-G3BP1, GFP-DDX6, GFP-DCP1A, GFP-FMRP, GFP-UBAP2L, GFP-EDC3, or GFP alone. The co-IP of HECW1 was assessed by WB using an anti-Flag antibody.

4.4.2 Investigation into HECW1 role in RNPs dynamics

Prompted by these results, we decided to investigate potential effects of HECW1 on RNP dynamics in human neurons. To this aim, we performed immunostaining analysis to detect and compare frequency, size and dynamics of SGs and PBs in control and HECW1-depleted neurons in basal or stressed conditions.

4.4.2.1 HECW1 and SGs

SGs are large cytoplasmic RNA and protein aggregates that are normally absent in basal conditions and form transiently, in a dynamic and reversible process in response to different type of stress (Anderson and Kedersha, 2008; Fan and Leung, 2016; Standart and Weil, 2018; Wheeler et al., 2016). Pathological mutations in proteins that either increase the formation, or decrease the clearance of SGs, lead to accumulation of SG-like aggregates and are associated with neurodegenerative diseases (Wolozin and Ivanov, 2019). Considering the role of *Drosophila* Hecw in RNP dynamics (Fajner et al., 2021) and HECW1 interaction with components of these granules, we wondered whether HECW1 depletion in neurons may result in SG aggregation already in basal conditions or in altered dynamics of their stress-induced formation.

To evaluate the effect of HECW1 depletion on the dynamics of SGs formation or dissolution, we treated neurons with sodium arsenite (NaAsO2), a commonly used drug to induce SGs formation. NaAsO2 causes oxidative stress and protein misfolding, leading to the phosphorylation of the alpha subunit of polypeptide chain initiation factor eIF2, stalled translation, and SG assembly (Kedersha et al., 1999).

We differentiated control and HECW1-KD neurons for 10 days, exposed them to 0.5 mM NaAsO2 for 1 hour before fixation and then performed immunostaining analysis of the SGs component FMRP. As expected, in untreated conditions, FMRP showed a mainly diffuse cytoplasmic staining with small puncta in the soma of both control and HECW1-KD neurons (**Fig. 41**, left). As expected, again, upon exposure to NaAsO2, the majority of the neurons produced SGs, as seen by the formation of large FMRP-aggregates (**Fig. 41**, middle). However, control and HECW1-KD neurons showed a similar response in terms of number of cells forming SGs or SG size, indicating that the acute formation of SGs was not affected by HECW1 depletion.

To investigate whether the lack of HECW1 could influence neuronal capability to dissolve SGs upon stress removal, after the acute NaAsO2 treatment, we restored normal cell culture conditions (NaAsO2-free medium) for 1 hour before fixation and FMRP staining. Unexpectedly, we did not observe disappearance of cytoplasmic granules, neither in the control nor in HECW1-KD neurons (**Fig. 41**, right), indicating that longer recovery time is possibly needed for neurons. We are currently performing new experiments extending the recovery phase after treatment.

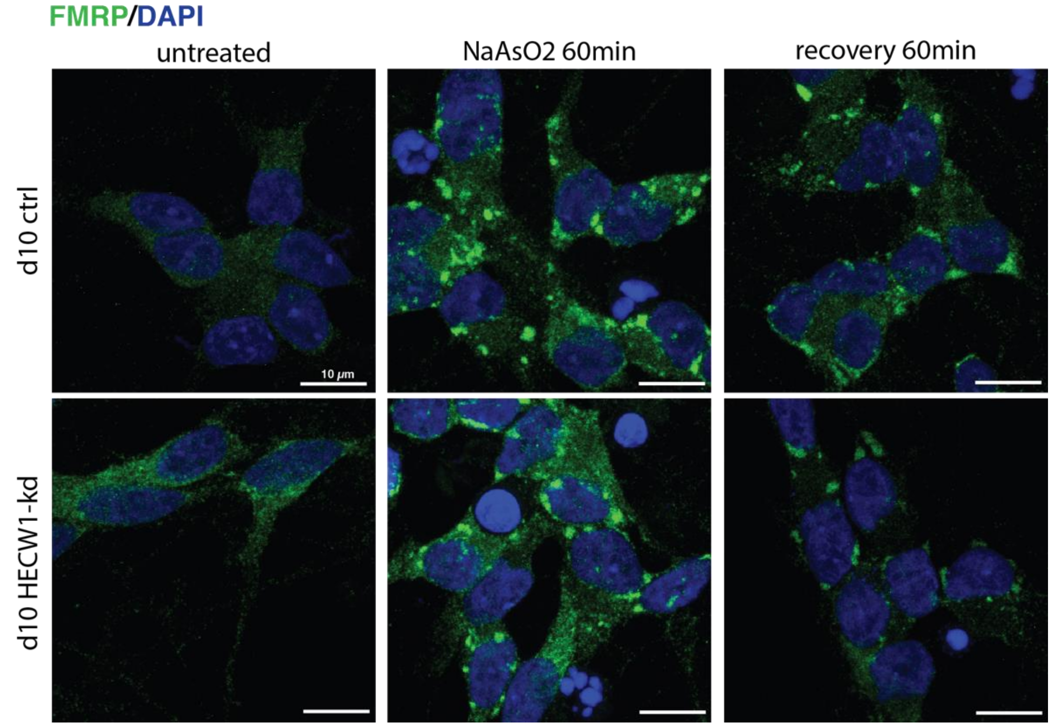

Figure 41 Acute formation of SGs is not affected by HECW1 depletion

IF analysis of control (ctrl) and HECW1-kd neurons for FMRP expression. The cells were differentiated for 10 days, untreated (left) or treated with 0,5 mM of sodium arsenite (NaAsO2) for 1 hour and fixed right after the treatment (middle) or allowed to recover in NaAsO2-free medium for 1 hour before fixation (right). FMRP is stained in green and the nuclei in blue (DAPI). Scale bar: 10 µm.

We also investigated basal SG status with different SG markers and in more mature neurons, in which HECW1 is expressed at higher levels. To this end, we generated control and HECW1-KO neurons and, after 23 days of differentiation in unstressed condition, we immunoassayed the neurons using the SG markers G3BP1 or UBAP2L. In the absence of stress stimuli, G3BP1 revealed a diffuse cytoplasmic staining, with small puncta in the cell soma, both in control and HECW1-KO neurons (**Fig. 42**). UBAP2L behaved similarly, showing a diffuse signal in the soma, but also a dotted staining along filaments. This observation suggests that in the absence of stress, G3BP1 and UBAP2L may have a different localization, participating to different RNP granules. Nevertheless, no major differences were observed also in the UBAP2L staining between control and HECW1-KO neurons (**Fig. 42**). Thus, together with the results obtained for FMRP staining performed on less-differentiated neurons, these results indicate that HECW1 depletion does not lead to SGs formation in the absence of cellular stress.

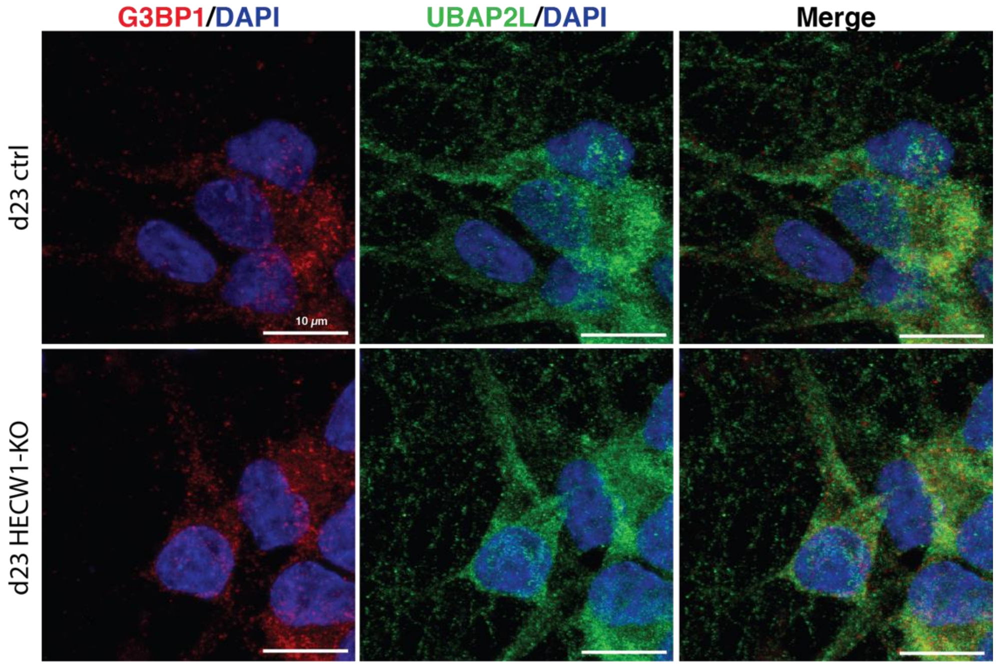

Figure 42 SGs detection in iPSC-derived neurons

Immunofluorescence analysis of ctrl and HECW1-KO neurons differentiated for 23 days for the SG markers G3BP1 and UBAP2L. G3BP1 is stained in red, UBAP2L in green and nuclei in blue (DAPI). Scale bar: 10 μm.

In the future, we aim to test the involvement of HECW1 in regulating the dynamics of SGs induced by other stressors, such as heat shock-induced SGs, for the disassembly of which ubiquitination plays an essential role during recovery from stress (Gwon et al., 2021; Maxwell et al., 2021).

4.4.2.2 HECW1 and PBs

Whereas SGs form transiently in response to stress, PBs are distinct cytoplasmic foci that are present constitutively and can disappear upon stress (Standart and Weil, 2018). Treatment with the translational inhibitors cycloheximide (CHX) stabilizes mRNAs and prevents mRNAs from exiting translation and entering PBs, thus leading to their disappearance (Cougot et al., 2004). As for SGs, impairments in PBs are associated with neurodegenerative diseases (Aulas et al., 2015). Considering the interaction of

HECW1 with PB proteins, we wondered whether HECW1 may have a role in the regulation of this type of RNPs, for example, by contributing to the control of constitutive PB formation and/or clearance, or stress-dependent PB dynamics.

We first performed immunostaining analysis to detect neuronal PBs in basal conditions. To this aim, we differentiated control and HECW1-KO neurons for 15 or 20 days before fixation and staining for the PB markers EDC3, DCP1A or DDX6 (**Fig. 43**). As expected, we observed, for all the three markers, distinct cytoplasmic dots, mainly localized in the neuronal soma. EDC3, DCP1A and DDX6 staining was comparable between control and HECW1-KO neurons, indicating that, at the macroscopic level, PB formation was not affected by HECW1 depletion.

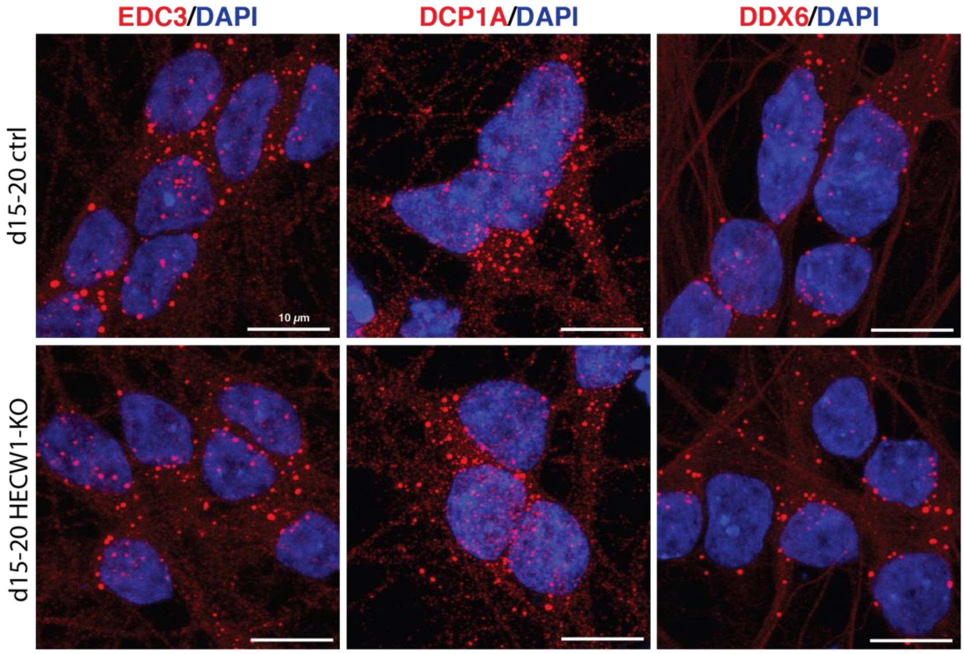

Figure 43 PBs detection in iPSC-derived neurons

IF analysis of control (ctrl) and HECW1-KO neurons. Neurons were differentiated for 15-20 days and stained for the p-body markers EDC3, DCP1A and DDX6. EDC3, DCP1A and DDX6 are stained in red and the nuclei in blue (DAPI). Scale bar: 10 µm.

To investigate more in detail the consequence of the lack of HECW1 on PBs number and dynamics in neurons, we performed a quantitative image analysis in unstressed neurons or upon treatments that influence PBs formation or dissolution. To this aim, we differentiated control and HECW1-KO neurons for 24 days and treated them with cycloheximide, or with 4% 1,6 hexanediol (Hexa), an aliphatic alcohol that disrupts weak hydrophobic bonds and thus a typical promoter of liquid droplets and RNP granules. Using DCP1A as a marker, we counted the total number of PBs in each condition (**Fig. 44A** for representative IF images). Interestingly, in unstressed condition, we observed a significant increase in the number of PBs per cell in HECW1-KO neurons compared to control (**Fig. 44B**, grey dots). PBs number was reduced upon 1,6 hexanediol or cycloheximide treatment in both control and HECW1-KO neurons compared to the relatively unstressed condition (**Fig. 44B**, red dots). This analogous stress-induced dissociation indicates that control and HECW1-KO PBs have similar biophysical properties, in contrast to what we observed for Hecw in *Drosophila*. Also in treated conditions, HECW1-KO neurons showed an increase in the number of PBs compared to control neurons treated with both 1,6 hexanediol or cycloheximide (**Fig. 44B**).

Considering the neuronal autophagy defects caused by the lack of HECW1 and the involvement of this pathway in maintaining SGs and PBs homeostasis (Buchan et al., 2013; Frankel et al., 2017), the increase in the number of PBs could be a consequence of an impaired autophagy-dependent PBs clearance. Further analyses will be performed to unravel the cause of this phenotype.

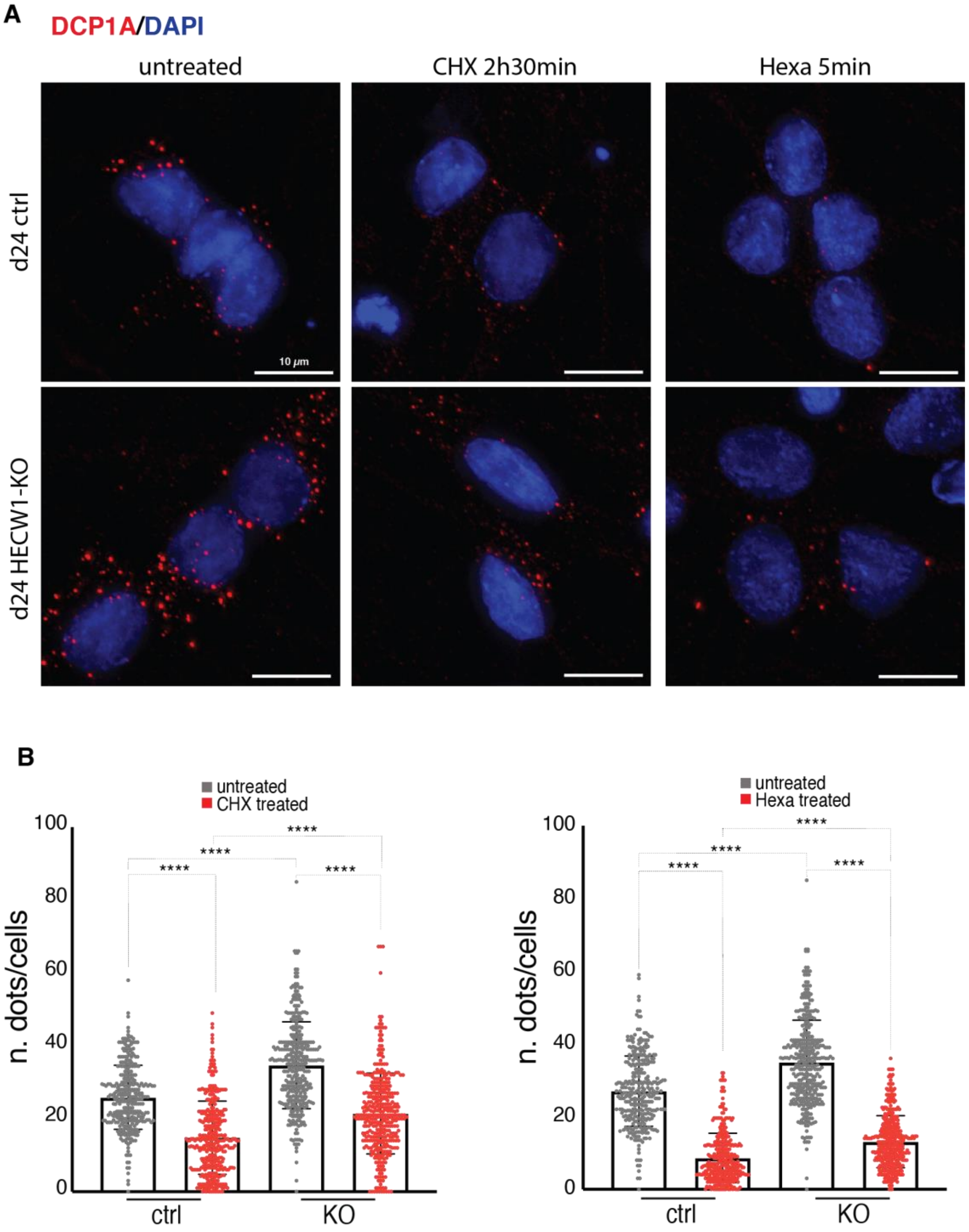

Figure 44 HECW1-KO neurons present a higher number of constitutive PBs than control neurons

A) IF analysis of control (ctrl) and HECW1-KO neurons for the PB marker DCP1A. Neurons were differentiated for 24 days, untreated (left), treated with 7,5 ug/ml of cycloheximide (CHX) for 2 hours and 30 minutes (middle) or with 4% 1,6 hexanediol (HEXA) for 5 minutes (right). DCP1A is stained in red and nuclei in blue (DAPI). Scale bar: 10 µm.

*B) Quantification of the number of individual PBs per cell. ****: p-value <0,0001 (>300 cells per sample were counted in total, from two experiments with two technical replicates each.*

5 Discussion

In this thesis we aimed at characterizing the physiological and pathological functions of the human E3 ligase HECW1 in neurons, where this enzyme is specifically expressed. We optimized the protocol to differentiate neurons from human iPSCs and we generated HECW1-KO iPSCs. Results obtained with this *in vitro* neuronal model system have uncovered an involvement of HECW1 in the regulation of the autophagy/endolysosomal pathway in neurons and a possible contribution in controlling the homeostasis of ribonucleoprotein particles (RNPs).

5.1 iPSC-derived neurons as an in vitro model for studying human neurodegeneration

The two main *in vitro* model systems for studying cellular and molecular neuroscience have been human immortalized cell lines and rodent primary neurons (Fernandopulle et al., 2018; Klionsky et al., 2021). Human immortalized cell lines, such as HeLa, HEK293T, and U2OS, are easily cultured, relatively homogenous, scalable, and readily manipulated genetically. However, lacking a truly neuronal phenotype, they are poorly suited to study neuron-specific biology such as axonal or synaptic phenomena. Moreover, neurons are unique among cell types in their large and functionally polarized structure, post-mitotic state and also dynamics and compartmentalization of autophagy (Fernandopulle et al., 2018; Maday and Holzbaur, 2016). These reasons outline the importance of studying HECW1 function in a neuronal model system that recapitulates the physiological context.

Mouse primary neurons have specialized machineries unique to neurons, can be obtained from specific brain regions, and quickly re-establish synaptic contacts *in vitro*. However, as they originate from another species, these cells may not recapitulate relevant aspects of human genetics or diseases (Fernandopulle et al., 2018). In addition, primary neurons are time-consuming to isolate, can vary in quality from preparation to preparation, are difficult to scale up and challenging to genetically engineer once isolated (Fernandopulle et al., 2018).

A promising tool to obtain human disease-relevant cell types overcoming most of the problems listed above, is represented by Human pluripotent stem cell (hPSC)-derived model systems. Nowadays, embryonic stem cells (ESCs) and induced pluripotent stem cells (iPSCs) are the two major classes of hPSCs. They are similar in morphology, proliferation, self-renewal and differentiation capacity into any cells of embryonic origin (Seranova et al., 2020; Shi et al., 2017; Takahashi et al., 2007; Takahashi and Yamanaka, 2006; Yu et al., 2007). *In vitro* derivation of embryos-derived ESCs is not easily achieved due to limited access to early human embryos and ethical implications. Moreover, ESCs cannot module diseases that are genetically complex or with unknown genetic components (Seranova et al., 2020; Shi et al., 2017; Takahashi et al., 2007; Takahashi and Yamanaka, 2006; Yu et al., 2007). On the contrary, iPSC, being the product of cellular reprogramming of adult somatic cells (Shi et al., 2017), can be generated from patient fibroblasts obtained with non-invasive procedures, thus solving ethical issue and ensuring conservation of the genetic components of each particular disease. iPSC can be gene-edited *in vitro* to correct disease-causing mutations ensuring the advantage of parallel isogenic controls; alternatively, a particular mutation under investigation can be introduced in commercially available iPSCs derived from healthy subjects (Shi et al., 2017; Soldner et al., 2011). The described potentialities of iPSC-technology prompted us to used it as the principal *in vitro* cellular model to investigate into HECW1 physiological and disease-relevant neuronal function.

5.2 Transcription factor mediated differentiation protocol to model human neurons

Aiming at setting up an efficient and reproducible procedure to *in vitro* generate iPSC-derived neurons, we firstly tested a neuronal differentiation protocol that relies on a combination of small molecules, growth factors and pathway inhibitors, to drive iPSCs toward neuroectodermal development. This method involves the intermediate generation of neural progenitor cells (NPCs), that are then further differentiated into neurons of various subtypes (Yan et al., 2013). With this protocol, we managed to obtain *in vitro* human cortical neurons and to confirm the specific expression of HECW1, which is absent in NPCs and it is highly induced during neuronal differentiation (**Fig. 13**). The concomitant upregulation of mRNA and protein levels indicates that HECW1 regulation mainly happen at the transcriptional level. We then generated iPSCs and NPCs lines that stably express GFP-HECW1 or an shRNA to deplete HECW1, in order to study the effect of HECW1 modulation in the derived neurons. Unfortunately, we faced different technical problems while working with this protocol. First, NPCs have a low proliferation rate, limiting the number of starting cells and the possibility of scaling up the experiment. In addition, differentiation is rarely reproducible resulting in a heterogeneous population of mature neurons, neural progenitors and glial cells at various percentage. All these issues affect downstream biochemical analysis and led us to search for more effective and reliable approaches.

We overcome these problems optimizing a protocol that directly generate neurons from iPSCs through overexpression of the neuronal transcription factor NGN2 [(Fernandopulle et al., 2018); **Fig. 19**]. First, iPSCs are characterized by a high proliferative capacity; thus, resolving limitation in the available number of starting cells. Second, we always recorded a nearly total and pure neuronal differentiation, as observed by cellular morphology and immunostaining for characteristic cortical neuron markers in the final population, where no iPSCs remained undifferentiated nor non-neuronal cells were detected. We also verified the compatibility of this protocol with the compartmentalized culturing system, a microfluidic device that physically separates axons from soma and dendrites and allows the characterization of organelle and protein trafficking (**Fig. 37**).

With this protocol, we confirmed the specific neuronal expression of HECW1, absent in iPSCs, while highly induced at both mRNA and protein level during neuronal differentiation (**Fig. 20**). Interestingly, the NEDD4 family members HECW2 and NEDD4 did not share a similar behavior, indicating a selective regulation, and thus a specific role, of HECW1 in neurons.

The efficiency and reproducibility of the NGN2-protocol allowed us to module HECW1-expression, firstly by siRNA-mediated knockdown during differentiation (**Fig. 21**), then by generation of the isogenic HECW1-KO iPSCs (**Fig. 24**). Consistent with what we observed for Hecw in the *Drosophila* model (Fajner et al., 2021) and others published for HECW1-KO mice (Qiu et al., 2016), HECW1 did not result to be an essential gene for neuronal differentiation or early neurons viability.

Interestingly, HECW1 protein levels, which continued to increase until day 25 of differentiation, decreased at later time points (**Fig. 20**), again in line with the progressive age-dependent decrease in the *Drosophila* Hecw expression levels whose absence causes premature motor-neuron dysfunction (Fajner et al., 2021). This behavior is characteristic of components of the ubiquitin proteasome system (UPS) and the autophagy/endolysosomal pathway, the two main clearance systems responsible for protein homeostasis and quality control (Vilchez et al., 2014). These observations, together with the reported implication of HECW1 in human neurodegeneration (Miyazaki et al., 2004; Zhang et al., 2011), suggest a neuronal protective role for HECW1. Being a K63-specific E3-ligase, HECW1 might be important at the level of autophagy/endolysosomal pathway and its mutation or absence could worsen the age-dependent decrease functionality of this pathway, leading to a premature impairment in neuronal homeostasis control and anticipated neurodegeneration. Investigation into this hypothesis prompted us to evaluate HECW1 substrates.

5.3 Proteomics analysis implicates HECW1 in the autophagy/endolysosomal pathway and RNPs dynamics

To gain insights into the underlying molecular mechanisms of HECW1 function, our laboratory previously performed a co-immunoprecipitation (CO-IP) coupled with Mass Spectrometry (MS) analysis (Table 1, Introduction). Corroborating our hypothesis, GO enrichment analysis highlighted proteins involved in vesicle trafficking, membrane fusion and autophagy, such as sorting nexin, cortactin, and ATG2A and BAG3. A second enriched category is represented by mRNA binding proteins implicated at various steps of mRNA processing. This was the top hit category also in the *Drosophila* Hecw interactome (Fajner et al., 2021). Most of the identified proteins are part of two RNP complexes responsible for mRNA translation regulation; the P Bodies (PBs) components DCP1A, EDC3, ILF3 and DDX6, and the Stress granules (SGs) proteins G3BP1, UBAP2L and FMRP. Interestingly, dysregulation in both the autophagy/endolysosomal pathway and RNPs dynamics are key hallmarks of the molecular pathology of different neurodegenerative diseases such as ALS, polyglutamine (polyQ) disorders and PD (Mandrioli et al., 2020).

In order to identify the physiological and disease-relevant cellular processes influenced by HECW1, we decided to performed proteomic analysis in the human iPSC-derived neuronal model. The first analysis was carried out during generation of the HECW1-KO iPSC lines and thus performed in control and HECW1-siRNA depleted neurons. We selected day 10 of differentiation as the time point for the analysis, as the HECW1 is already expressed in control neurons and remains efficiently depleted by a single siRNA transfection performed at day 3. LC-MS/MS-based proteomics performed to investigate differences in global expression pattern due to HECW1-depletion, let us identify around 200 deregulated proteins. Despite the limited size of this list and of the values, we found a GO enrichment in protein categories previously identified from the interactome analysis (**Table 2**). In the future we will focus our attention on proteins involved in vesicle traffic and kinase activity that were implicated in autophagy, and RNA metabolism (**Table 3**).

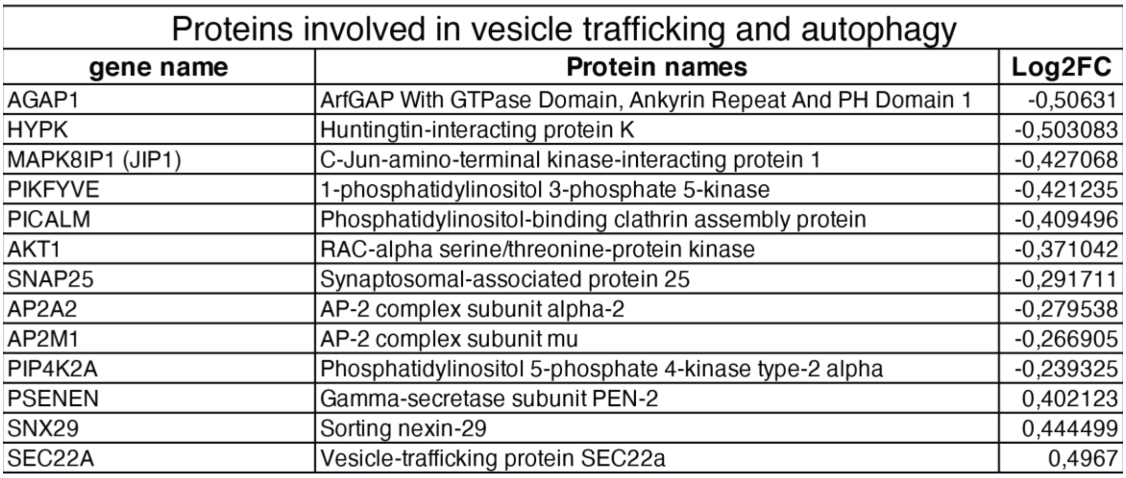

Proteins involved in vesicle trafficking and autophagy		
gene name	**Protein names**	**Log2FC**
AGAP1	ArfGAP With GTPase Domain, Ankyrin Repeat And PH Domain 1	-0,50631
HYPK	Huntingtin-interacting protein K	-0,503083
MAPK8IP1 (JIP1)	C-Jun-amino-terminal kinase-interacting protein 1	-0,427068
PIKFYVE	1-phosphatidylinositol 3-phosphate 5-kinase	-0,421235
PICALM	Phosphatidylinositol-binding clathrin assembly protein	-0,409496
AKT1	RAC-alpha serine/threonine-protein kinase	-0,371042
SNAP25	Synaptosomal-associated protein 25	-0,291711
AP2A2	AP-2 complex subunit alpha-2	-0,279538
AP2M1	AP-2 complex subunit mu	-0,266905
PIP4K2A	Phosphatidylinositol 5-phosphate 4-kinase type-2 alpha	-0,239325
PSENEN	Gamma-secretase subunit PEN-2	0,402123
SNX29	Sorting nexin-29	0,444499
SEC22A	Vesicle-trafficking protein SEC22a	0,4967

Table 3 Partial list of proteins involved in vesicle trafficking and autophagy identified among the deregulated proteins in HECW1-kd neurons

With the aim of confirming the results and identifying proteins specifically modulated by HECW1 in mature neurons, we are currently repeating MS analysis on samples collected from control and HECW1-KO neurons after 30 days of differentiation. We also intend to repeat the interactome analysis in iPSC-derived neurons using HECW1-KO neurons as negative controls, in order to select the best neuronal specific HECW1-interactors/substrates.

Confirming the efficiency and reproducibility of the NGN2 system, RNA-seq based transcriptome analysis, performed in parallel to the LC-MS/MS experiment, revealed neuronal expression profile for both control and HECW1-knockdown neurons already at 10 days after differentiation (**Fig. 25**) . In this timeframe we did not observed major changes in the absence of HECW1, indicating that the differences observed by MS analysis are due to post-transcriptional mechanisms. This is somehow expected being HECW1 an E3 ligase. Again, further experiments are needed to investigate the effect of HECW1 depletion at later time points.

Considering the established role of the *Drosophila* Hecw in regulating RNPs dynamics (Fajner et al., 2021) and the interactome of HECW1, we intend also to evaluate its possible role in regulating the axonal transport of mRNA from the soma to distal tips. To this end, we would specifically compare control and HECW1-KO axonal transcriptome taking advantages of a recently developed axon-sequencing (axon-seq) approach that combines microfluidics compartmentalized neuronal system, spatial RNA sequencing, and bioinformatics analysis (Nijssen et al., 2018). Of note, SOD1-mutant motor axons, but not the relative soma compartment, showed deregulated expression of key transcripts involved in neuronal function, axon maintenance, and growth (Nijssen et al., 2018).

Taken together, proteomic results point to a possible role of HECW1 in regulating autophagy/endolysosomal pathway and RNA metabolism and prompted us to assess whether there is a connection between the two.

5.4 HECW1 role in neuronal autophagy and the endo-lysosomal pathway

5.4.1 HECW1-depletion leads to accumulation of endolysosomal/autophagic compartments

The morphological analysis of HECW1-depleted neurons showed an accumulation of endolysosomal/autophagic compartments. In particular, IF analysis revealed an accumulation of enlarged organelles positive for the autophagic and endo-lysosomal marker LAMP1 (**Fig. 28, 29, 30, 31**), while negative for the early endosomal antigen 1 (EEA1) (**Fig. 29**), suggesting that HECW1-depletion impacts on autophagosome, late endosome or lysosome without disturbing early steps of endocytosis. In parallel, EM analysis showed a strong accumulation of endolysosomal/autophagic related structures along filaments and in distal axon of HECW1-depleted neurons (**Fig. 34-35**). The heterogeneous morphology observed among them suggests they are endolysosomal/autophagic compartments at different stages of maturation/fusion. Vesicles with sealed double-membrane bilayers separated by an electron-lucent cleft were reminiscent of early stage initial autophagic vacuoles, while multilamellar structure and multivesicular bodies likely represented endosomes or intermediates of endocytic and autophagic pathways originated by the fusion between autophagosomes and late endosomes or lysosomes (Klionsky et al., 2021). Moreover, as observed by dual-label WGA live-cells imaging performed in the compartmentalized culturing system (**Fig. 38**), distal tips of HECW1-KO neurons showed the accumulation of large static-WGA-aggregates locally originated in the axon. This observation indicates an increase in the size of endosomal compartments generated in neuronal protrusions upon HECW1-depletion, that could be due to uncontrolled formation and maturation, or defective transport/loading onto microtubules and consequently fusion between stacked vesicles. Of note, we did not observe WGA-axonally generated aggregates in the soma. This could be due to the limited time setting of the experiment, and extending WGA incubation time will allow us to determine whether these aggregates are stacked in the protrusions or travel toward the soma. On the other hand, aggregates are not positive for the autophagic receptor p62 or ubiquitin (**Fig. 32**), suggesting that this E3 ligase does not have a major impact on p62/ubiquitin mediated autophagy in the absence of cellular stress. Data obtained so far suggest that HECW1 could be relevant in the late endosomal pathway and in the bulk basal autophagy, both highly active in neuronal cells. LAMP1-accumulated organelles led by HECW1-depletion were not associated with the autophagic marker LC3 (**Fig. 32**), suggesting that they are more likely lysosomes, late endosomes or endolysosomes rather than amphisomes generated by the fusion of autophagosomes with late-endosomes (Cheng et al., 2018). It is otherwise possible that HECW1-depletion results in a defective recruitment of LC3 to autophagosome membrane and thus LC3-negative autophagosomes and amphisomes. To better determine the nature of these organelles, we will combine LAMP1 staining with other endosome and autophagosome markers, such as, respectively, Rab and ATG proteins, or with activity-based lysosome probes to monitor degradative lysosomes.

Taken together, proteomics, IF and EM data pointed to an involvement of HECW1 in endolysosomal/autophagic vesicular maturation or trafficking. Further investigations are needed to uniquely identify the structures accumulated in HECW1-KO neurons and elucidate HECW1 role in neuronal endolysosomal pathway and autophagy in temporal and a spatial manner (i.e., which are the impaired steps during the pathway). Unlike non-neuronal cells, autophagy is spatially regulated in neurons, as autophagosomes form in distal axons and mature during their retrograde transport along microtubules to the cell soma, which contains the majority of lysosomes. IF analysis of neurons grown on the compartmentalized culturing device will allow us to spatially resolve the HECW1-depletein dependent accumulation of LAMP1-enlarged organelles, and to reveal correlation, or interaction, between LAMP1 and WGA aggregates. To clarify corresponding between the endolysosomal/autophagic structures and the LAMP1-organelles observed, respectively, by EM and IF, we will perform Correlative Light and Electron Microscopy (CLEM) analysis, a technique that involves the use of fluorescent microscopy to define regions-of-interest, in our cases LAMP1-positive organelles, that are subsequently traced back in the EM to provide morphological and subcellular context information (Klionsky et al., 2021). In parallel, immuno-EM with gold-labelling (Mayhew, 2007) using gold-tagged WGA, antibodies for the autophagosomal protein

LC3 or markers for other of autophagic compartments, will further help us in identifying the structures accumulated in HECW1-depleted neuronal protrusions. Presence of WGA inside them would suggest they derived, at least in part, from endocytic traffic.

We also aim to generate GFP-LAMP1-iPSC-lines, useful tool to follow LAMP1-trafficking by live cell imaging analysis performed on the compartmentalized culturing system, as well as to perform IMMUNO-EM or CLEM analysis. Furthermore, future dedicated experiments will be instrumental to examine the impact of HECW1 in selective autophagy pathways, such as “aggrephagy”, “ERphagy” and “mitophagy” (Stavoe and Holzbaur, 2019), and in stressed-induced autophagy. WB analysis will be performed to measure expression and activation of different autophagy pathway, such as the mTOR pathway, in basal and stress conditions.

5.4.2 Potential role of HECW1 on the formation and maturation endolysosomal/autophagic compartments

Disturbances within and accumulation of endolysosomal/autophagic compartments can be caused by impairments at the level of their formation, maturation or transport toward the soma for degradation (Cheng et al., 2015; Maday et al., 2012), thus raising the fundamental question of which among these events are affected by HECW1-depletion.

Correlation between alterations caused by HECW1-depletion and similar phenotypes reported in literature, allow us to hypothesize different scenario. In primary DRG neurons, depletion of the dynein motor adaptor protein Snapin impairs late endosome loading onto microtubules and thus their retrograde transport, resulting in amphisome accumulation at the axon tips (Cheng et al., 2015). Additional studies highlighted the role of Snapin in promoting autophagic clearance at presynaptic terminals in a mice model of Alzheimer’s disease (Tammineni et al., 2017). Intriguingly, the accumulated vesicles in the absence of Snapin closely resemble the ones observed in our model, suggesting an impairment in the transport of amphisomes or late endosomes in the absence of HECW1 activity. In line with this hypothesis, it will be interesting to test whether Snapin-overexpression could rescue HECW1-depletion dependent phenotype or, if Snapin-depletion exacerbates it.

On the other hand, lack of HECW1 has no detectable impact on lysotracker-positive vesicles moving along axon (**Fig. 33**), suggesting that the observed accumulation is not due to an impaired lysosome/late-endosome trafficking. Nonetheless, HECW1 could have a specific role in regulating retrograde transport of late endosomes, without affecting anterograde transport. This scenario is hardly detectable with the traditional neuronal culture system where lysotracker staining does not allow directionality measurement. Having set up the compartmentalized culturing system, we are currently in the best conditions to perform more precise live cell imaging analysis combining different fluorescent probes with specific organelles markers.

Another possibility is that HECW1 may contribute to directly loading autophagosome onto microtubules, regulating motor adaptor complex via ubiquitination. In support of this hypothesis, among the proteins downregulated in HECW1-depleted neurons, we identified JIP1, a motor scaffolding protein that interacts with LC3 and maintains autophagosome retrograde transport through inactivating anterograde motor KIF5 (Birgisdottir and Johansen, 2020; Fu and Holzbaur, 2014; Fu et al., 2014).

Autophagic vesicle accumulation could also result from defective autophagosome maturation. Stavoe and colleagues identified a decrease in the rate of constitutive autophagosome biogenesis during aging and observed, in the axon of neurons from aged mice, a pronounced accumulation of morphological aberrant autophagosomes, characterized by excess membrane build-up, that retain markers of early step of autophagosome biogenesis, such as ATG9 and ATG13, while fail to recruit lipidated

LC3B, due to defective dephosphorylation of WIPI2B at the phagophore (Stavoe et al., 2019). Prolonged association of ATG9, which works in concert with ATG2 to provide lipids to the growing autophagosome membrane (Birgisdottir and Johansen, 2020; Fu and Holzbaur, 2014; Fu et al., 2014), could enable unregulated lipid transfer to the stalled vesicles, resulting in the observed multilamellar structures (Stavoe et al., 2019). The identification of ATG2A as a possible HECW1 interactor, the multilamellar structure for some of the autophagic vesicles accumulated in HECW1-depleted neurons and the LC3 negativeness of LAMP1-enlarged organelles observed by IF, well fit with this mechanism. This hypothesis will be tested analyzing HECW1-mediated regulation of ATG2A and its contribution to the correct phospholipid transfers and LC3 recruitment at the autophagic vesicles. As observed for the K63-polyubiquitination mediated by the E3-ligases TRAF6 and TRIM16 (Grumati et al., 2018), HECW1 could have a role in stabilizing autophagy-related proteins.

Finally, an alternative scenario to investigate is represented by the defective fusion of autophagosomes with late endosomes or lysosomes. Indeed, blocking this event by knockdown of the autophagosome-localized SNAREs STX17 inhibits autophagosome transport along the axons of primary DRG neurons, causing aberrant structures (Cheng et al., 2015). We identified different SNARE proteins by our proteomics analysis, in particular SEC16A as a possible HECW1-interactor, and SEC22A upregulated in HECW1-depleted neurons. In addition, another downregulate protein in HECW1-KD neurons is PI(3)P 5-kinase Fab1 (PIK-fyve), the kinase responsible for the generation of PI(3,5)P2 and PI(5)P phospholipids that impact at different step of the autophagy/endo-lysosomal pathway, from phagophore initiation and autophagosome maturation to transport and fusion with late endosomes and lysosomes (de Lartigue et al., 2009; Dooley et al., 2014; Ferguson et al., 2009; Nakamura and Yoshimori, 2017; Seranova et al., 2020; Vicinanza et al., 2015; Zhao et al., 2013). Interestingly, PIK-fyve inhibition in hippocampal neurons leads to an increase in LAMP1-vesicles and morphological alterations in the endolysosomal system (Martin et al., 2013) that resemble the ones we observed in iPSC-derived HECW1-depleted neurons. Moreover, the accumulated large electron-lucent vacuoles along neurites upon PIK-fyve inhibition contained endocytosed WGA (Martin et al., 2013). Considering the WGA-aggregated we detected, we suggest that HECW1-depletion may impair endolysosomal/autophagic compartments in part through downregulation, or regulation, of PIK-fyve. To investigate this possibility, PIK-fyve level will be tested in HECW1 KD at different time points and in KO neurons and we will also combine PIK-fyve inhibition with HECW1-depletion.

All the above-mentioned designed experiments will be instrumental to identify the most promising HECW1 function to further dissect.

5.5 HECW1 role in RNPs dynamics

Our recent study on the *Drosophila Melanogaster* model system highlighted a specific role of Hecw-mediated ubiquitination in regulating the activity of RBPs by maintaining the liquid-like nature of RNPs in both oocytes and neurons (Fajner et al., 2021).

The common enrichment in Hecw and HECW1 interactomes for RNPs components, in particular Fmrp/FMRP and lingerer/UBAP2L, suggest that also the human HECW1 could act as a regulator of RNPs dynamics and RBPs activity in human neurons, and consequently contribute to maintaining neuronal homeostasis. Recent literature has, indeed, made a clear link between impaired RNPs dynamics and trafficking and the generation of protein aggregates toxic for neurons. Importantly, several causative genes in ALS and FTD, such as TDP43, FUS, and ATX2 are components of RNPs (Dudman and Qi, 2020; Le Guerroue and Youle, 2021).

By CO-IP analysis we confirmed HECW1 interaction with the SG protein FMRP and the PB components EDC3. We are now performing experiments to validate HECW1 interaction with other selected candidates and we also aim to understand whether this interaction is direct or mediated by RNA molecules in a protein-RNA-protein complex. In parallel, we are performing experiments to assess the role of HECW1 in the formation and disassembly of different RNPs, such as SGs and PBs. As we revealed by quantification of DCP1A-positive RNPs (**Fig. 44**), in the absence of HECW1, iPSC-derived neurons presented an increase number of constitutive PBs compared to control. Comparable CHX- and HEXA-induced disassembly kinetic between PBs formed in control and HECW1-KO neurons suggests they have similar biophysical properties. Nevertheless, HECW1-KO HEXA- or CHX-treated neurons still exhibited a higher number of PB compared to the relative treated control. These results suggest a function of HECW1 in regulating constitutive PB formation or clearance. To further investigate into this hypothesis, we could measure HECW1 depletion effect on PBs number in the presence of cellular stresses that more specifically inhibit or induce PBs formation. Interestingly, depletion of the RNA binding proteins FUS or TDP-43 caused an increased number of constitutive PBs in HeLa cells (Aulas et al., 2015), suggesting an important link between RBP function, PB dynamics and ALS pathogenesis.

IF analysis for the SG components G3BP1, FMRP and UBAP2L indicated that HECW1-depletion does not result in SGs aggregates in basal condition nor impairment in NaAsO2-induced SGs formation, which was comparable between control and HECW1-KO neurons (**Fig. 41, 42**). SG disassembly assay was not informative as we did not observe dissolution of AS-induced SG upon 1 hour of stress removal. We are currently optimizing treatment conditions that would allow us to monitor more in details SGs dynamics in neurons.

A recent publication showed that, heat shock (HS) induces the targeted ubiquitination of a specific set of proteins, among which components of SGs, and that this ubiquitination, while dispensable for SG formation, is required for their disassembly during recovery from HS (Maxwell et al., 2021). Consistent with this, in both HEK293T cells and iPSC-derived neurons, treatment with an inhibitor of the E1 ubiquitin activating enzyme (UBA1), while not preventing their formation, impaired HS-induced SG disassembly after stress removal (Maxwell et al., 2021). Interestingly, K63-chain was the principal polyubiquitin signal accumulated in SGs upon HS and G3BP1 the main target. Consequent recruitment to SGs of the ubiquitin-dependent segregase p97/ VCP lead to G3BP1 removal from SGs that then disassemble (Gwon et al., 2021). Of particular note, the same SG constituents were not ubiquitinated in response to NaAsO2 stress and ubiquitination was dispensable for both assembly and disassembly of NaAsO2-induced SGs (Markmiller et al., 2019; Maxwell et al., 2021). Thus, the mechanisms whereby dynamic of SGs, and possibly other RNPs, are regulated depend upon the nature of the initiating stress. Prompted by these recent studies, we aim to investigate HECW1 in the setting of HS and other stressors. We will firstly use the HeLa-shRNA-HECW1 as a cellular model, taking advantages of the GFP-fused version of RNP-proteins we generated, which would allow us to follow the process of granules aggregation, trafficking, and disassembly in a dynamic way. Consequently, we will confirm results in iPSC-derived neurons.

5.6 Interplay between RNPs and autophagy

Mechanisms of RNPs dissolution depend on both the type and duration of stress (Gwon et al., 2021). Short-lived granules are rapidly disassembled, which permits recycling of constituents. In contrast, persistent RNPs, such as those that arise through chronic stress or disease mutations, are less dynamic and are eliminated by autophagy (Buchan et al., 2013; Gwon et al., 2021). Given the fact that HECW1-depletion in neurons is associate with both, impairment in the endolysosomal/autophagic pathways and increase in DCP1A-granules numbers, we wonder whether there could be a link between these two phenotypes. PBs quantification upon HECW1-depletion in combination with cellular stress to induce or inhibit autophagy would help in testing whether HECW1-dependent increased in constitutive PBs is a consequence of impaired autophagy-dependent clearance.

Beyond degradation, the endolysosomal/autophagic pathways is involved in RNA and RNPs regulation and trafficking in neurons (Abildgaard et al., 2020). RNA granules can use membrane-bound organelles, such as lysosomes and late endosomes, as vehicles to promote long-range transport to distal sites via microtubule-dependent transport (Cioni et al., 2019; Liao et al., 2019). Thus, it is possible that dysfunctional autophagic/endocytic vesicles may result in impaired RNPs trafficking and formation of RNA-proteins aggregates, as was shown for the RNA binding protein annexin 11 ANXA11, a molecular tether between RNA granules and lysosomes (Liao et al., 2019). ANXA11 interacts with lysosome through a membrane-binding domain, and with RNPs thought an N-terminal low complexity disordered region that facilitates the formation of transient phase-separated assemblies (Liao et al., 2019). Interestingly, this domain combination is present also at the N-terminal region of HECW1, with a calcium membrane binding domain (C2) close to a low complexity disordered region that could enable interaction within phase-separated RNA granules. This raises the possibility that also HECW1 acts as an adaptor between RNPs and membrane bound organelles. A biochemical characterization of this region in the context of RNPs interaction with late endosomes/lysosomes will help to investigate this hypothesis.

5.7 Animal models and neurodegeneration

We recently demonstrated that Hecw overexpression in flies causes neurodegenerative defects analogous to the ones observed in Hecw-mutant (Fajner et al., 2021), suggesting that it is the E3 ubiquitination activity that must be tightly regulated. Consistently, depletion and overexpression of HECW1 lead to parallel phenotypes also in mice. HECW1-KO mice, generated at the MRC Harwell institute in the Oxfordshire, are viable with no major morphological defects but show a motor-neurons dysfunction phenotype at the adult stage (online data available, MGI:2444115); similarly, transgenic mice overexpressing hHECW1 developed ALS-like symptoms, such as motor neuron degeneration and muscle atrophy (Zhang et al., 2011). HECW1-mediated ubiquitination of endocytic/autophagic proteins and/or motor adaptors could be important for their correct localization, interaction or function, thus promoting the maturation, fusion or transport of the related organelles. To ascribe the phenotypes observed in HECW1-KO neurons specifically to the lack of HECW1-dependent ubiquitination, it would be important to generate catalytic-inactive HECW1-iPSC lines by CRISPR/Cas9-mediated targeted mutagenesis.

The alterations observed in iPSC-derived neurons upon HECW1-depletion suggest that pathological mechanisms that may start before the onset of age-related disease, anticipating neurodegeneration and neuronal death. A difference between our in vitro models and the disease in patients is the age of the cells affected, which may be the reason why we do not observe major phenotypes in HECW1-KO neurons. Unfortunately, neuronal aging cannot be easily recapitulated *in vitro* with iPSC culture model. First, by reverting adult cells to a stem cell state, markers of age are erased (Shi et al., 2017), furthermore, maintaining long term iPSC-derived neuronal cultures is challenging. Indeed, we attempted to keep neurons in culture for long period, but we observed an exponential increase in cells death at around 40 days of differentiation. To solve this issue, premature aging can be induced treating iPSC-derived neurons with cellular stressors, such as MG-132 and pyraclostrobin, which respectively target protein degradation pathways or mitochondrial function (Cooper et al., 2012; Liu et al., 2012; Nguyen et al., 2011; Pearson et al., 2016; Shi et al., 2017; Sudol and Hunter, 2000). This model system might allow us to analyze the consequences of the endolysosomal/autophagic pathway dysfunction caused by HECW1 depletion on neuronal homeostasis and premature degeneration.

Among different neurodegenerative disorders, HECW1 has been particularly implicated in ASL, a disease that specifically affects motor neurons (Miyazaki et al., 2004; Zhang et al., 2011). In collaboration with the San Raffaele Hospital of Milan, we performed preliminary immunostaining with HECW1 antibody on a few normal and ALS human brains and we confirmed HECW1 expression in healthy motor neurons that clearly decreases in ALS patients. We also observed an inverse correlation between HECW1 expression and the presence of aggregates positive for ubiquitin, absent in neurons from healthy patients (data not shown). These initial observations suggest once again a protective role for HECW1 in neurons, which might be particularly relevant in motor neurons where RNPs play a critical role. In the absence of HECW1, RNPs may undergo solid-like transition (Fajner et al., 2021) causing aggregates recognized by the UPS system that ultimately try to eliminate them. Additionally, the lack of HECW1 could lead to defects in the endolysosomal/autophagic pathways that finally result in the formation of protein aggregates. We are currently collaborating with other hospitals to support this data and investigate deeply into the pathological relevance of HECW1.

Finally, we performed our analysis on iPSC-derived cortical neurons, but similar differentiation protocol allows the generation of lower motor neurons (i3LMNs) via the expression of the transcription factors Islet-1 (ISL1) and LIM Homeobox 3 (LHX3) along with NGN2 (hNIL) (Fernandopulle et al., 2018; Mazzoni et al., 2013; Shi et al., 2018). It will be interesting, in the future, to specifically investigate the protective role of HECW1 in the autophagy/endolysosomal pathway and RNPs dynamics in this particular type of neurons.

6 APPENDIX

6.1 Characterization of HECW1 in the cancer cell line A549

At the beginning of my PhD, I used the A549 lung adenocarcinoma cell line, to characterize the function of HECW1.

6.1.1 CRISPR/Cas9 mutagenesis of the HECW1 gene

6.1.1.1 Generation and characterization of HECW1-KO clones

A549 is one of the few immortalized cell lines that express the protein HECW1 (**Fig. 44A**). HECW1-KO A549-clones were previously generated in our laboratory using CRISPR/Cas9 approach. Briefly, A549 cells were transfected with a vector harboring the Cas9 nuclease fused with GFP, and two different gRNAs, called guide 14 and guide 15, positioned on Exon4 of HECW1 (the second coding exon). Clones were generated from GFP-sorted cells, screened by WB and IP for the absence of HECW1 protein and clone 14S6 was selected for further experiments. Unfortunately, the available commercial antibodies and the monoclonal anti-HECW1 antibodies generated by our group, while performing well in WB and IP, were not able to distinguish between A549 cells and the 14S6-HECW1-KO clone by IF, thus limiting our possibilities to define the subcellular localization of the endogenous protein.

This lack of specific staining could be possibly due to a low abundance of the HECW1 endogenous protein. To quantify the total amount of HECW1 protein expressed in different human and mouse cell lines, we performed a densitometric analysis including the 14S6-HECW1-KO cells as a negative control. All the tested cell lines expressed HECW1 at a very low level, in the range of 100-300 pg of protein per 50 ug of cell lysate (**Fig. 45**).

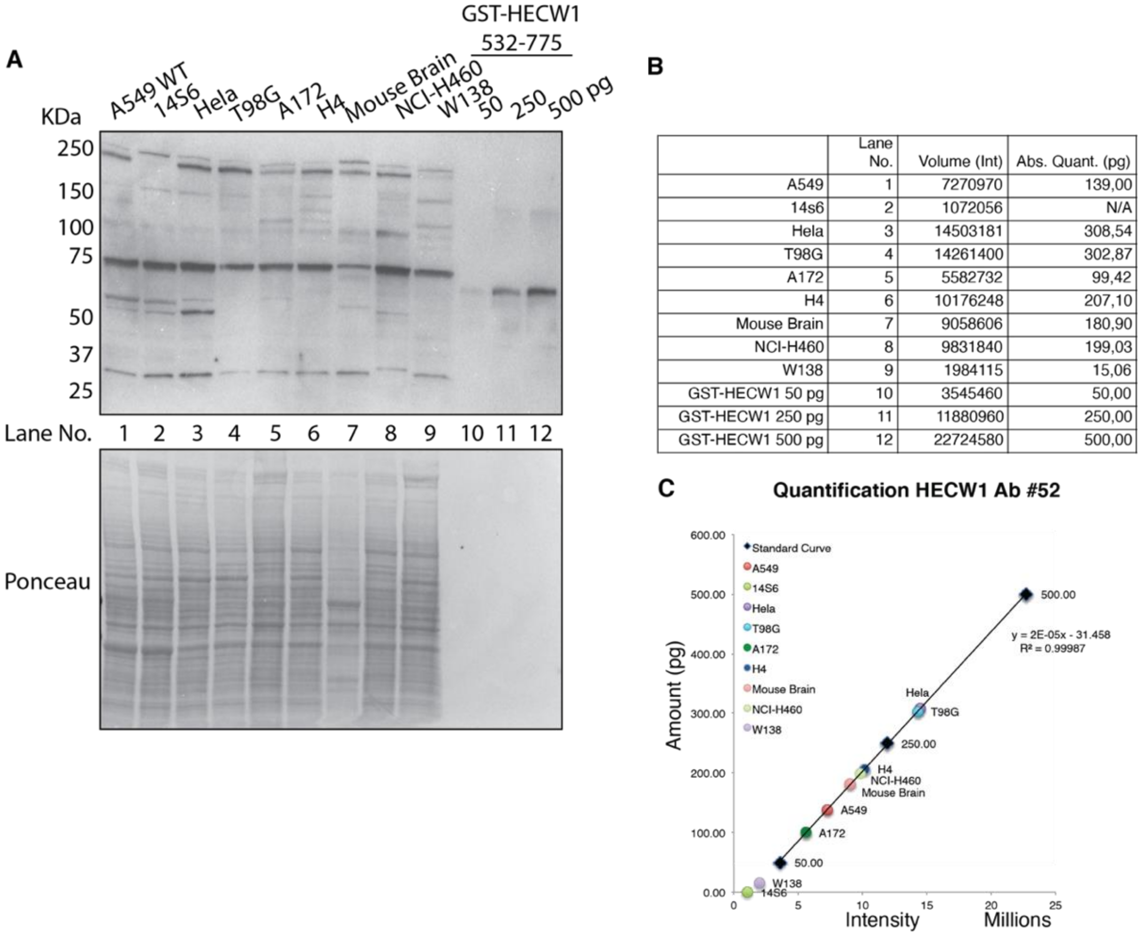

	Lane No.	Volume (Int)	Abs. Quant. (pg)
A549	1	7270970	139,00
14s6	2	1072056	N/A
Hela	3	14503181	308,54
T98G	4	14261400	302,87
A172	5	5582732	99,42
H4	6	10176248	207,10
Mouse Brain	7	9058606	180,90
NCI-H460	8	9831840	199,03
W138	9	1984115	15,06
GST-HECW1 50 pg	10	3545460	50,00
GST-HECW1 250 pg	11	11880960	250,00
GST-HECW1 500 pg	12	22724580	500,00

Figure 45 Quantification of HECW1 protein in different cell lines

(A) IB analysis with the "house-made" HECW1-antibody in cellular lysates and standard proteins. Ponceau staining is reported.

(B) Densitometric analysis, using the Image Lab software. The results are reported in the table.

(C) The intensity and amount (pg) of HECW1 band (250 kDa) for each lane (calculated with the Image Lab software) are reported on the horizontal and vertical axis, respectively.

To confirm that the lack of HECW1 signal in the IF analysis was due to a low expression of HECW1, A549 WT cells were transfected with a GFP-HECW1 construct and analyzed by IF with the "house-made" HECW1-antibody. GFP and HECW1 perfectly colocalized, and revealed a mainly cytoplasmic localization, with nuclear exclusion, and plasma membrane bound protein (**Fig. 46**).

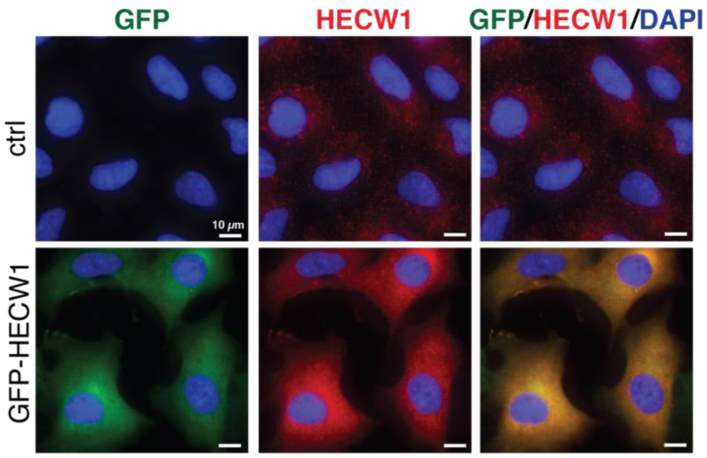

Figure 46 IF analysis of GFP-HECW1 overexpressing A549 cells

IF analysis of A549 cells transfected with GFP-HECW1 (bottom panels) or mock transfected (top panels), and stained for the "house-made" HECW1 antibody. GFP is stained in green, HECW1 in red and the nuclei in blue (DAPI). Scale bar: 10 µm.

6.1.2 The role of HECW1 in the Autophagy-Endolysosomal pathway

Results from HECW1-interactome analysis and characterization of the *Drosophila* orthologue *Hecw* suggested the involvement of HECW1 in vesicular trafficking and the autophagy pathway. Thus, we decided to explore the effect of HECW1-depletion on the autophagy-endolysosomal system in the A549 cell line.

A commonly used approach to monitor this pathway is by blocking the autophagic activity, for example with chloroquine (CQ), a compound that inhibits autophagy by impairing autophagosome fusion with lysosomes (Mauthe et al., 2018), and then monitoring the accumulation of autophagic structures using specific markers, such as LAMP1 for autophagic- and endo-lysosomal organelles, or LC3 for autophagosome and amphisome.

In our studies, we used the tandem-tagged RFP-GFP-LC3, a dual-fluorescence probe based on the sensitivity of GFP to acidic environments. While GFP-fluorescence is quenched by low pH, RFP is relatively more stable, thus only red fluorophore is visible in the acidic autolysosomes formed by the fusion of autophagosome with lysosome (Kimura et al., 2007). The ratio of double-positive versus RFP-positive structures allows measuring the fraction of autophagosomes and autolysosomes, respectively, and the assessment of the autophagic flux.

By transfection, selection for neomycin resistance and sorting for RFP-GFP expression, we established stable A549-WT and 14S6-HECW1-KO cells expressing RFP-GFP-LC3. To inhibit autophagy and obtain an accumulation of autophagic vesicles, RFP-GFP-LC3 cells were treated with chloroquine, followed by fixation and immunostaining with LAMP1 antibody to identify lysosomes.

As observed by IF analysis, HECW1 depletion, upon chloroquine treatment, led to an increase in the number and size of autophagosomes (LC3) and lysosomes (LAMP1) compared to A549-WT cells (**Fig. 47A**). The two compartments that were enriched also colocalized in 14S6-HECW1-KO cells more than in A549-WT cells, with LC3-autophagosomes surrounding the LAMP1-positive structures. Immunostaining for p62, the autophagic receptor for ubiquitinated proteins, or for Ubiquitin itself showed no defects in cargo accumulation upon induction of autophagy in the absence of HECW1 (**Fig. 47B**). These data suggest an effect of HECW1-depletion at the level of the constitutive endosome-lysosome/autophagosome fusion.

We confirmed this observation by performing Correlative Light-Electron Microscopy (CLEM) analysis, using a gold-bound GFP-antibody to detect LC3. Analysis of A549-WT and 14S6-HECW1-KO cells revealed that HECW1-depletion led to the formation of electron lucent vacuoles in the cytoplasm of the cells (**FIG. 47C**). These vacuoles appeared largely devoid of internal structures and contained small internal vesicles, intralumenal membranes and electron-dense material, and are consistent with aberrant multivesicular bodies (MVBs, late-endosomes that contain membrane-bound intraluminal vesicles) or aberrant amphisomes (organelles generated by the fusion of autophagosomes with late-endosomes or lysosomes). A few of these aberrant vesicles were also surrounded by GFP-LC3. Strikingly, these aberrant vacuoles were almost undetectable in control cells.

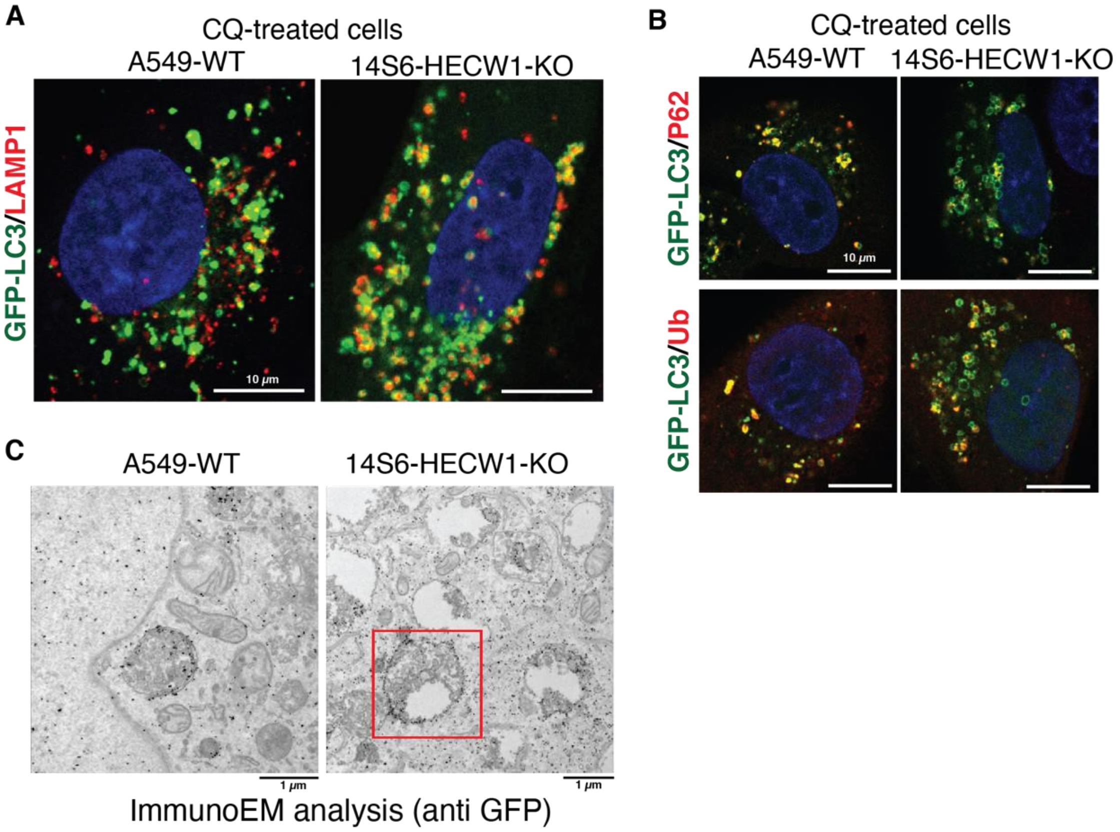

<u>Figure 47 HECW1 depletion impairs endosome-lysosome/autophagosome fusion in A549 cells</u>

A) IF analysis of A549 ctrl and 14S6-HECW1-KO cells stable-transfected with the tandem-labelled version of LC3 (RFP-GFP-LC3), treated with 100uM of chloroquine for 2h and stained with LAMP1-antibody. LC3 is stained in green, LAMP1 in red (true color far-red) and nuclei in blue (DAPI). Scale bar: 10 μm; CQ: chloroquine.

B) IF analysis for cells treated as in A stained with P62-antibody (top) or Ub-antibody (bottom). LC3 is stained in green, P62 and Ub in red (true color far-red) and nuclei in blue (DAPI). Scale bar: 10 μm; CQ: chloroquine.

C) CLEM analysis with gold-bound GFP-antibody for cells treated as in A. Scale bar: 1 μm

---

To test whether HECW1-depletion could have a general impact on vesicle trafficking or influence other endocytic organelles, we performed further IF experiments using known markers for different intracellular compartments. Upon HECW1-depletion in A549 cells, we did not detected alteration at the level of early endosomes (EE), as observed by immunostaining for the EE marker EEA1 (**Fig. 48A**). EGFR internalization in HECW1-KO A549 cells was also not affected (**Fig. 48B**), indicating that HECW1 depletion does not have a general impact on endo-lysosomal trafficking.

Taken together, these results suggest a role for HECW1 in the endo-lysosomal pathway that may be required for the correct formation and/or fusion of the autophagy compartments.

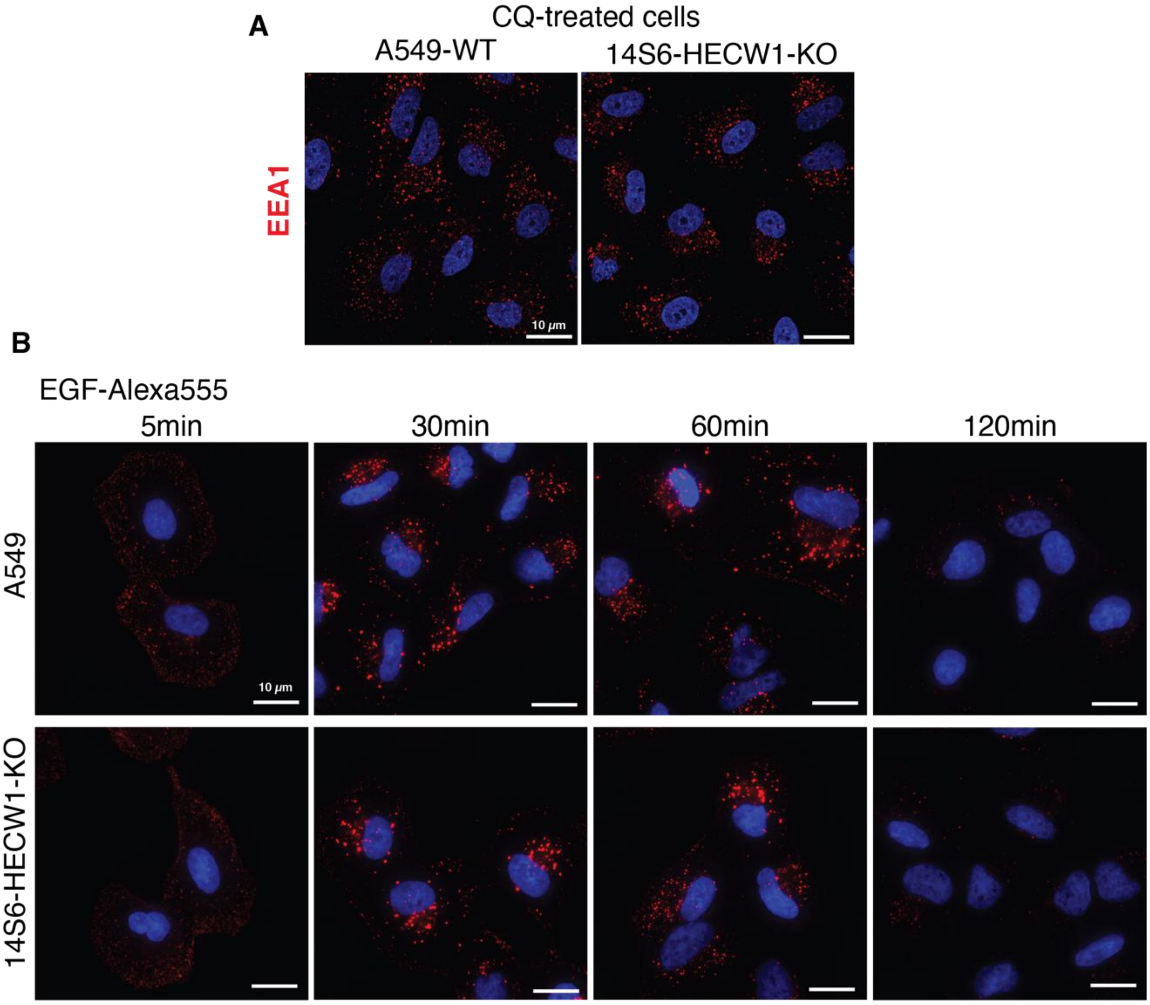

Figure 48 HECW1 depletion does not present EEA1 aggregates or defects in EGF internalization

A) IF analysis of A549 ctrl and 14S6-HECW1-KO cells treated with 100uM of chloroquine for 2h and stained with EEA1-antibody. EEA1 is stained in green and nuclei in blue (DAPI). Scale bar: 10 μm; CQ: chloroquine. B) EGFR endocytosis in A549 ctrl and 14S6-HECW1-KO cells was stimulated by adding EGF-Alexa555 upon an overnight serum starvation. Cells were fixed at the indicated time point post and analyzed by IF.. EGF is stained in red and nuclei in blue (DAPI). Scale bar: 10 μm

6.1.3 Generation and characterization of HECW1-WT and mutant reconstituted clones

To identify processes that are regulated by HECW1 expression level or catalytic activity, we generated stable inducible 14S6-HECW1-KO cell lines expressing a GFP-tagged fused version of the WT or catalytically inactive form of HECW1 (CS) where cysteine 1574 in the HECT domain is mutated into a serine that cannot catalyze substrate ubiquitination.

The lentiviral vector pSLIK-NEO-GFP-HECW1-WT was previously generated in our laboratory. This lentiviral vector harbors the neomycin resistance and a doxycycline-inducible version of GFP-HECW1. Through direct mutagenesis followed by sequencing, we generated the pSLIK-NEO-GFP-HECW1-CS vector. 14S6-HECW1-KO cells were infected with virus carrying these vectors, or with the pSLIK-NEO empty vector as a control, and selected for neomycin resistance.

By single cell cloning after GFP-sorting, we generated and screened clones for the expression of the fusion protein GFP-HECW1. Cl2_WT and Cl1_CS were selected for further experiments. WB analysis confirmed the re-expression of HECW1 upon doxycycline treatment in both clones (**Fig. 49A**), and IF analysis showed HECW1 cytoplasmic localization with complete colocalization of GFP and anti-HECW1 antibody staining (**Fig. 49B**).

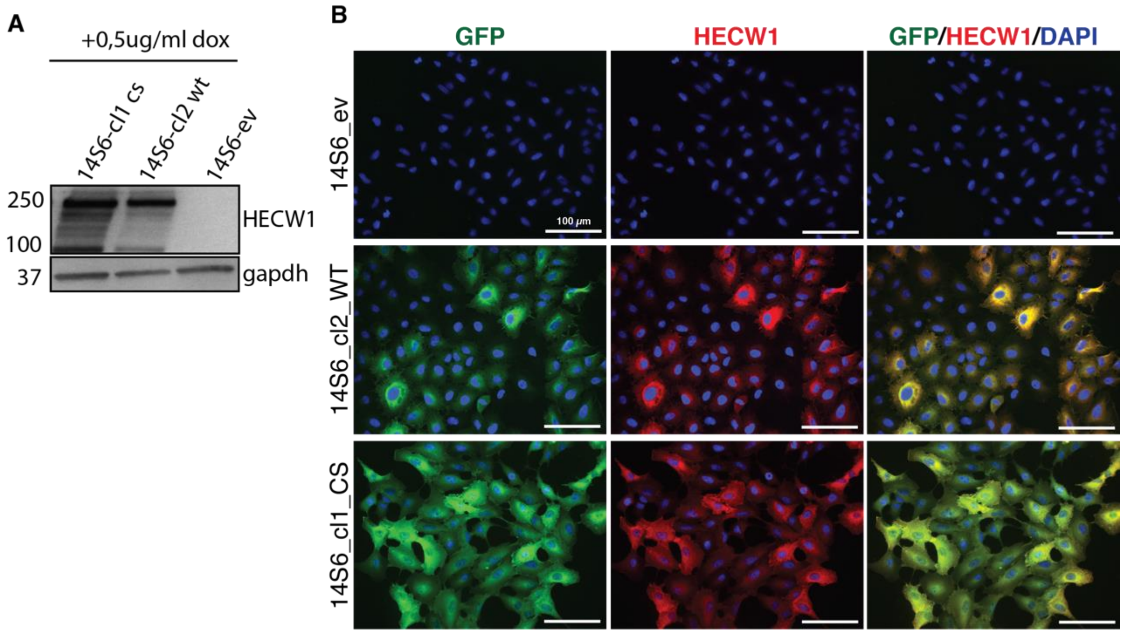

Figure 49 Characterization of HECW1-KO clones re-expressing WT or inactive GFP-HECW1 proteins upon doxycycline induction

14S6 HECW1-KO cells were transduced with pSLIK-NEO empty or pSLIK-NEO expressing a doxycycline-inducible GFP fused WT or inactive (CS) HECW1 protein, and single cell clones were chosen and characterized.

A) IB analysis of the selected clones 14S6-cl1_CS and 14S6-cl2_WT, and the cells transfected with the empty vector, treated with doxycycline (dox, 0,5ug/ml for 48 hours) to induce GFP-HECW1 expression.

B) IF analysis of the same cells as in A, stained for HECW1 and GFP expression. GFP is stained in green, HECW1 in red and the nuclei in blue (DAPI). Scale bar: 100 µm. dox: doxycycline; ev: empty vector.

The depletion of HECW1 or the absence of its catalytic activity do not have macroscopical effects on cell morphology or viability. To evaluate possible consequences on cell proliferation, we performed Cell Titer-Glo Luminescent Cell Viability Assay. This highly sensitive method assesses cell proliferation and cytotoxicity using the luciferase reaction to measure ATP, a global indicator of cellular metabolism. Cells depleted for HECW1 (EV) or lacking the catalytic activity (Cl1_CS) showed a growth curve similar to that of Cl2_WT (**Fig. 50**), indicating that HECW1 does not strongly impact on A549 cell proliferation and survival.

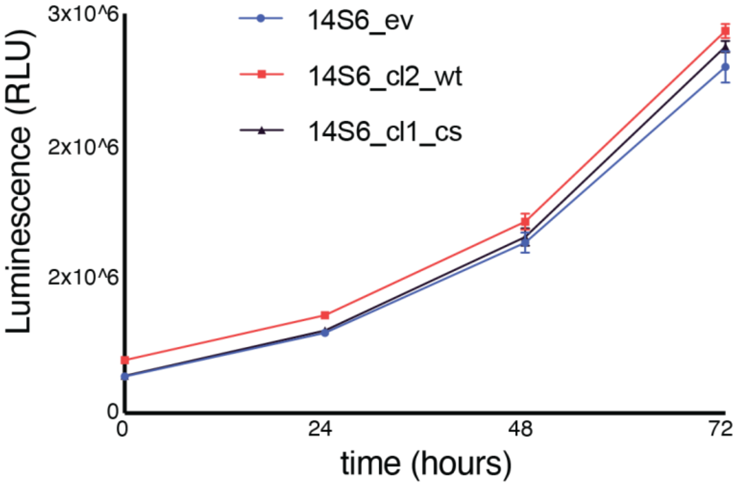

Figure 50 Growth curve of HECW1-reconstitued clones

Growth curve of 14S6-ev, 14S6-c2_WT and 14S6-cl1_CS cells treated with doxycycline to induce HECW1 expression. Cells were seeded into 96-well plates at a concentration of 3500 cells/well. At seeding (time 0) and every 24 hours (until 72h, day 3 from seeding), cells from three wells per condition were lysed with Cell Titer-Glo Luminescent Cell Viability Assay reagent (Promega) and luminescence (RLU) was read using the Envision plate reader. ev: empty vector; RLU: relative light units.

6.2 Conclusion

With A549 we could prove a general effect caused by HECW1 depletion that causes aberrant vesicles of the lysosomal/autophagosomal pathway. This role could be more relevant in neurons that are characterized by a high rate of basal constitutive autophagy to allow clearance of aggregated proteins and dysfunctional organelles that are not diluted by cell division (Maday and Holzbaur, 2014; Maday et al., 2012; Stavoe et al., 2019; Stavoe and Holzbaur, 2019). In addition, the distinctive structure of neurons adds a spatial dimension to each step of this pathway, with autophagic organelle biogenesis, transport, and degradation occurring in different subcellular compartments (Maday and Holzbaur, 2014). Hence, considering the specific neuronal expression of HECW1 and the unique characteristics of neuronal cells, we moved to iPSC-derived neurons as the principal cellular model to further characterize the role of HECW1 in the endolysosomal/autophagic pathway.

7 REFERENCES

Abildgaard, M.H., Brynjolfsdottir, S.H., and Frankel, L.B. (2020). The Autophagy-RNA Interplay: Degradation and Beyond. Trends Biochem Sci *45*, 845-857.

Abriel, H., Loffing, J., Rebhun, J.F., Pratt, J.H., Schild, L., Horisberger, J.D., Rotin, D., and Staub, O. (1999). Defective regulation of the epithelial Na+ channel by Nedd4 in Liddle's syndrome. J Clin Invest *103*, 667-673.

Acconcia, F., Sigismund, S., and Polo, S. (2009). Ubiquitin in trafficking: the network at work. Exp Cell Res *315*, 1610-1618.

Akutsu, M., Dikic, I., and Bremm, A. (2016). Ubiquitin chain diversity at a glance. J Cell Sci *129*, 875-880.

Amodio, N., Scrima, M., Palaia, L., Salman, A.N., Quintiero, A., Franco, R., Botti, G., Pirozzi, P., Rocco, G., De Rosa, N., *et al.* (2010). Oncogenic role of the E3 ubiquitin ligase NEDD4-1, a PTEN negative regulator, in non-small-cell lung carcinomas. Am J Pathol *177*, 2622-2634.

Anderson, P., and Kedersha, N. (2008). Stress granules: the Tao of RNA triage. Trends Biochem Sci *33*, 141-150.

Aulas, A., Caron, G., Gkogkas, C.G., Mohamed, N.V., Destroismaisons, L., Sonenberg, N., Leclerc, N., Parker, J.A., and Vande Velde, C. (2015). G3BP1 promotes stress-induced RNA granule interactions to preserve polyadenylated mRNA. J Cell Biol *209*, 73-84.

Ayache, J., Benard, M., Ernoult-Lange, M., Minshall, N., Standart, N., Kress, M., and Weil, D. (2015). P-body assembly requires DDX6 repression complexes rather than decay or Ataxin2/2L complexes. Mol Biol Cell *26*, 2579-2595.

Baumann, S., Pohlmann, T., Jungbluth, M., Brachmann, A., and Feldbrugge, M. (2012). Kinesin-3 and dynein mediate microtubule-dependent co-transport of mRNPs and endosomes. J Cell Sci *125*, 2740-2752.

Baumgartner, R., Stocker, H., and Hafen, E. (2013). The RNA-binding proteins FMR1, rasputin and caprin act together with the UBA protein lingerer to restrict tissue growth in Drosophila melanogaster. PLoS Genet *9*, e1003598.

Bento, C.F., Renna, M., Ghislat, G., Puri, C., Ashkenazi, A., Vicinanza, M., Menzies, F.M., and Rubinsztein, D.C. (2016). Mammalian Autophagy: How Does It Work? Annu Rev Biochem *85*, 685-713.

Bernassola, F., Karin, M., Ciechanover, A., and Melino, G. (2008). The HECT family of E3 ubiquitin ligases: multiple players in cancer development. Cancer Cell *14*, 10-21.

Berndsen, C.E., and Wolberger, C. (2014). New insights into ubiquitin E3 ligase mechanism. Nat Struct Mol Biol *21*, 301-307.

Besse, F., and Ephrussi, A. (2008). Translational control of localized mRNAs: restricting protein synthesis in space and time. Nat Rev Mol Cell Biol *9*, 971-980.

Beznoussenko, G.V., and Mironov, A.A. (2015). Correlative video-light-electron microscopy of mobile organelles. Methods Mol Biol *1270*, 321-346.

Beznoussenko, G.V., Parashuraman, S., Rizzo, R., Polishchuk, R., Martella, O., Di Giandomenico, D., Fusella, A., Spaar, A., Sallese, M., and Capestrano, M.G. (2014). Transport of soluble proteins through the Golgi occurs by diffusion via continuities across cisternae. Elife *3*, e02009.

Beznoussenko, G.V., Ragnini-Wilson, A., Wilson, C., and Mironov, A.A. (2016). Three-dimensional and immune electron microscopic analysis of the secretory pathway in Saccharomyces cerevisiae. Histochemistry and cell biology *146*, 515-527.

Bianco, A., Dienstbier, M., Salter, H.K., Gatto, G., and Bullock, S.L. (2010). Bicaudal-D regulates fragile X mental retardation protein levels, motility, and function during neuronal morphogenesis. Curr Biol *20*, 1487-1492.

Birgisdottir, A.B., and Johansen, T. (2020). Autophagy and endocytosis - interconnections and interdependencies. J Cell Sci *133*.

Blackwell, E., Zhang, X., and Ceman, S. (2010). Arginines of the RGG box regulate FMRP association with polyribosomes and mRNA. Hum Mol Genet *19*, 1314-1323.

Blot, V., Perugi, F., Gay, B., Prevost, M.C., Briant, L., Tangy, F., Abriel, H., Staub, O., Dokhelar, M.C., and Pique, C. (2004). Nedd4.1-mediated ubiquitination and subsequent recruitment of Tsg101 ensure HTLV-1 Gag trafficking towards the multivesicular body pathway prior to virus budding. J Cell Sci *117*, 2357-2367.

Boeynaems, S., Alberti, S., Fawzi, N.L., Mittag, T., Polymenidou, M., Rousseau, F., Schymkowitz, J., Shorter, J., Wolozin, B., Van Den Bosch, L.*, et al.* (2018). Protein Phase Separation: A New Phase in Cell Biology. Trends Cell Biol *28*, 420-435.

Boya, P., Reggiori, F., and Codogno, P. (2013). Emerging regulation and functions of autophagy. Nat Cell Biol *15*, 713-720.

Brinkman, E.K., Chen, T., Amendola, M., and van Steensel, B. (2014). Easy quantitative assessment of genome editing by sequence trace decomposition. Nucleic Acids Res *42*, e168.

Buchan, J.R., Kolaitis, R.M., Taylor, J.P., and Parker, R. (2013). Eukaryotic stress granules are cleared by autophagy and Cdc48/VCP function. Cell *153*, 1461-1474.

Buchan, J.R., and Parker, R. (2009). Eukaryotic stress granules: the ins and outs of translation. Mol Cell *36*, 932-941.

Buetow, L., and Huang, D.T. (2016). Structural insights into the catalysis and regulation of E3 ubiquitin ligases. Nat Rev Mol Cell Biol *17*, 626-642.

Cao, X.R., Lill, N.L., Boase, N., Shi, P.P., Croucher, D.R., Shan, H., Qu, J., Sweezer, E.M., Place, T., Kirby, P.A.*, et al.* (2008). Nedd4 controls animal growth by regulating IGF-1 signaling. Sci Signal *1*, ra5.

Carnio, S., LoVerso, F., Baraibar, M.A., Longa, E., Khan, M.M., Maffei, M., Reischl, M., Canepari, M., Loefler, S., Kern, H.*, et al.* (2014). Autophagy impairment in muscle induces neuromuscular junction degeneration and precocious aging. Cell Rep *8*, 1509-1521.

Chang, C., Jensen, L.E., and Hurley, J.H. (2021). Autophagosome biogenesis comes out of the black box. Nat Cell Biol *23*, 450-456.

Chastagner, P., Israel, A., and Brou, C. (2008). AIP4/Itch regulates Notch receptor degradation in the absence of ligand. PLoS One *3*, e2735.

Chekulaeva, M., Hentze, M.W., and Ephrussi, A. (2006). Bruno acts as a dual repressor of oskar translation, promoting mRNA oligomerization and formation of silencing particles. Cell *124*, 521-533.

Chen, C., Sun, X., Guo, P., Dong, X.Y., Sethi, P., Cheng, X., Zhou, J., Ling, J., Simons, J.W., Lingrel, J.B., *et al.* (2005). Human Kruppel-like factor 5 is a target of the E3 ubiquitin ligase WWP1 for proteolysis in epithelial cells. J Biol Chem *280*, 41553-41561.

Chen, C., Sun, X., Guo, P., Dong, X.Y., Sethi, P., Zhou, W., Zhou, Z., Petros, J., Frierson, H.F., Jr., Vessella, R.L.*, et al.* (2007). Ubiquitin E3 ligase WWP1 as an oncogenic factor in human prostate cancer. Oncogene *26*, 2386-2394.

Chen, E.Y., Tan, C.M., Kou, Y., Duan, Q., Wang, Z., Meirelles, G.V., Clark, N.R., and Ma'ayan, A. (2013). Enrichr: interactive and collaborative HTML5 gene list enrichment analysis tool. BMC Bioinformatics *14*, 128.

Chen, Z., Jiang, H., Xu, W., Li, X., Dempsey, D.R., Zhang, X., Devreotes, P., Wolberger, C., Amzel, L.M., Gabelli, S.B.*, et al.* (2017). A Tunable Brake for HECT Ubiquitin Ligases. Mol Cell *66*, 345-357 e346.

Cheng, X.T., Xie, Y.X., Zhou, B., Huang, N., Farfel-Becker, T., and Sheng, Z.H. (2018). Characterization of LAMP1-labeled nondegradative lysosomal and endocytic compartments in neurons. J Cell Biol *217*, 3127-3139.

Cheng, X.T., Zhou, B., Lin, M.Y., Cai, Q., and Sheng, Z.H. (2015). Axonal autophagosomes recruit dynein for retrograde transport through fusion with late endosomes. J Cell Biol *209*, 377-386.

Choi, K.S., Choi, H.J., Lee, J.K., Im, S., Zhang, H., Jeong, Y., Park, J.A., Lee, I.K., Kim, Y.M., and Kwon, Y.G. (2016). The endothelial E3 ligase HECW2 promotes endothelial cell junctions by increasing AMOTL1 protein stability via K63-linked ubiquitination. Cell Signal *28*, 1642-1651.

Chong, P.A., and Forman-Kay, J.D. (2016). Liquid-liquid phase separation in cellular signaling systems. Curr Opin Struct Biol *41*, 180-186.

Ciechanover, A., and Ben-Saadon, R. (2004). N-terminal ubiquitination: more protein substrates join in. Trends Cell Biol *14*, 103-106.

Cioni, J.M., Lin, J.Q., Holtermann, A.V., Koppers, M., Jakobs, M.A.H., Azizi, A., Turner-Bridger, B., Shigeoka, T., Franze, K., Harris, W.A., *et al.* (2019). Late Endosomes Act as mRNA Translation Platforms and Sustain Mitochondria in Axons. Cell *176*, 56-72 e15.

Cirillo, L., Cieren, A., Barbieri, S., Khong, A., Schwager, F., Parker, R., and Gotta, M. (2020). UBAP2L Forms Distinct Cores that Act in Nucleating Stress Granules Upstream of G3BP1. Curr Biol *30*, 698-707 e696.

Cooper, O., Seo, H., Andrabi, S., Guardia-Laguarta, C., Graziotto, J., Sundberg, M., McLean, J.R., Carrillo-Reid, L., Xie, Z., Osborn, T., *et al.* (2012). Pharmacological rescue of mitochondrial deficits in iPSC-derived neural cells from patients with familial Parkinson's disease. Sci Transl Med *4*, 141ra190.

Corbalan-Garcia, S., and Gomez-Fernandez, J.C. (2014). Signaling through C2 domains: more than one lipid target. Biochim Biophys Acta *1838*, 1536-1547.

Cougot, N., Babajko, S., and Seraphin, B. (2004). Cytoplasmic foci are sites of mRNA decay in human cells. J Cell Biol *165*, 31-40.

Coussens, L., Parker, P.J., Rhee, L., Yang-Feng, T.L., Chen, E., Waterfield, M.D., Francke, U., and Ullrich, A. (1986). Multiple, distinct forms of bovine and human protein kinase C suggest diversity in cellular signaling pathways. Science *233*, 859-866.

Cutrona, M.B., Beznoussenko, G.V., Fusella, A., Martella, O., Moral, P., and Mironov, A.A. (2013). Silencing of mammalian Sar1 isoforms reveals COPII-independent protein sorting and transport. Traffic *14*, 691-708.

Davidovic, L., Jaglin, X.H., Lepagnol-Bestel, A.M., Tremblay, S., Simonneau, M., Bardoni, B., and Khandjian, E.W. (2007). The fragile X mental retardation protein is a molecular adaptor between the neurospecific KIF3C kinesin and dendritic RNA granules. Hum Mol Genet *16*, 3047-3058.

de Lartigue, J., Polson, H., Feldman, M., Shokat, K., Tooze, S.A., Urbe, S., and Clague, M.J. (2009). PIKfyve regulation of endosome-linked pathways. Traffic *10*, 883-893.

Deshaies, R.J., and Joazeiro, C.A. (2009). RING domain E3 ubiquitin ligases. Annu Rev Biochem *78*, 399-434.

Di Malta, C., Cinque, L., and Settembre, C. (2019). Transcriptional Regulation of Autophagy: Mechanisms and Diseases. Front Cell Dev Biol *7*, 114.

Di Rita, A., Peschiaroli, A., P, D.A., Strobbe, D., Hu, Z., Gruber, J., Nygaard, M., Lambrughi, M., Melino, G., Papaleo, E., *et al.* (2018). HUWE1 E3 ligase promotes PINK1/PARKIN-independent mitophagy by regulating AMBRA1 activation via IKKalpha. Nat Commun *9*, 3755.

Donovan, P., and Poronnik, P. (2013). Nedd4 and Nedd4-2: ubiquitin ligases at work in the neuron. Int J Biochem Cell Biol *45*, 706-710.

Dooley, H.C., Razi, M., Polson, H.E., Girardin, S.E., Wilson, M.I., and Tooze, S.A. (2014). WIPI2 links LC3 conjugation with PI3P, autophagosome formation, and pathogen clearance by recruiting Atg12-5-16L1. Mol Cell *55*, 238-252.

Dou, H., Buetow, L., Hock, A., Sibbet, G.J., Vousden, K.H., and Huang, D.T. (2012). Structural basis for autoinhibition and phosphorylation-dependent activation of c-Cbl. Nat Struct Mol Biol *19*, 184-192.

Dove, K.K., and Klevit, R.E. (2017). RING-Between-RING E3 Ligases: Emerging Themes amid the Variations. J Mol Biol *429*, 3363-3375.

Dudman, J., and Qi, X. (2020). Stress Granule Dysregulation in Amyotrophic Lateral Sclerosis. Front Cell Neurosci *14*, 598517.

Dye, B.T., and Schulman, B.A. (2007). Structural mechanisms underlying posttranslational modification by ubiquitin-like proteins. Annu Rev Biophys Biomol Struct *36*, 131-150.

Eisenhaber, B., Chumak, N., Eisenhaber, F., and Hauser, M.T. (2007). The ring between ring fingers (RBR) protein family. Genome Biol *8*, 209.

Escobedo, A., Gomes, T., Aragon, E., Martin-Malpartida, P., Ruiz, L., and Macias, M.J. (2014). Structural basis of the activation and degradation mechanisms of the E3 ubiquitin ligase Nedd4L. Structure *22*, 1446-1457.

Fajner, V., Giavazzi, F., Sala, S., Oldani, A., Martini, E., Napoletano, F., Parazzoli, D., Cerbino, R., Maspero, E., Vaccari, T.*, et al.* (2021). Hecw controls oogenesis and neuronal homeostasis by promoting the liquid state of ribonucleoprotein particles. Nat Commun *12*, 5488.

Fajner, V., Maspero, E., and Polo, S. (2017). Targeting HECT-type E3 ligases - insights from catalysis, regulation and inhibitors. FEBS Lett *591*, 2636-2647.

Fan, A.C., and Leung, A.K. (2016). RNA Granules and Diseases: A Case Study of Stress Granules in ALS and FTLD. Adv Exp Med Biol *907*, 263-296.

Fang, N.N., Chan, G.T., Zhu, M., Comyn, S.A., Persaud, A., Deshaies, R.J., Rotin, D., Gsponer, J., and Mayor, T. (2014). Rsp5/Nedd4 is the main ubiquitin ligase that targets cytosolic misfolded proteins following heat stress. Nat Cell Biol *16*, 1227-1237.

Fecto, F., Yan, J., Vemula, S.P., Liu, E., Yang, Y., Chen, W., Zheng, J.G., Shi, Y., Siddique, N., Arrat, H., *et al.* (2011). SQSTM1 mutations in familial and sporadic amyotrophic lateral sclerosis. Arch Neurol *68*, 1440-1446.

Feng, X., Jia, Y., Zhang, Y., Ma, F., Zhu, Y., Hong, X., Zhou, Q., He, R., Zhang, H., Jin, J*., et al.* (2019). Ubiquitination of UVRAG by SMURF1 promotes autophagosome maturation and inhibits hepatocellular carcinoma growth. Autophagy *15*, 1130-1149.

Feng, Y., He, D., Yao, Z., and Klionsky, D.J. (2014). The machinery of macroautophagy. Cell Res *24*, 24-41.

Ferguson, C.J., Lenk, G.M., and Meisler, M.H. (2009). Defective autophagy in neurons and astrocytes from mice deficient in PI(3,5)P2. Hum Mol Genet *18*, 4868-4878.

Fernandopulle, M.S., Lippincott-Schwartz, J., and Ward, M.E. (2021). RNA transport and local translation in neurodevelopmental and neurodegenerative disease. Nat Neurosci *24*, 622-632.

Fernandopulle, M.S., Prestil, R., Grunseich, C., Wang, C., Gan, L., and Ward, M.E. (2018). Transcription Factor-Mediated Differentiation of Human iPSCs into Neurons. Curr Protoc Cell Biol *79*, e51.

Filimonenko, M., Isakson, P., Finley, K.D., Anderson, M., Jeong, H., Melia, T.J., Bartlett, B.J., Myers, K.M., Birkeland, H.C., Lamark, T.*, et al.* (2010). The selective macroautophagic degradation of aggregated proteins requires the PI3P-binding protein Alfy. Mol Cell *38*, 265-279.

Finley, K.D., Edeen, P.T., Cumming, R.C., Mardahl-Dumesnil, M.D., Taylor, B.J., Rodriguez, M.H., Hwang, C.E., Benedetti, M., and McKeown, M. (2003). blue cheese mutations define a novel, conserved gene involved in progressive neural degeneration. J Neurosci *23*, 1254-1264.

Fouladkou, F., Landry, T., Kawabe, H., Neeb, A., Lu, C., Brose, N., Stambolic, V., and Rotin, D. (2008). The ubiquitin ligase Nedd4-1 is dispensable for the regulation of PTEN stability and localization. Proc Natl Acad Sci U S A *105*, 8585-8590.

Frankel, L.B., Lubas, M., and Lund, A.H. (2017). Emerging connections between RNA and autophagy. Autophagy *13*, 3-23.

French, M.E., Klosowiak, J.L., Aslanian, A., Reed, S.I., Yates, J.R., 3rd, and Hunter, T. (2017). Mechanism of ubiquitin chain synthesis employed by a HECT domain ubiquitin ligase. J Biol Chem *292*, 10398-10413.

Fu, M.M., and Holzbaur, E.L. (2014). MAPK8IP1/JIP1 regulates the trafficking of autophagosomes in neurons. Autophagy *10*, 2079-2081.

Fu, M.M., Nirschl, J.J., and Holzbaur, E.L.F. (2014). LC3 binding to the scaffolding protein JIP1 regulates processive dynein-driven transport of autophagosomes. Dev Cell *29*, 577-590.

Fukuchi, M., Fukai, Y., Masuda, N., Miyazaki, T., Nakajima, M., Sohda, M., Manda, R., Tsukada, K., Kato, H., and Kuwano, H. (2002). High-level expression of the Smad ubiquitin ligase Smurf2 correlates with poor prognosis in patients with esophageal squamous cell carcinoma. Cancer Res *62*, 7162-7165.

Fukuda, Y., Pazyra-Murphy, M.F., Silagi, E.S., Tasdemir-Yilmaz, O.E., Li, Y., Rose, L., Yeoh, Z.C., Vangos, N.E., Geffken, E.A., Seo, H.S., *et al.* (2021). Binding and transport of SFPQ-RNA granules by KIF5A/KLC1 motors promotes axon survival. J Cell Biol *220*.

Fusella, A., Micaroni, M., Di Giandomenico, D., Mironov, A.A., and Beznoussenko, G.V. (2013). Segregation of the Qb-SNAREs GS27 and GS28 into Golgi vesicles regulates intra-Golgi transport. Traffic *14*, 568-584.

Gallagher, E., Gao, M., Liu, Y.C., and Karin, M. (2006). Activation of the E3 ubiquitin ligase Itch through a phosphorylation-induced conformational change. Proc Natl Acad Sci U S A *103*, 1717-1722.

Gamerdinger, M., Hajieva, P., Kaya, A.M., Wolfrum, U., Hartl, F.U., and Behl, C. (2009). Protein quality control during aging involves recruitment of the macroautophagy pathway by BAG3. EMBO J *28*, 889-901.

Gatti, M., Pinato, S., Maiolica, A., Rocchio, F., Prato, M.G., Aebersold, R., and Penengo, L. (2015). RNF168 promotes noncanonical K27 ubiquitination to signal DNA damage. Cell Rep *10*, 226-238.

Geng, J., and Klionsky, D.J. (2008). The Atg8 and Atg12 ubiquitin-like conjugation systems in macroautophagy. 'Protein modifications: beyond the usual suspects' review series. EMBO Rep *9*, 859-864.

Georgieva, M.V., de Pablo, Y., Sanchis, D., Comella, J.X., and Llovera, M. (2011). Ubiquitination of TrkA by Nedd4-2 regulates receptor lysosomal targeting and mediates receptor signaling. J Neurochem *117*, 479-493.

Glock, C., Heumuller, M., and Schuman, E.M. (2017). mRNA transport & local translation in neurons. Curr Opin Neurobiol *45*, 169-177.

Green, D.R., and Levine, B. (2014). To be or not to be? How selective autophagy and cell death govern cell fate. Cell *157*, 65-75.

Grumati, P., and Dikic, I. (2018). Ubiquitin signaling and autophagy. J Biol Chem *293*, 5404-5413.

Grumati, P., Dikic, I., and Stolz, A. (2018). ER-phagy at a glance. J Cell Sci *131*.

Gu, Z., Eils, R., and Schlesner, M. (2016). Complex heatmaps reveal patterns and correlations in multidimensional genomic data. Bioinformatics *32*, 2847-2849.

Gwon, Y., Maxwell, B.A., Kolaitis, R.-M., Zhang, P., Kim, H.J., and Taylor, J.P. (2021). Ubiquitination of G3BP1 mediates stress granule disassembly in a context-specific manner. Science *372*.

Hansen, M., Rubinsztein, D.C., and Walker, D.W. (2018). Publisher Correction: Autophagy as a promoter of longevity: insights from model organisms. Nat Rev Mol Cell Biol *19*, 611.

Harvey, K.F., Dinudom, A., Cook, D.I., and Kumar, S. (2001). The Nedd4-like protein KIAA0439 is a potential regulator of the epithelial sodium channel. J Biol Chem *276*, 8597-8601.

Harvey, K.F., and Kumar, S. (1999). Nedd4-like proteins: an emerging family of ubiquitin-protein ligases implicated in diverse cellular functions. Trends Cell Biol *9*, 166-169.

Hasegawa, J., Iwamoto, R., Otomo, T., Nezu, A., Hamasaki, M., and Yoshimori, T. (2016). Autophagosome-lysosome fusion in neurons requires INPP5E, a protein associated with Joubert syndrome. EMBO J *35*, 1853-1867.

Herhaus, L., and Dikic, I. (2015). Expanding the ubiquitin code through post-translational modification. EMBO Rep *16*, 1071-1083.

Hicke, L. (2001). Protein regulation by monoubiquitin. Nat Rev Mol Cell Biol *2*, 195-201.

Hoege, C., Pfander, B., Moldovan, G.L., Pyrowolakis, G., and Jentsch, S. (2002). RAD6-dependent DNA repair is linked to modification of PCNA by ubiquitin and SUMO. Nature *419*, 135-141.

Hofmann, S., Kedersha, N., Anderson, P., and Ivanov, P. (2021). Molecular mechanisms of stress granule assembly and disassembly. Biochim Biophys Acta Mol Cell Res *1868*, 118876.

Huang L, K.E., Wang G, Beaudenon S, Howley PM, Huibregtse JM, Pavletich NP. (1999). Structure of an E6AP-UbcH7 complex: insights into ubiquitination by the E2-E3 enzyme cascade. Science *12*, 1321-1326.

Huang, Y.S., Jung, M.Y., Sarkissian, M., and Richter, J.D. (2002). N-methyl-D-aspartate receptor signaling results in Aurora kinase-catalyzed CPEB phosphorylation and alpha CaMKII mRNA polyadenylation at synapses. EMBO J *21*, 2139-2148.

Huibregtse JM1, S.M., Beaudenon S, Howley PM. (1995). A family of proteins structurally and functionally related to the E6-AP ubiquitin-protein ligase. PNAS *92*, 2563-2525-2567.

Huttelmaier, S., Zenklusen, D., Lederer, M., Dictenberg, J., Lorenz, M., Meng, X., Bassell, G.J., Condeelis, J., and Singer, R.H. (2005). Spatial regulation of beta-actin translation by Src-dependent phosphorylation of ZBP1. Nature *438*, 512-515.

Ingham, R.J., Colwill, K., Howard, C., Dettwiler, S., Lim, C.S., Yu, J., Hersi, K., Raaijmakers, J., Gish, G., Mbamalu, G.*, et al.* (2005). WW domains provide a platform for the assembly of multiprotein networks. Mol Cell Biol *25*, 7092-7106.

Iwai, K., Fujita, H., and Sasaki, Y. (2014). Linear ubiquitin chains: NF-kappaB signalling, cell death and beyond. Nat Rev Mol Cell Biol *15*, 503-508.

Jain, A., and Vale, R.D. (2017). RNA phase transitions in repeat expansion disorders. Nature *546*, 243-247.

Johansen, T., and Lamark, T. (2020). Selective Autophagy: ATG8 Family Proteins, LIR Motifs and Cargo Receptors. J Mol Biol *432*, 80-103.

Juhasz, G., Erdi, B., Sass, M., and Neufeld, T.P. (2007). Atg7-dependent autophagy promotes neuronal health, stress tolerance, and longevity but is dispensable for metamorphosis in Drosophila. Genes Dev *21*, 3061-3066.

Kamadurai, H.B., Qiu, Y., Deng, A., Harrison, J.S., Macdonald, C., Actis, M., Rodrigues, P., Miller, D.J., Souphron, J., Lewis, S.M.*, et al.* (2013). Mechanism of ubiquitin ligation and lysine prioritization by a HECT E3. Elife *2*, e00828.

Kamadurai, H.B., Souphron, J., Scott, D.C., Duda, D.M., Miller, D.J., Stringer, D., Piper, R.C., and Schulman, B.A. (2009). Insights into ubiquitin transfer cascades from a structure of a UbcH5B approximately ubiquitin-HECT(NEDD4L) complex. Mol Cell *36*, 1095-1102.

Kamynina, E., Debonneville, C., Bens, M., Vandewalle, A., and Staub, O. (2001). A novel mouse Nedd4 protein suppresses the activity of the epithelial Na+ channel. FASEB J *15*, 204-214.

Karanasios, E., Walker, S.A., Okkenhaug, H., Manifava, M., Hummel, E., Zimmermann, H., Ahmed, Q., Domart, M.C., Collinson, L., and Ktistakis, N.T. (2016). Autophagy initiation by ULK complex assembly on ER tubulovesicular regions marked by ATG9 vesicles. Nat Commun *7*, 12420.

Katz, M., Shtiegman, K., Tal-Or, P., Yakir, L., Mosesson, Y., Harari, D., Machluf, Y., Asao, H., Jovin, T., Sugamura, K.*, et al.* (2002). Ligand-independent degradation of epidermal growth factor receptor involves receptor ubiquitylation and Hgs, an adaptor whose ubiquitin-interacting motif targets ubiquitylation by Nedd4. Traffic *3*, 740-751.

Kawabe, H., Neeb, A., Dimova, K., Young, S.M., Jr., Takeda, M., Katsurabayashi, S., Mitkovski, M., Malakhova, O.A., Zhang, D.E., Umikawa, M.*, et al.* (2010). Regulation of Rap2A by the ubiquitin ligase Nedd4-1 controls neurite development. Neuron *65*, 358-372.

Kedersha, N., Cho, M.R., Li, W., Yacono, P.W., Chen, S., Gilks, N., Golan, D.E., and Anderson, P. (2000). Dynamic shuttling of TIA-1 accompanies the recruitment of mRNA to mammalian stress granules. J Cell Biol *151*, 1257-1268.

Kedersha, N., Stoecklin, G., Ayodele, M., Yacono, P., Lykke-Andersen, J., Fritzler, M.J., Scheuner, D., Kaufman, R.J., Golan, D.E., and Anderson, P. (2005). Stress granules and processing bodies are dynamically linked sites of mRNP remodeling. J Cell Biol *169*, 871-884.

Kedersha, N.L., Gupta, M., Li, W., Miller, I., and Anderson, P. (1999). RNA-binding proteins TIA-1 and TIAR link the phosphorylation of eIF-2 alpha to the assembly of mammalian stress granules. J Cell Biol *147*, 1431-1442.

Kerscher, O., Felberbaum, R., and Hochstrasser, M. (2006). Modification of proteins by ubiquitin and ubiquitin-like proteins. Annu Rev Cell Dev Biol *22*, 159-180.

Khaminets, A., Behl, C., and Dikic, I. (2016). Ubiquitin-Dependent And Independent Signals In Selective Autophagy. Trends Cell Biol *26*, 6-16.

Kim, H.C., and Huibregtse, J.M. (2009). Polyubiquitination by HECT E3s and the determinants of chain type specificity. Mol Cell Biol *29*, 3307-3318.

Kim, J.H., and Richter, J.D. (2006). Opposing polymerase-deadenylase activities regulate cytoplasmic polyadenylation. Mol Cell *24*, 173-183.

Kimura, S., Noda, T., and Yoshimori, T. (2007). Dissection of the autophagosome maturation process by a novel reporter protein, tandem fluorescent-tagged LC3. Autophagy *3*, 452-460.

Kirkin, V., Lamark, T., Sou, Y.S., Bjorkoy, G., Nunn, J.L., Bruun, J.A., Shvets, E., McEwan, D.G., Clausen, T.H., Wild, P.*, et al.* (2009). A role for NBR1 in autophagosomal degradation of ubiquitinated substrates. Mol Cell *33*, 505-516.

Klionsky, D.J., Abdel-Aziz, A.K., Abdelfatah, S., Abdellatif, M., Abdoli, A., Abel, S., Abeliovich, H., Abildgaard, M.H., Abudu, Y.P., Acevedo-Arozena, A*., et al.* (2021). Guidelines for the use and interpretation of assays for monitoring autophagy (4th edition)(1). Autophagy *17*, 1-382.

Kochl, R., Hu, X.W., Chan, E.Y., and Tooze, S.A. (2006). Microtubules facilitate autophagosome formation and fusion of autophagosomes with endosomes. Traffic *7*, 129-145.

Komander, D., and Rape, M. (2012). The ubiquitin code. Annu Rev Biochem *81*, 203-229.

Koppers, M., Cagnetta, R., Shigeoka, T., Wunderlich, L.C., Vallejo-Ramirez, P., Qiaojin Lin, J., Zhao, S., Jakobs, M.A., Dwivedy, A., Minett, M.S.*, et al.* (2019). Receptor-specific interactome as a hub for rapid cue-induced selective translation in axons. Elife *8*.

Korac, J., Schaeffer, V., Kovacevic, I., Clement, A.M., Jungblut, B., Behl, C., Terzic, J., and Dikic, I. (2013). Ubiquitin-independent function of optineurin in autophagic clearance of protein aggregates. J Cell Sci *126*, 580-592.

Krisenko, M.O., Higgins, R.L., Ghosh, S., Zhou, Q., Trybula, J.S., Wang, W.H., and Geahlen, R.L. (2015). Syk Is Recruited to Stress Granules and Promotes Their Clearance through Autophagy. J Biol Chem *290*, 27803-27815.

Kulak, N.A., Geyer, P.E., and Mann, M. (2017). Loss-less Nano-fractionator for High Sensitivity, High Coverage Proteomics. Mol Cell Proteomics *16*, 694-705.

Kulak, N.A., Pichler, G., Paron, I., Nagaraj, N., and Mann, M. (2014). Minimal, encapsulated proteomic-sample processing applied to copy-number estimation in eukaryotic cells. Nat Methods *11*, 319-324.

Kulathu, Y., and Komander, D. (2012). Atypical ubiquitylation - the unexplored world of polyubiquitin beyond Lys48 and Lys63 linkages. Nat Rev Mol Cell Biol *13*, 508-523.

Kumar, A., Mazzanti, M., Mistrik, M., Kosar, M., Beznoussenko, G.V., Mironov, A.A., Garre, M., Parazzoli, D., Shivashankar, G.V., Scita, G.*, et al.* (2014). ATR mediates a checkpoint at the nuclear envelope in response to mechanical stress. Cell *158*, 633-646.

Kumar, N., Leonzino, M., Hancock-Cerutti, W., Horenkamp, F.A., Li, P., Lees, J.A., Wheeler, H., Reinisch, K.M., and De Camilli, P. (2018). VPS13A and VPS13C are lipid transport proteins differentially localized at ER contact sites. J Cell Biol *217*, 3625-3639.

Laine, A., and Ronai, Z. (2007). Regulation of p53 localization and transcription by the HECT domain E3 ligase WWP1. Oncogene *26*, 1477-1483.

Lazarou, M., Sliter, D.A., Kane, L.A., Sarraf, S.A., Wang, C., Burman, J.L., Sideris, D.P., Fogel, A.I., and Youle, R.J. (2015). The ubiquitin kinase PINK1 recruits autophagy receptors to induce mitophagy. Nature *524*, 309-314.

Le Guerroue, F., and Youle, R.J. (2021). Ubiquitin signaling in neurodegenerative diseases: an autophagy and proteasome perspective. Cell Death Differ *28*, 439-454.

Li, Y., Ozaki, T., Kikuchi, H., Yamamoto, H., Ohira, M., and Nakagawara, A. (2008). A novel HECT-type E3 ubiquitin protein ligase NEDL1 enhances the p53-mediated apoptotic cell death in its catalytic activity-independent manner. Oncogene *27*, 3700-3709.

Li, Y., Zhou, Z., Alimandi, M., and Chen, C. (2009). WW domain containing E3 ubiquitin protein ligase 1 targets the full-length ErbB4 for ubiquitin-mediated degradation in breast cancer. Oncogene *28*, 2948-2958.

Liao, Y.C., Fernandopulle, M.S., Wang, G., Choi, H., Hao, L., Drerup, C.M., Patel, R., Qamar, S., Nixon-Abell, J., Shen, Y.*, et al.* (2019). RNA Granules Hitchhike on Lysosomes for Long-Distance Transport, Using Annexin A11 as a Molecular Tether. Cell *179*, 147-164 e120.

Lin, A., Hou, Q., Jarzylo, L., Amato, S., Gilbert, J., Shang, F., and Man, H.Y. (2011). Nedd4-mediated AMPA receptor ubiquitination regulates receptor turnover and trafficking. J Neurochem *119*, 27-39.

Lin, D., Pestova, T.V., Hellen, C.U., and Tiedge, H. (2008). Translational control by a small RNA: dendritic BC1 RNA targets the eukaryotic initiation factor 4A helicase mechanism. Mol Cell Biol *28*, 3008-3019.

Lin, Q., Dai, Q., Meng, H., Sun, A., Wei, J., Peng, K., Childress, C., Chen, M., Shao, G., and Yang, W. (2017). The HECT E3 ubiquitin ligase NEDD4 interacts with and ubiquitylates SQSTM1 for inclusion body autophagy. J Cell Sci *130*, 3839-3850.

Linke, K., Mace, P.D., Smith, C.A., Vaux, D.L., Silke, J., and Day, C.L. (2008). Structure of the MDM2/MDMX RING domain heterodimer reveals dimerization is required for their ubiquitylation in trans. Cell Death Differ *15*, 841-848.

Liu, G.H., Qu, J., Suzuki, K., Nivet, E., Li, M., Montserrat, N., Yi, F., Xu, X., Ruiz, S., Zhang, W.*, et al.* (2012). Progressive degeneration of human neural stem cells caused by pathogenic LRRK2. Nature *491*, 603-607.

Liu, Y.C. (2007). The E3 ubiquitin ligase Itch in T cell activation, differentiation, and tolerance. Semin Immunol *19*, 197-205.

Love, M.I., Huber, W., and Anders, S. (2014). Moderated estimation of fold change and dispersion for RNA-seq data with DESeq2. Genome Biol *15*, 550.

Lu, K., Psakhye, I., and Jentsch, S. (2014). Autophagic clearance of polyQ proteins mediated by ubiquitin-Atg8 adaptors of the conserved CUET protein family. Cell *158*, 549-563.

Lu, L., Hu, S., Wei, R., Qiu, X., Lu, K., Fu, Y., Li, H., Xing, G., Li, D., and Peng, R. (2013). The HECT type ubiquitin ligase NEDL2 is degraded by anaphase-promoting complex/cyclosome (APC/C)-Cdh1, and its tight regulation maintains the metaphase to anaphase transition. Journal of Biological Chemistry *288*, 35637-35650.

Maday, S., and Holzbaur, E.L. (2014). Autophagosome biogenesis in primary neurons follows an ordered and spatially regulated pathway. Dev Cell *30*, 71-85.

Maday, S., and Holzbaur, E.L. (2016). Compartment-Specific Regulation of Autophagy in Primary Neurons. J Neurosci *36*, 5933-5945.

Maday, S., Twelvetrees, A.E., Moughamian, A.J., and Holzbaur, E.L. (2014). Axonal transport: cargo-specific mechanisms of motility and regulation. Neuron *84*, 292-309.

Maday, S., Wallace, K.E., and Holzbaur, E.L. (2012). Autophagosomes initiate distally and mature during transport toward the cell soma in primary neurons. J Cell Biol *196*, 407-417.

Mandrioli, J., Mediani, L., Alberti, S., and Carra, S. (2020). ALS and FTD: Where RNA metabolism meets protein quality control. Semin Cell Dev Biol *99*, 183-192.

Mantripragada, K.K., Diaz de Stahl, T., Patridge, C., Menzel, U., Andersson, R., Chuzhanova, N., Kluwe, L., Guha, A., Mautner, V., Dumanski, J.P.*, et al.* (2009). Genome-wide high-resolution analysis of DNA copy number alterations in NF1-associated malignant peripheral nerve sheath tumors using 32K BAC array. Genes Chromosomes Cancer *48*, 897-907.

Marchese, A., Raiborg, C., Santini, F., Keen, J.H., Stenmark, H., and Benovic, J.L. (2003). The E3 ubiquitin ligase AIP4 mediates ubiquitination and sorting of the G protein-coupled receptor CXCR4. Dev Cell *5*, 709-722.

Mari, S., Ruetalo, N., Maspero, E., Stoffregen, M.C., Pasqualato, S., Polo, S., and Wiesner, S. (2014). Structural and functional framework for the autoinhibition of Nedd4-family ubiquitin ligases. Structure *22*, 1639-1649.

Markmiller, S., Fulzele, A., Higgins, R., Leonard, M., Yeo, G.W., and Bennett, E.J. (2019). Active Protein Neddylation or Ubiquitylation Is Dispensable for Stress Granule Dynamics. Cell Rep *27*, 1356-1363 e1353.

Markmiller, S., Soltanieh, S., Server, K.L., Mak, R., Jin, W., Fang, M.Y., Luo, E.C., Krach, F., Yang, D., Sen, A.*, et al.* (2018). Context-Dependent and Disease-Specific Diversity in Protein Interactions within Stress Granules. Cell *172*, 590-604 e513.

Martin, S., Harper, C.B., May, L.M., Coulson, E.J., Meunier, F.A., and Osborne, S.L. (2013). Inhibition of PIKfyve by YM-201636 dysregulates autophagy and leads to apoptosis-independent neuronal cell death. PLoS One *8*, e60152.

Maspero, E., Valentini, E., Mari, S., Cecatiello, V., Soffientini, P., Pasqualato, S., and Polo, S. (2013). Structure of a ubiquitin-loaded HECT ligase reveals the molecular basis for catalytic priming. Nat Struct Mol Biol *20*, 696-701.

Mauthe, M., Orhon, I., Rocchi, C., Zhou, X., Luhr, M., Hijlkema, K.J., Coppes, R.P., Engedal, N., Mari, M., and Reggiori, F. (2018). Chloroquine inhibits autophagic flux by decreasing autophagosome-lysosome fusion. Autophagy *14*, 1435-1455.

Maxwell, B.A., Gwon, Y., Mishra, A., Peng, J., Zhang, K., Kim, H.J., and Taylor, J.P. (2021). Ubiquitination is essential for recovery of cellular activities following heat shock. bioRxiv.

Mayhew, T.M. (2007). Quantitative immunoelectron microscopy: alternative ways of assessing subcellular patterns of gold labeling. Methods Mol Biol *369*, 309-329.

Mazzoni, E.O., Mahony, S., Closser, M., Morrison, C.A., Nedelec, S., Williams, D.J., An, D., Gifford, D.K., and Wichterle, H. (2013). Synergistic binding of transcription factors to cell-specific enhancers programs motor neuron identity. Nat Neurosci *16*, 1219-1227.

Meer, E.J., Wang, D.O., Kim, S., Barr, I., Guo, F., and Martin, K.C. (2012). Identification of a cis-acting element that localizes mRNA to synapses. Proc Natl Acad Sci U S A *109*, 4639-4644.

Mejlvang, J., Olsvik, H., Svenning, S., Bruun, J.A., Abudu, Y.P., Larsen, K.B., Brech, A., Hansen, T.E., Brenne, H., Hansen, T.*, et al.* (2018). Starvation induces rapid degradation of selective autophagy receptors by endosomal microautophagy. J Cell Biol *217*, 3640-3655.

Melino, G., Cecconi, F., Pelicci, P.G., Mak, T.W., and Bernassola, F. (2019). Emerging roles of HECT-type E3 ubiquitin ligases in autophagy regulation. Mol Oncol *13*, 2033-2048.

Mendez, R., and Richter, J.D. (2001). Translational control by CPEB: a means to the end. Nat Rev Mol Cell Biol *2*, 521-529.

Menzies, F.M., Fleming, A., Caricasole, A., Bento, C.F., Andrews, S.P., Ashkenazi, A., Fullgrabe, J., Jackson, A., Jimenez Sanchez, M., Karabiyik, C.*, et al.* (2017). Autophagy and Neurodegeneration: Pathogenic Mechanisms and Therapeutic Opportunities. Neuron *93*, 1015-1034.

Metzger, M.B., Hristova, V.A., and Weissman, A.M. (2012). HECT and RING finger families of E3 ubiquitin ligases at a glance. J Cell Sci *125*, 531-537.

Metzger, M.B., Pruneda, J.N., Klevit, R.E., and Weissman, A.M. (2014). RING-type E3 ligases: master manipulators of E2 ubiquitin-conjugating enzymes and ubiquitination. Biochim Biophys Acta *1843*, 47-60.

Meyer, H.J., and Rape, M. (2014). Enhanced protein degradation by branched ubiquitin chains. Cell *157*, 910-921.

Mironov, A.A., and Beznoussenko, G.V. (2013). Correlative microscopy. Methods Cell Biol *113*, 209-255.

Mironov, A.A., Colanzi, A., Polishchuk, R.S., Beznoussenko, G.V., Mironov, A.A., Jr., Fusella, A., Di Tullio, G., Silletta, M.G., Corda, D., De Matteis, M.A.*, et al.* (2004). Dicumarol, an inhibitor of ADP-ribosylation of CtBP3/BARS, fragments golgi non-compact tubular zones and inhibits intra-golgi transport. Eur J Cell Biol *83*, 263-279.

Miyazaki, K., Fujita, T., Ozaki, T., Kato, C., Kurose, Y., Sakamoto, M., Kato, S., Goto, T., Itoyama, Y., Aoki, M.*, et al.* (2004). NEDL1, a novel ubiquitin-protein isopeptide ligase for dishevelled-1, targets mutant superoxide dismutase-1. J Biol Chem *279*, 11327-11335.

Miyazaki, K., Ozaki, T., Kato, C., Hanamoto, T., Fujita, T., Irino, S., Watanabe, K., Nakagawa, T., and Nakagawara, A. (2003). A novel HECT-type E3 ubiquitin ligase, NEDL2, stabilizes p73 and enhances its transcriptional activity. Biochem Biophys Res Commun *308*, 106-113.

Mizushima, N., Yoshimori, T., and Ohsumi, Y. (2011). The role of Atg proteins in autophagosome formation. Annu Rev Cell Dev Biol *27*, 107-132.

Monahan, Z., Ryan, V.H., Janke, A.M., Burke, K.A., Rhoads, S.N., Zerze, G.H., O'Meally, R., Dignon, G.L., Conicella, A.E., Zheng, W.*, et al.* (2017). Phosphorylation of the FUS low-complexity domain disrupts phase separation, aggregation, and toxicity. EMBO J *36*, 2951-2967.

Moore, A.S., and Holzbaur, E.L. (2016). Dynamic recruitment and activation of ALS-associated TBK1 with its target optineurin are required for efficient mitophagy. Proc Natl Acad Sci U S A *113*, E3349-3358.

Nagano, S., and Araki, T. (2021). Axonal Transport and Local Translation of mRNA in Neurodegenerative Diseases. Front Mol Neurosci *14*, 697973.

Nakamura, S., and Yoshimori, T. (2017). New insights into autophagosome-lysosome fusion. J Cell Sci *130*, 1209-1216.

Napoli, I., Mercaldo, V., Boyl, P.P., Eleuteri, B., Zalfa, F., De Rubeis, S., Di Marino, D., Mohr, E., Massimi, M., Falconi, M.*, et al.* (2008). The fragile X syndrome protein represses activity-dependent translation through CYFIP1, a new 4E-BP. Cell *134*, 1042-1054.

Narayanan, U., Nalavadi, V., Nakamoto, M., Pallas, D.C., Ceman, S., Bassell, G.J., and Warren, S.T. (2007). FMRP phosphorylation reveals an immediate-early signaling pathway triggered by group I mGluR and mediated by PP2A. J Neurosci *27*, 14349-14357.

Nazio, F., Strappazzon, F., Antonioli, M., Bielli, P., Cianfanelli, V., Bordi, M., Gretzmeier, C., Dengjel, J., Piacentini, M., Fimia, G.M.*, et al.* (2013). mTOR inhibits autophagy by controlling ULK1 ubiquitylation, self-association and function through AMBRA1 and TRAF6. Nat Cell Biol *15*, 406-416.

Nguyen, H.N., Byers, B., Cord, B., Shcheglovitov, A., Byrne, J., Gujar, P., Kee, K., Schule, B., Dolmetsch, R.E., Langston, W.*, et al.* (2011). LRRK2 mutant iPSC-derived DA neurons demonstrate increased susceptibility to oxidative stress. Cell Stem Cell *8*, 267-280.

Niccoli, T., and Partridge, L. (2012). Ageing as a risk factor for disease. Curr Biol *22*, R741-752.

Nijssen, J., Aguila, J., Hoogstraaten, R., Kee, N., and Hedlund, E. (2018). Axon-Seq Decodes the Motor Axon Transcriptome and Its Modulation in Response to ALS. Stem Cell Reports *11*, 1565-1578.

Nixon, R.A. (2017). Amyloid precursor protein and endosomal-lysosomal dysfunction in Alzheimer's disease: inseparable partners in a multifactorial disease. FASEB J *31*, 2729-2743.

Nussbacher, J.K., Tabet, R., Yeo, G.W., and Lagier-Tourenne, C. (2019). Disruption of RNA Metabolism in Neurological Diseases and Emerging Therapeutic Interventions. Neuron *102*, 294-320.

O'Donnell, A.M., Coyle, D., and Puri, P. (2016). Decreased expression of NEDL2 in Hirschsprung's disease. J Pediatr Surg *51*, 1839-1842.

Ogunjimi, A.A., Briant, D.J., Pece-Barbara, N., Le Roy, C., Di Guglielmo, G.M., Kavsak, P., Rasmussen, R.K., Seet, B.T., Sicheri, F., and Wrana, J.L. (2005). Regulation of Smurf2 ubiquitin ligase activity by anchoring the E2 to the HECT domain. Mol Cell *19*, 297-308.

Pak, Y., Glowacka, W.K., Bruce, M.C., Pham, N., and Rotin, D. (2006). Transport of LAPTM5 to lysosomes requires association with the ubiquitin ligase Nedd4, but not LAPTM5 ubiquitination. J Cell Biol *175*, 631-645.

Palmieri, M., Pal, R., Nelvagal, H.R., Lotfi, P., Stinnett, G.R., Seymour, M.L., Chaudhury, A., Bajaj, L., Bondar, V.V., Bremner, L.*, et al.* (2017). Corrigendum: mTORC1-independent TFEB activation via Akt inhibition promotes cellular clearance in neurodegenerative storage diseases. Nat Commun *8*, 15793.

Pankiv, S., Clausen, T.H., Lamark, T., Brech, A., Bruun, J.A., Outzen, H., Overvatn, A., Bjorkoy, G., and Johansen, T. (2007). p62/SQSTM1 binds directly to Atg8/LC3 to facilitate degradation of ubiquitinated protein aggregates by autophagy. J Biol Chem *282*, 24131-24145.

Parker, R., and Sheth, U. (2007). P bodies and the control of mRNA translation and degradation. Mol Cell *25*, 635-646.

Pearson, B.L., Simon, J.M., McCoy, E.S., Salazar, G., Fragola, G., and Zylka, M.J. (2016). Identification of chemicals that mimic transcriptional changes associated with autism, brain aging and neurodegeneration. Nat Commun *7*, 11173.

Pei, G., Buijze, H., Liu, H., Moura-Alves, P., Goosmann, C., Brinkmann, V., Kawabe, H., Dorhoi, A., and Kaufmann, S.H.E. (2017). The E3 ubiquitin ligase NEDD4 enhances killing of membrane-perturbing intracellular bacteria by promoting autophagy. Autophagy *13*, 2041-2055.

Persaud, A., Alberts, P., Amsen, E.M., Xiong, X., Wasmuth, J., Saadon, Z., Fladd, C., Parkinson, J., and Rotin, D. (2009). Comparison of substrate specificity of the ubiquitin ligases Nedd4 and Nedd4-2 using proteome arrays. Mol Syst Biol *5*, 333.

Persaud, A., Alberts, P., Hayes, M., Guettler, S., Clarke, I., Sicheri, F., Dirks, P., Ciruna, B., and Rotin, D. (2011). Nedd4-1 binds and ubiquitylates activated FGFR1 to control its endocytosis and function. EMBO J *30*, 3259-3273.

Persaud, A., Alberts, P., Mari, S., Tong, J., Murchie, R., Maspero, E., Safi, F., Moran, M.F., Polo, S., and Rotin, D. (2014). Tyrosine phosphorylation of NEDD4 activates its ubiquitin ligase activity. Sci Signal *7*, ra95.

Pham, N., and Rotin, D. (2001). Nedd4 regulates ubiquitination and stability of the guanine-nucleotide exchange factor CNrasGEF. J Biol Chem *276*, 46995-47003.

Pickart, C.M. (2000). Ubiquitin in chains. Trends Biochem Sci *25*, 544-548.

Pickford, F., Masliah, E., Britschgi, M., Lucin, K., Narasimhan, R., Jaeger, P.A., Small, S., Spencer, B., Rockenstein, E., Levine, B.*, et al.* (2008). The autophagy-related protein beclin 1 shows reduced expression in early Alzheimer disease and regulates amyloid beta accumulation in mice. J Clin Invest *118*, 2190-2199.

Pirmoradian, M., Budamgunta, H., Chingin, K., Zhang, B., Astorga-Wells, J., and Zubarev, R.A. (2013). Rapid and deep human proteome analysis by single-dimension shotgun proteomics. Mol Cell Proteomics *12*, 3330-3338.

Platta, H.W., Abrahamsen, H., Thoresen, S.B., and Stenmark, H. (2012). Nedd4-dependent lysine-11-linked polyubiquitination of the tumour suppressor Beclin 1. Biochem J *441*, 399-406.

Plechanovova, A., Jaffray, E.G., Tatham, M.H., Naismith, J.H., and Hay, R.T. (2012). Structure of a RING E3 ligase and ubiquitin-loaded E2 primed for catalysis. Nature *489*, 115-120.

Pohlmann, T., Baumann, S., Haag, C., Albrecht, M., and Feldbrugge, M. (2015). A FYVE zinc finger domain protein specifically links mRNA transport to endosome trafficking. Elife *4*.

Polo, S. (2012). Signaling-mediated control of ubiquitin ligases in endocytosis. BMC Biol *10*, 25.

Qiu, X., Wei, R., Li, Y., Zhu, Q., Xiong, C., Chen, Y., Zhang, Y., Lu, K., He, F., and Zhang, L. (2016). NEDL2 regulates enteric nervous system and kidney development in its Nedd8 ligase activity-dependent manner. Oncotarget *7*, 31440-31453.

Reiter, K.H., and Klevit, R.E. (2018). Characterization of RING-Between-RING E3 Ubiquitin Transfer Mechanisms. Methods Mol Biol *1844*, 3-17.

Riggs, C.L., Kedersha, N., Ivanov, P., and Anderson, P. (2020). Mammalian stress granules and P bodies at a glance. J Cell Sci *133*.

Rodrigues, E.M., Scudder, S.L., Goo, M.S., and Patrick, G.N. (2016). Abeta-Induced Synaptic Alterations Require the E3 Ubiquitin Ligase Nedd4-1. J Neurosci *36*, 1590-1595.

Rossier, B.C., Pradervand, S., Schild, L., and Hummler, E. (2002). Epithelial sodium channel and the control of sodium balance: interaction between genetic and environmental factors. Annu Rev Physiol *64*, 877-897.

Rotem, N., Magen, I., Ionescu, A., Gershoni-Emek, N., Altman, T., Costa, C.J., Gradus, T., Pasmanik-Chor, M., Willis, D.E., Ben-Dov, I.Z.*, et al.* (2017). ALS Along the Axons - Expression of Coding and Noncoding RNA Differs in Axons of ALS models. Sci Rep *7*, 44500.

Rotin, D., Kanelis, V., and Schild, L. (2001). Trafficking and cell surface stability of ENaC. Am J Physiol Renal Physiol *281*, F391-399.

Rotin, D., and Kumar, S. (2009). Physiological functions of the HECT family of ubiquitin ligases. Nat Rev Mol Cell Biol *10*, 398-409.

Rubino, E., Rainero, I., Chio, A., Rogaeva, E., Galimberti, D., Fenoglio, P., Grinberg, Y., Isaia, G., Calvo, A., Gentile, S.*, et al.* (2012). SQSTM1 mutations in frontotemporal lobar degeneration and amyotrophic lateral sclerosis. Neurology *79*, 1556-1562.

Rubinsztein, D.C., Codogno, P., and Levine, B. (2012). Autophagy modulation as a potential therapeutic target for diverse diseases. Nat Rev Drug Discov *11*, 709-730.

Russell, R.C., Tian, Y., Yuan, H., Park, H.W., Chang, Y.Y., Kim, J., Kim, H., Neufeld, T.P., Dillin, A., and Guan, K.L. (2013). ULK1 induces autophagy by phosphorylating Beclin-1 and activating VPS34 lipid kinase. Nat Cell Biol *15*, 741-750.

Sanchez-Tena, S., Cubillos-Rojas, M., Schneider, T., and Rosa, J.L. (2016). Functional and pathological relevance of HERC family proteins: a decade later. Cell Mol Life Sci *73*, 1955-1968.

Savio, M.G., Wollscheid, N., Cavallaro, E., Algisi, V., Di Fiore, P.P., Sigismund, S., Maspero, E., and Polo, S. (2016). USP9X Controls EGFR Fate by Deubiquitinating the Endocytic Adaptor Eps15. Curr Biol *26*, 173-183.

Saxton, R.A., and Sabatini, D.M. (2017). mTOR Signaling in Growth, Metabolism, and Disease. Cell *168*, 960-976.

Scheffner, M., and Kumar, S. (2014). Mammalian HECT ubiquitin-protein ligases: biological and pathophysiological aspects. Biochim Biophys Acta *1843*, 61-74.

Schindelin, J., Arganda-Carreras, I., Frise, E., Kaynig, V., Longair, M., Pietzsch, T., Preibisch, S., Rueden, C., Saalfeld, S., Schmid, B.*, et al.* (2012). Fiji: an open-source platform for biological-image analysis. Nat Methods *9*, 676-682.

Schmidt, M.F., Gan, Z.Y., Komander, D., and Dewson, G. (2021). Ubiquitin signalling in neurodegeneration: mechanisms and therapeutic opportunities. Cell Death Differ *28*, 570-590.

Seranova, E., Palhegyi, A.M., Verma, S., Dimova, S., Lasry, R., Naama, M., Sun, C., Barrett, T., Rosenstock, T.R., Kumar, D.*, et al.* (2020). Human Induced Pluripotent Stem Cell Models of Neurodegenerative Disorders for Studying the Biomedical Implications of Autophagy. J Mol Biol *432*, 2754-2798.

Settembre, C., Di Malta, C., Polito, V.A., Garcia Arencibia, M., Vetrini, F., Erdin, S., Erdin, S.U., Huynh, T., Medina, D., Colella, P.*, et al.* (2011). TFEB links autophagy to lysosomal biogenesis. Science *332*, 1429-1433.

Shah, S.S., and Kumar, S. (2021). Correction to: Adaptors as the regulators of HECT ubiquitin ligases. Cell Death Differ.

Sheng, Y., Hong, J.H., Doherty, R., Srikumar, T., Shloush, J., Avvakumov, G.V., Walker, J.R., Xue, S., Neculai, D., Wan, J.W., *et al.* (2012). A human ubiquitin conjugating enzyme (E2)-HECT E3 ligase structure-function screen. Mol Cell Proteomics *11*, 329-341.

Shenoy, S.K., Xiao, K., Venkataramanan, V., Snyder, P.M., Freedman, N.J., and Weissman, A.M. (2008). Nedd4 mediates agonist-dependent ubiquitination, lysosomal targeting, and degradation of the beta2-adrenergic receptor. J Biol Chem *283*, 22166-22176.

Shi, Y., Inoue, H., Wu, J.C., and Yamanaka, S. (2017). Induced pluripotent stem cell technology: a decade of progress. Nat Rev Drug Discov *16*, 115-130.

Shi, Y., Lin, S., Staats, K.A., Li, Y., Chang, W.H., Hung, S.T., Hendricks, E., Linares, G.R., Wang, Y., Son, E.Y., *et al.* (2018). Haploinsufficiency leads to neurodegeneration in C9ORF72 ALS/FTD human induced motor neurons. Nat Med *24*, 313-325.

Shimura, H., Mizuno, Y., and Hattori, N. (2012). Parkin and Parkinson disease. Clin Chem *58*, 1260-1261.

Shinada, K., Tsukiyama, T., Sho, T., Okumura, F., Asaka, M., and Hatakeyama, S. (2011). RNF43 interacts with NEDL1 and regulates p53-mediated transcription. Biochem Biophys Res Commun *404*, 143-147.

Sielaff, M., Kuharev, J., Bohn, T., Hahlbrock, J., Bopp, T., Tenzer, S., and Distler, U. (2017). Evaluation of FASP, SP3, and iST Protocols for Proteomic Sample Preparation in the Low Microgram Range. J Proteome Res *16*, 4060-4072.

Sigismund, S., Polo, S., and Di Fiore, P.P. (2004). Signaling through monoubiquitination. Curr Top Microbiol Immunol *286*, 149-185.

Simonsen, A., Birkeland, H.C., Gillooly, D.J., Mizushima, N., Kuma, A., Yoshimori, T., Slagsvold, T., Brech, A., and Stenmark, H. (2004). Alfy, a novel FYVE-domain-containing protein associated with protein granules and autophagic membranes. J Cell Sci *117*, 4239-4251.

Simonsen, A., Cumming, R.C., Brech, A., Isakson, P., Schubert, D.R., and Finley, K.D. (2008). Promoting basal levels of autophagy in the nervous system enhances longevity and oxidant resistance in adult Drosophila. Autophagy *4*, 176-184.

Sluimer, J., and Distel, B. (2018). Regulating the human HECT E3 ligases. Cell Mol Life Sci *75*, 3121-3141.

Snyder, P.M. (2005). Minireview: regulation of epithelial Na+ channel trafficking. Endocrinology *146*, 5079-5085.

Soldner, F., Laganiere, J., Cheng, A.W., Hockemeyer, D., Gao, Q., Alagappan, R., Khurana, V., Golbe, L.I., Myers, R.H., Lindquist, S., *et al.* (2011). Generation of isogenic pluripotent stem cells differing exclusively at two early onset Parkinson point mutations. Cell *146*, 318-331.

Song, E.J., Werner, S.L., Neubauer, J., Stegmeier, F., Aspden, J., Rio, D., Harper, J.W., Elledge, S.J., Kirschner, M.W., and Rape, M. (2010). The Prp19 complex and the Usp4Sart3 deubiquitinating enzyme control reversible ubiquitination at the spliceosome. Genes Dev *24*, 1434-1447.

Sopjani, M., Alesutan, I., Dermaku-Sopjani, M., Fraser, S., Kemp, B.E., Foller, M., and Lang, F. (2010). Down-regulation of Na+-coupled glutamate transporter EAAT3 and EAAT4 by AMP-activated protein kinase. J Neurochem *113*, 1426-1435.

Spence, J., Gali, R.R., Dittmar, G., Sherman, F., Karin, M., and Finley, D. (2000). Cell cycle-regulated modification of the ribosome by a variant multiubiquitin chain. Cell *102*, 67-76.

Spencer, B., Potkar, R., Trejo, M., Rockenstein, E., Patrick, C., Gindi, R., Adame, A., Wyss-Coray, T., and Masliah, E. (2009). Beclin 1 gene transfer activates autophagy and ameliorates the neurodegenerative pathology in alpha-synuclein models of Parkinson's and Lewy body diseases. J Neurosci *29*, 13578-13588.

Standart, N., and Weil, D. (2018). P-Bodies: Cytosolic Droplets for Coordinated mRNA Storage. Trends Genet *34*, 612-626.

Staub, O., Yeger, H., Plant, P.J., Kim, H., Ernst, S.A., and Rotin, D. (1997). Immunolocalization of the ubiquitin-protein ligase Nedd4 in tissues expressing the epithelial Na+ channel (ENaC). Am J Physiol *272*, C1871-1880.

Stavoe, A.K., Gopal, P.P., Gubas, A., Tooze, S.A., and Holzbaur, E.L. (2019). Expression of WIPI2B counteracts age-related decline in autophagosome biogenesis in neurons. Elife *8*.

Stavoe, A.K., Hill, S.E., Hall, D.H., and Colon-Ramos, D.A. (2016). KIF1A/UNC-104 Transports ATG-9 to Regulate Neurodevelopment and Autophagy at Synapses. Dev Cell *38*, 171-185.

Stavoe, A.K.H., and Holzbaur, E.L.F. (2019). Autophagy in Neurons. Annu Rev Cell Dev Biol *35*, 477-500.

Stavoe, A.K.H., and Holzbaur, E.L.F. (2020). Neuronal autophagy declines substantially with age and is rescued by overexpression of WIPI2. Autophagy *16*, 371-372.

Stewart, G.S., Panier, S., Townsend, K., Al-Hakim, A.K., Kolas, N.K., Miller, E.S., Nakada, S., Ylanko, J., Olivarius, S., Mendez, M.*, et al.* (2009). The RIDDLE syndrome protein mediates a ubiquitin-dependent signaling cascade at sites of DNA damage. Cell *136*, 420-434.

Sudol, M., and Hunter, T. (2000). NeW wrinkles for an old domain. Cell *103*, 1001-1004.

Sugeno, N., Hasegawa, T., Tanaka, N., Fukuda, M., Wakabayashi, K., Oshima, R., Konno, M., Miura, E., Kikuchi, A., Baba, T.*, et al.* (2014). Lys-63-linked ubiquitination by E3 ubiquitin ligase Nedd4-1 facilitates endosomal sequestration of internalized alpha-synuclein. J Biol Chem *289*, 18137-18151.

Sun, A., Wei, J., Childress, C., Shaw, J.H.t., Peng, K., Shao, G., Yang, W., and Lin, Q. (2017). The E3 ubiquitin ligase NEDD4 is an LC3-interactive protein and regulates autophagy. Autophagy *13*, 522-537.

Swatek, K.N., and Komander, D. (2016). Ubiquitin modifications. Cell Res *26*, 399-422.

Tajima, Y., Goto, K., Yoshida, M., Shinomiya, K., Sekimoto, T., Yoneda, Y., Miyazono, K., and Imamura, T. (2003). Chromosomal region maintenance 1 (CRM1)-dependent nuclear export of Smad ubiquitin regulatory factor 1 (Smurf1) is essential for negative regulation of transforming growth factor-beta signaling by Smad7. J Biol Chem *278*, 10716-10721.

Takahashi, K., Tanabe, K., Ohnuki, M., Narita, M., Ichisaka, T., Tomoda, K., and Yamanaka, S. (2007). Induction of pluripotent stem cells from adult human fibroblasts by defined factors. Cell *131*, 861-872.

Takahashi, K., and Yamanaka, S. (2006). Induction of pluripotent stem cells from mouse embryonic and adult fibroblast cultures by defined factors. Cell *126*, 663-676.

Tammineni, P., Ye, X., Feng, T., Aikal, D., and Cai, Q. (2017). Impaired retrograde transport of axonal autophagosomes contributes to autophagic stress in Alzheimer's disease neurons. Elife *6*.

Tan, J.M., Wong, E.S., Kirkpatrick, D.S., Pletnikova, O., Ko, H.S., Tay, S.P., Ho, M.W., Troncoso, J., Gygi, S.P., Lee, M.K.*, et al.* (2008). Lysine 63-linked ubiquitination promotes the formation and autophagic clearance of protein inclusions associated with neurodegenerative diseases. Hum Mol Genet *17*, 431-439.

Tang, L.Y., Yamashita, M., Coussens, N.P., Tang, Y., Wang, X., Li, C., Deng, C.X., Cheng, S.Y., and Zhang, Y.E. (2011). Ablation of Smurf2 reveals an inhibition in TGF-beta signalling through multiple mono-ubiquitination of Smad3. EMBO J *30*, 4777-4789.

Thapa, P., Shanmugam, N., and Pokrzywa, W. (2020). Ubiquitin Signaling Regulates RNA Biogenesis, Processing, and Metabolism. Bioessays *42*, e1900171.

Thurston, T.L., Ryzhakov, G., Bloor, S., von Muhlinen, N., and Randow, F. (2009). The TBK1 adaptor and autophagy receptor NDP52 restricts the proliferation of ubiquitin-coated bacteria. Nat Immunol *10*, 1215-1221.

Tinevez, J.Y., Perry, N., Schindelin, J., Hoopes, G.M., Reynolds, G.D., Laplantine, E., Bednarek, S.Y., Shorte, S.L., and Eliceiri, K.W. (2017). TrackMate: An open and extensible platform for single-particle tracking. Methods *115*, 80-90.

Tofaris, G.K., Kim, H.T., Hourez, R., Jung, J.W., Kim, K.P., and Goldberg, A.L. (2011). Ubiquitin ligase Nedd4 promotes alpha-synuclein degradation by the endosomal-lysosomal pathway. Proc Natl Acad Sci U S A *108*, 17004-17009.

Tooze, S.A., and Yoshimori, T. (2010). The origin of the autophagosomal membrane. Nat Cell Biol *12*, 831-835.

Tsang, B., Arsenault, J., Vernon, R.M., Lin, H., Sonenberg, N., Wang, L.Y., Bah, A., and Forman-Kay, J.D. (2019). Phosphoregulated FMRP phase separation models activity-dependent translation through bidirectional control of mRNA granule formation. Proc Natl Acad Sci U S A *116*, 4218-4227.

Tumbarello, D.A., Manna, P.T., Allen, M., Bycroft, M., Arden, S.D., Kendrick-Jones, J., and Buss, F. (2015). The Autophagy Receptor TAX1BP1 and the Molecular Motor Myosin VI Are Required for Clearance of Salmonella Typhimurium by Autophagy. PLoS Pathog *11*, e1005174.

Tushev, G., Glock, C., Heumuller, M., Biever, A., Jovanovic, M., and Schuman, E.M. (2018). Alternative 3' UTRs Modify the Localization, Regulatory Potential, Stability, and Plasticity of mRNAs in Neuronal Compartments. Neuron *98*, 495-511 e496.

Van Huysse, J.W., Amin, M.S., Yang, B., and Leenen, F.H. (2012). Salt-induced hypertension in a mouse model of Liddle syndrome is mediated by epithelial sodium channels in the brain. Hypertension *60*, 691-696.

Verdecia, M.A., Bowman, M.E., Lu, K.P., Hunter, T., and Noel, J.P. (2000). Structural basis for phosphoserine-proline recognition by group IV WW domains. Nat Struct Biol *7*, 639-643.

Verdecia MA, J.C., Wells NJ, Ferrer JL, Bowman ME, Hunter T, Noel JP. (2003). Conformational flexibility underlies ubiquitin ligation mediated by the WWP1 HECT domain E3 ligase. Mol Cell *11*, 249-259.

Vicinanza, M., Korolchuk, V.I., Ashkenazi, A., Puri, C., Menzies, F.M., Clarke, J.H., and Rubinsztein, D.C. (2015). PI(5)P regulates autophagosome biogenesis. Mol Cell *57*, 219-234.

Vieira, N., Rito, T., Correia-Neves, M., and Sousa, N. (2021). Sorting Out Sorting Nexins Functions in the Nervous System in Health and Disease. Mol Neurobiol *58*, 4070-4106.

Vijay-Kumar, S., Bugg, C.E., and Cook, W.J. (1987). Structure of ubiquitin refined at 1.8 A resolution. J Mol Biol *194*, 531-544.

Vilchez, D., Saez, I., and Dillin, A. (2014). The role of protein clearance mechanisms in organismal ageing and age-related diseases. Nat Commun *5*, 5659.

Vina-Vilaseca, A., Bender-Sigel, J., Sorkina, T., Closs, E.I., and Sorkin, A. (2011). Protein kinase C-dependent ubiquitination and clathrin-mediated endocytosis of the cationic amino acid transporter CAT-1. J Biol Chem *286*, 8697-8706.

Wan, W., You, Z., Zhou, L., Xu, Y., Peng, C., Zhou, T., Yi, C., Shi, Y., and Liu, W. (2018). mTORC1-Regulated and HUWE1-Mediated WIPI2 Degradation Controls Autophagy Flux. Mol Cell *72*, 303-315 e306.

Wang, C., Ward, M.E., Chen, R., Liu, K., Tracy, T.E., Chen, X., Xie, M., Sohn, P.D., Ludwig, C., Meyer-Franke, A., *et al.* (2017). Scalable Production of iPSC-Derived Human Neurons to Identify Tau-Lowering Compounds by High-Content Screening. Stem Cell Reports *9*, 1221-1233.

Wang, H., Sun, R.Q., Camera, D., Zeng, X.Y., Jo, E., Chan, S.M., Herbert, T.P., Molero, J.C., and Ye, J.M. (2016). Endoplasmic reticulum stress up-regulates Nedd4-2 to induce autophagy. FASEB J *30*, 2549-2556.

Wang, Z., Liu, Z., Chen, X., Li, J., Yao, W., Huang, S., Gu, A., Lei, Q.Y., Mao, Y., and Wen, W. (2019). A multi-lock inhibitory mechanism for fine-tuning enzyme activities of the HECT family E3 ligases. Nat Commun *10*, 3162.

Weber, J., Polo, S., and Maspero, E. (2019). HECT E3 Ligases: A Tale With Multiple Facets. Front Physiol *10*, 370.

Wei, R., Qiu, X., Wang, S., Li, Y., Wang, Y., Lu, K., Fu, Y., Xing, G., He, F., and Zhang, L. (2015). NEDL2 is an essential regulator of enteric neural development and GDNF/Ret signaling. Cell Signal *27*, 578-586.

Wenzel, D.M., and Klevit, R.E. (2012). Following Ariadne's thread: a new perspective on RBR ubiquitin ligases. BMC Biol *10*, 24.

Wertz, I.E., and Dixit, V.M. (2008). Ubiquitin-mediated regulation of TNFR1 signaling. Cytokine Growth Factor Rev *19*, 313-324.

Wheeler, J.R., Jain, S., Khong, A., and Parker, R. (2017). Isolation of yeast and mammalian stress granule cores. Methods *126*, 12-17.

Wheeler, J.R., Matheny, T., Jain, S., Abrisch, R., and Parker, R. (2016). Distinct stages in stress granule assembly and disassembly. Elife *5*.

Wiederschain, D., Wee, S., Chen, L., Loo, A., Yang, G., Huang, A., Chen, Y., Caponigro, G., Yao, Y.M., Lengauer, C., *et al.* (2009). Single-vector inducible lentiviral RNAi system for oncology target validation. Cell Cycle *8*, 498-504.

Wiesner, S., Ogunjimi, A.A., Wang, H.R., Rotin, D., Sicheri, F., Wrana, J.L., and Forman-Kay, J.D. (2007). Autoinhibition of the HECT-type ubiquitin ligase Smurf2 through its C2 domain. Cell *130*, 651-662.

Woelk, T., Oldrini, B., Maspero, E., Confalonieri, S., Cavallaro, E., Di Fiore, P.P., and Polo, S. (2006). Molecular mechanisms of coupled monoubiquitination. Nat Cell Biol *8*, 1246-1254.

Woelk, T., Sigismund, S., Penengo, L., and Polo, S. (2007). The ubiquitination code: a signalling problem. Cell Div *2*, 11.

Wolozin, B., and Ivanov, P. (2019). Stress granules and neurodegeneration. Nat Rev Neurosci *20*, 649-666.

Wong, E., and Cuervo, A.M. (2010). Integration of clearance mechanisms: the proteasome and autophagy. Cold Spring Harb Perspect Biol *2*, a006734.

Wong, Y.C., and Holzbaur, E.L. (2014). The regulation of autophagosome dynamics by huntingtin and HAP1 is disrupted by expression of mutant huntingtin, leading to defective cargo degradation. J Neurosci *34*, 1293-1305.

Worby, C.A., and Dixon, J.E. (2002). Sorting out the cellular functions of sorting nexins. Nat Rev Mol Cell Biol *3*, 919-931.

Wu, C.H., Fallini, C., Ticozzi, N., Keagle, P.J., Sapp, P.C., Piotrowska, K., Lowe, P., Koppers, M., McKenna-Yasek, D., Baron, D.M., *et al.* (2012). Mutations in the profilin 1 gene cause familial amyotrophic lateral sclerosis. Nature *488*, 499-503.

Wu, H., Zhou, J., Zhu, T., Cohen, I., and Dictenberg, J. (2020). A kinesin adapter directly mediates dendritic mRNA localization during neural development in mice. J Biol Chem *295*, 6605-6628.

Yamano, K., Matsuda, N., and Tanaka, K. (2016). The ubiquitin signal and autophagy: an orchestrated dance leading to mitochondrial degradation. EMBO Rep *17*, 300-316.

Yan, Y., Shin, S., Jha, B.S., Liu, Q., Sheng, J., Li, F., Zhan, M., Davis, J., Bharti, K., Zeng, X., *et al.* (2013). Efficient and rapid derivation of primitive neural stem cells and generation of brain subtype neurons from human pluripotent stem cells. Stem Cells Transl Med *2*, 862-870.

Yang, C., Danielson, E.W., Qiao, T., Metterville, J., Brown, R.H., Jr., Landers, J.E., and Xu, Z. (2016). Mutant PFN1 causes ALS phenotypes and progressive motor neuron degeneration in mice by a gain of toxicity. Proc Natl Acad Sci U S A *113*, E6209-E6218.

Yang, F., Shen, Y., Camp, D.G., 2nd, and Smith, R.D. (2012). High-pH reversed-phase chromatography with fraction concatenation for 2D proteomic analysis. Expert Rev Proteomics *9*, 129-134.

Yang, H., Yu, N., Xu, J., Ding, X., Deng, W., Wu, G., Li, X., Hou, Y., Liu, Z., Zhao, Y., *et al.* (2018). SMURF1 facilitates estrogen receptor a signaling in breast cancer cells. J Exp Clin Cancer Res *37*, 24.

Ye, X., Wang, L., Shang, B., Wang, Z., and Wei, W. (2014). NEDD4: a promising target for cancer therapy. Curr Cancer Drug Targets *14*, 549-556.

Yu, J., Vodyanik, M.A., Smuga-Otto, K., Antosiewicz-Bourget, J., Frane, J.L., Tian, S., Nie, J., Jonsdottir, G.A., Ruotti, V., Stewart, R., *et al.* (2007). Induced pluripotent stem cell lines derived from human somatic cells. Science *318*, 1917-1920.

Yuan, W.C., Lee, Y.R., Lin, S.Y., Chang, L.Y., Tan, Y.P., Hung, C.C., Kuo, J.C., Liu, C.H., Lin, M.Y., Xu, M., *et al.* (2014). K33-Linked Polyubiquitination of Coronin 7 by Cul3-KLHL20 Ubiquitin E3 Ligase Regulates Protein Trafficking. Mol Cell *54*, 586-600.

Zachari, M., and Ganley, I.G. (2017). The mammalian ULK1 complex and autophagy initiation. Essays Biochem *61*, 585-596.

Zaessinger, S., Busseau, I., and Simonelig, M. (2006). Oskar allows nanos mRNA translation in Drosophila embryos by preventing its deadenylation by Smaug/CCR4. Development *133*, 4573-4583.

Zeitelhofer, M., Karra, D., Macchi, P., Tolino, M., Thomas, S., Schwarz, M., Kiebler, M., and Dahm, R. (2008). Dynamic interaction between P-bodies and transport ribonucleoprotein particles in dendrites of mature hippocampal neurons. J Neurosci *28*, 7555-7562.

Zhang, L., Haraguchi, S., Koda, T., Hashimoto, K., and Nakagawara, A. (2011). Muscle atrophy and motor neuron degeneration in human NEDL1 transgenic mice. J Biomed Biotechnol *2011*, 831092.

Zhang, Y., Chang, C., Gehling, D.J., Hemmati-Brivanlou, A., and Derynck, R. (2001). Regulation of Smad degradation and activity by Smurf2, an E3 ubiquitin ligase. Proc Natl Acad Sci U S A *98*, 974-979.

Zhang, Y.E. (2018). Mechanistic insight into contextual TGF-beta signaling. Curr Opin Cell Biol *51*, 1-7.

Zhao, H., Zhao, Y.G., Wang, X., Xu, L., Miao, L., Feng, D., Chen, Q., Kovacs, A.L., Fan, D., and Zhang, H. (2013). Mice deficient in Epg5 exhibit selective neuronal vulnerability to degeneration. J Cell Biol *200*, 731-741.

Zhao, Y.G., and Zhang, H. (2019). Autophagosome maturation: An epic journey from the ER to lysosomes. J Cell Biol *218*, 757-770.

Acknowledgment

I would like to thank all the people, family, friends and colleagues, who made this work possible.

Above all, I would like to thank my supervisor, Prof. Simona Polo, for giving me the opportunity to join her lab and for her constant mentoring during these years. Her trust and encouragement she gave me every day, and her scientific and, most importantly, human support have been essential for both enjoying successes and overcoming difficulties faced during this journey.

A very special thanks goes to Elena Maspero, my lab-coach, for her precious teaching, practical and theoretical help, from the beginning to the end of my PhD. She has always been present, no matter what I needed and despite her many duties.

I am grateful to all the members of Polo group, for the mutual scientific and human support, for being always helpful and kind, and for all the inspiring discussions. The friendly environment that welcomes everyone in the Polo's Lab is something extraordinary.

I would like to thank all my family and friends, for loving and supporting me, and especially for making me discover that *"no man is a failure who has friends"* (from the movie It's a Wonderful Life).